ASSEMBLING AN ARCHEAN MAGMATIC PLUMBING SYSTEM: GEOCHEMICAL EVOLUTION, EMPLACEMENT, AND METALLOGENIC IMPLICATIONS OF SUBVOLCANIC INTRUSIONS IN THE YELLOWKNIFE GREENSTONE BELT, N.W.T., CANADA

by

Sarah Catherine Speight

M. Sc., Laurentian University, 2013
B. Sc.-H., University of New Brunswick, 2011

A Dissertation Submitted in Partial Fulfillment
of the Requirements for the Degree of

Doctor of Philosophy

in the Graduate Academic Unit of Earth Sciences

Supervisors: Chris McFarlane, Ph. D., Department of Earth Sciences
Jacob Hanley, Ph. D., Department of Geology, Saint Mary's University

Examining Board: Cliff Shaw, Ph. D., Department of Earth Science
Joe White, Ph. D., Department of Earth Sciences
Sara Eisler, Ph. D., Department of Chemistry

External Examiner: Andrew Conly, Ph. D., Department of Geology, Lakehead University

This dissertation is accepted by the
Dean of Graduate Studies

THE UNIVERSITY OF NEW BRUNSWICK

February 2023

© Sarah Speight, 2023

ABSTRACT

The Yellowknife greenstone belt (YGB), located in the Archean Slave Province in the Northwest Territories, Canada, consists of mafic and felsic metavolcanic sequences intruded by dikes and regional plutons. The locally known "#9" dikes comprise three generations of intrusions that were not geochemically differentiated or genetically linked to a parental source, including, feldspar-quartz porphyry (FQP), quartz porphyry (QZP), and aplite dikes. Despite the spatial association with mineralization and inferred relationship to overlying volcaniclastic units, the dikes remain poorly understood. Therefore, a multi-analytical approach was needed to characterize the evolution, emplacement, and metallogenic signature of YGB magmatism.

The lithogeochemical signatures of the dikes, combined with U-Pb zircon geochronology, differentiated them into three groups: 1) the Ryan Lake Pluton (RLP), represented by tonalites (2662 Ma) and granodiorites (2647 Ma), and the FQP (2674 – 2662 Ma) and aplite-1(a) dikes (2663 Ma); 2) the Defeat Suite granite (2580 Ma) and aplite-1(b) dikes (2662 Ma); and 3) the Duckfish granite (2576 Ma) and the aplite-2 dikes (ca. 2611 Ma). The intrusions were also compared to the overlying felsic volcaniclastics of the Townsite Formation and Banting Group. When combined with field observations, this confirms that only the FQP dikes are subvolcanic feeders to these units. The ambiguous lithogeochemistry of the QZP dikes (2770 Ma) and the age gap with the main diking event (ca. 2662 Ma) did not allow for a plutonic connection. Rather, the QZP and one FQP dike proximal to the Duckfish granite may reflect magmatism related to the Central Slave

Basement Complex. Additionally, macro- and micro-scale textural analysis of the aplite dikes provided evidence of emplacement during crystallization of the parental magmas. The three groups of aplite dikes (1(a), 1(b), and 2) commonly have quartz cores and discontinuous quartz pods at the outcrop scale that reflect crystallization from a volatile-saturated melt.

Finally, analysis of zircon-hosted melt inclusions (MI) from a subset of YGB dikes and plutons showed evidence of early precious metal-enrichment. Careful data filtering to remove contaminated inclusions produced the first MI dataset from the Archean YGB which represents primary silicate melts. Zircon-hosted MI that contains accidentally trapped phases also provide valuable information, despite the semi-quantitative nature of the data. These mixed MI provide direct evidence of Ti- and H_20-saturation through the presence of (Fe)-Ti-oxides and hydrous minerals (e.g., biotite, amphibole). This preliminary work establishes that critical information related to primary metal signatures in the YGB can be obtained from Archean MI.

ACKNOWLEDGEMENTS

My thesis would not have been possible without the assistance and support of my co-supervisors, Dr. Chris McFarlane and Dr. Jacob Hanley. Chris and Jake's time and effort into my project and mentorship are invaluable, and I will always be appreciative and grateful to them. They helped me figure out a way forward at every turn and through every obstacle. Along with Dr. Stefan Kruse, the committee has provided critical feedback on numerous drafts of my thesis; after each revision, my thesis was better, and I learned.

I am very thankful for the opportunity to work in Yellowknife with Gold Terra Resource Corp., the company that initiated and in part funded this project. Thanks to Dr. David Lentz, I was introduced to the Yellowknife crew, who started this project and provided guidance in the early stages. I was given the opportunity to travel to a new place, study rocks that I love, and meet new people, which I am grateful for. I am thankful to everyone at Gold Terra Resources for their continuous support and patience as I navigated my thesis and life. I would like to thank Hendrik Falck and the Northwest Territories Geologic Survey who provided important insight into the Yellowknife geology and valuable resources.

Last but certainly not least, I would like to acknowledge the love and support that I received from my family and friends from day one. Working on my thesis has been one of the most challenging and rewarding experiences of my life, and I know that it would not have been possible without the balance that my family and friends bring to my life. To Ethan and Jay, always remember that a dream and hard work can get you anywhere once

you set your mind to it. Finally, to my husband and partner in crime, Matt, thank you for everything you have done and sacrificed for me. I will never forget your unwavering support and how you believed in me. I love you, always.

Table of Contents

ABSTRACT ii
ACKNOWLEDGEMENTS iv
TABLE OF CONTENTS vi
LIST OF TABLES x
LIST OF FIGURES xi
LIST OF SYMBOLS, NOMENCLATURE OR ABBREVIATIONS xiv
1. Introduction and dissertation overview 1
1.1. Statement of collaboration 1
1.2. Dissertation history 2
1.3. Field area overview 3
1.4. Detailed regional geology review 5
1.4.1. Basement Rocks 6
1.4.2. The Kam Group 7
1.4.3. The Banting Group 11
1.4.4. The Duncan Lake Group 12
1.4.5. The Jackson Lake Formation 12
1.4.6. Plutonism 13
1.4.7. Metamorphism and deformation 15
1.4.8. Mineralization 16
1.5. Dissertation hypotheses and objectives 18
1.6. Dissertation structure 21
1.7. References 25
2. Geodynamic evolution of felsic magmatism in the Yellowknife greenstone belt, N.W.T., Canada: evidence for Archean magmatism in a volatile-saturated environment 30
2.1. Abstract 30
2.2. Introduction 32
2.3. Regional Geology 34
2.4. Methods 37
2.5. Results 39
2.5.1. Sample descriptions 39
2.5.2. Petrography and mineral chemistry 46
2.5.3. Whole-rock geochemistry 54

2.5.4. Magmatic evolution and element mobility 61
2.5.5. Tectonic discrimination 63
2.5.6. Granite discrimination 65
2.5.7. TTG versus post-2.5 Ga granitoid signatures 67
2.6. Discussion 70
2.6.1. Stages of aplite dike emplacement and evidence for volatile saturation .. 70
2.6.2. Geochemical comparison of aplites and the stage of dike emplacement . 76
2.6.3. Genetic link between dikes and parental plutons 78
2.6.4. Magmatic fractionation in the Archean 82
2.6.5. The geotectonic setting and granite differentiation of YGB dikes and plutons 86
2.6.6. Primary magma chemistry of YGB intrusions 88
2.7. Conclusions 91
2.8. References 122
3. U-Pb geochronology and zircon mineral chemistry of syn-volcanic and plutonic intrusions in the Yellowknife greenstone belt, NWT, Canada: understanding an Archean magmatic plumbing system 128
3.1. Abstract 128
3.2. Introduction 130
3.3. Geological setting 133
3.4. Methods 135
3.4.1. Sample collection and processing 135
3.4.2. Petrography 136
3.4.3. U-Pb geochronology and zircon mineral chemistry 137
3.5. Results 139
3.5.1. Lithogeochemical classification 139
3.5.2. Sample descriptions 141
3.5.3. Optical petrography 144
3.5.4. SEM-EDS and µXRF 147
3.5.5. U-Pb geochronology 148
3.5.6. Zircon mineral chemistry 160
3.6. Discussion 167
3.6.1. U-Pb geochronology of the YGB dikes and plutons 167

3.6.2. Zircon mineral chemistry link between YGB dikes and plutons 181
3.6.3. FQP connection to the Banting Group and Townsite Formation 183
3.6.4. The magmatic plumbing system of the YGB dikes, plutons, and related volcaniclastic rocks..... 186
3.7. Conclusions..... 188
3.8. References..... 221
4. Preliminary zircon-hosted silicate melt and mineral inclusion data from plutonic rocks of the Yellowknife greenstone belt, NWT: insights into pre-eruptive Archean magmas..... 228
4.1. Abstract 228
4.2. Introduction..... 229
4.3. Regional Geology..... 233
4.3.1. YGB mineralization..... 235
4.4. Methods 236
4.5. Results 239
4.5.1. Petrography 239
4.5.2. LA-ICP-MS results for zircon-hosted SMI and mixed MMI 242
4.6. Discussion..... 253
4.6.1. Implications of SMI and mixed MMI mineralogy..... 254
4.6.2. SMI composition compared to lithogeochemistry 256
4.6.3. Metal characteristics of YGB magmas: insights into mineralization 259
4.7. Conclusions..... 264
4.8. Future work..... 265
4.9. References..... 302
5. Conclusions 308
5.1. Dissertation contributions..... 313
5.2. Future work..... 314
Appendix 1: Geodynamic evolution of felsic magmatism in the Yellowknife greenstone belt, N.W.T., Canada: evidence for Archean magmatism in a volatile-saturated environment 316
Table A1.1 317
Table A1.2 319

Appendix 2: U-Pb geochronology and zircon mineral chemistry of syn-volcanic and plutonic intrusions in the Yellowknife greenstone belt, NWT, Canada: understanding an Archean magmatic plumbing system 337
Appendix 2.1 338
Table A2.1 341
Table A2.2 350
Table A2.3 354
Curriculum Vitae

List of Tables

Table 2-1: Summary of petrographic characteristics used by Hibbard (1980) and Hibbard and Watters (1985) to determine the stage of dike emplacement 120
Table 2-2: Petrographically determined stage of emplacement for aplite dikes in the YGB following the characteristics determined by Hibbard (1980) and Hibbard and Watters (1985) 121
Table 3-1: A summary of the distribution of each zircon colour population as they relate to each sample and lithology. 213
Table 3-2: Summary of U-Pb geochronology ages separated by type of age calculation. 214
Table 3-3: Summary of CA-TIMS calculated weighted mean ages for 5 of 6 samples selected for analysis chosen to refine the Concordia ages determined by LA-ICP-MS. 216
Table 3-4: Summary of minimum, maximum, and average zircon trace element chemistry 217
Table 4-1: Summary of the type of inclusion encountered in each sample analyzed by LA-ICP-MS 285
Table 4-2: Zircon-hosted melt and mineral inclusion data from four lithologies from the YGB, including three FQP dikes, a QZP dike, tonalitic RLP, and Defeat Suite granite 286

List of Figures

Fig. 1.1: Simplified geologic map and stratigraphic column (and ages) of the YGB in the Archean Slave province of the Canadian Shield (modified and complied from Ootes and Lentz 2002, Bleeker and Hall 2007, Ootes et al. 2007)..... 23
Fig. 2.1: Textures and contact relationships between aplite dikes from the southern (aplite-1) and northern (aplite-2) field areas. The dikes were found hosted in mafic volcanic flow (MVF), granodiorite (GND), and tonalite (TON). 95
Fig. 2.2: Common hand sample textures of aplite dikes. 97
Fig. 2.3: Field and hand sample images of granitic dikes with continuous quartz cores and discontinuous quartz pods, all found in dikes hosted by mafic volcanics and not in the RLP. 99
Fig. 2.4: Hand sample images of representative textures and samples from: (A) feldspar-quartz porphyry, (B) quartz porphyry, (C) intermediate dike, (D) intermediate volcanic tuff, (E) tonalite, (F) granodiorite, (G) Defeat Suite granite, and (H) Duckish granite. 101
Fig. 2.5: Multi-element μXRF compositional maps of standard polished thin sections, focusing on aplite dikes. Each colour represents a different element indicated in the image..... 102
Fig. 2.6: Petrographic images for aplite-1 and aplite-2 dikes, along with examples for each stage of emplacement 103
Fig. 2.7: Petrographic images of representative textures taken in cross-polarized light: (A) feldspar-quartz porphyry, (B) quartz porphyry, (C) intermediate dike, and (D) intermediate volcanic tuff. 105
Fig. 2.8: Petrographic images of representative textures taken in cross-polarized light: (A) tonalite, (B) granodiorite, (C) Defeat Suite granite, (D) Duckfish granite. 106
Fig. 2.9: Chondrite-normalized REE diagrams, separated by similarity and lithology (Sun and McDonough 1989). 107
Fig. 2.10: General element ratio (GER) diagram of molar K/Al plotted against molar (2Ca+Na+K)/Al for YGB samples. 108
Fig. 2.11: Geochemical classification of felsic and intermediate rocks from the YGB using major and trace elements..... 109
Fig. 2.12: Magmatic evolution and element mobility diagrams comparing major and trace elements to Zr/TiO_2 (ppm/wt. %), with three groups highlighted, including the aplite-1(a), aplite-1(b), and aplite-2 dikes and potentially associated parental plutons (Torró et al. 2017). 111
Fig. 2.13: Tectonic discrimination diagrams of felsic to intermediate rocks from the YGB, using trace elements to determine the tectonic setting of each lithology. 113
Fig. 2.14: Geochemical discrimination diagrams using major and trace elements to classify felsic and intermediate rocks of the YGB. 114
Fig. 2.15: Trace element diagrams indicating the tonalite-trondhjemite-granodiorite (TTG) and arc signatures of felsic and intermediate rocks of the YGB..... 115

Fig. 2.16: Schematic depiction of locally-sourced dikes and their relative timing based on models by Hibbard (1980) and Hibbard and Watters (1985). 116
Fig. 2.17: Geochemical comparison of aplitic dikes based on their petrographically determined stage of emplacement after Hibbard (1980) and Hibbard and Watters (1985). 117
Fig. 2.18: Trace element discrimination diagram comparing La_N/Yb_N vs. Yb_N (chondrite-normalized) with three Archean tholeiite partial melting curves added. 119
Fig. 3.1: Field and hand sample images of representative lithologies. 193
Fig. 3.2: Petrographic images of polished thin sections from each lithology, including (A-E) FQP, (F) QZP, (G-H) aplite 1(a), (I) tonalite, (J) granodiorite, (K) Defeat Suite granite, (L) Duckfish granite. 194
Fig. 3.3: Multi-element µXRF images of standard polished thin sections that are 27x46 mm. 197
Fig. 3.4: SEM-BSE of *in-situ* zircon grains in polished thin sections, showing their relative locations and associated mineralogy. 198
Fig. 3.5: A selection of SEM-EDS back-scatter electron images that have been contrast-adjusted to highlight the internal structures of zircons, including oscillatory zoning, irregular and patchy zoning, fractures, inclusions, inherited zircon cores, and sieve texture. 199
Fig. 3.6: Concordia diagrams of U-Pb data from YGB intrusions. 200
Fig. 3.7: U-Pb isotopic data for QZP sample SS18-082. 203
Fig. 3.8: Comparison of zircon mineral chemistry data through time. (A) Th/U, (B) Hf (C) Eu/Eu*. 204
Fig. 3.9: Comparison of zircon trace element data for concordant analyses. 205
Fig. 3.10: Chondrite-normalized REE diagrams showing zircon mineral chemistry for each sample, grouped by lithology and filtered by the crystallization age of each sample (Sun and McDonough 1989). 206
Fig. 3.11: Comparison of zircon trace element data to the calculated Ti-in-zircon temperatures. 207
Fig. 3.12: Summary of events within the Slave craton, focusing on those related to the formation of the YGB, as they relate to the new U-Pb ages presented in this study [modified from Bleeker and Hall (2007) and Ootes et al. (2011)]. 208
Fig. 3.13: Comparison of whole-rock geochemistry data from this study and the data presented by Cousens et al. (2002) for the Banting Group and Cousens (2000) and Finnigan (2000) for the Townsite Formation. 210
Fig. 3.14: Schematic depiction (not to scale) of tonalitic and granodioritic intrusion (Ryan Lake Pluton) at ca. 2662 Ma. 211
Fig. 4.1: Schematic diagram of zircon with four types of inclusions, including silicate melt, sulfide melt or mineral, oxide mineral, and a mixed silicate and mineral inclusion. 267
Fig. 4.2: Scanning electron microscope backscatter electron image of a polished zircon with exposed inclusions and fractures along the exterior of the grain and cartoon

illustration of laser-drilling for zircon-hosted melt inclusions that are encapsulated in the host phase. 268
Fig. 4.3: Hand sample images of each sample selected for melt inclusion analysis..... 269
Fig. 4.4: Transmitted light photomicrographs of zircon-hosted melt inclusions from (A) Defeat Suite granite, and (B) FQP dike. 270
Fig. 4.5: Scanning electron microscope-backscatter electron images of exposed zircon-hosted inclusions. 271
Fig. 4.6: Raw LA-ICP-MS signals from three different zircon-hosted inclusions, all with different chemical characteristics..... 272
Fig. 4.7: Flow chart illustrating the data filtering protocol used to isolate data representing bulk silicate melt inclusions. 273
Fig. 4.8: Illustration indicating the types of inclusions encountered in this study from four different lithologies..... 274
Fig. 4.9: Comparison of major and trace element data to SiO_2 for SMI and MMI of the YGB, including A) Na_2O, B) K_2O, C) CaO, D) Mg #, E) TiO_2, F) Cs, and G) As. 275
Fig. 4.10: Comparison of SMI (filled symbols) from this study to average lithogeochemistry of Speight et al., (2023a). 276
Fig. 4.11: Comparison of metal concentrations to the Mg # of SMI and average lithogeochemical data and the upper continental crust. 277
Fig. 4.12: Comparison of Ag and As concentrations in mixed melt and mineral inclusion (MMI) data from this study..... 278
Fig. 4.13: Comparison of Mo and Cu concentrations in mixed melt and mineral inclusion (MMI) data from this study..... 280
Fig. 4.14: Comparison of W and Sn concentrations in mixed melt and mineral inclusion (MMI) data from this study..... 282
Fig. 4.15: Schematic depiction of RLP magmatic plumping system within the YGB, showing the relative location of aplite dikes-1(a) and -1(b) and the Defeat Suite granite (Speight et al. 2023b). 284

List of Symbols, Nomenclature or Abbreviations

%Pb*	percentage of radiogenic Pb
µm	micrometer
µXRF	micro-X-Ray Fluorescence
ap	apatite
APL 1(a)	aplite-1(a)
APL 1(b)	aplite-1(b)
BIF	banded iron formation
bt	biotite
ca.	circa
CA-TIMS	Chemical abrasion-thermal ionization mass spectrometry
CSBC	Central Slave Basement Complex
CSCG	Central Slave Cover Group
feld	feldspar
Fm	Formation
FQP	feldspar-quartz porphyry
Ga	billion years
GND	granodiorite
GRN 1	Defeat Suite granite
GRN 2	Duckfish granite
km	kilometer
LA-ICP-MS	Laser ablation-inductively coupled plasma-mass spectrometry
Ma	million years
MSWD	mean squared weighted deviation
MVF	mafic volcanic flow
n	number of analyses
ppb	parts per billion
ppm	parts per million
qtz	quartz
QZP	quartz porphyry
REE	rare earth element
RLP	Ryan Lake Pluton
SEM-BSE	scanning electron microscope-backscatter electron
TON	tonalite
UNB	University of New Brunswick
wt. %	weight percent
YGB	Yellowknife greenstone belt
YRFZ	Yellowknife River Fault Zone
zr	zircon

1. Introduction and dissertation overview

1.1. Statement of collaboration

This dissertation is based on field work and results from the Yellowknife greenstone belt (YGB) in the Northwest Territories, Canada. The project was initiated by Dr. David Lentz and the industry partner Gold Terra Resource Corp. Sampling and field mapping was carried out by the student and occasional samples were obtained and documented by geologists of the Gold Terra Resources team. The research and results presented in Chapters 2, 3, and 4 were greatly supported by discussions with both supervisors, Dr. Chris McFarlane and Dr. Jacob Hanley.

As co-supervisors, Dr. McFarlane and Dr. Hanley contributed to each chapter with thoughtful comments, feedback, and edits throughout the writing and data collection process. All petrography, lithogeochemical sample submission, data interpretations, and writing were carried out by the student as the lead author on each manuscript, with input from co-supervisors. For Chapter 2, micro-X-Ray Fluorescence (μXRF) was assisted by lab technician Brandon Boucher at the University of New Brunswick (UNB). Chapter 3 benefited from the addition of scanning electron microscopy-backscatter electron (SEM-BSE) images and mineral chemistry collected by Dr. Hanley at St. Mary's University and chemical abrasion-thermal ionization mass spectrometry (CA-TIMS) analysis of zircons by Dr. Jim Crowley at Boise State University. The collection of U-Pb geochronology and zircon mineral chemistry was assisted by Brandon Boucher and Dr. McFarlane at the UNB. An early draft of this chapter was improved with feedback from Luke Ootes, Hendrik Falck,

and Gold Terra Resource Corp. The melt inclusion data presented in Chapter 4 was collected at the University of Toronto by Dr. Hanley and Dr. Zoltán Zajacz. All final chapters were improved with the comments and feedback from Dr. McFarlane, Dr. Hanley, and Dr. Stefan Kruse.

This dissertation was financially supported by several organizations, industry partners and personal scholarships, including Gold Terra Resource Corp., Natural Sciences and Engineering Research Council of Canada – PGS-D and Discovery Grants, the UNB, St. Mary's University Mineral Exploration and Ore Fluids Laboratory, and the Northwest Territories Geologic Survey.

1.2. Dissertation history

Active exploration in the Yellowknife Greenstone belt (YGB) by Gold Terra Resource Corp. provided an excellent opportunity to collect samples and partake in mapping initiatives. The early phases of the project were spent in the field with Gold Terra Resources collecting preliminary samples to identify gaps in current YGB knowledge. The YGB has been an area of mining, exploration, and research since the early 1900s and is host to the historic Con and Giant mines (Helmstaedt 2006). These shear zone-hosted, orogenic deposits produced approximately 13 Moz gold between 1938 and 2004 before the Con and Giant mines were shut down (Bullen and Robb 2006, Moir et al. 2006, Silke 2009).

Initial examination of YGB samples and literature determined that there is a lack of dedicated research about the magmatic history in the belt and what role magmatism played in the development of gold mineralization. Therefore, the areas proximal to the

Ryan Lake Pluton (RLP), Defeat Suite granite, and Duckfish granite were chosen based on their spatial association with the main dike field. However, samples reflecting the Defeat Suite granite came from the eastern margin of the YGB. Preliminary sampling took place during the 2016 field season, and information derived from this field work was used to delineate the areas for final sampling in 2018. The samples from this thesis reflect a stratigraphic succession from three field areas including: 1) the RLP, adjacent porphyries and aplites within the main dike field within the Kam Group, 2) the Duckfish granite and proximal dikes hosted in mafic volcanic flows of the Kam Group and, finally 3) two samples from the Defeat Suite granite near Mason Lake in the eastern YGB.

1.3. Field area overview

The YGB occupies the southwestern margin of the Archean Slave province in the Northwest Territories, Canada (Fig. 1.1). It is a north-south trending sequence consisting of mafic and felsic metavolcanic and intrusive bodies, with an unconformably overlying conglomeratic package (Henderson and Brown 1966, Helmstaedt and Padgham 1986, Bleeker et al. 1999a). The belt developed over a period of 200 million years, including syn- and post-volcanic intrusions and sedimentation (Isachsen and Bowring 1994). The YGB is a homoclinal sequence with a sub-vertical dip and southeast younging direction. The area has undergone regional metamorphism to greenschist-amphibolite facies, and deformation that has resulted in multiple folding and faulting events, initiated at 2630 Ma with the intrusion of the Defeat Suite granite (Martel and Lin 2006, Thompson 2006). Proterozoic faults have dismembered the YGB into four major segments (Helmstaedt and

Padgham 1986, Martel 2003, Martel and Lin 2006). The overall stratigraphy put forth by Helmstaedt and Padgham (1986) was reviewed during the EXTECH III project (Helmstaedt 2006). A detailed review of the Yellowknife regional geology and current literature is provided here, and a summary of the relevant geologic settings are given in each chapter.

The YGB is one of Canada's largest historic gold camps and has been widely explored and studied. Despite the significant research conducted, questions remain related to the magmatic history of the YGB and the role that magmatism played concerning mineralization events and metal remobilization (Bleeker and Hall 2007). To date, there have been several ideas put forth for the development of gold mineralization, which include a shear zone-hosted orogenic origin, metamorphically driven processes, and enrichment by fluids derived from local metasediments (Groves et al. 1998, van Hees et al. 1999, Ootes et al. 2007). However, there are also local spatial associations between gold mineralization and dikes in the belt, as well as an early intrusion-related metal enrichment that requires further investigation (Finnigan and Duke 2006, Hubbard et al. 2006, Ootes et al. 2006, Siddorn et al. 2006). It remains unclear how the regional plutons and dikes may have contributed to the multiple mineralizing events. For instance, mineralization at the Con Mine has been linked to the late-stage granite bloom (ca. 2590 Ma) and associated metamorphism (Ootes et al. 2011). This relationship has been noted but the genetic and temporal connection between the intrusions and mineralization has not been defined. By studying magmatism in the YGB, we can gain a deeper understanding of the intrusions and their evolution, emplacement, and crystallization

history. Conducting further research on these aspects of the YGB magmatic history will hopefully provide insights into the origin of gold mineralization.

1.4. Detailed regional geology review

The YGB is part of the Yellowknife Domain, defined by Bleeker and Beaumont-Smith (1995), consisting of the Anton Complex, the YGB, the Burwash Formation, the Cameron River and Beaulieu River greenstone belts, and the Sleepy Dragon Complex. Within the YGB region, the basement rocks are the Central Slave Basement Complex (CSBC). The supracrustal rocks are comprised of the Central Slave Cover Group (CSCG) and Yellowknife Supergroup (Henderson and Brown 1966, Helmstaedt and Padgham 1986). The Yellowknife Supergroup consists of the Kam Group, Banting Group, Duncan Lake Group, and the Jackson Lake Formation (Fig. 1.1; Henderson and Brown 1966, Helmstaedt and Padgham 1986). This dissertation focuses on the Yellowknife Supergroup and the multiple generations of syn- and post-volcanic intrusions, locally known as the "#9" dikes (Henderson and Brown 1966). These dikes consist of feldspar quartz porphyry (FQP), quartz porphyry (QZP), and aplite dikes. The Kam and Banting Groups of the Yellowknife Supergroup are overlain by the Jackson Lake Formation; the contact occurs as an unconformity or as a local disconformity (Martel and Lin 2006). The basement and supracrustal rocks were successively intruded by the RLP, the Defeat Plutonic Suite, the Duckfish granite and the Prosperous Suite (Bleeker et al. 1999b, 1999a, Davis and Bleeker 1999).

Although the terms FQP and QZP dike are not recognized nomenclature for plutonic bodies, they do constitute the locally known names for these porphyritic dikes in the YGB and will continue to be used from this point forward. Furthermore, the primary classification of igneous rocks should be done using modal mineralogy, however, the variable, fine-grained to aphanitic nature of some YGB dikes prevents this (le Maitre 2002). Instead, a chemical classification was applied to all YGB dikes and plutons in this study to maintain a consistent data set that can be used to compare dike and pluton chemistry, and still classify dikes that have indeterminate modal mineralogy. For example, using a Total-Alkali-Silica diagram for chemical classification of samples that are too fine-grained is a recommended alternative by the International Union of Geological Sciences in this case (le Maitre 2002). By moving forward in this way, this study can focus on establishing genetic relationships between parental plutons, sub-volcanic dikes, and overlying volcaniclastic units using consistent chemical classification.

1.4.1. Basement Rocks

The CSBC encompasses three Archean terranes, the Sleepy Dragon Complex, the Jolly Lake Complex and the Anton Complex (Henderson 1985, Thompson et al. 1995, Bleeker et al. 1999a). The CSBC occurs as a heterogeneous mixture of dioritic to tonalitic gneisses that have migmatitic layering. This layering is commonly cut by mafic dikes that are also deformed and metamorphosed and further intruded by younger granitoids (Bleeker et al. 1999a). Ages for the CSBC range from 2.8 to 3.3 Ga, including zircon ages of 2945 ± 1 Ma from the Anton Complex and 2930-2950 Ma, ca. 3.15 Ga, and ca. 3.32 Ga from the Sleepy

Dragon Complex (Isachsen 1992, Isachsen and Bowring 1997, Bleeker et al. 1999a). One granodioritic gneiss dated by Bleeker et al. (1999a) yielded an age of 3325 ± 8 Ma, with two additional metamorphic ages of 2723 ± 3 Ma from zircon and ca. 2680 Ma from titanite. The contact between the CSBC and CSCG is marked by a regional high-strain zone that predates 2687 ± 1 Ma dikes (Bleeker et al. 1999b).

The unconformable CSCG is a thin unit of varying components, consisting of ultramafic, mafic and minor felsic volcanic rocks, rhyolite, conglomerates, banded iron formation (BIF), and chromite-bearing quartzite (Isachsen and Bowring 1997, Bleeker et al. 1999a). The CSCG is deformed and locally imbricated, containing a distinctive fuchsitic quartzite. Geochronology of the CSCG yielded precise U-Pb ages from felsic volcanic units, giving an age of 2853 Ma and 2826 Ma (Ketchum and Bleeker 2000). Bleeker et al. (1999a) were able to synthesize previous research and determined that the age of the CSCG is between 2734 and 2924 Ma (Isachsen and Bowring 1997, Bleeker et al. 1999b).

1.4.2. The Kam Group

The Kam Group is roughly 10 km thick and dominated by basaltic to intermediate volcanic rocks with thin layers of intermediate to felsic tuffaceous rocks (Fig. 1.1). The Kam Group consists of four formations that overlie the CSBC and the CSCG. From oldest to youngest and moving from west to east is the Chan, Crestaurum, Townsite, and Yellowknife Bay Formations (Helmstaedt and Padgham 1986). The historic Con and Giant mines are hosted within the Yellowknife Bay Formation of the Kam Group (Siddorn et al. 2006, Siddorn 2011). All the formations are dominated by tholeiitic mafic metavolcanic rocks except for

the Townsite Formation, which is a predominantly felsic, calc-alkaline metavolcanic sequence (Finnigan and Duke 2006). There is considerable lateral continuity in the Kam Group which has aided in the reconstruction of the belt; many of the mafic flows, interflow sediments, and tuffs extend for >10 km (Helmstaedt and Padgham 1986, Finnigan 2000, Finnigan and Duke 2006). There are abundant gabbro dikes, sills and an anorthosite that intrude the sequence (Henderson and Brown 1966, Helmstaedt and Padgham 1986). U-Pb zircon geochronology yielded a crystallization age between 2722 to 2701 Ma (± 1 to 4 Ma) for the Kam Group; cherty felsic tuffs have inherited zircons up to 2820 Ma (Isachsen 1992, Isachsen and Bowring 1994).

The Kam Group is in faulted contact with the younger Banting Group along the Yellowknife River Fault Zone (YRFZ) when they are not separated by the Jackson Lake Formation (Martel and Lin 2006). The Kam Group occurs to the west of the YRFZ, and the Banting Group is found to the east (Martel and Lin 2006). In the northern part of the YGB, the Kam Group is truncated by the unconformable Jackson Lake Formation.

1.4.2.1. The Chan Formation

The Chan Formation is the lowermost member of the Kam Group and comprises a minimum 6 km thick section of greenschist-amphibolite facies massive and pillowed tholeiitic basalts, gabbro and other mafic dikes (Helmstaedt and Padgham 1986). The dikes of the Chan Formation may represent a sheeted dike complex, an indicator of seafloor spreading (Helmstaedt et al. 1986). Gabbro dikes and the RLP intrude the Chan Formation (Henderson and Brown 1966, Ootes 2004). The absolute age of the Chan

Formation is unknown and may be part of the underlying CSCG (Cousens et al. 2006a). The Ranney Chert marker horizon indicates the top of the Chan Formation; it marks a period of sediment accumulation and felsic volcanism (Henderson and Brown 1966).

1.4.2.2. The Crestaurum Formation

The Crestaurum Formation conformably overlies the Chan Formation and consists of massive to pillowed tholeiitic basalt flows, intercalated cherts, felsic tuffs, and local BIF (Ootes and Lentz 2002). The basalts are locally bleached, a feature of syn-volcanic alteration and likely due to silicification and iron leaching (Ootes and Lentz 2002). There are less gabbro dikes present in the Crestaurum Formation than in the underlying Chan Formation (Helmstaedt and Padgham 1986). The upper boundary of the Crestaurum Formation is marked by the conformable dacitic flows of the Townsite Formation and the transition to calc-alkaline volcanism.

1.4.2.3. The Townsite Formation

The Townsite Formation is dominated by felsic calc-alkaline volcanic rocks in contrast to the other members of the Kam Group (Helmstaedt and Padgham 1986, Finnigan 2000, Finnigan and Duke 2006). There is a major gabbroic sill complex which has intruded the Townsite Formation. The unit typically consists of interbedded rhyodacite breccias, tuffs (occasionally welded), and pillowed dacites (Helmstaedt and Padgham 1986). Helmstaedt and Padgham (1986) noted that some areas of the Townsite Formation have been deposited under subaerial conditions, rather than the subaqueous conditions indicated by the pillowed basalts found stratigraphically above and below.

The Townsite Formation has been dismembered by Proterozoic faults into three lenses, the Brock, Niven, and Vee Lake lenticles. These lenses are marker horizons used to reconstruct the YGB. In the Giant mine area, the Townsite Formation is often found proximal to gold-bearing shear zones (Finnigan and Duke 2006). There are three generations of intrusive and extrusive felsic rocks found in the Townsite Formation, however it can be difficult to distinguish between them due to pervasive alteration.

The gabbro sills and felsic intrusions in the Townsite Formation are considered coeval due to a lack of chill margins and their interfingering and undulose contacts. The Brock and Vee Lake lenticles have pyroclastic rocks that are considered vent proximal facies. Finnigan and Duke (2006) proposed two methods for the development of the Townsite Formation: 1) the intrusive components (dikes and sills) of the Townsite formed by partial melting of basaltic andesites while the extrusive units were deposited, followed by *in-situ* fractionation of the partial melts to form the intermediate and quartz-feldspar porphyries; 2) the intrusive rocks act as feeders to the extrusive rocks of the Townsite Formation.

1.4.2.4. The Yellowknife Bay Formation

The Yellowknife Bay Formation is the uppermost unit of the Kam Group, consisting of ~5 km of massive and pillowed mafic flows, variolitic pillowed flows, pillow breccias, and interflow sediments (Helmstaedt and Padgham 1986, Canam 2006, Hauser et al. 2006). There are also variable amounts of cherty tuffs and tuffaceous sediments throughout the formation, which transition to coarse turbiditic sandstones towards the top of the unit;

the Bode turbidites. These sediments and the variolitic pillowed flows are marker horizons within the Yellowknife Bay Formation that can be traced for 10 km on either side of the Giant deposit (Helmstaedt and Padgham 1986). Both the Con and Giant deposits are hosted within the Yellowknife Bay Formation, although they have been dismembered by Proterozoic faulting (Siddorn et al. 2006, Siddorn 2011).

1.4.3. The Banting Group

The Banting Group is dominated by intermediate to felsic volcanic rocks that unconformably overly the Kam Group (Helmstaedt and Padgham 1986, Isachsen 1992). The unit consists of felsic tuffs, ash-flow tuffs, QZP, massive and pillowed flows, and volcaniclastic sedimentary rocks (Helmstaedt and Padgham 1986, Isachsen and Bowring 1997, Martel and Lin 2006). Two dates obtained from the Banting Group yielded ages of 2662 ± 3 Ma and 2664 ± 1 Ma (Isachsen 1992). Zircons with inherited cores were also found, suggesting some degree of basement interaction and assimilation.

Shearing has obscured the primary contact relationship between the Banting Group and underlying Kam Group (Cousens et al. 2006a, Martel and Lin 2006). The felsic porphyries have been proposed as the link between the two groups as they crosscut the Kam Group but have a Banting age (2658 ± 2 and 2664 ± 1 Ma; Isachsen 1992). It has been suggested that the porphyries are feeders to the Banting Group, however, there is insufficient research to determine which of the three generations of "#9" dikes are feeders to the Banting Group (Ootes et al. 2006, and references therein).

1.4.4. The Duncan Lake Group

The Duncan Lake Group consists of two dominantly sedimentary units, the Walsh and Burwash Formations, that are conformable to the Banting Group (Helmstaedt and Padgham 1986, Cousens et al. 2006a, Martel and Lin 2006). The Walsh Formation is a thinly bedded unit of graphitic argillite and siltstones. The Burwash Formation consists of thicker beds of sandstone and siltstone, ~0.1 to 1 m, and has an age of 2.66 Ga (Bleeker and Villeneuve 1995). Both the Walsh and Burwash Formations are considered basin-fill sediments (Henderson 1985, Helmstaedt and Padgham 1986). Work by van Hees et al. (1999) suggested that these metasediments contributed to the Giant Mine ore system as a hydrothermal fluid conduit and/or fluid source, providing enrichments in As, S, and Sb.

1.4.5. The Jackson Lake Formation

The Jackson Lake Formation is a 50 to 300 m thick, east-facing Molasse-type sequence consisting of a locally derived basal breccia unit, conglomerate, sandstone with parallel- and cross-bedding, and argillite (Martel and Lin, 2006). There is an angular unconformity between the Jackson Lake Formation and the underlying Kam Group, and a faulted contact between the Jackson Lake Formation and the Banting Group, corresponding to the YRFZ (Martel and Lin 2006). A granitic clast from the conglomerate yielded a detrital zircon with the youngest age of 2605 ± 6 Ma; other ages include 2595, 2688, and 2689 Ma from clasts (Isachsen 1992, Martel and Lin 2006, and references therein). A cross-cutting mafic dike was found to have a minimum age of 2096 Ma (Padgham 1996). The

YRFZ consistently occurs along the Jackson Lake-Banting Group contact, wherever the Jackson Lake Formation is present (Martel and Lin 2006).

The mapping carried out by Martel and Lin (2006) confirmed that the Jackson Lake Formation was deposited after the first deformation event (D_1), i.e., the rotation of the volcanic pile and formation of S_1. Most of the Jackson Lake sediments are locally derived from Kam Group, however, there was no development of an S_1 foliation in the Jackson Lake Formation itself. The unit has been deformed and metamorphosed by later regional events, which constrain the deformation and metamorphism of the entire belt to later than 2605 Ma (Isachsen and Bowring 1994, Martel and Lin 2006).

The Jackson Lake Formation contains shear zone hosted and paleoplacer showings of anomalous gold concentrations (Roscoe 1990). When structural, metamorphic, and mineralization data are combined, it suggests that there were at least two gold-bearing events, one that predates the deposition of the Jackson Lake Formation, and another associated with cross-cutting shear zones (Martel and Lin 2006).

1.4.6. Plutonism

There are four major plutonic phases found within or near to the YGB, which includes the RLP (2675 Ma), the Defeat Plutonic Suite (ca. 2630-2615 Ma), the Duckfish granite (2608 Ma), and the eastern Prosperous Suite (2596 Ma; Bethune et al. 1999, Davis and Bleeker 1999, Ootes et al. 2007). The Prestige pluton of the Prosperous Suite has been recently dated, yielding an age of 2608 ± 4 Ma (Palmer 2018). There are pegmatites that crosscut

the Prestige pluton with ages of 2588 and 2593 Ma, which fall within error of the ages given by Davis and Bleeker (1999).

The multi-phase RLP is an intermediate intrusion consisting of tonalite and granodiorite that has been dated by Re-Os molybdenite geochronology to 2675 ± 7 Ma, within error of a U-Pb zircon age of 2671 +6/-5 Ma (Ootes et al. 2007). The pluton is partly obscured by the Defeat Suite but has been found along the eastern margin of the Defeat Suite granite (Ootes et al. 2006, 2007). The Defeat Suite intruded the YGB during regional metamorphism and comprises tonalite, granodiorite, diorite and granite (Davis and Bleeker 1999). The Defeat Suite has been weakly metamorphosed and is responsible for contact metamorphism and related amphibolite facies of the YGB (Thompson 2006). The Duckfish Granite has an early to late syn-orogenic character and a distinct magnetic and radiometric geophysical signature (Ootes et al. 2007). The Prosperous Suite is considered a late syn-orogenic granite that post-dates the metamorphism and typically consists of two-mica leucogranites with extensive associated pegmatites. The Defeat, Duckfish, and Prosperous Suite are all mildly peraluminous plutons (Cousens et al. 2006a). It has been suggested that the cause of plutonism may be anatexis related to crustal thickening, continental arc magmatism, decompression melting in the mantle during post-collision extension, lithospheric delamination, or some combination of these tectonic events (Davis and Bleeker 1999, and references therein).

1.4.7. Metamorphism and deformation

The metamorphic and deformational history for the YGB was established through field observations, geochronology and petrographic studies. Development of the YGB is estimated to have taken roughly 200 million years and which includes deformational and metamorphic events (Isachsen and Bowring 1994). Thompson (2006) has characterized four major metamorphic processes, including seafloor metamorphism, regional metamorphism, contact metamorphism, and metasomatism. Isachsen and Bowring (1994) considered most of the deformation to have occurred from 2.62 to 2.60 Ga, after deposition of sedimentary and volcanic sequences but before intrusion of the late-stage granites at 2.59–2.56 Ga (King et al. 1992, Relf 1992). The belt (and craton) was then subjected to post-orogenic plutonism, slow uplift, and cooling (Isachsen and Bowring 1994).

The most recent structural review of the belt was done by Martel and Lin (2006) during the EXTECH III project. Earlier workers have described three deformation events (D_1–D_3), however, Martel and Lin (2006) identified four generations of ductile deformation events (G_1-G_4), three of which encompass the D_1–D_3 of earlier research, and a previously unidentified later event (G_4; Jolliffe 1942, 1946, Henderson and Brown 1966, Hauer 1979, Easton et al. 1982). Early G_1 (D_1) structures are poorly preserved and not observed in the Jackson Lake Formation at all (Martel and Lin 2006). However, tilting of the Kam Group, deposition of at least one stage of mineralization, development of an axial planar S_1 foliation, the intrusion of the Defeat Suite, and deposition of the Jackson

Lake Formation must have taken place prior to G_2, (Davis and Bleeker 1999, Martel and Lin 2006). G_2 (D_2) deformation consists of an east-west compressional event that produced regional folding and reverse shearing. G_3 structures correspond to late-D_2 deformation and were the result of dextral shearing (Bleeker and Beaumont-Smith 1995, Martel and Lin 2006). G_4 ductile structures caused transposition and shearing of the YGB, corresponding to a predicted late-D_3 deformation event described by Davis and Bleeker (1999). Finally, largely sinistral Proterozoic faulting (post-G_4) occurred along pre-existing shear zones and other planes of weakness (Martel and Lin 2006).

There are two end-member tectonic models for the YGB (Martel and Lin 2006, and references therein). First, an intra-cratonic rift basin has been proposed, which would consist of a collapsed ensialic rift basin and corresponding granitic magmatism, further intruded by younger granitoids. The second model postulates a collisional-accretionary margin consisting of a variation of an Andean-type margin, continent collision, or island arc. Other intermediate models that have been proposed include back-arc basins, crustal thinning and reworking, and marginal basin development.

1.4.8. Mineralization

The first gold brick was poured in 1938 at the Con mine and 1948 at the Giant mine (Moir et al. 2006). The mines have produced a total of approximately 13 Moz of gold; 5.8 Moz were produced from the Con mine at 0.48 oz/ton and 7.1 Moz were produced from the Giant mine at 0.45 oz/ton (Siddorn et al. 2006). Gold mineralization occurs in different proportions at both mines as both refractory and free-milling ore. The refractory ore

consists of extremely fine-grained to submicroscopic gold hosted in mainly arsenopyrite, but also in arsenian pyrite (Armstrong 1997, Siddorn et al. 2006). Free-milling gold occurs as native gold, or in a gold assemblage, such as gold-pyrite, gold-pyrrhotite. The mineralization at the Con and Giant mines is associated with different mineral assemblages. The refractory ore is associated with paragonitic muscovite, aluminum-rich chlorite, Fe-Mg carbonate, arsenopyrite, and pyrite (Armstrong 1997). In contrast, the free-milling gold is associated with phengitic muscovite, chlorite, calcite, pyrite, and pyrrhotite (Armstrong 1997). Zoned alteration is observed at both mines, consisting of propylitic to phyllic alteration, with silicification and carbonatization (or ankeritization) at the core.

Early research in the YGB focused on the origin of the gold deposits, with authors leaning towards a metamorphic or magmatic origin (Boyle 1959, 1961, Ames 1962, McConnell 1964). Boyle (1959) argued that the gold-quartz deposits formed by the secretion of elements and fluids from the host rocks during regional metamorphism and orogenesis and finally depositing in dilatant shear zones. Ames (1962) indicated that there should be depletion halos around the shear zones if the mineralizing elements are being drawn from the country rocks which is not observed and instead favoured a hydrothermal origin. McConnell (1964) suggested that previous data could point to a magmatic-hydrothermal origin.

Previous studies of gold mineralization from the deposit, and throughout the YGB, implies that there were multiple mineralizing events. Gold is found hosted in shear zones

that transect mafic volcanics and is considered orogenic (Groves et al. 1998, Ootes et al. 2007, and references therein). Metamorphically-driven processes are also considered part of ore formation, with mineralization forming as metamorphic fluids passed through shear zones and deposited gold in dilation zones and chemical traps. There is also evidence that ore at the Giant mine was enriched by fluids derived from proximal metasediments (van Hees et al. 1999, 2006a). This enrichment includes As, S, and Sb that correlates with gold in the Giant deposit. The hydrothermal fluids containing these metals and gold encountered Ti-rich tholeiitic basalts which caused the reduction of fluids and deposition of gold (van Hees et al. 1999). Finally, there is an observed spatial association between gold mineralization and porphyry dikes in the belt, as well as an early intrusion-related metal enrichment (Finnigan and Duke 2006, Ootes et al. 2006, 2007). Therefore, it appears as though multiple gold-bearing processes were involved during the development of the YGB. The debate regarding the source of gold in the YGB is ongoing and thus requires further research.

1.5. Dissertation hypotheses and objectives

Mineral exploration in the YGB provided a unique opportunity to collaborate with industry and develop a deeper understanding of the geologic processes in the belt. The locally termed “#9” dikes represent multiple generations of intrusions (aplite, FQP, and QZP dikes) that have not been thoroughly distinguished during previous research. If these generations of dikes can be reliably differentiated, it may be possible to genetically link them to a plutonic source and understand their emplacement characteristics. Presently,

the “#9” dikes have been postulated to represent feeders to the overlying volcaniclastic units, however, a genetic link with one or more of these dikes has not been established. Therefore, a multi-analytical approach, including detailed petrographic, lithogeochemical, and geochronologic analysis will aid in discriminating these lithologies and establish their timing in the current YGB framework. If it is possible to determine the dike-pluton relationships in the belt, this data could then be compared to the potentially related volcaniclastic sequences (Townsite Formation, Banting Group) and determine the overall plutonic-volcanic setting. Finally, the large collection of zircons used for U-Pb geochronology were assessed for the presence of melt inclusions. These Archean zircons and inclusions were evaluated to determine the viability of obtaining meaningful melt inclusion data from zircons of this age. This collection of data may reflect bulk silicate melt or mixed mineral and melt inclusions, which could then be used to make inferences on the primary magma chemistry. This information would provide a deeper understanding of magmatic-hydrothermal processes and potentially clarify the dike-pluton relationship to mineralization in the YGB.

Based on initial field work and a literature review, the following goals were established for this dissertation:

I. To obtain a full lithogeochemical dataset for the intrusions of interest and perform a geochemical comparison to determine the genetic relationships between regional plutons and multiple generations of dikes within the YGB. These dikes, locally grouped and known as the “#9” dikes will be assessed for geochemical

differences. At present, the source of these dikes has not been definitively established.

II. Perform a petrographic and textural analysis of aplite dikes identified during preliminary field work to gain a better understanding of magmatic-hydrothermal characteristics in the YGB.

III. Complete a widespread U-Pb geochronology study of magmatic zircons to establish the timing of dike and pluton emplacement while placing them in the greater context of previous geochronology and geotectonic events in the YGB. This will expand the geochronologic database and allow us to solidify the relationships between dikes and plutons.

IV. Refine the temporal and geochemical connection between YGB dikes that crosscut the Kam Group and the volcaniclastic units of the Townsite Formation and Banting Group.

V. Explore the relationship between intrusions and mineralization through the lens of zircon-hosted melt inclusions and assess the magmatic contribution to mineralizing events documented in the YGB. The geochemistry and magmatic evolution of primary magmas represented by the melt inclusions will be determined through interpretation of LA-ICP-MS data.

By focusing on these aspects of the geologic history of the YGB, this dissertation provides new data related to the geochemical evolution, emplacement, and metallogenic characteristics of multiple generations of dikes and their parental plutons within the belt.

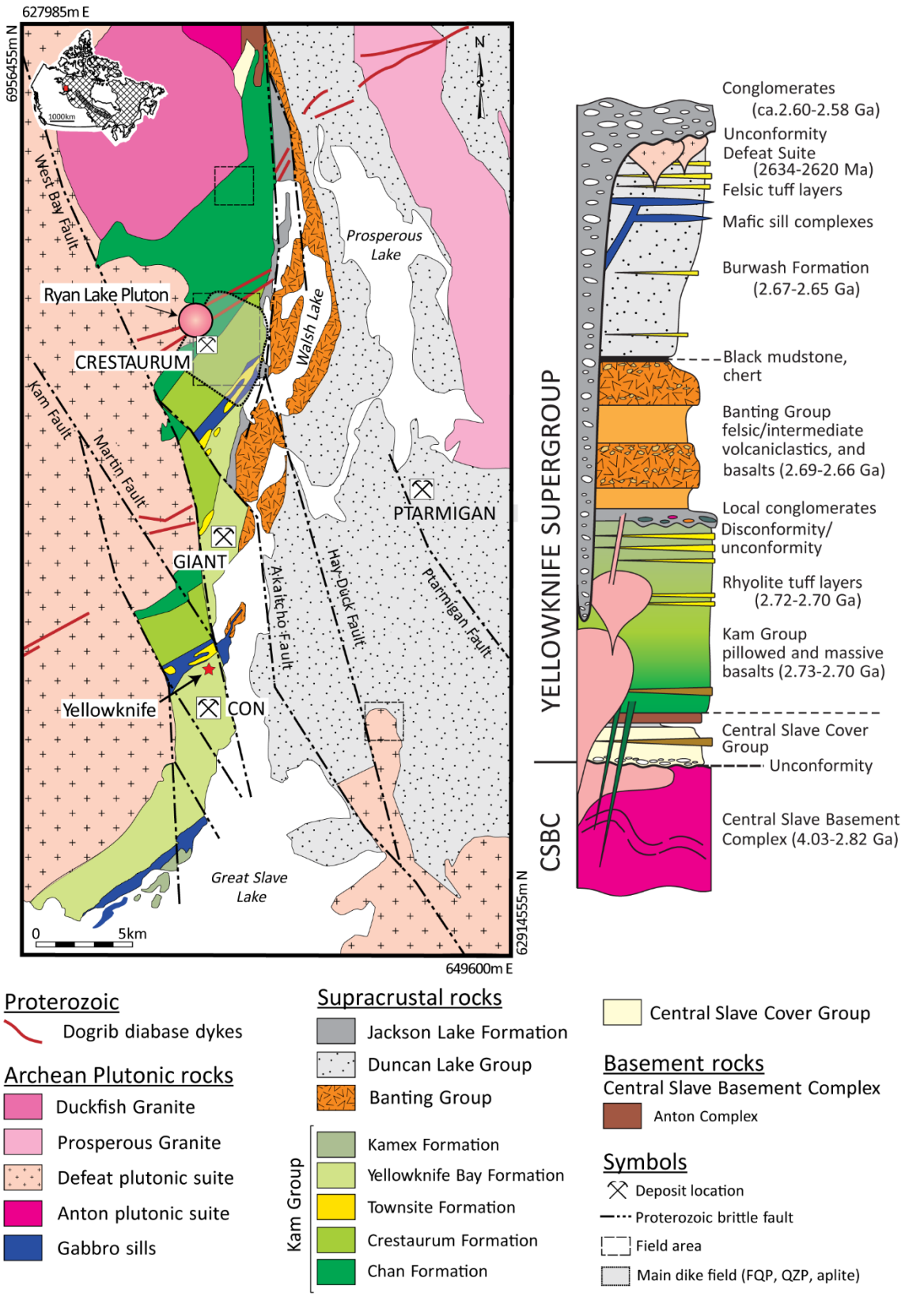
1.6. Dissertation structure

This is an article-based dissertation that is divided into 5 chapters, including an introduction to the project and field area (Chapter 1), three chapters relating to the research goals (Chapters 2, 3, and 4), and a concluding chapter that summarizes the overall findings (Chapter 5). We assume that the reader has a basic knowledge of lithogeochemistry, U-Pb geochronology, melt inclusion analysis, and igneous petrology. Where applicable, these concepts are reviewed within the introduction and discussion of the relevant chapters.

This research was accomplished using a multi-analytical approach to characterize the geochemical evolution, emplacement, timing, and metallogenic implications of dikes and plutons in the YGB. Chapter 2 provides the full lithogeochemical dataset for the YGB dikes and plutons of this study along with a detailed petrographic analysis of aplite dikes. This paper provides the first level of evidence regarding the magmatic history of the YGB and the parental relationships between multiple generations of dikes and plutons. Chapter 3 contains results from LA-ICP-MS and CA-TIMS analysis of zircons obtained from mineral separates of representative YGB dikes and plutons. This chapter provides a detailed analysis of U-Pb geochronology from a large population of zircons, a discussion of the inheritance observed, and precise $^{207}Pb/^{206}Pb$ ages that place the dikes and plutons within the temporal history of the YGB. Chapter 4 presents the results from a preliminary zircon-hosted melt inclusion study that endeavoured to collect semi-quantitative melt inclusion data from these Archean intrusions. Chapter 4 provides metal-enrichment data related to

primary magmas trapped in zircons, which offer insights into the early mineralization characteristics of the YGB intrusions. By focusing each chapter on separate but related objectives, the results provided in subsequent chapters continue to build through the thesis. This dissertation was written as a series of articles to publish the results in peer-reviewed journals. Chapters 2 and 3 will be submitted together as complimentary Part 1 and 2 articles in the Canadian Journal of Earth Sciences and Chapter 4 will be submitted to Economic Geology.

Fig. 1.1: *Following page*. Simplified geologic map and stratigraphic column (and ages) of the YGB in the Archean Slave province of the Canadian Shield (modified and complied from Ootes and Lentz 2002, Bleeker and Hall 2007, Ootes et al. 2007). The map and stratigraphic column show the location of historic gold deposits, major shear zones, intrusions, and field areas. Cross-cutting feldspar-quartz porphyry, quartz porphyry, and aplite dikes do not appear at this scale; therefore, the main dike field is highlighted (grey box) and their relative position is illustrated in the stratigraphic column.


627985m E
6956455m N
1000km
N
West Bay Fault
Ryan Lake Pluton
CRESTAURUM
Kam Fault
Martin Fault
Prosperous Lake
Walsh Lake
PTARMIGAN
GIANT
Akaitcho Fault
Hay Duck Fault
Ptarmigan Fault
Yellowknife
CON
Great Slave Lake
0
5km
649600m E
6291455m N
Conglomerates (ca.2.60-2.58 Ga)
Unconformity
Defeat Suite (2634-2620 Ma)
Felsic tuff layers
Mafic sill complexes
Burwash Formation (2.67-2.65 Ga)
Black mudstone, chert
Banting Group felsic/intermediate volcaniclastics, and basalts (2.69-2.66 Ga)
Local conglomerates
Disconformity/ unconformity
Rhyolite tuff layers (2.72-2.70 Ga)
Kam Group pillowed and massive basalts (2.73-2.70 Ga)
Central Slave Cover Group
Unconformity
Central Slave Basement Complex (4.03-2.82 Ga)
YELLOWKNIFE SUPERGROUP
CSBC
Proterozoic
Dogrib diabase dykes
Archean Plutonic rocks
Duckfish Granite
Prosperous Granite
Defeat plutonic suite
Anton plutonic suite
Gabbro sills
Supracrustal rocks
Jackson Lake Formation
Duncan Lake Group
Banting Group
Kam Group
Kamex Formation
Yellowknife Bay Formation
Townsite Formation
Crestaurum Formation
Chan Formation
Central Slave Cover Group
Basement rocks
Central Slave Basement Complex
Anton Complex
Symbols
Deposit location
Proterozoic brittle fault
Field area
Main dike field (FQP, QZP, aplite)

1.7. References

Ames, R.L. 1962. The origin of the gold-quartz deposits, Yellowknife, N.W.T. Economic Geology, **57**: 1137–1140. New Haven, Connecticut.

Armstrong, J.P. 1997. Variations in silicate and sulphide mineral chemistry between free-milling "metallic" and refractory "invisible" gold ores, Con Mine, Yellowknife, N.W.T. Ph. D., University of Western Ontario, London, Ontario.

Bethune, K.M., Villeneuve, M.E., Bleeker, W., Bethune, K.M., Villeneuve, M.E., and Bleeker, W. 1999. Laser 40Ar/39Ar thermochronology of Archean rocks in Yellowknife Domain, southwestern Slave Province: insights into the cooling history of an Archean granite-greenstone terrane. Canadian Journal of Earth Sciences, **36**: 1189–1206.

Bleeker, W., and Beaumont-Smith, C. 1995. Thematic structural studies in the Slave province: preliminary results and implications for the Yellowknife Domain, Northwest Territories. Geological Survey of Canada.

Bleeker, W., and Hall, B. 2007. The Slave Craton: Geology and Metallogenic Evolution. *In* Mineral Deposits of Canada: A Synthesis of Major Deposit-Types, District Metallogeny, the Evolution of Geological Provinces, and Exploration Methods: Geological Association of Canada. *Edited by* W.D. Goodfellow. Mineral Deposits Division. pp. 849–879.

Bleeker, W., Ketchum, J.W., Jackson, V.A., Villeneuve, M.E. 1999a. The Central Slave Basement Complex, Part I: its structural topology and autochthonous cover. Canadian Journal of Earth Sciences, **36**: 1083–1109.

Bleeker, W., Ketchum, J.W.F., and Davis, W.J. 1999b. The Central Slave Basement Complex, Part II: age and tectonic significance of high-strain zones along the basement-cover contact. Canadian Journal of Earth Sciences, **36**: 1111–1130.

Bleeker, W., and Villeneuve, M.E. 1995. Structural Studies along the Slave portion of the Snorcle Transect.

Boyle, R.W. 1959. The geochemistry, origin, and role of carbon dioxide, water, sulfur, and boron in the Yellowknife gold deposits Northwest Territories, Canada. Economic Geology, **54**: 1506–1524.

Boyle, R.W. 1961. The geology, geochemistry, and origin of the gold deposits of the Yellowknife district. Memoir 310. pp. 193.

Bullen, W., and Robb, M. 2006. Economic contributions of gold mining in the Yellowknife Mining District. *In* Gold in the Yellowknife Greenstone Belt, Northwest Territories: Results of the EXTECH III Multidisciplinary Research Project, Special Pub. No. 3. *Edited by* C.D. Anglin, H. Falck, D.F. Wright, and E.J. Ambrose. Geologic Association of Canada Mineral Deposits Division. pp. 38–48.

Canam, T.W. 2006. Discovery, mine production, and geology of the Giant mines. *In* Gold in the Yellowknife Greenstone Belt, Northwest Territories: Results of the EXTECH III Multidisciplinary Research Project, Special Pub. No. 3. *Edited by* C.D. Anglin, H. Falck,

D.F. Wright, and E.J. Ambrose. Geologic Association of Canada Mineral Deposits Division. pp. 188–196.

Cousens, B., Falck, H., Ootes, L., Jackson, V., Mueller, W., Corcoran, P., Finnigan, C., van Hees, E., Facey, C., and Alcazar, A. 2006. Regional correlations, tectonic settings, stratigraphic solutions in the Yellowknife greenstone belt and adjacent areas from geochemical and Sm-Nd isotopic analyses of volcanic and plutonic rocks. *In* Gold in the Yellowknife Greenstone Belt, Northwest Territories: Results of the EXTECH III Multidisciplinary Research Project, Special Pub. No. 3. *Edited by* C.D. Anglin, H. Falck, D.F. Wright, and A.J. Ambrose. Geological Association of Canada Mineral Deposits Division. pp. 70–94.

Davis, W.J., and Bleeker, W. 1999. Timing of plutonism, deformation, and metamorphism in the Yellowknife Domain, Slave Province, Canada. Canadian Journal of Earth Sciences, **36**: 1169–1187.

Easton, R.M., Ellis, C., Helmstaedt, H., Jackson, V., O'Hearn, B., Dean, M., Bruneau, H.C., and Wahlroth, J. 1982. Geology of the east side of Yellowknife Bay, NTS 85 J/8,9. Department of Indian Affairs and Northern Development, Geological Division.

Finnigan, C.S. 2000. The Townsite Formation: an aborted rift setting in the Yellowknife greenstone belt, NWT. M. Sc., University of Western Ontario, London, Ontario.

Finnigan, C.S., and Duke, N.A. 2006. Geology and Geochemistry of the Townsite Formation: Recognition of Felsic Porphyritic Intrusions Adjacent to Gold-Bearing Shear Zones in the Yellowknife Greenstone Belt, NWT. *In* Gold in the Yellowknife Greenstone Belt, Northwest Territories: Results of the EXTECH III Multidisciplinary Research Project. *Edited by* C.D. Anglin, H. Falck, D.F. Wright, and E.J. Ambrose. pp. 58–69.

Groves, D.I., Goldfarb, R.J., Gebre-Mariam, M., Hagemann, S.G., and Robert, F. 1998. Orogenic gold deposits: A proposed classification in the context of their crustal distribution and relationship to other gold deposit types. Ore Geology Reviews, **13**: 7–27.

Hauer, L.M. 1979. Preliminary Geological Map, Northern End of the Yellowknife Greenstone Belt, Parts of 85 J/9. Department of Indian and Northern Development, NWT Division, Yellowknife.

Hauser, R.L., McDonald, D.W., and Siddorn, J.P. 2006. Geology of the Miramar Con mine. *In* Gold in the Yellowknife Greenstone Belt, Northwest Territories: Results of the EXTECH III Multidisciplinary Research Project, Special Pub. No. 3. *Edited by* C.D. Anglin, H. Falck, D.F. Wright, and E.J. Ambrose. Geologic Association of Canada Mineral Deposits Division. pp. 173–187.

van Hees, E.H., Kirkham, G.D., Sirbescu, M.-L., Shelton, K.L., Hauser, R.L., and Falck, H. 2006. Large lithogeochemical alteration halos around Yellowknife gold deposits and implications for fluid pathways. *In* Gold in the Yellowknife Greenstone Belt, Northwest Territories: Results of the EXTECH III Multidisciplinary Research Project, Special Pub. No. 3. *Edited by* C.D. Anglin, H. Falck, D.F. Wright, and F. Ambrose. Geological Association of Canada Mineral Deposits Division. pp. 232–248.

van Hees, E.H., Shelton, K.L., McMenamy, T.A., Ross Jr., L.M., Cousens, B.L., Falck, H., Robb, M.E., and Canam, T.W. 1999. Metasedimentary influence on metavolcanic-rock-hosted greenstone gold deposits-Geochemistry of the Giant mine, Yellowknife, NWT. Geology, **1**: 71–74.

Helmstaedt, H., and Padgham, W.A. 1986. A new look at the stratigraphy of the Yellowknife Supergroup at Yellowknife, N.W.T. — implications for the age of gold-bearing shear zones and Archean basin evolution. Canadian Journal of Earth Sciences, **23**: 454–475. Available from www.nrcresearchpress.com.

Helmstaedt, H., Padgham, W.A., and Brophy, J.A. 1986. Multiple dikes in Lower Kam Group, Yellowknife greenstone belt: Evidence for Archean sea-floor spreading? Geology, **14**: 562–566.

Helmstaedt, H.H. 2006. Evolution of geological understanding of the Yellowknife Domain. *In* Gold in the Yellowknife Greenstone Belt, Northwest Territories: Results of the EXTECH III Multidisciplinary Research Project, Special Pub. No. 3. *Edited by* C.D. Anglin, H. Falck, D.F. Wright, and E.J. Ambrose. Geological Association of Canada Mineral Deposits Division. pp. 29–37.

Henderson, J.B. 1985. Geology of the Yellowknife-Hearne Lake Area, District of Mackenzie: A segment across an Archean Basin. Geological Survey of Canada.

Henderson, J.F., and Brown, I.C. 1966. Geology and structure of the Yellowknife greenstone belt, District of Mackenzie. *In* Bulletin 141. Geological Survey of Canada.

Hubbard, L.J., Marshall, D.D., Anglin, C.D., Thorkelson, D., and Robinson, M.H. 2006. Giant Mine: Alteration, Mineralization, and Ore-Zone Structures with an Emphasis on the Supercrest Zone. *In* Gold in the Yellowknife Greenstone Belt, Northwest Territories: Results of the EXTECH III Multidisciplinary Research Project. *Edited by* C.D. Anglin, H. Falck, D.F. Wright, and E.J. Ambrose. pp. 197–212.

Isachsen, C.E. 1992. U-Pb zircon geochronology of the Yellowknife volcanic belt and subjacent rocks, N.W.T., Canada: Constraints on the timing, duration, and mechanics of greenstone belt formation. Ph. D., Washington University, St. Louis, Mo.

Isachsen, C.E., and Bowring, S.A. 1994. Evolution of the Slave craton. Geology, **22**: 917–920.

Isachsen, C.E., and Bowring, S.A. 1997. The Bell Lake group and Anton Complex: a basement – cover sequence beneath the Archean Yellowknife greenstone belt revealed and implicated in greenstone belt formation. Canadian Journal of Earth Sciences, **34**: 169–189.

Jolliffe, A.W. 1942. Yellowknife Bay, Map 709A, scale 1:63 360, District of Mackenzie, Northwest Territories. Geological Survey of Canada.

Jolliffe, A.W. 1946. Prosperous Lake, Map 868A, scale 1:63 360, District of Mackenzie, Northwest Territories. Geologic Survey of Canada.

Ketchum, J.W.F., and Bleeker, W. 2000. New field and U-Pb data from the Central Slave Cover Group near Yellowknife and the Central Slave Basement Complex at Point

Lake. *In* Slave-Northern Cordillera Lithospheric Experiment (SNORCLE) Transect Meeting. *Edited by* F. Cook and P. Erdmer. pp. 27–31.

King, J.E., Davis, W.J., and Relf, C. 1992. Late Archean tectono-magmatic evolution of the central Slave Province, Northwest Territories. Canadian Journal of Earth Science, **29**: 2156–2170. NRC Research Press Ottawa, Canada.

le Maitre, R.W. 2002. Igneous Rocks: A Classification and Glossary of Terms, Recommendations of the International Union of Geological Sciences, Sub-Commission on the Systematics of Igneous Rocks. *In* 2nd Edition. Cambridge University Press.

Martel, E. 2003. The Structural Evolution of the Yellowknife Greenstone Belt, Slave Province, NWT: New Insights on Its Stratigraphy and the Potential for Gold in the Jackson Lake Formation. M. Sc., University of Waterloo, Waterloo, Ontario.

Martel, E., and Lin, S. 2006. Structural Evolution of the Yellowknife Greenstone Belt, with Emphasis on the Yellowknife River Fault Zone and the Jackson Lake Formation. *In* Gold in the Yellowknife Greenstone Belt, Northwest Territories: Results of the EXTECH III Multidisciplinary Research Project, Special Pub. No. 3. *Edited by* C.D. Anglin, H. Falck, D.F. Wright, and E.J. Ambrose. pp. 95–115.

McConnell, G.W. 1964. Yellowknife gold-quartz deposits. Economic Geology, **59**: 328–330.

Moir, I., Falck, H., Hauser, R.L., and Robb, M. 2006. The history of mining and its impact on the development of Yellowknife. *In* Gold in the Yellowknife Greenstone Belt, Northwest Territories: Results of the EXTECH III Multidisciplinary Research Project, Special Pub. No. 3. *Edited by* C.D. Anglin, H. Falck, D.F. Wright, and E.J. Ambrose. Geological Association of Canada Mineral Deposits Division. pp. 11–28.

Ootes, L. 2004. Geology of the Crestaurum gold deposit, Yellowknife greenstone belt, Northwest Territories, Canada. M. Sc., University of New Brunswick, Fredericton, New Brunswick.

Ootes, L., and Lentz, D.R. 2002. Occurrence of bleached mafic flows and their association with stockwork sulphides and banded iron-formation in the Crestaurum Formation of the late Archean Yellowknife Greenstone Belt, Northwest Territories. *In* Current Reseach-E5. Geological Survey of Canada.

Ootes, L., Lentz, D.R., Cabri, L.J., and Hall, D.C. 2006. Geology and Gold Mineralization in the Crestaurum Mine Area, Northern Yellowknife Greenstone Belt, N. W. T. *In* Gold in the Yellowknife Greenstone Belt, Northwest Territories: Results of the EXTECH III Multidisciplinary Research Project, Special Pub. No. 3. *Edited by* C.D. Anglin, H. Falck, D.F. Wright, and E.J. Ambrose. pp. 249–269.

Ootes, L., Lentz, D.R., Creaser, R.A., Ketchum, J.W.F., and Falck, H. 2007. Re-Os molybdenite ages from the Archean Yellowknife greenstone belt: Comparison to U-Pb ages and evidence for metal introduction at ~2675 Ma. Economic Geology, **102**: 511–518.

Ootes, L., Morelli, R.M., Creaser, R.A., Lentz, D.R., Falck, H., and Davis, W.J. 2011. The timing of Yellowknife gold mineralization: a temporal relationship with crustal anatexis? Economic Geology, **106**: 713–720.

Padgham, W.A. 1996. Slave conglomerate dating. Yellowknife, Open File 1996-12.

Palmer, E.M. 2018. Petrogenesis of the Archean Prestige leucogranite and spatially associated LCT pegmatites, NWT: insights from whole-rock and muscovite trace element geochemistry and apatite U-Pb geochronology. M. Sc., University of New Brunswick, Fredericton, NB.

Relf, C. 1992. Two distinct shortening events during late Archean orogeny in the west-central Slave Province, Northwest Territories, Canada. Canadian Journal of Earth Science, **29**: 2104–2117. NRC Research Press Ottawa, Canada.

Roscoe, S.M. 1990. Quartzose arenites and possible paleoplacers in Slave Structural Province, N.W.T. Geological Survey of Canada, Current Research, **Paper 90-1C**: 231–239.

Siddorn, J.P. 2011. The Giant-Con gold deposit: a once-linked Archean lode-gold system. Ph. D., University of Toronto, Toronto, ON.

Siddorn, J.P., Cruden, A.R., Hauser, R.L., Armstrong, J.P., and Kirkham, G. 2006. The Giant-Con gold deposits: Preliminary integrated structural and mineralization history. *In* Gold in the Yellowknife Greenstone Belt, Northwest Territories: Results of the EXTECH III Multidisciplinary Research Project, Special Pub. No. 3. *Edited by* C.D. Anglin, H. Falck, D.F. Wright, and E.J. Ambrose. Geological Association of Canada Mineral Deposits Division. pp. 213–231.

Silke, R. 2009. The Operational History of Mines in the Northwest Territories, Canada. Northwest Territories Geologic Survey. Available from www.nwtgeoscience.ca.

Thompson, P.H. 2006. Metamorphic Constraints on the Geological Setting, Thermal Regime, and Timing of Alteration and Gold Mineralization in the Yellowknife Greenstone Belt, NWT, Canada. *In* Gold in the Yellowknife Greenstone Belt, Northwest Territories: Results of the EXTECH III Multidisciplinary Research Project, Special Pub. No. 3. *Edited by* C.D. Anglin, H. Falck, D.F. Wright, and E.J. Ambrose. Geological Association of Canada Mineral Deposits Division. pp. 142–172.

Thompson, P.H., Russell, I., Paul, D., Kerswill, J.A., and Froese, E. 1995. Regional geology and mineral potential of the Winter Lake-Lac de Gras area, central Slave Province, Northwest Territories. Geological Survey of Canada, Current Research, **Paper 1995-C**: 107–119. Geologic Association of Canada.

2. Geodynamic evolution of felsic magmatism in the Yellowknife greenstone belt, N.W.T., Canada: evidence for Archean magmatism in a volatile-saturated environment

2.1. Abstract

The Yellowknife greenstone belt (YGB) hosts three generations of felsic to intermediate dikes and associated regional plutons that intrude mafic and felsic metavolcanic supracrustal rocks in the Archean Slave province, N.W.T., Canada. The three generations of dikes comprise feldspar-quartz porphyry (FQP), quartz porphyry (QZP), and aplitic dikes locally termed the "#9" dikes. Regional intrusive bodies include the Ryan Lake Pluton (RLP), Defeat Suite granite, and Duckfish granite. Lithogeochemical data (e.g., major and trace elements, REE, HFSE) was used to discriminate between the dikes and plutons of interest. Chondrite-normalized REE patterns for these intrusions differentiate three aplite groups and their genetically related parental plutons, including aplite-1(a) dikes and the RLP, aplite-1(b) dikes and the Defeat Suite granite, and finally, aplite-2 dikes and the Duckfish granite.

The tonalite and granodiorite of the RLP and coeval aplite-1(a) dikes have smooth REE profiles that decrease from LREE to HREE and share this profile with the FQP, QZP, an intermediate dike, and an intermediate volcanic tuff, all considered part of the same geochemical group (average $La_N/Lu_N = 31$, Eu/Eu* = 0.41, Ce/Ce* = 1.0). In contrast, the Defeat Suite granite and aplite-1(b) dikes also have smooth but flatter REE patterns with

a strong negative Eu anomaly (average La_N/Lu_N = 6.1, Eu/Eu* = 0.29, Ce/Ce* = 1.4). Finally, the Duckfish granite and aplite-2 dikes share concave-up REE patterns with weak positive Ce (up to Ce/Ce* = 3.1) and strong negative Eu anomalies (average La_N/Lu_N = 7.3, Eu/Eu* = 0.44, Ce/Ce* = 1.6). These parameters geochemically separate aplite-1(a) and -1(b) dikes that are otherwise spatially, petrographically, and geochemically similar in terms of major element chemistry. The tonalite and granodiorite samples of the RLP are consistently the least fractionated in this dataset and, together with their associated dikes, have a magnesian, I/S-type, volcanic arc signature. The Defeat Suite granite and aplite-1(b) have a more ferroan A-type, volcanic arc to syn-collisional signature, locally transitioning to a within-plate tectonic signature. The Duckfish granite and aplite-2 dikes occasionally overlap with the Defeat Suite group and have a ferroan, A-type, syn-collisional to within-plate granite signature.

The YGB aplite dikes were further characterized petrographically, and data were integrated and compared to existing petrogenetic models that establish four stages of dike emplacement during progressive crystallization of a parental pluton. Four stages of dike emplacement have been established for aplite-1(a) dikes related to the RLP (*main magmatic*, *late magmatic*, *early post-magmatic*, and *late post-magmatic*), while aplite-1(b) dikes were emplaced during only three stages of emplacement (*main magmatic*, *late magmatic*, e*arly post-magmatic*). Finally, the aplite-2 dikes were only emplaced during two stages (*main magmatic*, *late magmatic*). These petrographically determined stages of emplacement can be linked to geochemical trends that show increasing differentiation

with progressive crystallization (e.g., decreasing Al_2O_3, MgO, TiO_2, total REE, and Eu/Eu*). The abundance of aplite-1(a) dikes related to all stages of RLP crystallization compared to the narrower window of emplacement for the aplite-1(b) and aplite-2 dikes suggests that the tectonic environment was becoming less active by the time of Duckfish granite intrusion. Changes from a volatile-saturated volcanic arc setting to a volatile-poor within-plate tectonic setting are reflected in the emplacement of the aplite dikes. Dikes emplaced during the *late magmatic*, *early post-magmatic*, or *late post-magmatic* stages of pluton crystallization represent intrusions from a volatile-saturated melt. This feature manifests macroscopically as cm-scale quartz cores and discontinuous quartz pods within the aplitic dikes, observed in each group of aplite dikes. Further study of the volatile evolution (e.g., timing, volatile composition) related to the RLP and its relationship to potential mineralization is warranted.

Keywords

Aplite; Archean geochemistry; Archean magmatism; TTG; hydrous magmas; volatile saturation

2.2. Introduction

The Yellowknife greenstone belt (YGB) is in the Archean Slave province of the Northwest Territories, Canada (Fig. 1.1). Granitic dikes with an aplitic texture have been mapped proximal to, and within, the Ryan Lake Pluton (RLP; quartz diorite, granodiorite, tonalite), Defeat Suite (tonalite, granodiorite, diorite, and granite), and the Duckfish Granite (Henderson and Brown 1966, van Breemen et al. 1992, Davis and Bleeker 1999,

Cousens et al. 2006b, Ootes et al. 2006, 2007). At least two other generations of feldspar-quartz porphyry (FQP) and quartz porphyry (QZP) dikes are also reported (Henderson and Brown 1966, Finnigan and Duke 2006, Ootes et al. 2006). Together, these dikes are locally described as the "#9" dikes. It has been suggested that these dikes represent subvolcanic feeders to overlying volcaniclastic units. Additionally, a spatial association between the dikes and gold mineralization has been noted; however, this aspect of their evolution has not been studied in detail (Green and Baadsgaard 1971, Helmstaedt and Padgham 1986, Cousens et al. 2002, Finnigan and Duke 2006, Ootes et al. 2006, 2007, Bleeker and Hall 2007).

Aplite dikes were evaluated using macroscopic field observations and petrography to determine their stage of emplacement and whether they showed textural evidence of volatile saturation. The FQP, QZP, and minor intermediate dike and intermediate volcanic tuff samples were compared to determine genetic associations with regional plutons, specifically the multi-phase Ryan Lake Pluton (RLP), Defeat Suite granite, and Duckfish granite (Henderson and Brown 1966, van Breemen et al. 1992, Davis et al. 1994, Bleeker et al. 1999a, 1999b, Davis and Bleeker 1999, Finnigan 2000, Cousens et al. 2006b, Finnigan and Duke 2006, Ootes et al. 2006, 2007). Lithogeochemical data are used to investigate these associations and ascertain changes in magma chemistry and the tectonic environment that the YGB intrusions evolved from. Combining geochemistry and petrography enables these dikes to be placed within the current geotectonic framework for the YGB and further constrain the parental pluton and dike relationships.

If these dikes can be petrographically or geochemically distinguished, then they may be genetically linked to a regional parental pluton and understand their emplacement characteristics. Finally, the data can be compared to the overlying volcaniclastic sequences of the Townsite Formation and Banting Groups to confirm whether one more of these dikes are part of a subvolcanic feeder system. Therefore, this study undertakes a detailed petrographic study and lithogeochemical classification of aplitic dikes and major felsic and intermediate YGB intrusions. Late-stage aplitic dikes have been linked to intrusions crystallizing in a volatile-saturated environment with fluids that can contain dissolved metals (Hibbard 1980, Carter et al. 2021, Speight et al. 2023b). Analysis of aplitic dikes in the YGB leads to a better understanding of magmatic-hydrothermal systems and associated mineralization (Carter et al. 2021). This study also provides an improved understanding of the genetic relationship between regional plutons (Ryan Lake Pluton, Defeat Suite granite, Duckfish granite) and the abundant FQP and QZP dikes will strengthen our understanding of the YGB geotectonic environment.

2.3. Regional Geology

The YGB is a north-south trending series of mafic and felsic metavolcanic rocks located in the southwest Archean Slave province, which developed over a timespan of ~200 Ma (Fig. 1.1; Henderson and Brown 1966, Helmstaedt and Padgham 1986, Isachsen and Bowring 1994, Cousens et al. 2006, Helmstaedt and Pehrsson 2012). The belt is sub-vertically dipping toward the southeast, which correlates to the younging direction. The YGB can be divided into several groups of rocks, including the dioritic and tonalitic

gneisses of the Central Slave Basement Complex (CSBC), supracrustal rocks of the Central Slave Cover Group (CSCG) and Yellowknife Supergroup, and syn- to post-volcanic intrusions.

The Yellowknife Supergroup unconformably overlies the CSBC and CSCG and is divided into the Kam Group, Banting Group, Duncan Lake Group, and Jackson Lake Formation (Henderson and Brown 1966, Helmstaedt and Padgham 1986, Helmstaedt and Pehrsson 2012). The Jackson Lake Formation represents a molasse-type sedimentary package that unconformably overlies the Kam and Banting Groups (Martel and Lin 2006).

The Kam Group is subdivided into five units: the Chan Formation, Crestaurum Formation, Townsite Formation, Yellowknife Bay Formation, and Kamex Formation (Henderson and Brown 1966, Helmstaedt and Padgham 1986, Isachsen and Bowring 1994, Helmstaedt and Pehrsson 2012). Each formation within the Kam Group is composed of dominantly tholeiitic mafic metavolcanics except for the Townsite Formation, which has a higher proportion of calc-alkaline felsic volcaniclastics, and intrusions combined with mafic sills (Cousens 2000). The Kam Group was intruded by abundant felsic to intermediate dikes collectively known as the "#9" dikes, comprised of FQP, QZP, and aplitic dikes (Henderson and Brown 1966, Cousens et al. 2006b, Finnigan and Duke 2006). Previous research grouped the "#9" dikes as coeval due to their abundance in the Kam Group metavolcanics and interpreted them as feeder dikes to the overlying Banting Group, despite contrasting textural and geochemical features in the three dike populations (Henderson and Brown 1966, Cousens et al. 2002). The upper contact of the

Kam Group (Kamex Formation) is in faulted contact with the overlying Banting Group, occurring as the Yellowknife River Fault Zone (Martel and Lin 2006). The Kam and Banting Groups are typically separated by the Jackson Lake Formation, which is found in and along the Yellowknife River Fault Zone.

Syn- and post-volcanic intrusions include three generations of felsic to intermediate dikes (the “#9” dikes) and four major plutonic phases known as the Ryan Lake Pluton (RLP), the Defeat Plutonic Suite, the Duckfish granite (a member of the Anton Complex), and the Prosperous Suite plutons (Henderson and Brown 1966, van Breemen et al. 1992, Bethune et al. 1999, Davis and Bleeker 1999, Cousens et al. 2006b, Ootes et al. 2007, Palmer 2018). The intrusion of these plutonic bodies was associated with the final tectonic events that stabilized the Slave craton (Davis et al. 1994). A genetic connection between the Kam and Banting Groups has not been established, although it has been proposed that the dikes that crosscut the Kam group could be feeders to the overlying Banting Group. Previous studies have shown a preliminary link between the collective "#9" dikes but have not distinguished whether the FQP, QZP or both have a connection to the Banting Group (Henderson and Brown 1966, Henderson 1985, Isachsen 1992, Cousens et al. 2002, Ootes et al. 2006).

The YGB has been subjected to a minimum of four cycles of metamorphism and alteration, including seafloor (e.g., bleached pillow basalts), regional and contact metamorphism, and hydrothermal alteration (Helmstaedt et al. 1986, Ootes and Lentz 2002, Thompson 2006). The Defeat Suite was responsible for contact metamorphism that

caused a metamorphic aureole to develop in the supracrustal rocks proximal to the intrusion, with metamorphism reaching amphibolite grade proximal to the Defeat Suite (Thompson 2006). Multiple deformation events caused folding, thrusting, and shear zone development throughout the YGB (Martel and Lin 2006). This deformation occurred after the deposition of supracrustal rocks but before the intrusion of post-collisional granites (Martel and Lin 2006). Finally, the YGB was dismembered by Proterozoic faults that preferentially formed along planes of weakness in pre-existing shear zones (Helmstaedt and Padgham 1986, Martel and Lin 2006).

2.4. Methods

This study focuses on establishing connections between macroscopic field observations, petrographic data, and lithogeochemical data to classify and distinguish felsic and intermediate intrusions in the YGB. A total of 52 samples were collected for petrographic and lithogeochemical analysis; sample locations are summarized in Appendix 1, Table A1.1. Aplite dikes from two field areas were sampled, comprising 12 aplite-1 dikes proximal to, or crosscutting, the RLP and Defeat Suite granite, and eight aplite-2 dikes adjacent to the Duckfish granite (part of the Anton Complex). Representative samples from other felsic and intermediate YGB intrusions were taken, including eight FQP, four QZP, five tonalite, nine granodiorites, two Defeat Suite granite, and two Duckfish granite samples. Two samples were also taken from intermediate lithologies that were difficult to classify in the field, including one intermediate dike and one intermediate volcanic tuff.

Sampled rocks were submitted for standard polished thin section preparation at the University of New Brunswick. A subset of samples was sent to Activation Laboratories Ltd. (Ancaster, Ontario) for crushing and subsequent whole-rock geochemical analysis. Fifty-two samples were crushed and pulverized using a mild steel mill to a particle size such that 85% passed through a 75-micron mesh screen. Fused glass beads were obtained by lithium borate fusion and then dissolved in a 5% nitric acid solution, followed by inductively coupled plasma-optical emissions spectrometry (ICP-OES) and ICP-mass spectrometry (ICP-MS) analysis for major oxides and trace elements, respectively. Five standards (NIST 694, DNC-1, W-2a, SY-4, BIR-1a), 3 duplicate samples, and 3 blanks were interspersed throughout the geochemical analysis to monitor accuracy and precision. Analysis of the standard and duplicate data indicate that the major elements varied an average of 0.5% (K_2O and P_2O_5 varied an average of 5%), while trace elements varied an average of 1.6% except for Be, Pb, Zr, Ni, Cu, Cr, Ag, and Sb which varied an average of 10% and Tl, W, Ge, and Bi varied an average of 32%.

Petrographic analysis of standard polished thin sections was carried out on a Nikon Labophot polarizing microscope, and corresponding photomicrographs were taken with a Google Pixel 4a mobile equipped with a 12.2-megapixel camera. The same thin sections were analyzed by micro-X-ray Fluorescence Spectrometry (µXRF) to assess (using mapped major and trace element distribution) the mineralogy, textures, and alteration more readily observed at the full thin section scale. A Bruker M4 Tornado µXRF at the University of New Brunswick was used to obtain the element intensity maps of each polished thin

section. The mapping used a Rh tube excitation source operated at 50 kV and 400 µA with a spot size of 20 µm. Each analyzed spot collected a complete elemental analysis as the beam rastered across the thin section.

Finally, preliminary mineral chemistry data were collected at St. Mary's University using a TESCAN MIRA 3 LMU VPS field emission SEM equipped with a solid-state EDS detector. The SEM analyses were done with an accelerating voltage of 25 kV, a beam current of 2 nA, and a working distance of 17 mm. EDS spectra collection and analysis were done using the INCA platform (ETAS GmbH) software.

2.5. Results

2.5.1. Sample descriptions

Detailed imaging and field observations were made to document crosscutting relationships and macroscopic textural information. Geographic coordinates for each sample and their host rock associations are summarized in Appendix 1, Table A1.1. The sampled dikes and intrusions have naturally variable and heterogeneous grain sizes, particularly the porphyritic samples; therefore, the following grain size terms are used throughout: very fine-grained (aphanitic, no clear grain boundaries), fine-grained (<1 mm), medium-grained (1 – 5 mm), and coarse-grained (>5 mm; Jerram and Petford 2011, Frost and Frost 2014). Initial examination of the geochemical data showed that the aplite dikes in the southern field area, proximal to the RLP and Defeat Suite granite, are

geochemically distinct from the northern aplite dikes near the Duckfish granite and have been classified as such (aplite-1 and aplite-2, respectively).

2.5.1.1. Aplite dikes

Aplitic dikes occur proximal to the RLP, the Defeat Suite granite, and the Duckfish granite and were initially grouped based on their spatial associations. Dikes sampled in or around the RLP and Defeat Suite granite were spatially grouped as aplite-1 dikes, and those found near the Duckfish granite are referred to as aplite-2 dikes. The contact relationships are shown in Fig. 2.1 and the approximate distance from the plutons are given to establish the extent of aplite occurrences. Aplitic textures are shown on a fresh rock surface in Fig. 2.2, and macroscopic volatile saturation textures (e.g., quartz cores) are shown in Fig. 2.3. During progressive fractionation and crystallization of an intrusion, a volatile-rich phase separation occurs and crystallizes *in-situ* if the fluids do not migrate; the resulting texture typically manifests as quartz-dominated cores within the dike (Hibbard 1980, Candela 1997).

Aplite-1 dikes occur within the RLP, crosscutting tonalite and granodiorite, and up to 780 m away from the Ryan Lake Pluton and Defeat Suite granite contacts, hosted within mafic volcanic flows of the Chan Formation. Twelve dikes were selected for petrographic and geochemical analysis, five of which are hosted within the RLP. Aplite dikes found crosscutting the multi-phase RLP (and tonalites and granodiorites) are approximately 500 m from the historic Crestaurum deposit. These dikes are, on average, 35 cm wide but can reach a width of 1 m and, locally, have branching and bifurcating offshoots. Very narrow

dikes have the appearance of hematized quartz veins (Fig. 2.1A-C). The aplite dikes have a pink to orange-pink weathered surface and a pink-white fresh surface (Fig. 2.1B). The dikes show weak to moderate potassic and hematitic alteration and an aphanitic texture. Xenoliths were found in one aplite, comprising tonalite from the tonalite host rock (Fig. 2.1D). All dikes have sharp and undulating contacts and lack chilled margins with their host rock, independent of the host lithology. The dikes are typically very fine- to fine-grained, rarely medium-grained; they are siliceous and dominated by quartz and K-feldspar, with variable amounts of very fine- to fine-grained, disseminated biotite, ranging from trace amounts to 10 vol. % (Fig. 2.2A-D). Local deformation zones offset the dikes, and two aplite-1 dikes contain trace, fine-grained, disseminated pyrite. One dike occurs proximal to the molybdenite-bearing quartz veins hosted in shears that crosscut the RLP pluton; the aplite dike itself was crosscut by quartz veins that contained trace, medium- to coarse-grained pyrite (Ootes et al. 2007). Six dikes have cm-scale, mainly continuous quartz cores along the dike lengths or locally occurring as discontinuous quartz pods.

Aplite-2 dikes were sampled in the northern field area near the Duckfish granite, ~5 km away from aplite-1 dikes associated with the RLP and Defeat Suite granite (Fig. 1.1). In this area, all aplite dikes were found within mafic volcanic host rock adjacent to the Duckfish granite, and none were observed within the pluton. Six of the aplite dikes are 10 to 100 m from the Duckfish granite contact, and two are ~375 m away. The dikes have an aphanitic, cherty texture with a pink-white weathered and fresh surface (Fig. 2.1E, Fig. 2.2E). They are very fine- to fine-grained and dominated by quartz, feldspar, trace biotite,

and rare trace pyrite. One dike is likely an offshoot of the Duckfish granite as it was found only 10 m away from the contact and trends toward the pluton, although direct contact is covered by overburden; this dike is more coarse-grained than typical (Fig. 2.1F and Fig. 2.2F). Aplite-2 dikes are typically wider than aplite 1 dikes, having an average width of ~1 m (compared to 35 cm). Only two of the aplite-2 dikes were found to have quartz pods.

Continuous quartz cores and discontinuous quartz pods, two distinct textures, were observed in both aplite-1 and aplite-2 dikes (Fig. 2.3). These quartz textures were only observed in aplites hosted in mafic volcanic flows and not within the RLP. The quartz cores and pods run parallel to the dike orientation and vary in size, typically from <1 cm to 5 cm wide (Fig. 2.3A-C). Potassium-feldspar is a typical phase that occurs along growth zones in the quartz cores (Fig. 2.3D). Discontinuous quartz cores are the more common texture for aplite-2 dikes and are rarely observed along dike margins (Fig. 2.3E). One dike has a quartz core that is 15 to 30 cm wide and could be mistaken for a quartz vein as it pinches and swells along the length of the dike (Fig. 2.3F).

2.5.1.2. Feldspar-quartz porphyry dikes

Seven FQP dikes were sampled from various locations within the Kam Group, proximal to the RLP and Defeat Suite granite, moving up sequence through the Chan, Crestaurum, and Townsite Formations for a total distance of 3 km from the pluton margins (Fig. 1.1). One FQP sample was taken from the northern field area, 90 m from the Duckfish granite. The FQP dikes are porphyritic, 1 to 5 m wide, and weathered to a light buff-pink to grey colour with a grey-white fresh surface (Fig. 2.4A). The dikes have sharp contacts with no

observable chill margins and an occasional weak, biotite-defined foliation. The phenocrysts in the FQP dikes are dominated by medium- to coarse-grained, blocky feldspar and fine- to medium-grained, subrounded to rounded quartz. The groundmass of the FQP dikes is medium to dark grey, very fine- to fine-grained, and dominantly quartz. Trace amounts of fine-grained biotite are occasionally present in these dikes, and trace amounts of disseminated, very fine- to fine-grained pyrite. White quartz veins occasionally crosscut the sampled dikes. Feldspar compositions range from oligoclase to andesine.

2.5.1.3. Quartz porphyry dikes

Four QZP dikes were sampled from the YGB, three of which were taken from the main dike field in the RLP and Defeat Suite area, and one was sampled proximal to the Duckfish granite (Fig. 1.1). The QZP dikes are weathered to a buff-yellow colour and have a light grey-white fresh surface (Fig. 2.4B). The dikes are 2 to 5 m wide and typically have a siliceous, cherty appearance with sharp contacts. The QZP dikes have fine- to medium-grained rounded quartz phenocrysts set in a microcrystalline quartz groundmass. The dikes are often mineralized with trace, disseminated, and very fine- to fine-grained pyrite.

2.5.1.4. Intermediate dike and volcanic tuff

One sample of the intermediate dike and one sample of intermediate volcanic tuff were taken to compare with the FQP and QZP dikes as they have textural similarities in the field and can be difficult to distinguish. The intermediate dike was sampled from the northern Duckfish granite area, and the intermediate volcanic tuff was taken from within

the Townsite Formation. The intermediate dike has a grey-white-pink weathered surface and a grey-buff fresh surface (Fig. 2.4C). On the weathered surface, the dike appears to have fine- to medium-grained feldspar phenocrysts; however, they are less visible on a fresh surface, which has a more cherty appearance. Trace amounts of very fine-grained, disseminated pyrite were observed in this dike. The intermediate volcanic tuff is similar to the intermediate dike and has the same weathering characteristics (Fig. 2.4D). The intermediate volcanic tuff has a higher proportion of fine- to medium-grained quartz phenocrysts and lesser feldspars. This unit has poorly defined, gradational contacts with the surrounding felsic volcanic tuffs of the Townsite Formation.

2.5.1.5. Tonalite

Four tonalitic samples were gathered from the multiphase RLP and have gradational contacts with granodioritic areas. One sample was taken 480 m from the RLP contact near Milner Lake, occurring in a >15 m outcrop near the lake edge; this sample was coarser than tonalite from the Ryan Lake area. The tonalite is differentiated from the granodiorite based on grain size and composition, with tonalite having a higher abundance of mafic minerals (Fig. 2.4E). The tonalite is homogeneous, equigranular, fine- to medium-grained, and has a grey-white weathered surface and grey-green fresh surface. There are occasional patches of light pink colouration due to K-feldspar. The tonalite is dominated by quartz, plagioclase, biotite, and amphibole, with trace amounts of fine-grained pyrite.

2.5.1.6. Granodiorite

Nine granodiorite samples were obtained from the RLP, all proximal to the tonalite samples, and found east of Ryan Lake. The granodiorites have a different weathered surface than the tonalites, with a white-pink weathered surface and a grey-white-pink fresh surface (Fig. 2.4F). Samples were taken from homogeneous, equigranular areas that are medium-grained and dominated by quartz, plagioclase, biotite, and trace to 1 vol. %, disseminated fine-grained pyrite. The granodiorite has a rare grey-green weathered surface due to the presence of chloritized biotite. Some outcrops have crosscutting quartz veins mineralized with fine-grained, disseminated pyrite.

2.5.1.7. Defeat Suite granite

Two samples were taken from the Defeat Suite granite near Mason Lake in the southeastern field area (Fig. 1.1). The outcrops are more than 3 m wide and extend into the lake. The granites are homogeneous, equigranular, and coarse-grained with a pink-grey weathered surface and a pink-white fresh surface (Fig. 2.4G). They are dominated by quartz and K-feldspar, with lesser plagioclase and biotite.

2.5.1.8. Duckfish granite

Two samples were taken from the Duckfish granite in the northern field area from 10 and 40 m from the intrusion contact. The Duckfish granite has a pink weathered surface with a pink fresh surface (Fig. 2.4H). The granite occasionally has a pegmatitic texture but is typically medium- to coarse-grained and equigranular and is dominated by quartz and

K-feldspar with minor plagioclase and biotite. The granite is occasionally crosscut by 5 to 10 centimeter-wide, white quartz veins. No pyrite was observed in these samples, or the crosscutting quartz veins.

2.5.2. Petrography and mineral chemistry

Polished thin sections were obtained for each sample submitted for whole rock geochemical analysis. Multi-element μXRF compositional maps of major element distribution from polished thin sections were obtained to aid in the characterization of aplite dikes concerning their mineralogically constrained stages of emplacement, shown in Fig. 2.5. Multi-element μXRF maps show the macroscopic textural associations that may not be apparent when examined with a petrographic microscope since the μXRF scans are collected at a larger scale. The polished thin sections of each lithology were subsequently examined petrographically, summarized below, and images are shown in Fig. 2.6 to Fig. 2.8.

2.5.2.1. Aplite-1 dikes

The aplite dikes may represent a singular lithology; however, their mineralogy and petrographic characteristics vary, particularly evident at the microscopic versus macroscopic scale. Fig. 2.5 shows Si, K, and Ca combined in the left column to illustrate the distribution of quartz (Si), K-feldspar (K), and calcite (Ca); the right column combines Ca, Fe, and Ti to show the occurrence of calcite (Ca), biotite (possibly altered to chlorite) or pyrite (Fe), and Ti-oxides (e.g., rutile, ilmenite). Aplite dikes commonly have centimeter-scale, branching offshoots and apophyses, one of which is imaged along with

the mafic volcanic flow host rock (Fig. 2.5A-B). This µXRF scan effectively shows the sharp contact relationship between the aplite dike and host rock, differentiated by the abundance of Fe- and Ca-rich phases, which reflect chlorite and calcite. Within the dike are commonly observed millimeter-scale growth zones where comb-textured quartz can be observed near parallel to the dike contacts (Fig. 2.5A-B). A common texture in the aplite dikes is myrmekite, and graphic intergrowths of quartz and feldspar are observed on a near macroscopic scale in Fig. 2.5C-D.

Petrographic examination of aplite-1 dikes indicates they are very fine- to fine-grained and show rare medium-grained textures (e.g., comb-textured quartz). The samples are dominated by quartz, K-feldspar, and plagioclase with trace amounts of biotite, opaques, and variable moderately developed hematite alteration along grain boundaries. Quartz grains are very fine- to medium-grained, anhedral to subhedral, and often show evidence of deformation (e.g., undulose extinction and recrystallized mosaic textures); recrystallization is most apparent along grain boundaries. Some growth zones within the aplite dikes show associated comb-textured quartz. Quartz often occurs interstitial to K-feldspar and plagioclase and often contains feldspar inclusions (Fig. 2.6A).

Potassium-feldspar shows weakly-developed sericite alteration, varying to strongly-developed, pervasive sericite alteration. Potassium-feldspars grains are fine- to medium-grained and show weak to moderate perthite development and rare tartan twinning. Plagioclase is fine- to medium-grained, anhedral to subhedral, and shows weakly to moderately developed sericite alteration. Two samples contain plagioclase with

magmatic zoning that exhibit alternating zones of sericite alteration. Plagioclase shows rare secondary overgrowths of K-feldspar. Rarely plagioclase grains are deformed. Myrmekite was observed in four aplite-1 samples; one of these samples was dominated by myrmekite.

Trace, fine-grained, chloritized biotite, with rare zircon inclusions, occurs disseminated throughout the aplite dikes. Biotite grains occasionally have inclusions of very fine- to fine-grained, titanite and rutile, exsolved during metamorphism. Trace, fine-grained oxides and sulfides are disseminated throughout the aplite dikes and occasionally occur with biotite in clusters. One aplite-1 sample contains high-relief, colourless (plane-polarized light), and round apatite grains (Fig. 2.6A). One aplite-1 sample contains abundant muscovite throughout, occurring as very fine-grained crystals (within feldspars) and as fine- to medium-grained blades with a fan texture.

2.5.2.2. Aplite-2 dikes

The multi-element μXRF compositional maps of aplite-2 dikes also show the variety of textures and mineralogy as aplite-1 dikes, despite being classified as the same lithology geochemically. Increased Si and K is observed in a coarser-grained section of the aplite-2 dike in Fig. 2.5E, representing a quartz zone that is intergrown with K-feldspar, with patchy areas of elevated Ti in quartz observed in Fig. 2.5F. The second aplite-2 dike shows cm-scale aplite injection and part of a second dikelet branch, with mafic host rock in between. Within the aplite, a zone of increased K, Ca, and Fe can be observed along the

margins of the aplite-2 injection (Fig. 2.5G-H). The Fe- and Ca-rich area between the two aplites dikes reflects the location of mafic volcanic host rock.

Petrographic examination of aplite-2 dikes, sampled from the northern field area proximal to the Duckfish granite, revealed very similar mineralogy and textures to aplite-1 dikes from the RLP and Defeat Suite areas but tend to have more consistent features as a group. They are dominated by quartz, K-feldspar, and plagioclase with variable amounts of finer-grained biotite and opaques; overall grain size varies from very fine- to medium-grained (Fig. 2.6B). The quartz grains are anhedral and often have a recrystallized mosaic texture along grain boundaries. Potassium-feldspar shows the development of rare tartan twinning and weak perthite. Rare, broken plagioclase grains contain quartz backfilling these fractures. Plagioclase grains are subhedral, occasionally show a blocky shape, and often appear interstitial to quartz and K-feldspar; three of the aplite-2 dikes contain myrmekite. Plagioclase grain boundaries often appear recrystallized, and all feldspars are weakly to moderately altered to sericite. Trace amounts of very fine- to fine-grained disseminated biotite can be observed in some aplite-2 dikes and was weakly altered to chlorite. One aplite-2 dike is porphyritic, with phenocrysts of medium-grained quartz and altered plagioclase; plagioclase is altered to sericite and calcite. Trace amounts of fine-grained calcite is disseminated through some dikes.

2.5.2.3. Feldspar-quartz porphyry dikes

The FQP dikes have plagioclase and quartz phenocrysts hosted in a very fine- to fine-grained matrix of quartz and feldspars, with minor biotite and opaques (Fig. 2.7A). The

plagioclase phenocrysts are coarse-grained, subrounded, and often show magmatic zoning where obscured by alteration. The FQP dikes have variable intensity of alteration, ranging from weakly developed, patchy sericite alteration to strongly developed, complete alteration of feldspars leaving remnant pseudomorphs. Some FQP dikes show very strongly developed and pervasive alteration, with muscovite and calcite developed as pseudomorphs after feldspar. Rounded, fine- to medium-grained quartz phenocrysts are also present in the FQP, typically showing embayed textures. Quartz phenocrysts are much less abundant than plagioclase. There are minor, medium-grained (rarely coarse-grained) chloritized biotite grains disseminated throughout the FQP dikes, typically occurring with fine-grained intergrown opaque phases. Rarely, the coarse-grained biotite have a sagenitic texture, occurring as asterisk-shaped, crystallographically-controlled exsolved rutile or titanite (Shau et al. 1991). Some samples show evidence of blocky sericite-rich pseudomorphs after feldspar that were flattened and broken.

Preliminary mineral chemistry data were collected by SEM-EDS on three primary magmatic plagioclase grains from two FQP samples and rare primary biotite from one FQP. The data indicate that plagioclase composition ranges from oligoclase to andesine in composition, and biotite is annitic.

2.5.2.4. Quartz porphyry dikes

The QZP dikes have medium-grained quartz phenocrysts that are subhedral to euhedral with blocky to hexagonal cross-sections; quartz phenocrysts are variably embayed (Fig. 2.7B). The QZP dikes have a microcrystalline matrix of quartz, calcite, and

muscovite, with trace opaques disseminated throughout. Feldspars are not visible in hand samples but are observed in thin section that are completely altered to sericite (with rare, remnant polysynthetic twinning). Trace, anhedral to subhedral, fine-grained titanite with high relief was observed.

2.5.2.5. Intermediate dike

The intermediate dike is porphyritic, with rounded, medium-grained quartz phenocrysts and blocky, medium-grained feldspars that were altered to sericite (Fig. 2.7C). The sericite pseudomorphs after feldspars were only evident in thin section, and not discernible in hand sample. The groundmass is comprised of microcrystalline quartz with very fine-grained disseminated biotite, rarely occurring in clusters with opaque grains. In general, alteration is less pervasive in the intermediate dike than in the intermediate volcanic tuff.

2.5.2.6. Intermediate volcanic tuff

The intermediate volcanic tuff shows evidence of strongly developed, pervasive alteration such that sericite pseudomorphs after feldspars are the only remnants of phenocrysts (Fig. 2.7D). There are aggregates of very fine-grained chlorite and rectangular, fine-grained quartz that, combined with the sericite pseudomorphs, give the intermediate volcanic tuff a porphyritic texture in thin section that is not obvious in hand sample. The groundmass is comprised of very fine- to fine-grained quartz and sericite

altered feldspars. There are microveins containing fine-grained biotite and commonly also contain very fine- to fine-grained opaques.

2.5.2.7. Tonalite

The tonalite is generally medium-grained, equigranular, and dominated by plagioclase, quartz, amphibole, and biotite (Fig. 2.8A). The plagioclase is anhedral, moderately altered to sericite and with polysynthetic twinning evident in the less altered areas. The plagioclase shows remnant magmatic zoning present and secondary feldspar overgrowths. Quartz is fine- to medium-grained with abundant recrystallization textures and is interstitial to plagioclase, biotite, and amphibole; rare myrmekite was observed. The amphibole exhibit green pleochroism and are typically medium-grained; there are rare coarse-grained amphibole with secondary amphibole rims on earlier amphibole cores. The biotite is typically medium-grained, rarely coarse-grained, weakly-moderately chloritized, and has a sagenitic texture (exsolved rutile needles). Trace amounts of euhedral, fine-grained apatite are disseminated through the tonalite, and trace fine-grained titanite are occasionally associated with amphibole. Mineral chemistry data were collected for primary amphibole in one tonalite sample; the amphibole range from magnesiohornblende to edenite composition.

2.5.2.8. Granodiorite

The granodiorite contains abundant altered feldspars, biotite, and quartz with trace amounts of amphibole, titanite, and zircon included in biotite (Fig. 2.8B). The quartz is

fine- to medium-grained, and grains have an irregular, cuspate shape, occurring interstitially to feldspar and biotite grains. The feldspars are variably altered to sericite and occasionally have a mantled texture involving quartz around the feldspars. Biotite is fine- to medium-grained, often bent, shows weakly developed, patchy chlorite alteration, and a mottled to sagenitic texture.

2.5.2.9. Defeat Suite granite

The Defeat Suite granite samples are generally coarse-grained, phaneritic, with weakly developed sericitic alteration (Fig. 2.8C). The samples are dominated by coarse-grained quartz and K-feldspar with an interlocking, crystalline texture and curvilinear grain boundaries. Potassium-feldspar typically exhibits either tartan twinning or a perthitic texture. Rare myrmekite occurs throughout the samples. Plagioclase is anhedral, medium- to coarse-grained, and much less abundant than K-feldspar. Plagioclase alteration is variably developed, ranging from weakly to strongly developed sericite alteration, with fine-grained sericite occasionally showing a transition to medium-grained muscovite. Medium-grained biotite is also present in the Defeat Suite granites and typically has weakly to moderately developed chlorite alteration.

2.5.2.10. Duckfish granite

The Duckfish granite is phaneritic, coarse- to very coarse-grained, and is dominated by K-feldspar, quartz, and plagioclase with minor biotite (Fig. 2.8D). Potassium-feldspar shows perthite or tartan twinning and contains rare plagioclase inclusions. Quartz shows

abundant recrystallization textures such as undulose extinction, deformation bands, grain boundary migration, and sub-grain development; there is weakly developed hematite alteration along grain boundaries. Plagioclase is medium- to coarse-grained and shows faint magmatic zoning, highlighted by preferred alteration of some zones to sericite. Trace, fine- to medium-grained biotite with moderate chloritization occurs and contains zircon inclusions.

2.5.3. Whole-rock geochemistry

2.5.3.1. Major, trace, and REE discrimination

Lithogeochemical data for each lithology was used to compare their geochemical signatures and evaluate links between the FQP, QZP, and aplite dikes and potentially parental plutons (e.g., the tonalites and granodiorites of the RLP, the Defeat Suite granites, and Duckfish granite). The results described in this section focus on using trace elements (REE, Zr, Ti, Nb, Y, Rb, Ta, Yb, Ga, Hf, Cs, Sr) in conjunction with major element diagrams (Appendix 1, Table A1.2). This was done to minimize the impact of hydrothermal alteration on the classification of the felsic intrusions since weak to strong alteration was observed in all samples. Preliminary examination of the REE geochemistry shows that the aplite-1 dikes can be additionally subdivided into aplite-1(a) and aplite-1(b) based on their REE compositions, as described below. These three groups of aplite dikes have therefore been split and named as such from this point forward (i.e., aplite-1(a), aplite-1(b), and aplite-2).

Depending on the discrimination diagram used, data may separate into two groups or plot in a continuous array, particularly when comparing major element geochemistry. The first group consists of the tonalites, granodiorites, FQP dikes, intermediate dike and intermediate volcanic samples. In contrast, the second group consists of the more felsic Defeat Suite and Duckfish granites, the QZP dikes, and aplite dikes. The QZP dikes are the most variable in composition and cluster with either the intermediate or felsic samples. Overall, the data set typically trends from the intermediate tonalitic samples toward the more felsic granite and aplite samples; however, not all these intrusions are considered coeval. U-Pb geochronologic data was obtained for thirteen of the samples presented in this lithogeochemical study and indicates that the tonalite, granodiorite, FQP dikes, and aplite-1(a) dikes are approximately the same age (ca. 2662 Ma) and considered coeval (Speight et al. 2023b). Four of the five FQP dikes have ages ranging from 2674 to 2662 Ma and one FQP dike is older, with an age of 2746 Ma. One QZP dike was analyzed and is the oldest sample in the dataset, with an age of 2770 Ma and an unknown source. The aplite-1(b) dikes have an age of 2662 Ma, which overlaps with the intermediate rocks, although they are geochemically distinct and considered geochemically related to the younger Defeat Suite granite (ca. 2630 Ma; Davis and Bleeker 1999, Speight et al. 2023). The geochronologic study did not include any aplite-2 samples for comparison with the Duckfish granite, however, previous work has dated the Duckfish granite to 2610 Ma and one proximal aplite dike to 2611 Ma (Ootes et al. 2007).

2.5.3.2. Chondrite-normalized REE diagrams

Chondrite-normalized trace element diagrams generally show two different REE patterns that can be differentiated by the presence or absence of an Eu-anomaly (Fig. 2.9). The Eu anomaly ($Eu/Eu^* = Eu_N/[Sm_N \times Gd_N]^{½}$) and Ce anomaly ($Ce/Ce^* = Ce_N/[Nd_N^2/Sm_N]$) were calculated using chondrite-normalized values (Sun and McDonough 1989). The FQP, QZP, intermediate dike and volcanic tuff (average La_N/Lu_N = 30, Eu/Eu^* = 0.97, Ce/Ce^* = 1.1) show the same smooth REE profiles as the tonalite, granodiorite, and aplite-1(a) dikes (average La_N/Lu_N = 32, Eu/Eu^* = 0.91, Ce/Ce^* = 0.97). These lithologies all show smooth REE profiles with relative enrichment in light-REE (LREE) and relative depletion in heavy-REE (HREE) with no Eu or Ce anomalies (Fig. 2.9A-D). In contrast, the Defeat Suite granite (GRN 1) and aplite-1(b) dikes have similar patterns with relatively enriched LREE over HREE, but these lithologies have a pronounced negative Eu-anomaly (average La_N/Lu_N = 6.1, Eu/Eu^* = 0.29, Ce/Ce^* = 1.4; Fig. 2.9E). The Duckfish granite (GRN 2) and the aplite-2 dikes have similar concave-up REE profiles, with a weak positive Ce anomaly (maximum Ce/Ce^* = 3.1) and a negative Eu-anomaly, although the LREE are still enriched compared to the HREE (average La_N/Lu_N = 7.3, Eu/Eu^* = 0.44, Ce/Ce^* = 1.6; Fig. 2.9F).

2.5.3.3. General element ratio diagram

The lithological classification of these rocks can be impacted by alteration, as previously mentioned; therefore, the effects of hydrothermal alteration were evaluated using a general element ratio (GER) plot that compares molar K/Al to (2Ca+Na+K)/Al, with

the location of pure K-feldspar, albite, anorthite, muscovite, and epidote indicated to show the changes in chemistry in relation to alteration mineral abundance (Fig. 2.10; Stanley 1998, 2020). The data cluster near the albite/anorthite node, reflecting the predominance of primary plagioclase over K-feldspar in most samples although the Defeat Suite granite, Duckfish granite, and aplite-2 dikes lie mid-range along the albite-K-feldspar line, which correctly reflects the abundant primary K-feldspar observed in those samples. This could represent near-complete albitization of primary K-feldspar, but no petrographic evidence supports this. All the data except the tonalite, two granodiorites, and one aplite-1(b) dike are variably shifted towards the muscovite node relative to the primary albite-K-feldspar line, indicating sericitization which was observed in every sample to some degree. The tonalite samples, one granodiorite, and one aplite-1(b) dike show a shift toward the epidote node, which should reflect an increased abundance of epidote in these samples (e.g., sausseritization of plagioclase); however, there was no evidence of epidote alteration observed in thin section or hand sample. The tonalites are enriched in amphibole that may explain this array of samples may plotting towards the epidote node, due to an overall elevated Ca content in these samples not related to epidote specifically.

2.5.3.4. AFM diagram

An AFM diagram shows that all the YGB felsic and intermediate rocks analyzed in this study follow a calc-alkaline differentiation trend; the tonalite is the least fractionated sample, occurring in a separate cluster with the granodiorite, FQP dikes, and intermediate

volcanic tuff compared to the remaining lithologies. The Defeat Suite granites, aplite-1(b) dikes, Duckfish granites, aplite-2 dikes, intermediate dike, and QZP dikes all cluster separately from the intermediate samples, representing the most fractionated samples within the calc-alkaline field (Fig. 2.11A; Irvine and Baragar 1971).

2.5.3.5. Alkalis vs. SiO_2 diagram

The same geochemical array from the least fractionated tonalite to granites can also be observed in a plot of alkalis versus SiO_2 in which all samples fall within the subalkaline field (Fig. 2.11B; Irvine and Baragar 1971). The samples follow a trend of increasing alkali concentrations with increasing SiO_2, and the same lithological clusters can be observed as in the AFM diagram. The tonalite, granodiorite, FQP dikes, and intermediate volcanic tuff plot together at lower SiO_2 concentrations than the Defeat Suite granites, aplite-1(b) dikes, Duckfish granites, aplite-2 dikes, intermediate volcanic dike, and QZP dikes.

2.5.3.6. MALI diagram

A modified alkali-lime index (MALI) shows that the samples all have increasing SiO_2 with increasing Na_2O+K_2O-CaO concentrations and are mainly calcic to calc-alkalic but ranging to the alkalic field (Fig. 2.11C; Frost et al. 2001, Frost and Frost 2008). The tonalites, granodiorites, FQP dikes, and intermediate volcanic tuff fall within the calcic to calc-alkalic fields and in part overlap with the aplite-1(a) dikes at higher SiO_2 values (65-70 wt. %). The more granitic lithologies, including the aplite-1(a) dikes, Defeat Suite granites, aplite-1(b) dikes, Duckfish granites, aplite-2 dikes, intermediate volcanic dike,

and QZP dikes fall within the calcic to alkali calcic fields, particularly at higher SiO_2 concentrations (> 75 wt. %). Two aplite dikes plot separately from the remaining samples, including an aplite-1(b) dike that is more alkali calcic than the others and one aplite-2 dike which plots in the alkalic field.

2.5.3.7. Shand's Index diagram

Shand's Index comparing molar alkali ratios characterizes the samples as all metaluminous to peraluminous (Fig. 2.11D; Maniar and Piccoli 1989). All the tonalite samples fall within the metaluminous field, while the granodiorites and FQP dikes fall across the boundary between the metaluminous and peraluminous fields. The remaining samples, including the Defeat Suite granites, aplite dikes, Duckfish granites, QZP dikes, and the intermediate volcanic tuff and dike all fall within the peraluminous field with only one exception. One aplite-1(b) that is considered coeval with the Defeat Suite granite falls within the metaluminous field. This diagram shows a similar data cluster as the previously mentioned figures, with the tonalite, granodiorite, and FQP dikes plotting together (in this case in the metaluminous to peraluminous fields), while the more granitic samples also plot together (in the peraluminous field).

2.5.3.8. Mg # vs. SiO_2

The same two clusters can be observed when comparing the SiO_2 content to the Mg # (molar $MgO/(MgO+FeO_T)*100$) of the YGB rocks (Fig. 2.11E; Pearce 1996). The more intermediate samples (tonalites, granodiorites, FQP dikes, and intermediate volcanic tuff)

plot at lower SiO_2 (54 – 70 wt. %) and higher Mg # values (Mg # = 34 – 62) compared to the more granitic samples. The Defeat Suite granites, aplite dikes, Duckfish granites, QZP dikes, and intermediate dike plot at higher SiO_2 (62 – 80 wt. %) and lower Mg # values (Mg # = 5 – 40). There are two aplite-1(a), one aplite-1(b), and one aplite-2 dike that has a small degree of overlap with the intermediate samples at lower SiO_2 concentrations. Fig. 2.11E indicates that the tonalitic and granodioritic samples of the RLP are the least fractionated (i.e., highest Mg # and lowest SiO_2) of the lithologies analyzed.

2.5.3.9. Zr/Ti vs. Nb/Y rock classification

Immobile trace element data were plotted to classify the subvolcanic YGB rocks, specifically comparing Zr/Ti to Nb/Y (Fig. 2.11F; Pearce 1996). The immobile trace element discrimination diagram shows two data clusters, with one array consisting of the tonalites and granodiorites of the RLP, the FQP, and intermediate dike and tuff, along with the QZP dikes, Defeat Suite granites, the aplite-1(a), and aplite-1(b) dikes. This array of samples ranges from basalt to alkali rhyolite (Fig. 2.11F). The second cluster distinguished on this diagram includes the Duckfish granites and aplite-2 dikes, which fall within the trachy-andesite, trachyte, and phonolite fields. Even though these samples overlap in these compositional fields, only the RLP tonalite, granodiorite, and FQP dikes have been confirmed to have the same geochronologic age of ca. 2662 Ma (Speight et al. 2023b). The QZP dikes overlap with both the intermediate samples and the more granitic rocks, however, the QZP dike analyzed during a separate geochronologic study indicates that the QZP are relatively older (2770 Ma). Likewise, the Defeat Suite granites and aplite-1(b)

overlap with these other lithologies but are not considered coeval with the QZP dikes or the rocks related to the RLP (tonalite, granodiorite, FQP). Therefore, the overlapping nature of these samples cannot solely be considered evidence for a genetic relationship between dikes and plutons.

2.5.4. Magmatic evolution and element mobility

Magmatic evolution diagrams showing element mobility and primary fractionation trends plot immobile elements against mobile elements to evaluate whether samples were affected by hydrothermal alteration or metamorphism, both prevalent in the YGB. These post-emplacement processes can lead to deviations in geochemical trends related to fractionation for otherwise cogenetic and coeval rocks (Hollis et al. 2014, Torró et al. 2017). In this case, Zr/TiO_2 was plotted against major and trace elements to first resolve primary magmatic fractionation trends within this set of intrusions and to assess the relative relationships between dikes and plutons (Fig. 2.12). One goal of this study is to determine which YGB dike suites are related to specific regional plutons. The three sets of aplite dikes are highlighted in Fig. 2.12 along with rocks having similar REE profiles shown in the chondrite-normalized REE diagrams in Fig. 2.9. Each coeval lithological group is examined below, which also corresponds to the geochronologic relationships determined by Speight et al. (2023).

2.5.4.1. Major elements vs. Zr/TiO_2 diagrams

Overall, the three highlighted groups (related to the differences in REE profiles) display overlapping Zr/TiO_2 ratios between 600 and 1000. The more intermediate rocks and related aplite-1(a) dikes have ratios ranging from 75 to 946 the Duckfish granites and aplite-2 dikes range from 571 to 2415, and the Defeat Suite granites and aplite-1(b) dikes range from 902 to 4273. When comparing SiO_2 and Na_2O, the aplite-1(a) and aplite-1(b) groups overlap with the aplite-2 samples at high SiO_2 values (>73 wt. %) and Na_2O concentrations above 3 wt. % (Fig. 2.12A-B). The comparison of K_2O to Zr/TiO_2 shows more variability, although there is a distinct gap between the more intermediate samples (tonalite, granodiorite, FQP, aplite-1(a) dikes) and the aplite-2 group and the aplite-1(b) group (Fig. 2.12C). There is some overlap between the aplite-1(b) samples and the aplite-1(a) group; however, three of the five aplite-1(b) dikes show K_2O depletion (and two aplite-2 dikes) due to chloritization. The Duckfish Granites and aplite-2 samples show a small degree of K_2O gain related to sericitization. The CaO figure shows consistent groupings between the aplite dike groups, with an overlap of the aplite-1(a) and aplite-1(b) dikes at CaO values <1 wt.% (Fig. 2.12D). There is a steady decrease in the Mg # compared with Zr/TiO_2, and two aplite-2 dikes and one Defeat Suite granite sample have relatively elevated Mg # due to increased FeO_t (Fig. 2.12E).

2.5.4.2. Trace elements vs. Zr/TiO_2 diagrams

Cesium (Cs) concentrations show a negative trend with increasing with Zr/TiO_2, with the intermediate rocks in the aplite-1(a) group (least fractionated) having the relatively

enriched Cs values (0.600 – 24.3 ppm) compared to the aplite-1(b) samples (Cs = 0.100 – 1.40 ppm) and aplite-2 group (Cs = 0.100 – 4.10 ppm) which are more evolved but have lower Cs concentrations (Fig. 2.12F). When Hf is compared to Zr/TiO_2, the three aplite groups show three linear groups (Fig. 2.12G). The intermediate rocks and aplite-1(a) have a steep positive array, the Duckfish granite and aplite-2 dikes have a mid-range positive array, and the Defeat Suite granites and aplite-1(b) dikes have a shallow positive array. Lastly, there is a distinct separation of aplite-1(a) dikes from aplite-1(b) and aplite-2 dikes when Eu/Eu* is compared to Zr/TiO_2 (Fig. 2.12H). Overall, the intermediate rocks (FQP, tonalite, granodiorite), QZP and the aplite-1(a) dikes are the least fractionated with higher Eu/Eu* values (>0.65) compared to the aplite-1(b) and aplite-2 groups, which overlap at lower Eu/Eu* values (<0.61) but generally higher Zr/TiO_2.

2.5.5. Tectonic discrimination

2.5.5.1. Rb vs. Y+Nb and Ta vs. Yb diagrams

Tectonic discrimination diagrams (e.g., Rb vs. Y + Nb and Ta vs. Yb) show that the data have two main clusters: first, the more numerous grouping consists of the RLP, FQP, Defeat Suite granites, and aplite-1(a) dikes, with the aplite-1(b) dikes following a linear trend within these data, but relatively depleted in Rb compared to the other samples in that cluster (Pearce et al. 1984, Rutanen et al. 2011, Wang et al. 2020). All these samples fall within the volcanic-arc granite field (Fig. 2.13A; Pearce et al. 1984). Second, the Duckfish granite and aplite-2 samples form another grouping and have relatively higher

Rb and Y + Nb but follow a similar linear trend. The Duckfish granite and aplite-2 samples fall in the syn-collisional granite field, with one aplite-2 dike in the within-plate granite field and one in the ocean-ridge granite field. A plot of Ta compared to Yb shows the same clustering with one exception, the aplite-1(b) dikes, which fall in the syn-collisional granite field along with the Duckfish granite and aplite-2 dikes (Fig. 2.13B; Pearce et al. 1984). One aplite-1(b) dike and two aplite-2 dikes fall in the within-plate granite (Fig. 2.13B).

2.5.5.2. Rb/30 vs. Hf vs. Ta*3 diagram

A ternary diagram utilizing Hf, Rb/30, and Ta*3 is subdivided by tectonic setting, and YGB data predominantly plot in the volcanic arc field. However, this figure also differentiates syn-collisional granites from late- to post-collisional granites (Fig. 2.13C; Rutanen et al. 2011). The Duckfish granites and two of the aplite-2 dikes plot in the syn-collisional granite field, while two other aplite-2 dikes fall in the late- to post-collisional granite fields, and three plot in the within-plate granite field; together, these samples form an array from syn-collisional to within-plate granites. Also plotting in the within-plate granite field are the aplite-1(b) dikes and two aplite-1(a); one QZP dike falls in the within-plate granite field, while the remaining samples have a volcanic arc signature (Rutanen et al. 2011).

2.5.5.3. Nb vs. Y vs. Ce diagram

A final ternary diagram that compares relative Y, Nb, and Ce concentrations can be segregated into two fields related to granites generated through continental rifting or within-plate granites and granites derived from the continental or underplated crust

(related to arc settings; Wang et al. 2020). This diagram separates the YGB rocks into two distinct populations, the main one consisting of the intermediate rocks including the FQP dikes, tonalites, granodiorites, QZP dikes, and aplite-1(a) dikes, compared to the Defeat Suite granites and aplite-1(b) dikes, of which all occur in the field related to magmas derived from underplated crust or continental crust (Fig. 2.13D; Wang et al. 2020). The Duckfish granites and the aplite-2 dikes occupy a distinct part of the field related to continental rift or intraplate granites. This is consistent with the syn-collisional and within-plate granite signature observed in the other tectonic discrimination diagrams presented.

2.5.6. Granite discrimination

Tectonic discrimination diagrams comparing major and trace elements can be used to determine the geotectonic environment that the YGB intrusions formed and evolved in; due to overlapping tendencies leading to sometimes ambiguous classifications in single diagrams, a variety of diagrams should be used together to best characterize the samples.

2.5.6.1. Fe* vs. SiO_2 diagram

A diagram of Fe* [$FeO_t/(FeO_t+MgO)$] versus SiO_2 shows that the intermediate tonalite, granodiorite, FQP, and aplite-1(a) dikes fall within the more magnesian, arc-related field, with only one aplite-1(a) and one granodiorite are exceptions that fall in the magnesian field but outside the arc-related field (Fig. 2.14A). There is some overlap between the arc-related and A-type granite fields in the more SiO_2-rich samples. The granitic samples fall in both the magnesian and ferroan fields, although dominantly in the ferroan field; all

Defeat Suite granite and aplite-1(b) dikes fall within the ferroan field, whereas the Duckfish granite, aplite-2, and QZP dikes lie along the boundary to the ferroan and magnesian fields. The data form a generally linear array from magnesian tonalite to ferroan granites and aplite samples, indicating a change from arc-related affinity to an A-type environment. The arc-related and A-type granite fields overlap along the ferroan-magnesian boundary and in the high SiO_2, high Fe* region of the diagram, making it challenging to determine the tectonic signature of the rocks with these elements alone.

2.5.6.2. Zr vs. 10^4Ga/Al diagram

The comparison of Zr to 10^4Ga/Al can discriminate between I/S-type and A-type granites and provides further differentiation ability within the fractionated I/S-type field (Wu et al. 2017). Although there is considerable overlap in the central portion of the diagram, nearly all the samples fall within one area within the I/S-type granite field, which overlaps with the extended A-type and fractionated I/S-type field (Fig. 2.14B). The overall array of these samples falls in the fractionated I/S-type granite field, with only four samples (two Duckfish granite and two aplite-2 dikes) occurring within the overlapping A-type and fractionated granite field.

2.5.6.3. Nb vs. 10^4Ga/Al diagram

Comparing Nb to the 10^4Ga/Al ratio, the same array can be observed; the intermediate rocks and the Defeat Suite granites and aplite-1(b) dikes fall within the I/S/M-type granite field (Fig. 2.14C). The Duckfish granite and four aplite-2 dikes have an A-type signature in

this diagram, along with one aplite-1(b) dike geochemically associated with the Defeat Suite granite. In this diagram comparing Nb to 10^4Ga/Al, the samples continue to follow a linear trend from the I/S/M-type granite field to the A-type granite.

2.5.6.4. (K_2O+Na_2O)/CaO vs. Zr+Nb+Ce+Y diagram

A comparison of the major element ratio (K_2O+Na_2O)/CaO to the sum of trace elements Zr+Nb+Ce+Y discriminates between normal I/S/M-type granites, fractionated felsic granites, and A-type granites (Fig. 2.14D). The YGB samples fall in a steep negative linear array from the normal I/S/M-type granite field, through the fractionated felsic granite field, to the A-type granite field, where only two aplite-2 dikes occur. Due to elevated Zr+Nb+Ce+Y, two samples also fall in the A-type granite field, one intermediate volcanic tuff and one aplite-1(a) dike, due to elevated Zr+Nb+Ce+Y. This diagram is consistent with the other tectonic discrimination diagrams, and together, they suggest that the intermediate rocks (tonalite, granodiorite, FQP, QZP, aplite-1(a) dikes, and intermediate tuff and dike) are geochemically associated with the RLP and the Defeat Suite granites and aplite-1(b) dikes have an I/S-type signature, while the Duckfish granite and some aplite-2 dikes have an A-type signature.

2.5.7. TTG versus post-2.5 Ga granitoid signatures

2.5.7.1. Sr/Y vs. Y diagram

To assess mineral fractionation trends and further characterize the tectonic setting of the YGB intrusions, trace element discrimination diagrams involving Sr, Y, La, and Yb were

evaluated. The data arrays observed on a Sr/Y - Y diagram suggest that most samples have a post-2.5 Ga granitoid signature but several granodiorites, QZP, aplite-1(a), and the intermediate dike fall specifically within the TTG field and lie along the expected fractionation path for garnet, amphibole, clinopyroxene, titanite, and zircon (Fig. 2.15A; Moyen 2009, Arndt 2013, Altherr et al. 2019). Within the post-2.5 Ga granitoid field, also considered the post-2.5 Ga plutonic field, are the bulk of the data, including the intermediate rocks (tonalite, granodiorite, FQP, volcanic tuff) and associated aplite-1(a) dikes, and the Defeat Suite granites and aplite-1(b). The Duckfish granite and aplite-2 samples also fall within the post-2.5 Ga granitoid field; these samples also define an approximate plagioclase fractionation trend.

2.5.7.2. La/Yb vs. Yb diagram

When these samples are plotted on a La/Yb versus Yb diagram a slightly different pattern can be seen; nearly all the intermediate rocks, Defeat Suite granites, QZP, and aplite-1(a) dikes have La/Yb > 20, falling within the TTG field and follow the mineral fractionation path shown in Fig. 2.15B (Moyen 2009, Arndt 2013, MacDonald and Piercey 2019). Some of these samples correlate to those plotting in the TTG field in Fig. 2.15A; however, a much larger proportion of samples are found in the TTG field on the La/Yb versus Yb diagram. The majority of aplite-1(b) and -2 dikes, fall within the post-2.5 Ga granitoid field; these dikes also follow the plagioclase fractionation trend. The aplite-1(b) and -2 dikes fall in the post-2.5 Ga granitoid domain in both the Sr/Y versus Y and La/Yb versus Yb figures.

2.5.7.3. Sr/Y vs. La/Yb diagram

Finally, several tectonic fields have been determined and highlighted on a Sr/Y versus La/Yb diagram, which shows the location of the I/S-type granite, post 2.5 Ga granitoid arc-related rocks, and TTG arc-related rocks (Fig. 2.15C; Martin and Moyen 2002, Richards and Kerrich 2007, Moyen 2009, Arndt 2013, MacDonald and Piercey 2019, Altherr et al. 2019). When the YGB samples are plotted on this diagram, most data plot in the TTG field, although there is some overlap with the I/S-type granite field. The remaining samples are all in an array plotting toward lower Sr/Y and La/Yb values within the I/S-type granite field, although the samples follow a shallower array than the field itself. There is one aplite-1(b) and four aplite-2 dikes that do not fall in any of the established tectonic fields on this diagram but are depleted in Sr/Y. Therefore, these samples do not fall in the post-2.5 Ga granitoid field but are also too depleted in La/Yb to fall in the I/S-type granite field. Therefore, depending on which diagrams and fields are being used, the YGB can have varying tectonic signatures, and multiple discriminating diagrams should be used to determine the overall tectonic regime. In this case, the tonalite, granodiorite, FQP, intermediate dike and volcanic, aplite-1(a), and QZP dikes have a TTG signature and the Defeat Suite granites, aplite-1(b), Duckfish granite, and aplite-2 dikes have a post 2.5 Ga granitoid signature.

2.6. Discussion

2.6.1. Stages of aplite dike emplacement and evidence for volatile saturation

Experimental research into two-feldspar granite with 3 wt. % H_2O and examination of natural samples by Hibbard (1980) led to a characterization and categorization method for locally derived dikes and micro-veins. Locally sourced micro-veins and dikes in that study were of the Westerly granite and interpreted to result from the mechanical release of intergranular fluids and melts in a crystallizing magmatic system (Fig. 2.16; Hibbard 1980). Physical changes to the geotectonic environment of a crystallizing pluton can cause fracturing that will penetrate the pluton if crystallization is at least 70 % complete (Hibbard 1980, Hibbard and Watters 1985). The fracturing of magma after >70 % crystallization leads to a dilatant zone of lower pressure that melt migrates to and crystallizes into veins and dikes genetically related to the pluton (Hibbard and Watters 1985). Many granitic magmas will become H_2O-saturated after more than 90 % crystallization depending on the initial H_2O concentration and pressure of the melt (Hibbard 1980).

Hibbard (1980) describes dikes and microveins sourced from intergranular fluids of a crystallizing intrusion and established petrographic characteristics for four different stages of crystallization and related dike emplacement. The mineralogy of dikes and microveins depends on the timing of fluid and volatile release, and the four stages of dike emplacement were categorized into *main magmatic*, *late magmatic*, *early post-magmatic*, and *late post-magmatic* intrusions. Mineralogical and textural characteristics

used to categorize aplitic dikes into their respective stage of emplacement are outlined in Table 2-1, extracted from the model determined by Hibbard (1980). Each stage of emplacement correlates to specific crystallization conditions, three of which correspond to stages in which intergranular melts are saturated in H_2O (Table 2-1).

Overall, the mineralogy of locally sourced dikes and veins will be very similar and dominated by quartz, plagioclase, and K-feldspar with lesser amounts of biotite and ore minerals (Hibbard 1980). Dikes from the *main magmatic stage* may be distinguished by the presence of biotite, minor myrmekite, and a lack of broken crystals. *Late magmatic* dikes are typically characterized by an abundance of myrmekite and secondary mineral overgrowths on earlier magmatic crystals (e.g., plagioclase, K-feldspar), particularly associated with feldspars. Broken crystals (with some rotation) may be observed in *late magmatic stage* dikes. *Early* and *late post-magmatic stage* dikes have more simplistic mineralogy than the *main* and *late magmatic* intrusions. *Early post-magmatic* dikes may be recognized by secondary K-feldspar overgrowths (on earlier magmatic crystals), a lack of myrmekite, and possible metal-bearing and sulfide minerals. Finally, *late post-magmatic* dikes typically consist of quartz and ore minerals having crystallized from the last volatile-rich fluids or melts. Both *early* and *late post-magmatic* dikes typically have abundant broken crystals. Hibbard (1980, and references therein) determined that the presence of quartz pods or cores in aplitic dikes indicates that the dikes were segregated and emplaced after volatile saturation occurred; therefore, any dikes found with these quartz features must be, at minimum, *late magmatic stage* dikes. The segregation and

emplacement of intergranular fluids may be reflected in a vein or the final textures and mineralogy of a dike. This model can be used to classify the YGB aplite dikes and evaluate whether lithogeochemical changes in the YGB intrusions correlate with each stage of dike emplacement.

During the petrographic examination of aplite dikes, these characteristics were noted and used to classify the stage of dike emplacement encountered in the YGB for each aplite dike, summarized in Table 2-2. In some cases, aplite dikes had characteristics that overlapped between two stages of emplacement and were classified as such. A preliminary review of the lithogeochemical data indicated that aplite-1 dikes could be subdivided based on geochemistry and location. Initially, the aplite dikes were separated by location; those in the southern field area proximal to the RLP and Defeat Suite granite were considered aplite-1 dikes, while those found ~5 km north and proximal to the Duckfish granite were considered aplite-2 dikes. Upon examining the whole rock geochemical data, specifically the trace elements, the aplite dikes and plutons have distinctive REE profiles that subdivided the aplite-1 dikes and showed the geochemical similarities between each aplite dike group and possible parental plutons. The samples were subsequently subdivided into aplite-1(a) and aplite-1(b), corresponding to aplites with RLP and Defeat suite granite affinity respectively, while aplite-2 dikes are geochemically like the Duckfish granite.

Aplite-1(a) dikes proximal to the tonalitic and granodioritic RLP have characteristics consistent with emplacement at all stages of crystallization, from *main magmatic* to *late*

post-magmatic emplacement. Aplite-1(b) dikes that are geochemically associated with the Defeat Suite granite were found to have been emplaced during the *main magmatic* to *early post-magmatic* stages of crystallization. Aplite-2 dikes from the northern Duckfish granite area showed the least diversity of emplacement characteristics, likely emplaced during the *main magmatic* and *late-magmatic* stages.

Main magmatic stage aplite dikes contain biotite, abundant plagioclase, and possible myrmekite; samples with abundant plagioclase but no biotite were classified as *main* to *late magmatic* stage dikes (Fig. 2.6C). Aplite dikes that contain some broken crystals but do not have abundant myrmekite were also classified as *main* to *late magmatic* stage dikes. The transition from *main magmatic* to *late magmatic* stage dikes is marked by the absence of biotite and the occurrence of secondary mineral overgrowths, particularly K-feldspar rims on plagioclase grains. Another defining characteristic of the *late magmatic* stage is the prevalence of myrmekite intergrowths (Fig. 2.6D). Aplite dikes that contain *early post-magmatic* textures and myrmekite were classified as *late magmatic* to *early post-magmatic* dikes. *Early post-magmatic* stage dikes have secondary overgrowths of K-feldspar and abundant broken crystals with residual melt infilling the fractures (Fig. 2.6E). Finally, only one aplite dike has *late post-magmatic* characteristics, consisting of nearly monomineralic mineralogy of quartz and opaque minerals (Fig. 2.6F). This aplite dike consists of a quartz matrix with trace sericite and comb-texture quartz, occurring within a quartz core observed in hand sample. Trace amounts of very fine- to fine-grained

opaques were observed in thin section, correlating to Fe-rich phases observed in the μXRF scans (Fig. 2.5B).

The textures and interpretations described here would not be possible by petrographic analysis alone and were complemented by both a micro- and macroscopic perspective in the field as additional layers of evidence. Aplite dikes associated with the three regional plutons discussed here show varying stages of emplacement and evidence for volatile saturation (Fig. 2.3, Table 2-2). The quartz cores and pods found within the aplite dikes at the macroscopic scale reflect the *in-situ* crystallization of exsolved volatiles during dike emplacement and provide direct evidence for volatile saturation. This was also corroborated during μXRF and petrographic analysis of polished thin sections (Fig. 2.5 and Fig. 2.6; Hibbard 1980, Hibbard and Watters 1985). This petrographic analysis showed myrmekite, comb-textured quartz, secondary mineral overgrowths, and quartz +/- ore minerals, which are all used to define the four stages of dike emplacement and categorize the aplite dikes (Hibbard 1980).

The aplite-1(a) dikes derived from the tonalitic and granodioritic RLP showed the widest range of textures and were emplaced during all four stages of crystallization (*main magmatic* to *late post-magmatic* stage). Therefore, the RLP crystallized in an active geotectonic environment which caused fracturing of the crystallizing pluton to occur at each of these stages, with or without volatiles (Hibbard 1980, Hibbard and Watters 1985). The characterized stages of emplacement for the aplite-1(b) and aplite-2 dikes associated with the Defeat Suite and Duckfish granites show decreasing variability and were

emplaced during only three of the four stages of emplacement, and two of the four stages of emplacement, respectively (Table 2-2). The aplite-1(b) dikes were intruded during the *main* to *early post-magmatic* stage (three of four stages), while the aplite-2 dikes were only emplaced during the *main* and *late magmatic* stages (only two of four stages). This decrease in the stages of emplacement suggests that less fracturing and structural activity was occurring during the evolution and crystallization of these intrusions, and the geotectonic environment was progressively stabilizing during sequential emplacement of the RLP, Defeat Suite, and finally Duckfish granite (and associated dikes; Table 2-2).

Concerning their relative timing, the tonalitic and granodioritic RLP and associated aplite-1(a) dikes were intruded first. Simultaneously, the Defeat Suite granite and aplite-1(b) were intruded, and finally, the Duckfish granite and aplite-2 dikes were intruded in the northern field area. This relative timing correlates with previously determined ages of the plutons, including the 2675 Ma RLP, the 2630 Ma Defeat Suite, and 2610 Ma Duckfish Granite (Davis and Bleeker 1999, Ootes et al. 2007). Current U-Pb geochronology of these specific samples indicates that the RLP tonalite and aplite-1(a) dikes were coeval at 2662 Ma (Speight et al. 2023b). One aplite-1(b) dike was also dated yielding an age of 2662 Ma, indicating that the magma chamber related to the Defeat Suite granite was present at depth at this time. This suggests that the aplite-1(b) dikes are early intrusions related to the Defeat Suite granite that were emplaced before final crystallization of the pluton.

2.6.2. Geochemical comparison of aplites and the stage of dike emplacement

Based on the model of Hibbard (1980) and Hibbard and Watters (1985), the petrographically determined stages of dike emplacement suggest that the aplite dikes represent a snapshot of magma chemistry related to that stage of crystallization. This can be observed when the geochemical data are compared to the interpreted stage of emplacement to assess the magmatic evolution of the aplites during progressive crystallization (Fig. 2.17). A total of 24 aplite dikes were petrographically examined and classified using the model outlined by Hibbard (1980) and Hibbard and Watters (1985), summarized in Table 2-1. Of the samples submitted for thin section analysis, geochemical data were obtained for 19 aplite dikes.

The data shown represent elements that most effectively discriminate between the three groups of aplite dikes while also showing increasing fractionation. The dikes all show a negative trend when Al_2O_3 is compared to the dikes' stage of emplacement, with the aplite-1(b) and aplite-2 dikes having a steeper negative trend than the aplite-1(a) dikes (Fig. 2.17A). When the K_2O content of the aplite dikes is compared, the aplite-1(a) dikes have a shallow negative trend, as do the aplite-1(b) dikes albeit at a lower K_2O concentration (Fig. 2.17B). The aplite-2 dikes are split, with half having lower K_2O concentrations (< 1.46 wt. % K_20) and overlapping with the aplite-1(b) dikes, and the other half the highest K_2O concentration at > 4.11 wt. %. A diagram comparing MgO to stage of emplacement shows the elevated signature of the aplite-1(a) dikes compared to the aplite-1(b) and aplite-2 dikes as only one aplite-1(a) sample overlaps with the other dikes

(Fig. 2.17C). The aplite-1(a) dikes have a steep negative covariance with MgO, and the aplite-1(b) and aplite-2 dikes have a very shallow negative trend occurring at < 0.5 wt. % MgO. The same trend can be seen when TiO_2 is compared to the stage of dike emplacement, and there is a moderate to steep negative covariance with increasing crystallization for all aplite dikes (Fig. 2.17D). The aplite-1(a) dikes have the most elevated TiO_2 compared to the aplite-1(b) and aplite-2 dikes, which overlap at concentrations below 0.11 wt. % TiO_2. Total REE concentrations for the aplite dikes were compared, and the aplite-1(a) dikes have a steep negative covariance with their stage of emplacement and generally have more elevated concentrations than the other aplites; the aplite-1(b) and aplite-2 dikes overlap at lower ΣREE concentrations (Fig. 2.17E). Finally, the Eu/Eu* ratios of the aplite dikes were compared, and it was found that the aplite-1(a) dikes have higher Eu/Eu* values than the aplite-1(b) and aplite-2 dikes, with only one exception. The aplite-1(a) dikes have Eu/Eu* from 0.65 – 1.2, while the aplite-1(b) and aplite 2 overlap at lower values that range from 0.10 – 0.45; only one aplite-2 dike has an Eu/Eu* of 1.2 (Fig. 2.17F).

The tonalite and granodiorite of the RLP are the least fractionated of the YGB samples studied and have higher concentrations of Al_2O_3, MgO, and TiO_2 compared to the Defeat Suite granite and Duckfish granite. This geochemical signature is mimicked by the aplite-1(a) dikes, which consistently have elevated concentrations of Al_2O_3, MgO, and TiO_2 compared to the aplite-1(b) and aplite-2 dikes, except K_2O (Fig. 2.17). When comparing the aplite-1(a) and -1(b) dikes, the elements that can be used to distinguish the two

groups include MgO, Na_2O, TiO_2, Ba, Cs, Lu, Rb, Sr, Ta, Yb, and Eu/Eu*, along with their REE profiles. These differences are not obvious during a petrographic or macroscopic examination of the samples and require geochemical differentiation.

2.6.3. Genetic link between dikes and parental plutons

Whole-rock geochemistry was evaluated to test a link between the "#9" dikes and regional plutons of the YGB to gain a better understanding of Archean magmatism in the study area. As many as four generations of dikes have been observed crosscutting the Kam Group, three of which were encountered in the field and have been studied here: the FQP, QZP, and aplite dikes (Henderson and Brown 1966, Isachsen et al. 1991, Isachsen 1992, Isachsen and Bowring 1994, Cousens et al. 2002). For comparison, samples of one intermediate dike and volcanic tuff were also collected to compare with the tonalitic and granodioritic RLP, Defeat Suite granite, and Duckfish granite to further evaluate any possible genetic relationship (data given in Appendix 1, Table A1.2).

2.6.3.1. Feldspar quartz porphyry and aplite dikes

Distinct REE patterns were used to distinguish three groups of rocks that correlate to the three groups of aplite dikes and their parental plutons (Fig. 2.10). These groupings also correlate with the geochronologic data obtained for a subset of samples, except for the older QZP dike (further discussed below). Based on the geochronologic data, the RLP tonalite and granodiorite are coeval with the FQP and aplite-1(a) dikes (2662 – 2663 Ma), based on available data (Speight et al. 2023b). This correlates with the first geochemically

distinct group which consists of the FQP, QZP, intermediate dike and volcanic tuff, tonalite (RLP), granodiorite (RLP), and aplite-1(a) dikes, which all have REE profiles that decrease from LREE to HREE (average La_N/Lu_N= 31, Eu/Eu* = 0.94, Ce/Ce* = 1.0). The second group consists of the Defeat Suite granites and aplite-1(b) dikes with flatter REE profiles, with a strong negative Eu/Eu* (average La_N/Lu_N = 6.1, Eu/Eu* = 0.29, Ce/Ce* = 1.4). The aplite-1(b) dike analyzed during the geochronologic study has an age of 2662 Ma, suggesting that a separate magma chamber related to the Defeat Suite granite was present at the same time the RLP was emplaced and crystallizing at ca. 2662 Ma (Speight et al. 2023b). Finally, the third group consists of the Duckfish granite and aplite-2 dikes with a weak positive Ce/Ce* (up to 3.1), pronounced negative Eu/Eu*, and concave up HREE pattern (average La_N/Lu_N = 7.3, Eu/Eu* = 0.44, Ce/Ce* = 1.6). Previous geochronologic data suggests that the Duckfish granite is 2610 Ma and an aplite dike proximal to the pluton has a crystallization age of ca. 2611 Ma, which further suggests that aplite dikes in this area are coeval with the Duckfish granite, correlating with the geochemical interpretation given here (Davis and Bleeker 1999, Ootes et al. 2007). The aplite-1(a) dikes occur within and along the eastern margin of the tonalitic and granodioritic RLP, whereas the aplite-1(b) dikes occur within mafic volcanic flows north of the RLP and proximal to the Defeat Suite granite. Finally, the aplite-2 dikes occur ~5 km north of the RLP and Defeat Suite granite, occurring proximal to the Duckfish granite (Fig. 1.1).

2.6.3.2. Quartz porphyry dikes

The QZP dikes are challenging to link to a parental pluton as they overlap in composition with other groups depending on the diagram, often plotting with the RLP and intermediate rocks, but also with the Defeat Suite and Duckfish granite on other diagrams. The high SiO_2, high alkali, and low Mg # of the QZP dikes cause them to frequently overlap with other high SiO_2 lithologies, including the aplite dikes, Defeat Suite granites, and Duckfish granites (e.g., Fig. 2.11A-E). The QZP dikes do not share the same Zr/TiO_2 and Nb/Y concentrations as the Duckfish granites and aplite-2 dikes when plotted on a rock classification diagram, suggesting they are not genetically related to the Duckfish granite (Fig. 2.11F). The major element chemistry of the QZP dikes would suggest that they are either an evolved member of the intermediate RLP group, or they are related to the Defeat Suite granite as aspects of their geochemistry also overlap (e.g., Fig. 2.11).

When evaluating the relative location of the QZP dikes when comparing major and trace elements to Zr/TiO_2 (Fig. 2.12), the dikes fall within the RLP and aplite-1(a) field, typically at the most evolved end, which can overlap with both the Defeat Suite and Duckfish granites (Torró et al. 2017). The K_2O and Eu/Eu* versus Zr/TiO_2 plots show complete separation of the QZP dikes from the Defeat Suite and Duckfish granites (Fig. 2.12C, H). In particular, the Eu/Eu* versus Zr/TiO_2 diagram shows the QZP overlapping with only the RLP-related samples, including the tonalites, granodiorites, FQP dikes, aplite-1(a), and intermediate dike and volcanic rocks. Therefore, this also indicates that the QZP dikes may be genetically related to the multi-phase RLP, but not the Defeat Suite

or Duckfish granite. The QZP dikes have a smooth, flat REE pattern, suggesting that these dikes are related to the RLP and not the Defeat Suite granites, which have pronounced negative Eu anomalies (Fig. 2.9B, E). The chondrite-normalized REE diagrams indicate that the QZP are the most depleted in REE of all intrusions related to the RLP (Fig. 2.10A-D). This is consistent with the QZP dikes being the most evolved rocks related to the RLP since the most evolved rocks would have the lowest REE concentrations. When all geochemical data are considered together, it is more likely that the QZP dikes represent evolved dikes related to the RLP.

Even though multiple major and trace element discrimination diagrams indicate an overlapping geochemical relationship between the QZP dikes and the RLP, the Cs concentrations show a different trend (Fig. 2.12F). If the QZP dikes represent evolved members of the RLP system, they would have comparatively elevated Cs concentrations, but the opposite was observed. The QZP dikes have 0.100 – 2.10 ppm Cs while the RLP tonalites and granodiorites have 2.40 – 24.3 ppm Cs. Primary biotite was observed in the tonalite and granodiorite during petrographic analysis and may have sequestered Cs early in the magmatic history of the RLP, although biotite only mildly fractionates Cs in granitic magmas (Nash and Crecraft 1985, Zall et al. 2019, Were and Keppler 2021). This would suggest that the QZP dikes could still be related to the RLP if the available Cs was sequestered in biotite before emplacement of the dikes. However, the geochronology of the QZP dikes does not support a genetic relationship between the dikes and the multi-phase RLP (Speight et al. 2023b). One QZP dike was found to have an age of 2770 Ma,

which is 108 Ma older than the 2662 Ma RLP tonalite which suggests that the QZP dikes are part of an older component of the YGB (Speight et al. 2023b). This 2770 Ma QZP dike was sampled roughly 5 km north of the three remaining QZP dikes in this lithogeochemical study and may not reflect the age of all QZP dikes. Further U-Pb geochronology data should be obtained for the QZP dikes to identify possible parental plutons since the geochemical data suggest multiple interpretations.

2.6.4. Magmatic fractionation in the Archean

One goal of this study is to refine the magmatic evolution of felsic intrusions and dikes in the YGB. A general element ratio (GER) diagram comparing modal K/Al to (2Ca+Na+K)/Al was used in conjunction with petrographic observations to determine the extent of sericitization (muscovite) and albitization (Fig. 2.10; Stanley 1998, 2020). The data show a range in whole rock chemistry along the K-feldspar-to-albite/anorthite join. Since no albitization is observed in thin section, this is considered to represent the primary igneous mineralogy of the samples and not alteration. Petrographic analysis of each lithology also supports this lack of albitization as primary plagioclase and K-feldspar were observed; variably intense sericitization and chloritization were most commonly noted. The data composition spread shows some dispersion away from the K-feldspar-to-albite/anorthite tie line toward the muscovite endmember, indicative of the weak to moderate sericitization observed in all samples. The most sericite-altered samples shown in Fig. 2.10 are the intermediate volcanic tuff, a QZP dike, and an FQP dike. The tonalite samples have shifted in the opposite direction toward the epidote node; however, no

epidote was observed in the thin section. This shift is likely due to an increase in Ca-rich amphibole in these samples.

The magmatic evolution of the YGB intrusions was evaluated using immobile trace elements to compare and establish the least and most fractionated samples. The ratio Zr/TiO_2 was used to monitor fractionation paths for various elements within a cogenetic and coeval suite and to establish whether the samples were affected by alteration if they do not follow the expected trend (Torró et al. 2017). Ti is considered a compatible element in granitic magmas as it can enter mafic minerals that crystallize early in an evolving magma (e.g., rutile, titanite, biotite, amphibole). The Zr/TiO_2 ratio can therefore be used to monitor progressive fractionation, which would typically fall along a single trend; samples affected by open system processes fall off the main trend (Fig. 2.12; Torró et al. 2017). In this case, the Zr/TiO_2 ratio is used to evaluate the relationships between the dikes and plutons, since certain YGB dikes are considered coeval with specific plutons (e.g., FQP dikes and the multi-phase RLP).

Of all the rocks in this YGB study, the tonalitic RLP was found to be the least fractionated unit, and the Defeat Suite granites and aplite-1(b) are the most fractionated, as shown in various geochemical figures (Fig. 2.12 and Fig. 2.13). There is evidence from major element chemistry that these samples have been affected by alteration, corroborated by the petrographic analysis and the previously mentioned GER diagram (Fig. 2.11). For example, two aplite dikes (-1(b) and -2) show elevated Na_2O, and five aplite dikes (-1(b) and -2) show a loss of K_2O compared to their parental plutons, the Defeat

Suite and Duckfish granites. These were the only two elements that differ significantly from the main geochemical groups related to the RLP, Defeat Suite granite and Duckfish granite. Two aplite dikes have elevated CaO compared to the three main groups; however, calcite was observed in these samples and is likely responsible for this increase. Hafnium concentrations increase with progressive fractionation, as expected, and three paths can be observed, each following the trend of the three aplite groups (Fig. 2.13G). The intermediate samples representing the RLP and aplite-1(a) dikes have the steepest linear trend, while the Duckfish granite and aplite-2 dikes have a moderately sloping linear trend, and the Defeat Suite granites and aplite-1(b) dikes have the shallowest Hf fractionation path (Fig. 2.13G). Finally, the distinction of the geochemical groups can be observed when Eu/Eu* is compared to Zr/TiO_2, showing a decrease in Eu/Eu* with increasing differentiation while also separating the intermediate samples related to the RLP and aplite-1(a) dikes from the Defeat Suite granites, Duckfish granites, and related aplite dikes (Fig. 2.13H). And as previously discussed, the Eu/Eu* concentration in the QZP dikes further links them to the RLP rather than the Defeat Suite or Duckfish Granite.

One element that does not follow an expected fractionation path for any of the YGB samples is Cs, which are found to decrease with increasing fractionation (i.e., increasing Zr/TiO_2). In fact, Cs should behave incompatibly and increase with increasing fractionation (Zajacz et al. 2008). This behaviour could be due to alteration and leaching of Cs from the rocks or differences related to coeval magma sources at different stages of differentiation. Since three separate populations of plutons and dikes have been

determined here (i.e., the intermediate RLP group, the Defeat Suite granite group, and the Duckfish granite group), their unexpected Cs trends may be related to each series of dikes and plutons having different and separate magmatic history, as they are only co-magmatic in time. The same trends in Cs can be observed with respect to other elements that systematically change with progressive fractionation, such as Zr and Nb. The whole rock lithogeochemistry indicates that Cs concentrations decrease with decreasing Zr and decreasing Nb, which is the opposite trend the samples should show. When Cs concentration is considered with respect to the GER diagram and alteration determined by geochemistry, the samples that have [(2Ca+Na+K)/Al] < 1 are considered altered, and these altered samples also correlate to low Cs values (Stanley 1998, 2020). This physically correlates to the intensity of alteration observed in hand sample and thin section; visually, the intermediate rocks are some of the least altered compared to the more granitic samples which have the lowest Cs values.

The lower Cs values could also be due to Cs partitioning into hydrothermal fluids (Zajacz et al. 2008). With progressive magmatic evolution and crystallization, Cs would partition into magmatic-hydrothermal fluids causing the Cs content of the intrusions to decrease, as observed in Fig. 2.13F. Textural evidence of the fluid-saturated nature of these plutons and dikes has been documented here and supports this interpretation. Another possible explanation for this unexpected trend in Cs concentrations could be related to the segregation of the aplite dikes from the main magma chamber (i.e., the RLP tonalites and granodiorites, and the Defeat Suite granites). This would cause these early

dikes to have low concentrations of Cs relative to the still crystallizing and fractionating main pluton. The incompatible Cs would therefore have a relatively higher concentration of Cs, as is observed here (Fig. 2.13F).

2.6.5. The geotectonic setting and granite differentiation of YGB dikes and plutons

Several tectonic discrimination diagrams involving trace elements were utilized to determine the geotectonic affinity and evolutionary relationships of the YGB intrusions. The diagrams indicate differences in the geotectonic environment, including a volcanic-arc to syn-collisional setting (RLP and Defeat Suite granite, and related dikes) and finally a within-plate granite setting (Duckfish granite and related dikes), generally trending from the QZP dikes to the RLP to the Duckfish granites and aplite-2 dikes (Fig. 2.14A-B). This trend is supported by the U-Pb geochronology data, where the QZP dikes have been identified as the oldest intrusion (2770 Ma) in this YGB sample set, followed by the RLP tonalite (2662 Ma), FQP dikes (2746 – 2662 Ma), aplite-1(a) dikes (2663 Ma), aplite-1(b) dikes (2662 Ma), Defeat Suite granite (2630 Ma), and finally the Duckfish granite (2610 Ma) and aplite-2 dikes (2611 Ma; Davis and Bleeker 1999, Ootes et al. 2007, Speight et al. 2023). Of the five FQP dikes dated, four have ages ranging from 2674 to 2662 Ma and one FQP dike is older, with an age of 2746 Ma (Speight et al. 2023b). The fact that the multi-phase RLP and associated dikes have a somewhat different tectonic affinity (volcanic arc only) compared to the Defeat Suite granites and related aplite-1(b) dikes (volcanic arc to syn-collisional granite) suggests that at ca. 2662 Ma both of these subvolcanic magmas

were present simultaneously in the YGB. A further change in the geotectonic regime then took place between the emplacement of the volcanic arc to syn-collisional RLP and Defeat Suite granites to the Duckfish granite, which has a within-plate granite affinity (Fig. 2.14D).

Aplite-1(b) dikes appear to be depleted in Rb since they often overlap with the aplite-2 dikes or plot in the syn-collisional to within-plate granite fields in diagrams that do not use Rb to classify the tectonic setting; however, when Rb is part of the characterization the aplite-1(b) dikes are relatively depleted in Rb compared to the rest (Fig. 2.14A vs. Fig. 2.14B). Earlier K-feldspar fractionation or biotite crystallization in the Defeat Suite granite could be responsible for a corresponding depletion in Rb of the aplite-1(b) dikes (Nash and Crecraft 1985, Dutch et al. 2013, Were and Keppler 2021).

The lithogeochemistry of different YGB intrusions was compared to determine the type of granites that these intrusions evolved from and whether the differences could be related to magmatic-hydrothermal activity. Ferroan granites can be formed from high-pressure fractionation of tholeiitic basalts, consistent with the indicated syn-collisional and within-plate granite signatures of the Duckfish granite and related aplite-2 dikes (Frost and Frost 2008). As previously noted, the tonalites and granodiorites of the RLP represent the least fractionated samples in this study, reflecting the least evolved magmatic signature observed, and the RLP and associated aplite-1(a) dikes are normal I/S/M-type granites (Fig. 2.15). The Defeat Suite granites and aplite-1(b) dikes fall along the boundary between the I/S/M-type and A-type granite field; however, Fig. 2.15D is further subdivided to include a fractionated felsic granite field where these samples plot.

The fractionated granite field has been correlated with magma which has a high temperature and is volatile rich (Wu et al. 2017). Of the YGB samples, those that fall into this field are dominantly the Defeat Suite granite and aplite-1(b) dikes, with fewer QZP, Duckfish granite, and aplite-2 dikes, reflecting the change from evolved QZP dikes formed in a volcanic-arc setting to the Defeat Suite and aplite-1(b) dikes formed in the volcanic-arc to the syn-collisional tectonic environment, likely during arc accretion (Speight et al. 2023b). Finally, very few samples fall consistently in the A-type granite field, typically only a few aplite2 dikes and the Duckfish granites. This A-type granite signature signifies a change from a hydrous environment associated with volcanic-arc magmatism to rocks forming in a more anhydrous environment related to anorogenesis (Fig. 2.15; Frost et al. 2001). This correlates with the previously described tectonic signatures of the YGB rocks, evolving from a volcanic-arc setting to syn-collisional and within-plate granites.

2.6.6. Primary magma chemistry of YGB intrusions

The YGB intrusions were found to have somewhat competing TTG and post-2.5 Ga granitoid arc signatures when Sr/Y versus Y and La/Yb versus Yb were compared (Fig. 2.15). The RLP tonalite, granodiorite, FQP, and aplite-1(a) have lower than expected Sr/Y ratios and plot along the boundary between the TTG and post-2.5 Ga granitoid suites; these samples plot within the TTG field of the La/Yb versus Yb diagram. This suggests that the RLP and related rocks are either depleted in Sr, enriched in Y, or it is an inherited signature from the magmatic source (Richards and Kerrich 2007, Smithies et al. 2019). Despite this slightly differing tectonic signature, this intermediate group of intrusions

related to the RLP broadly follows the mineral fractionation trend shown in Fig. 2.15A and B related to garnet, amphibole, clinopyroxene, titanite, and zircon crystallization (modelled from an average andesite composition; Richards and Kerrich 2007). These phases, specifically amphibole, titanites, and zircons were observed in the tonalites and rarely in the granodiorites of the RLP; however, they also contain abundant plagioclase which could explain their relatively decreased Sr/Y values. The Defeat Suite granite, Duckfish granite, aplite-1(b), and aplite-2 dikes plot below the plagioclase fractionation path in the post-2.5 Ga granitoid field of the Sr/Y versus Y diagram but weakly follow the same trend towards increased Y (Fig. 2.15A). There is a stronger association between plagioclase fractionation and the aplite-1(a) and aplite-2 dikes when La/Yb and Yb are compared, although still occurring in the post-2.5 Ga granitoid field (Fig. 2.15B). When the two ratios are compared (Sr/Y versus La/Yb), the tectonic affinity of the RLP tonalite, granodiorite, FQP, aplite-1(a), and intermediate dike becomes clearer and plots within the Archean TTG field, also correlating with the smooth and flat REE patterns that were previously described (Fig. 2.15C; Arndt 2013). The QZP dikes also fall within the Archean TTG field (with one exception), which correlates with the interpretation that they may be related to an older YGB component.

To better understand the magmatic sources and fractionation processes taking place during crystallization of the YGB intrusions, chondrite-normalized La_N/Yb_N versus Yb_N were compared (Fig. 2.18A; Moyen and Martin 2012, Arndt 2013). The partial melting curves related to an Archean tholeiitic basalt were added, showing the partial melting

curves (and therefore magma source) for a garnet free residual melt, a 10% garnet-bearing amphibolite residual, and a residual melt of eclogite composition (de Souza et al. 2001, and references therein). The YGB data show a range from a garnet-free source to eclogitic, but predominantly plot between a garnet-free and 10% garnet-bearing amphibolite residual melt. The location of the QZP dikes on the La_N/Yb_N versus Yb_N diagram suggests that these rocks are more evolved than the intermediate and RLP group since three of the four samples fall along the eclogite partial melting curve compared to the one remaining QZP which overlaps with the intermediate and RLP samples between the garnet-free and 10% garnet residual partial melting curves (Fig. 2.18A). The evolved rocks plot at lower Yb_N values, suggesting that residual garnet increased as the YGB rocks were fractionating (de Souza et al. 2001). The increased stability of garnet in the residual melt causes the observed decrease in Yb_N and increasing La_N (de Souza et al. 2001).

The geochemical fields related to the chondrite-normalized La_N/Yb_N versus Yb_N of Archean TTG and post-2.5 Ga granitoids have also been highlighted in Fig. 2.18A, and the chondrite-normalized REE diagrams are shown in Fig. 2.18B and Fig. 2.18C (Moyen and Martin 2012, Arndt 2013). There is an area of overlap from $4.5<Yb_N<8.5$ and $La_N/Yb_N \leq 20$, where the bulk of YGB data falls, however, the typical chondrite-normalized REE diagrams of Archean TTG and post-2.5 Ga granitoids aid in differentiating the units. The FQP dikes, QZP, aplite-1(a) dikes, tonalites, granodiorites, intermediate dike and volcanic tuff all share the REE signature of Archean TTG (Fig. 2.18B; Moyen and Martin 2012, Arndt 2013). In contrast, the aplite-1(b) dikes, Defeat Suite granites, aplite-2 dikes, and Duckfish

granites share an REE signature with post-2.5 Ga granitoids (Fig. 2.18C). The Defeat Suite granite and Duckfish granite are considered the youngest in the set of YGB samples (i.e., 2630 – 2620 Ma, 2610 Ma, respectively), however, they were emplaced before this interpreted geochemical change at ca. 2.5 Ga, as were the associated aplite-1(b) and -2 dikes (2662 Ma, and 2611 Ma, respectively; Davis and Bleeker 1999, Ootes et al. 2007, Speight et al. 2023). This suggests that major geochemical and geotectonic changes were taking place in Archean terranes before the occurrence of post-2.5 Ga granitoids.

2.7. Conclusions

A combination of field, petrographic, and geochemical techniques were used to characterize this suite of YGB intrusions and determine the parental plutons related to the "#9" dikes. A further goal of this study was to categorize the stage of dike emplacement related to aplite dikes that crosscut the mafic volcanic flows of the Chan Formation, the tonalite and granodiorite of the RLP and were proximal to the Defeat Suite granite. The following conclusions were made based on the available data:

I. The "#9" dikes were effectively discriminated using major, trace, and REE lithogeochemical data, which determined that the FQP and aplite-1(a) dikes in this study are geochemically and genetically related to the multi-phase tonalitic and granodioritic RLP. The Defeat Suite granite is genetically related to the aplite-1(b) dikes, and the Duckfish granite is related to the aplite-2 dikes. Chondrite-normalized REE diagrams effectively characterized the three groups of plutons and

dikes based on the presence (or lack of) of an Eu anomaly and the nature of the HREE.

II. The QZP dikes were not linked to a specific parental pluton examined in this study (i.e., the RLP tonalite, granodiorite, the Defeat Suite granite, or Duckfish granite) despite their geochemical similarities. The age of one QZP dike suggests that they are geochronologically older than any of the other intrusions examined in this study, although there is no age data for three of the four dikes studied. Further geochronologic analysis of those dikes could assist in establishing their magmatic source.

III. Trace element discrimination indicates that the YGB intrusions presented here initially formed in a magnesian, I/S-type, volcanic-arc setting (RLP group) and transitioned to a more ferroan, syn-collisional to A-type environment (Defeat Suite granite group), and finally a syn-collisional to within-plate granite tectonic environment (Duckfish granite group). The lithogeochemical classification of a large group of RLP samples (compared to previous studies) and the Defeat Suite and Duckfish granites will allow future geochemical surveys to identify geochemically associated rocks of either pluton quickly. This could aid mineral exploration by guiding future surveys.

IV. There are four stages of dike emplacement determined by Hibbard (1980) and Hibbard and Watters (1985) that can petrographically characterize intrusions and determine their relative timing in a magmatic suite. These stages include the *main*

magmatic, *late magmatic*, *early post-magmatic*, and *late post-magmatic*, all identified in the aplite dikes related to the multi-phase RLP, the Defeat Suite granite, and the Duckfish granite.

V. The *late magmatic*, *early post-magmatic*, and *late post-magmatic* granitic dikes all crystallized from volatile-saturated fluids. Aplite dikes that were emplaced during the *main magmatic* stage of crystallization were intruded before water saturation at >90 % crystallization. All three plutons and aplite dikes showed dike emplacement related to at least the *late magmatic* stage, although to lesser extents. The RLP and aplite-1(a) dikes had dikes emplaced during all four stages of crystallization, the Defeat Suite granite and aplite-1(b) dikes were emplaced only up to the *early post-magmatic* stage, and the Duckfish granite and aplite-2 dikes were only emplaced during the *main* to *late magmatic* stage. Aplite dikes with quartz cores and discontinuous pods represent *in-situ* evidence of volatile saturation.

VI. A geochemical comparison of aplite dikes associated with different stages of dike emplacement indicates that aplite-1(a) dikes associated with the RLP mimic the less evolved nature of their parental pluton compared to the aplite-1(b) and aplite-2 dikes. Overall, each group of dikes shows lithogeochemical data that follow expected fractionation trends with progressive stages of dike emplacement (i.e., the *main magmatic* stage dikes are less evolved than the *early post-magmatic* dikes).

VII. The determination of a hydrous magmatic environment related to the volcanic arc setting of the RLP pluton and dikes indicates that these rocks may be prospective for mineralization, particularly when compared to the increasingly dry conditions of the Defeat Suite granite, Duckfish granite, and associated dikes.

Future research programs could focus mapping and sampling initiatives on the northern and western parts of the RLP to expand the lithogeochemical dataset and explore for mineralization. Additional geochronologic studies of the YGB dikes and regional plutons (RLP, Defeat Suite granite, Duckfish granite) could assist in assessing their absolute timing and lead to a greater understanding of their relationships to mineralization. Finally, to better understand Archean fluid chemistry and its evolution during YGB magmatism, observed quartz-hosted fluid inclusions from the aplite dikes and corresponding plutons could be analyzed to determine initial magma fertility.

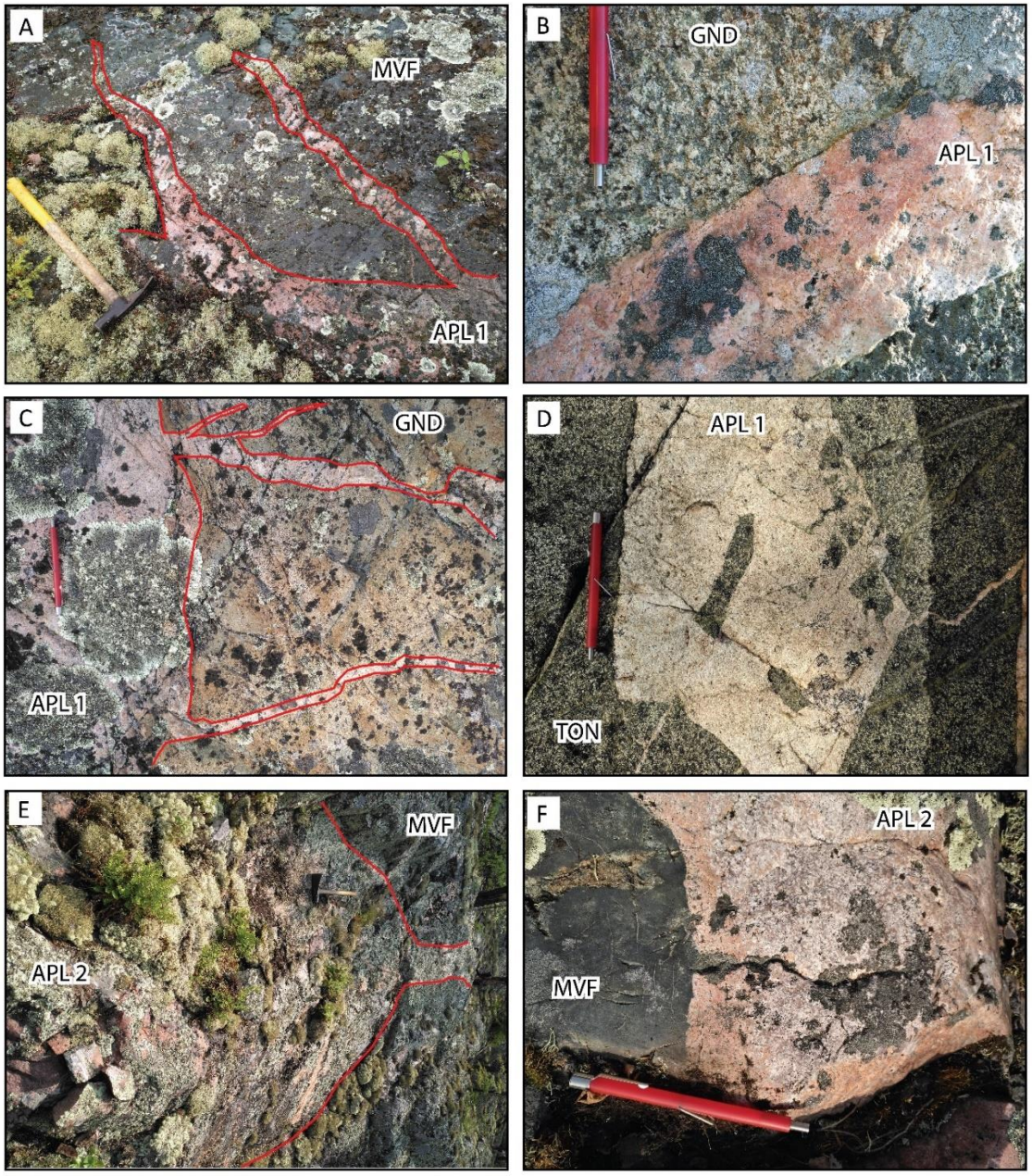


Fig. 2.1: Textures and contact relationships between aplite dikes from the southern (aplite-1) and northern (aplite-2) field areas. The dikes were found hosted in mafic volcanic flow (MVF), granodiorite (GND), and tonalite (TON). A) Branching granitic dike with two parallel arms; 90 m from RLP. B) Granitic dike is <15 cm wide, crosscuts granodiorite within the RLP; dark pink-orange colour due to hematite alteration. C) Dikes are 30 cm wide with narrow <1-4 cm injections into the granodiorite; within RLP. D) Aplite dike is ~30 cm with xenoliths of tonalite within the RLP; the darker area on the right of the image is underwater. E) Aplite dike is 4-5m wide and narrows to <1 m; 700 m from

the Duckfish granite. F) Aplite dike is 30 cm wide with cm-scale chill margin that coarsens toward the center, 10 m from Duckfish granite. Sledgehammer and pen magnet for scale. Aplite dike contacts in A, C, and E are highlighted in red. APL 1 = aplite-1; APL 2 = aplite-2.

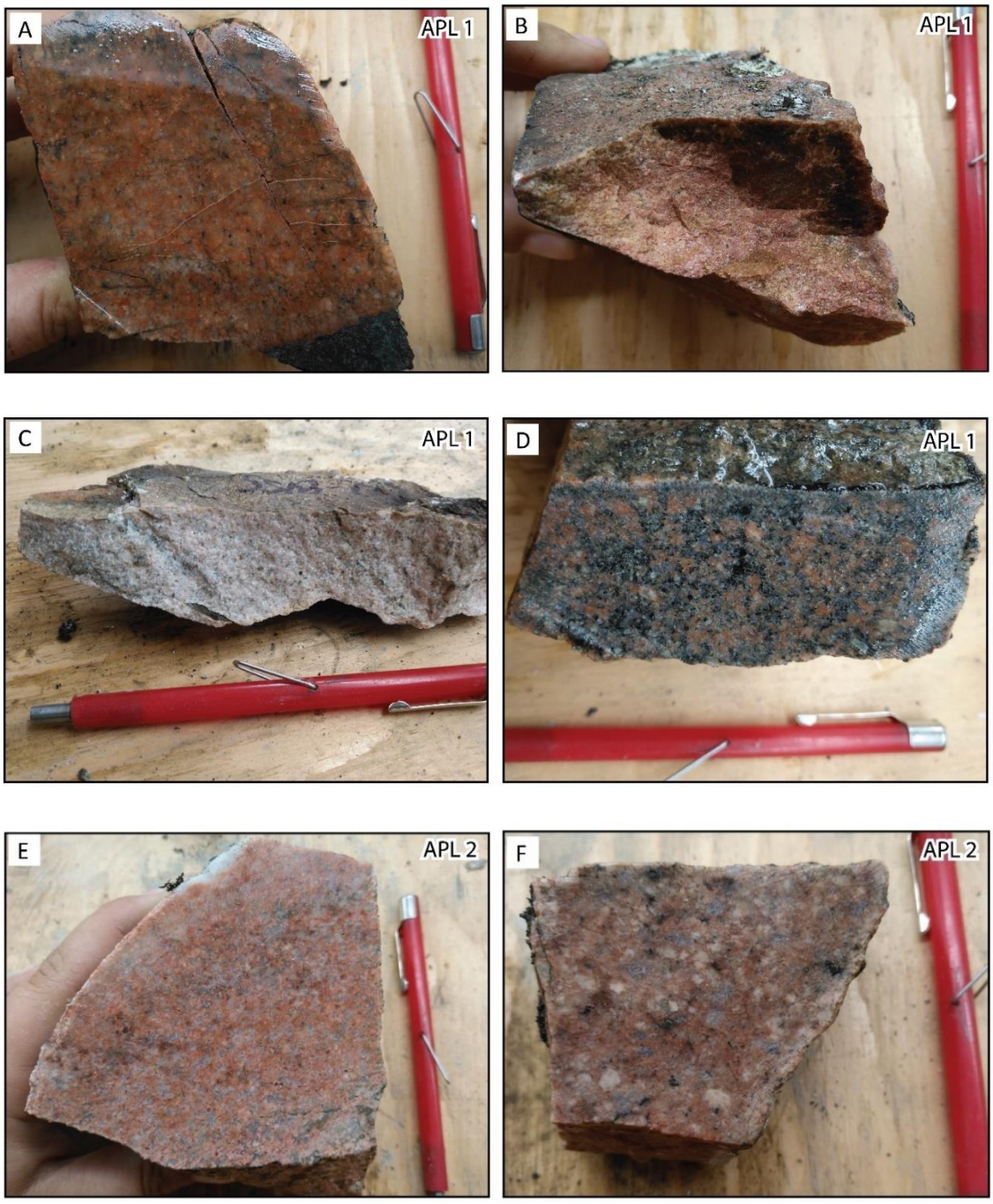


Fig. 2.2: Common hand sample textures of aplite dikes. Dikes are typically homogeneous, but there is variability in colour, grain size and biotite content between dikes. (A) Granitic dike with pervasive, moderate hematite alteration; 270 m from RLP. (B) 30–50 cm dike with trace fine-grained pyrite, cut by cm-scale quartz-calcite veins; 380 m from RLP. (C) Quartz- and plagioclase-rich granitic dike; within the RLP. (D) Potassium-feldspar- and biotite-rich aplite dike that crosscuts an area of granodiorite; within the RLP. (E) light pink,

very fine- to fine-grained aplite-2 dike, 10 m from the Duckfish granite. (F) A coarser aplite-2 dike found 75 m from Duckfish granite. Pen magnet for scale. APL 1 = aplite-1, APL 2 = aplite-2.

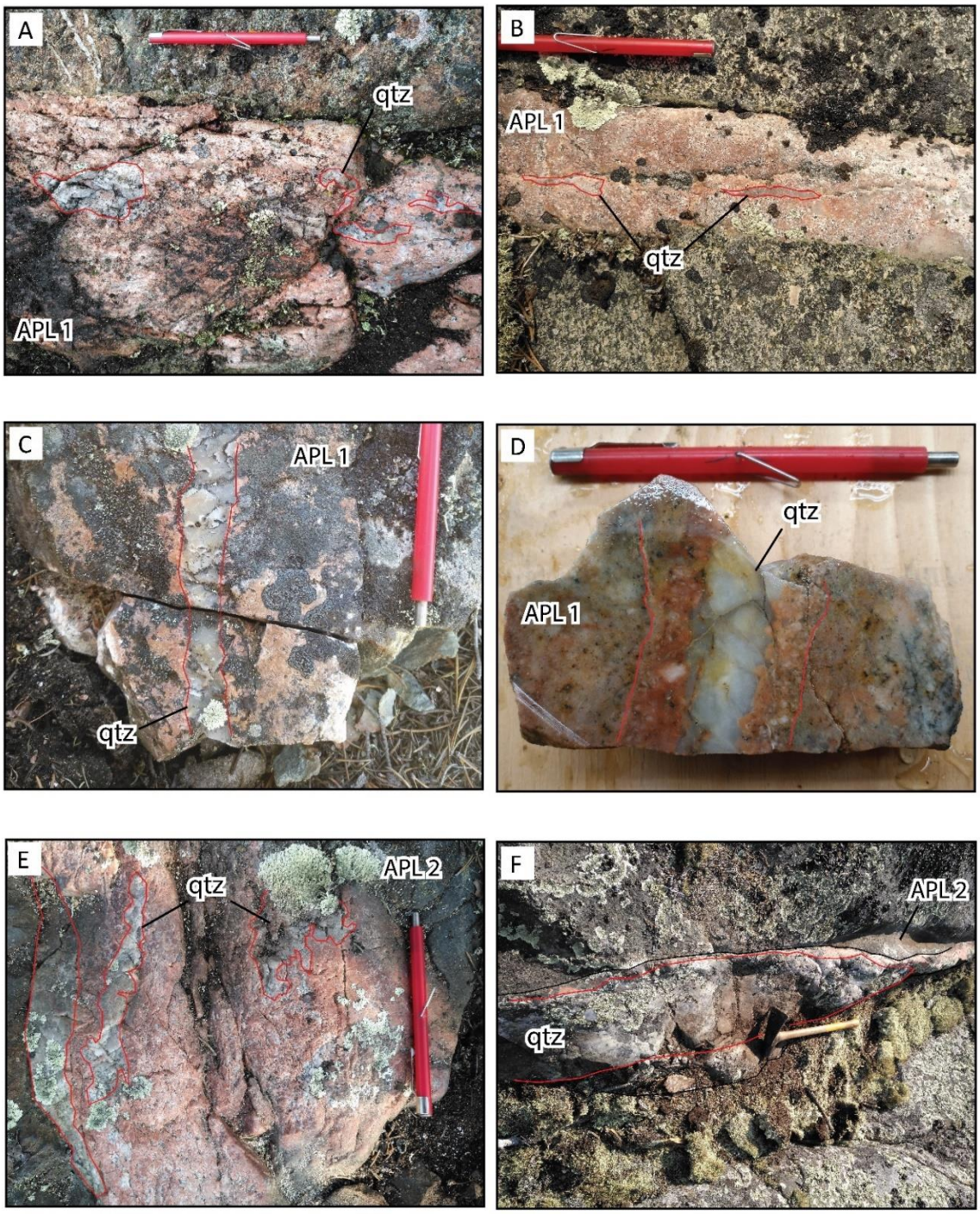


Fig. 2.3: Field and hand sample images of granitic dikes with continuous quartz cores and discontinuous quartz pods, all found in dikes hosted by mafic volcanics and not in the RLP. These quartz textures indicate a late H_2O-saturated fluid (Hibbard 1980). (A) Quartz pods throughout the aplite-1 dike, 100m from RLP. (B) Discontinuous quartz core along the center of an aplite-1 dike, within RLP. (C) Dike with quartz core with sharp contacts; 260m

from RLP. (D) Cross-section of the dike in Fig. 2.3C; the feldspar-rich growth zone surrounding the quartz core is more readily observed on the wet, cut surface. (E) Quartz pods within an aplite-2 dike, found throughout and along the dike contacts; 75 m from Ducfish granite. (F) 15–30 cm wide quartz core along the margin of an aplite-2 dike; 80 ms from the Duckfish granite. The quartz cores and pods are highlighted and red, with a pen magnet or sledgehammer for scale. APL 1 = aplite-1; APL 2 = aplite 2.

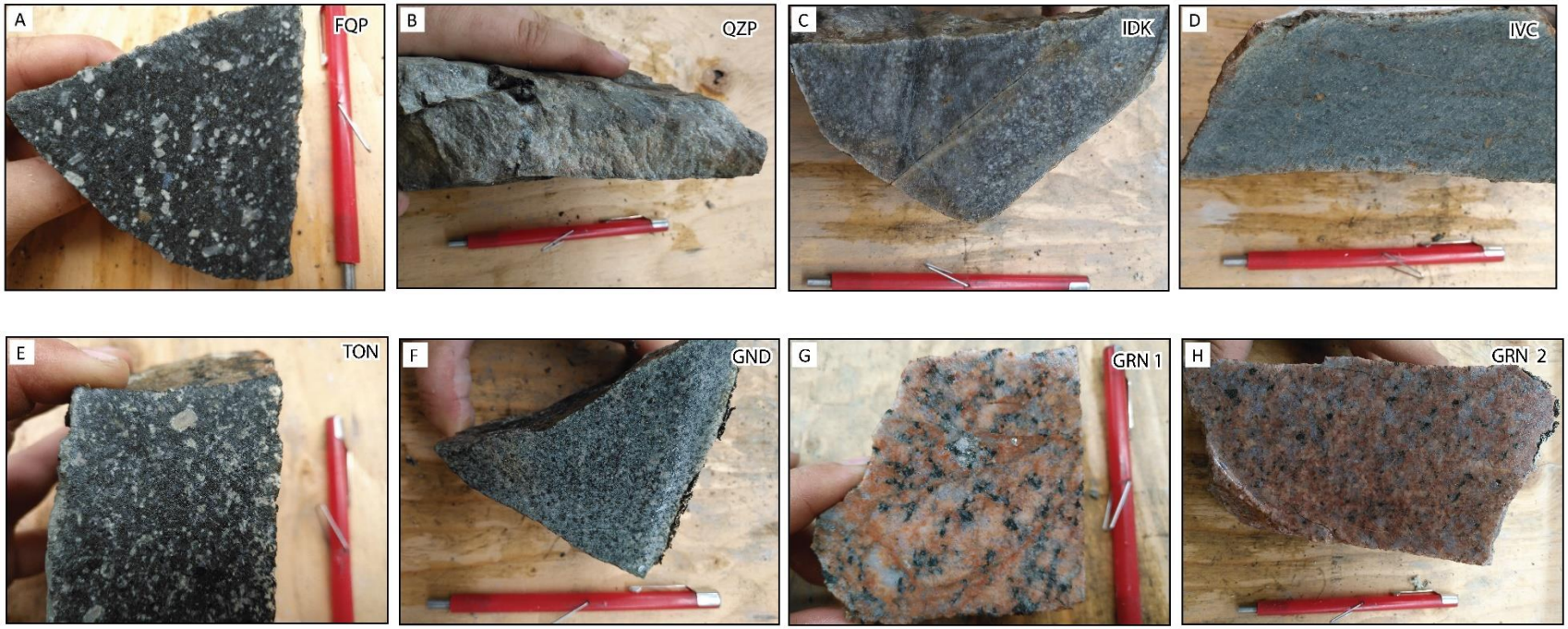


Fig. 2.4: Hand sample images of representative textures and samples from: (A) feldspar-quartz porphyry, (B) quartz porphyry, (C) intermediate dike, (D) intermediate volcanic tuff, (E) tonalite, (F) granodiorite, (G) Defeat Suite granite, and (H) Duckish granite. Pen magnet for scale. Samples are described in the text.

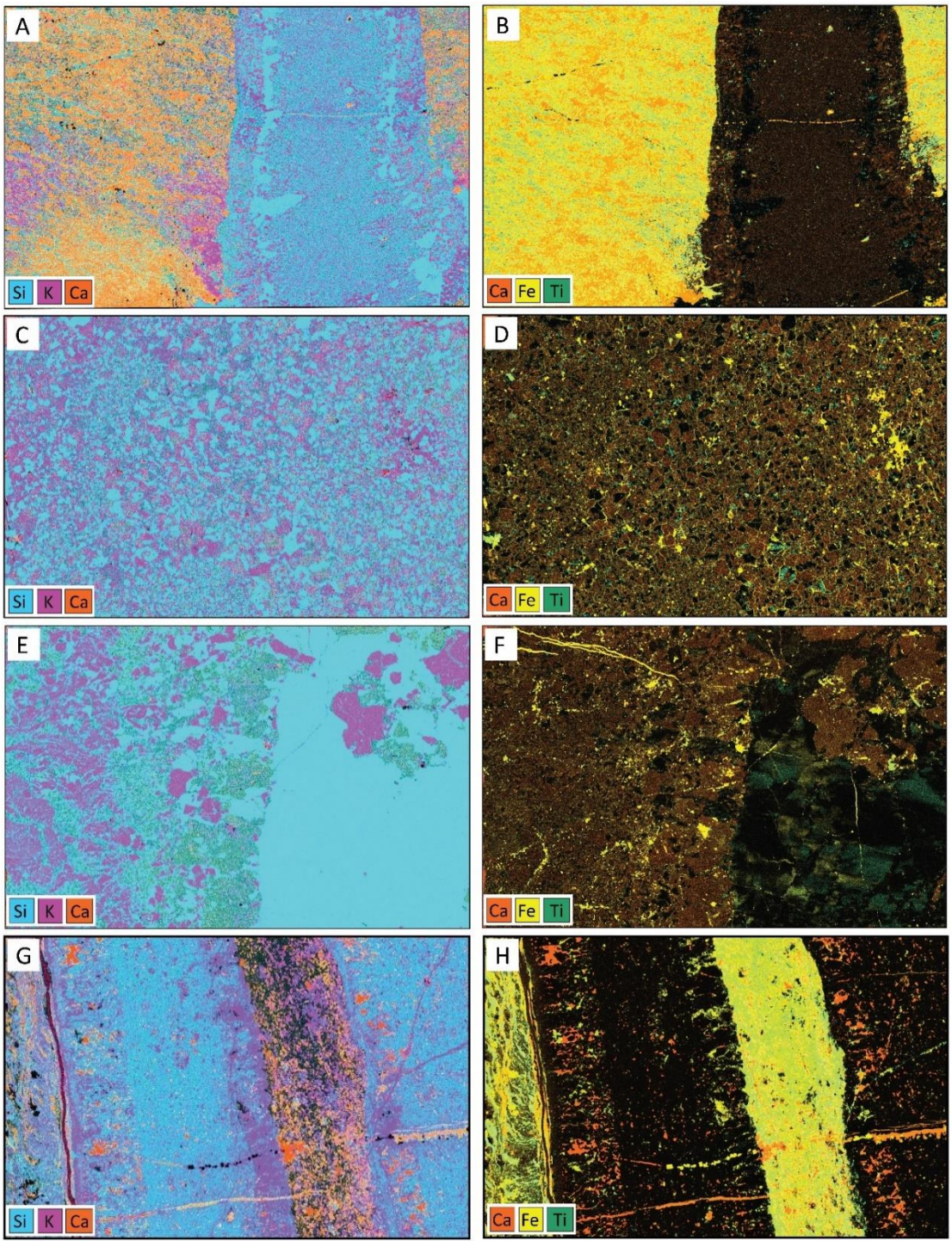


Fig. 2.5: Multi-element µXRF compositional maps of standard polished thin sections, focusing on aplite dikes. Each colour represents a different element indicated in the image. (A-D) aplite-1, (E-H) aplite-2. The left column shows the distribution of Si, K, and Ca, while the right shows Ca, Fe, and Ti in the same field of view. The images are 27 x 46 mm.

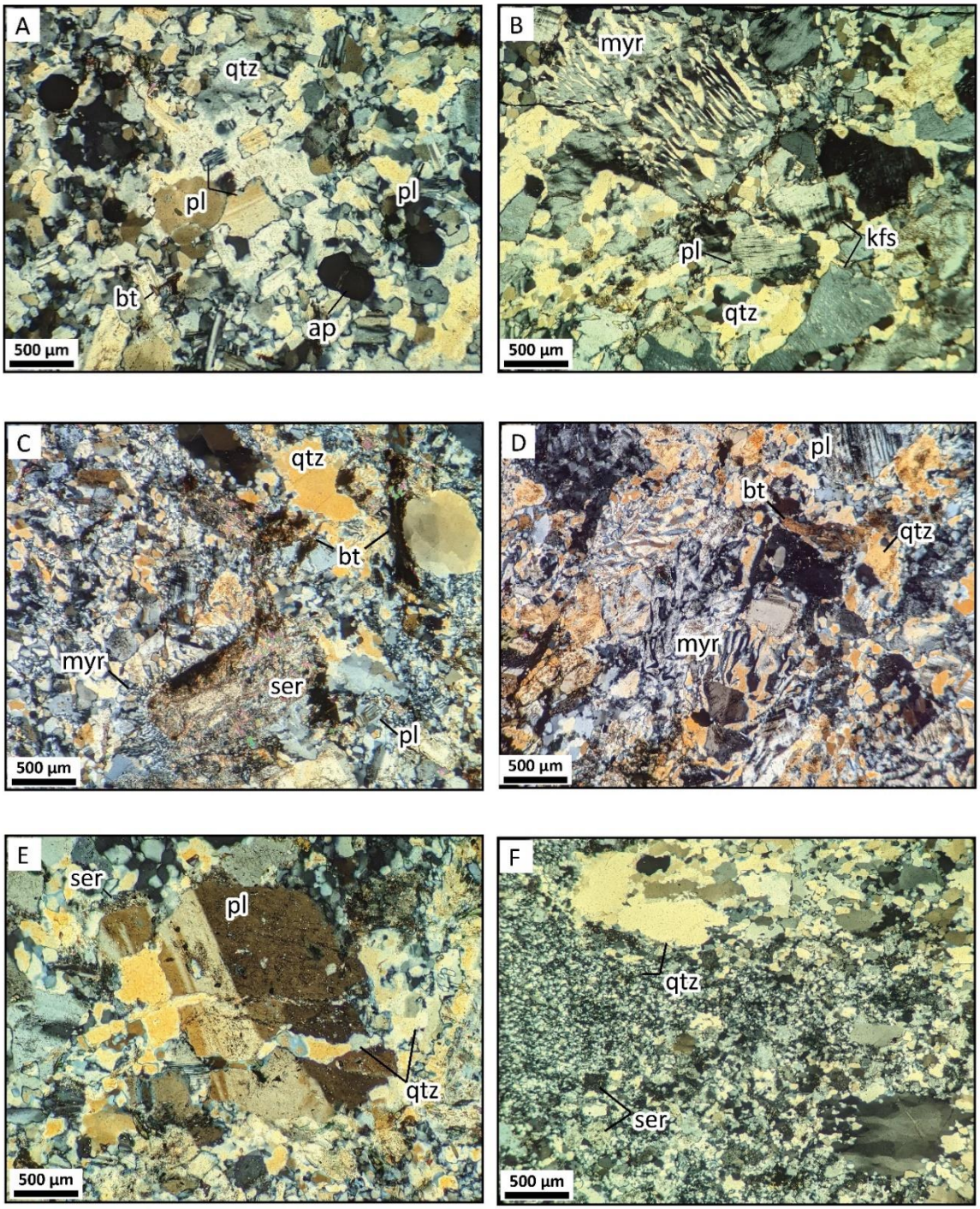


Fig. 2.6: Petrographic images for aplite-1 and aplite-2 dikes, along with examples for each stage of emplacement. (A) Aplite-1 dike; broken plagioclase grain included in quartz with rare fine-grained colourless garnet. (B) Aplite-2 dike; Coarse area of myrmekite with abundant K-feldspar, quartz, and plagioclase. (C) *Main magmatic* stage; quartz, altered plagioclase, minor biotite and rare myrmekite. (D) *Late magmatic* stage; abundant

myrmekite, quartz, and plagioclase. (E) *Early post-magmatic* stage; broken plagioclase grain with quartz infilling the fractures. (F) *Late post-magmatic* stage; abundant quartz, with the field of view showing comb-texture quartz. Cross-polarized light. Qtz = quartz; pl = plag; bt = biotite; amph = amphibole; ser = sericite; kfs = K-feldspar; cal = calcite; myr = myrmekite; ap = apatite.

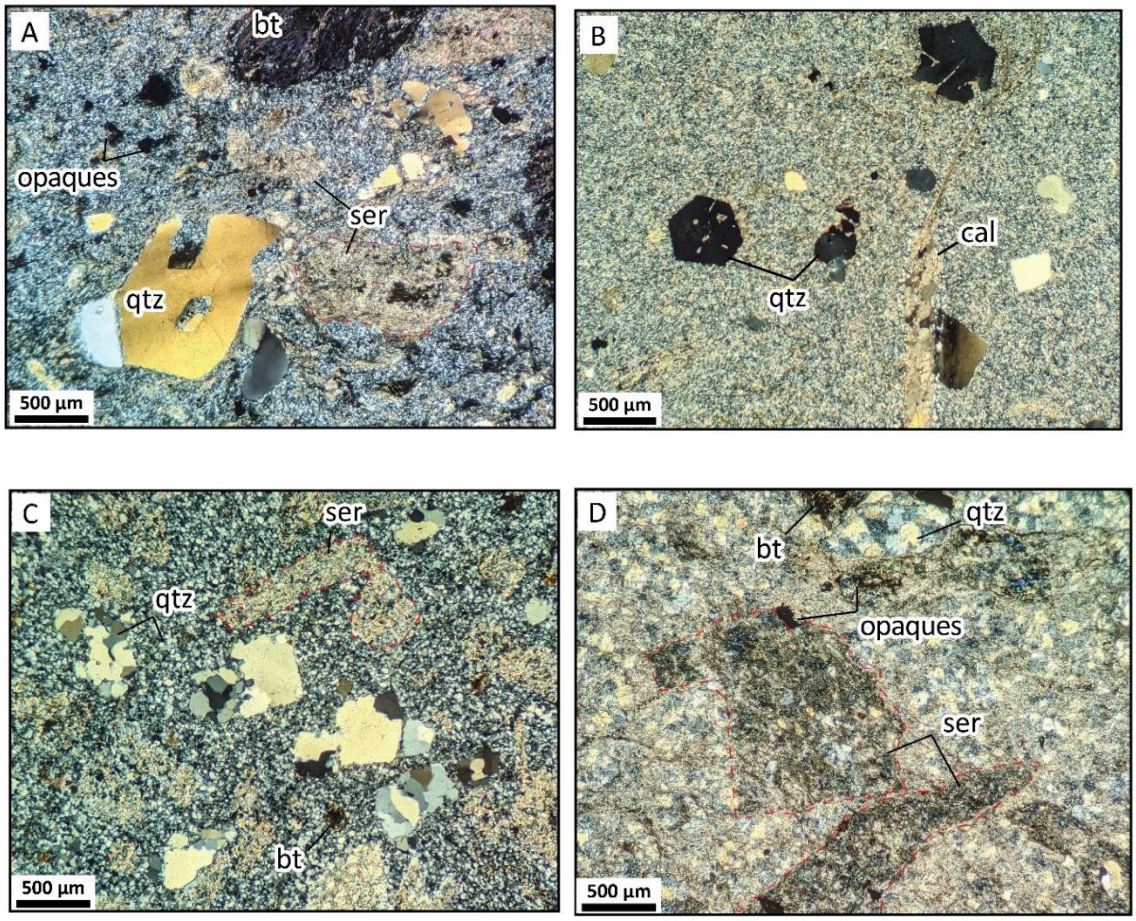


Fig. 2.7: Petrographic images of representative textures taken in cross-polarized light: (A) feldspar-quartz porphyry, (B) quartz porphyry, (C) intermediate dike, and (D) intermediate volcanic tuff. Samples are described in the text. Cross-polarized light. Abbreviations are given in Fig. 2.6.

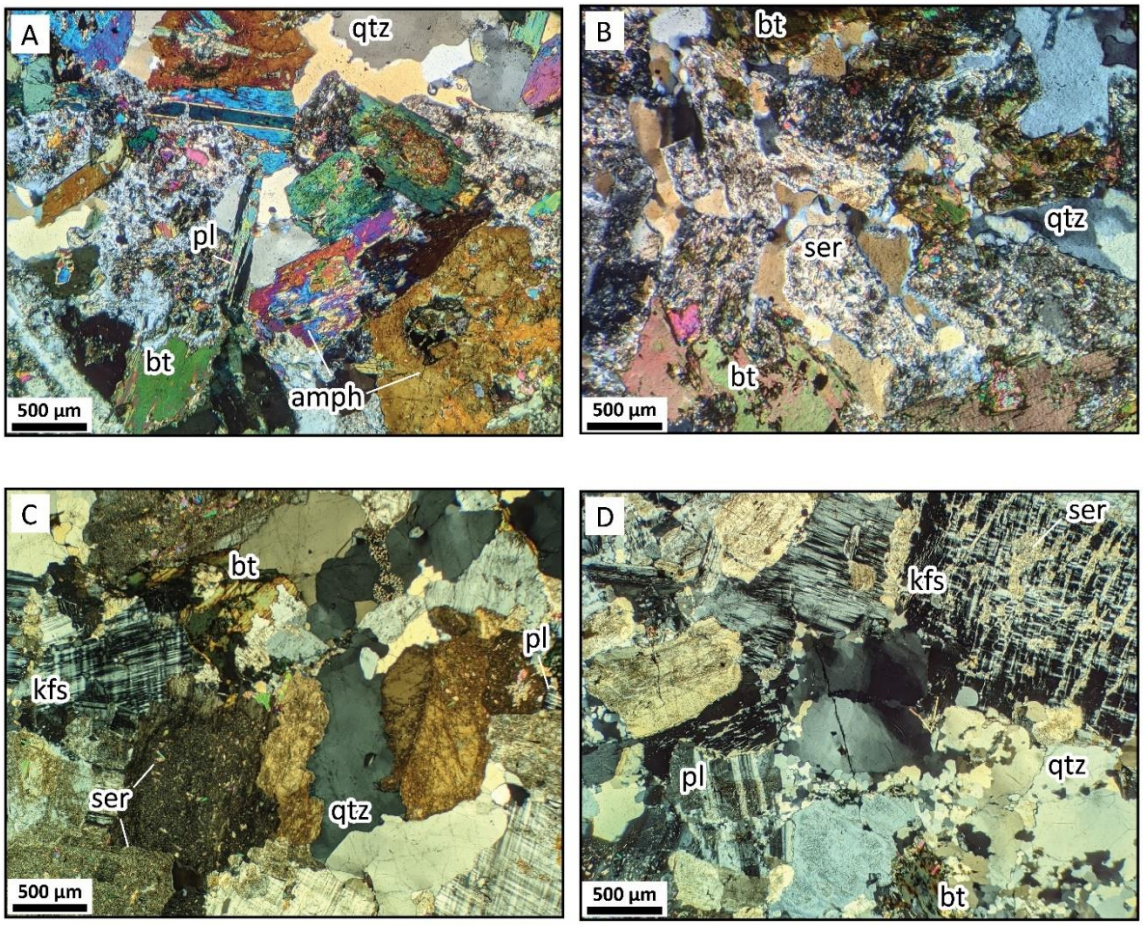


Fig. 2.8: Petrographic images of representative textures taken in cross-polarized light: (A) tonalite, (B) granodiorite, (C) Defeat Suite granite, and (D) Duckfish granite. Samples are described in the text. Cross-polarized light. Abbreviations are given in Fig. 2.6.

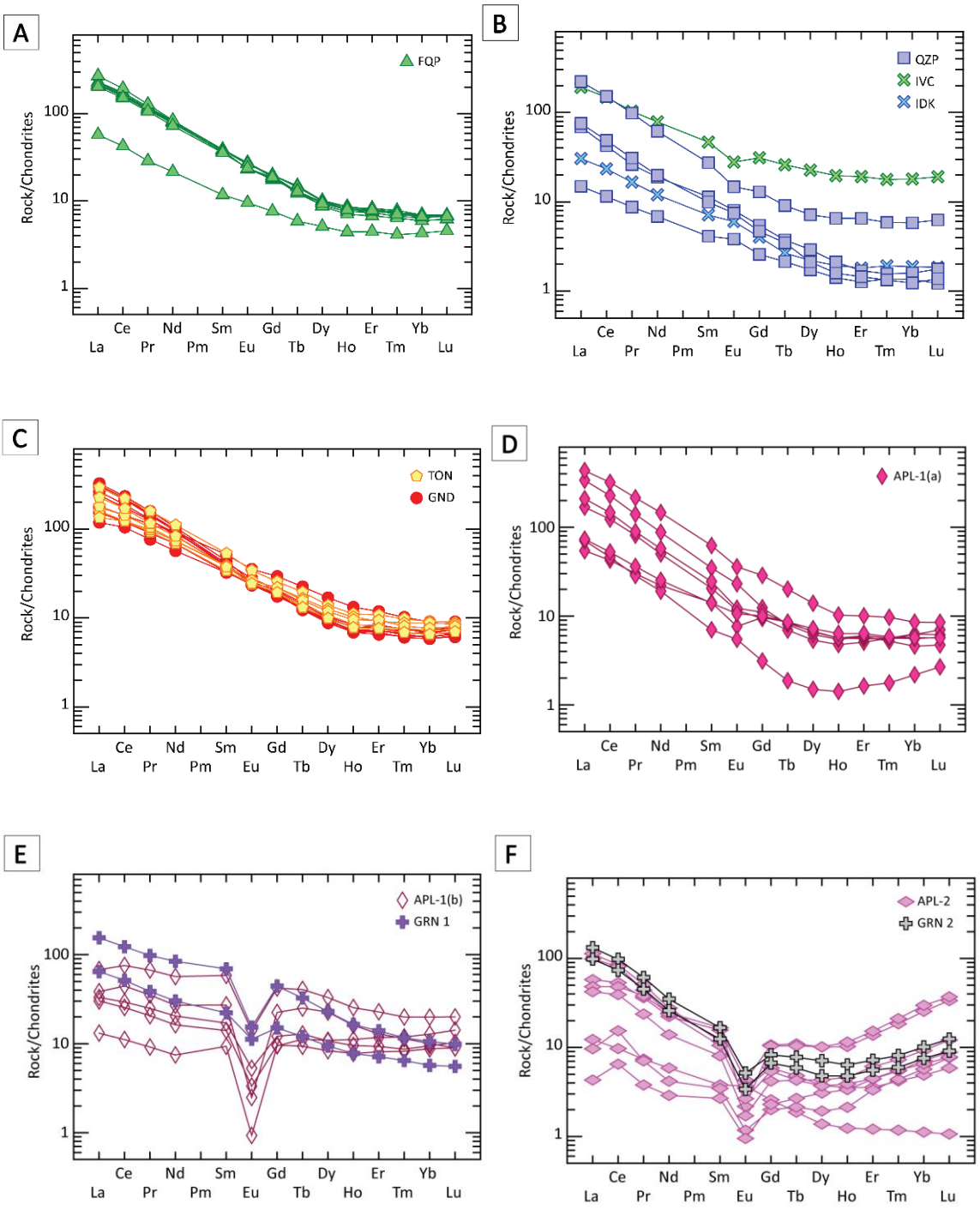


Fig. 2.9: Chondrite-normalized REE diagrams, separated by similarity and lithology (Sun and McDonough 1989). A–D) Intermediate to granitic samples, which include: FQP, QZP, intermediate dike, intermediate volcanic tuff, tonalite, granodiorite, and aplite-1(a). These samples have flat REE profiles that decrease from LREE to HREE. E-F) Granitic dikes and plutons, including aplite-1(b), aplite-2, Defeat Suite granite (GRN 1), and Duckfish

granite (GRN 2). The pronounced negative Eu anomaly separates the southern aplite-1 samples into two groups.

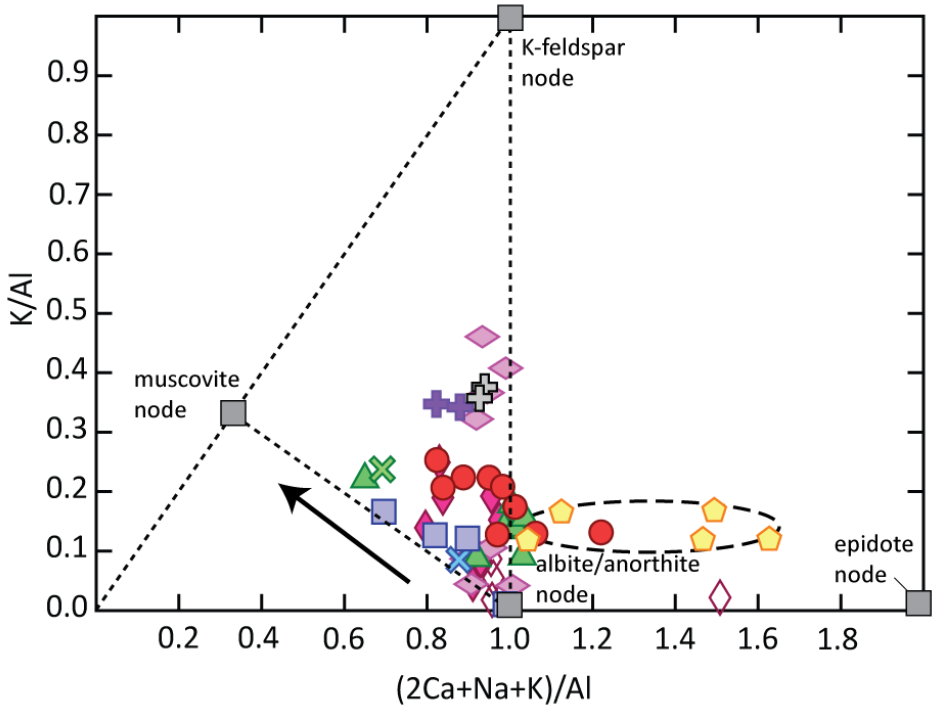


Fig. 2.10: General element ratio (GER) diagram of molar K/Al plotted against molar (2Ca+Na+K)/Al for YGB samples. The plot shows the alteration effects on each sample (Stanley 1998, 2020). The tonalite samples are highlighted in the dashed circle. Symbols are shown in Fig. 2.9.

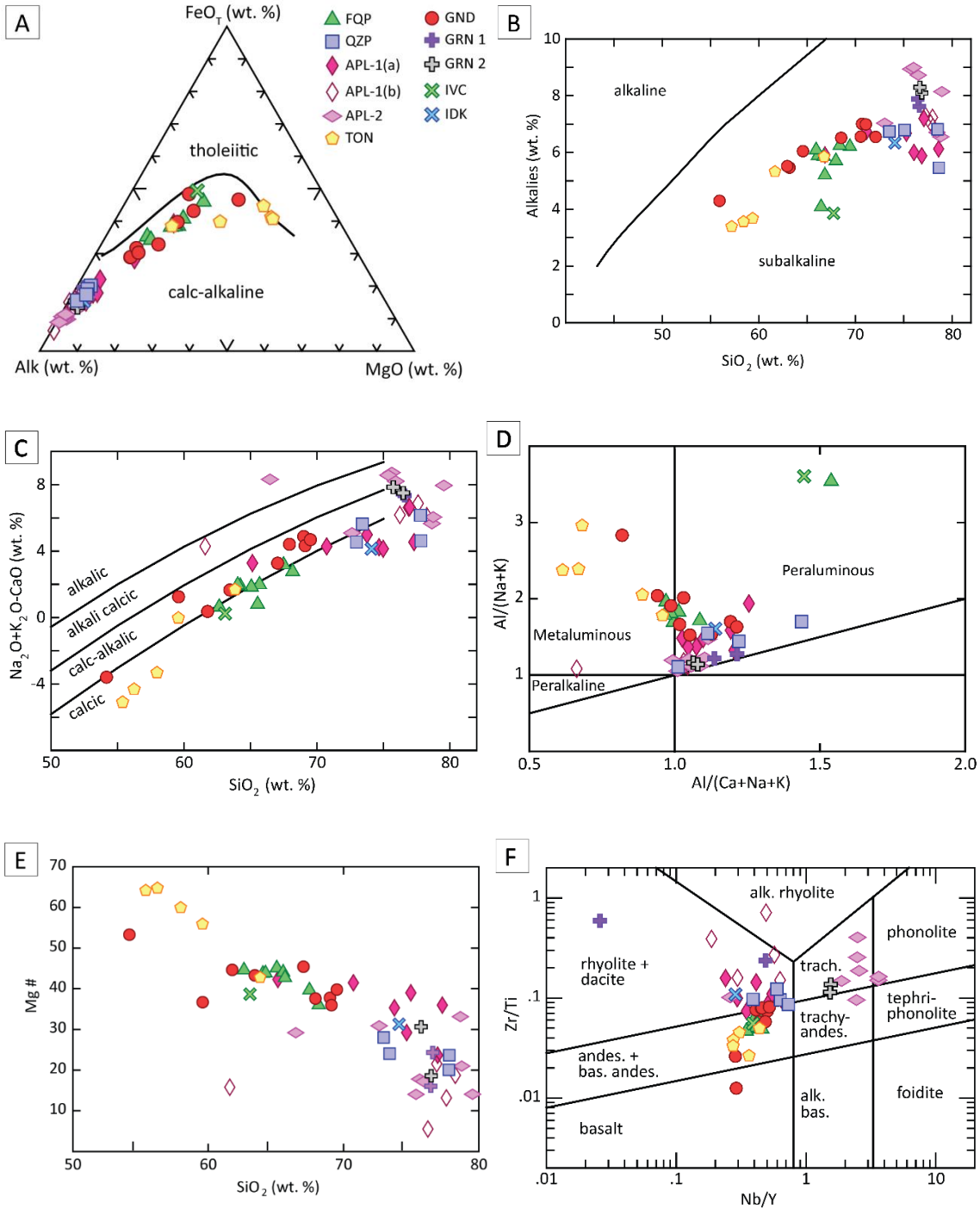


Fig. 2.11: Geochemical classification of felsic and intermediate rocks from the YGB using major and trace elements. (A) Alkalis-Iron-Magnesium (AFM) diagram (Irvine and Baragar 1971); (B) Alkalis vs. SiO_2 (Irvine and Baragar 1971); (C) MALI vs. SiO_2 (Frost et al. 2001, Frost and Frost 2008); (D) Shand's Index (Maniar and Piccoli 1989); (E) Mg # vs. SiO_2; (F)

Zr/Ti vs. Nb/Y (Pearce 1996). Symbols are shown in Fig. 2.11A. alk. bas. = alkali basalt; alk. rhyolite = alkali rhyolite; andes. = andesite; bas. = basaltic; trach. = trachyte.

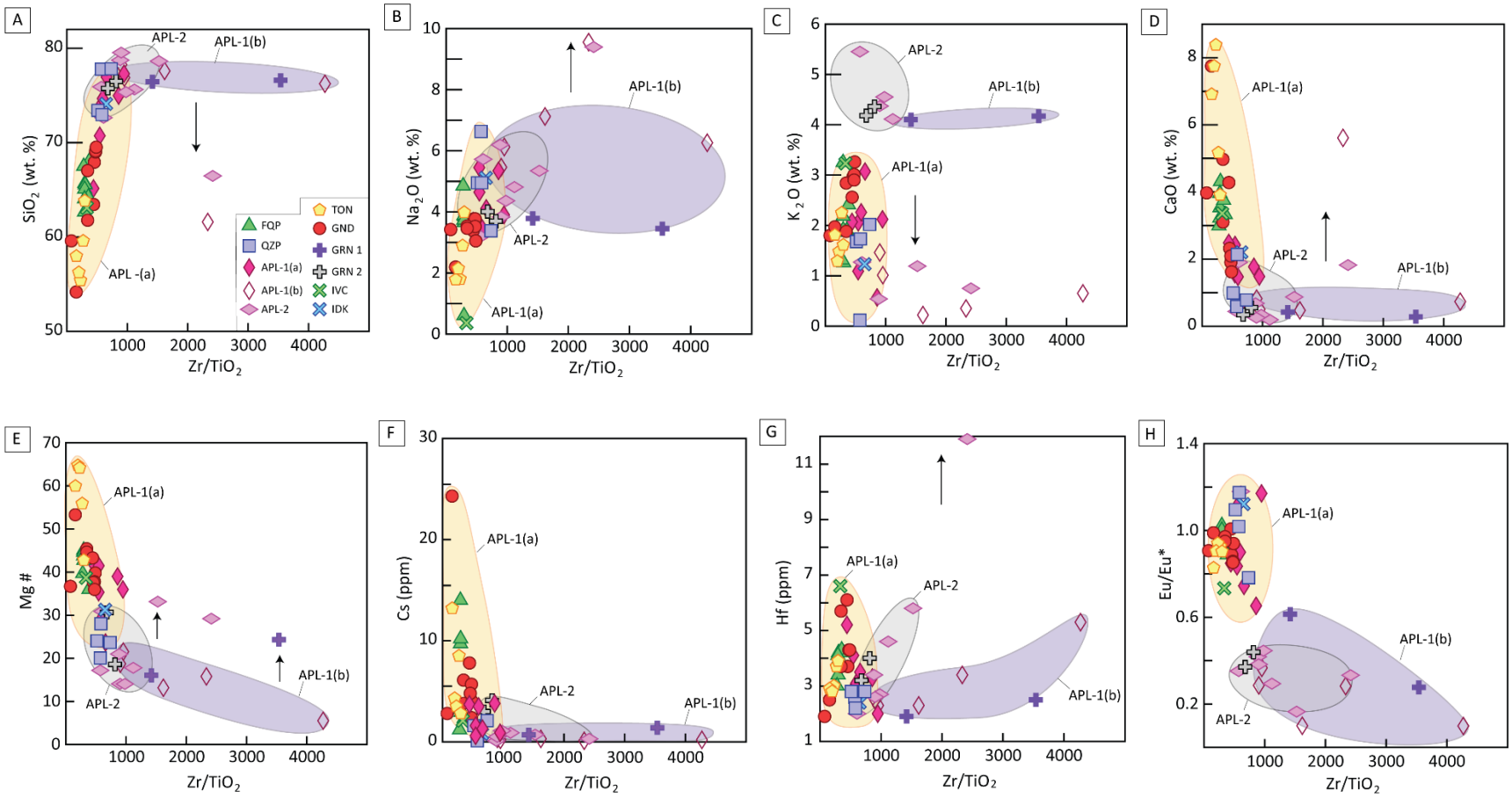


Fig. 2.12: Magmatic evolution and element mobility diagrams comparing major and trace elements to Zr/TiO_2 (ppm/wt. %), with three groups highlighted, including the aplite-1(a), aplite-1(b), and aplite-2 dikes and potentially associated parental plutons (Torró

et al. 2017). The three groups of aplite dikes were distinguished in chondrite-normalized REE diagrams. The legend can be found in Fig. 2.12A. Solid arrows indicate a gain or loss of elements that diverge from the main clusters.

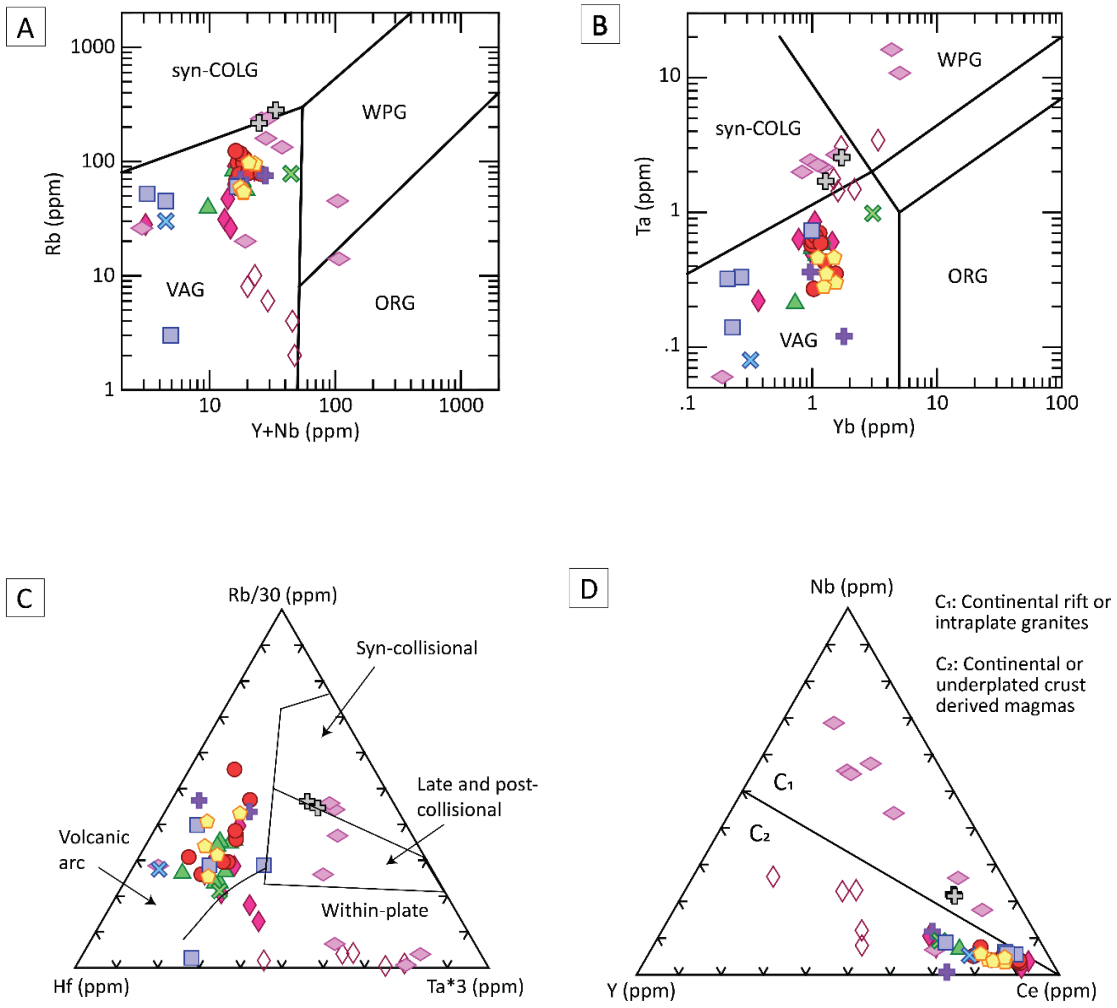


Fig. 2.13: Tectonic discrimination diagrams of felsic to intermediate rocks from the YGB, using trace elements to determine the tectonic setting of each lithology. (A) Rb vs. Y+Nb (Pearce et al. 1984); (B) Ta vs. Yb (Pearce et al. 1984); (C) Hf vs. Rb/30 vs. Ta*3 (Rutanen et al. 2011); (D) Y vs. Nb vs. Ce (Wang et al. 2020) Symbols shown in Fig. 2.11A. WPG = within-plate granite; VAG = volcanic-arc granite; syn-COLG = syn-collisional granite; ORG = ocean-ridge granite.

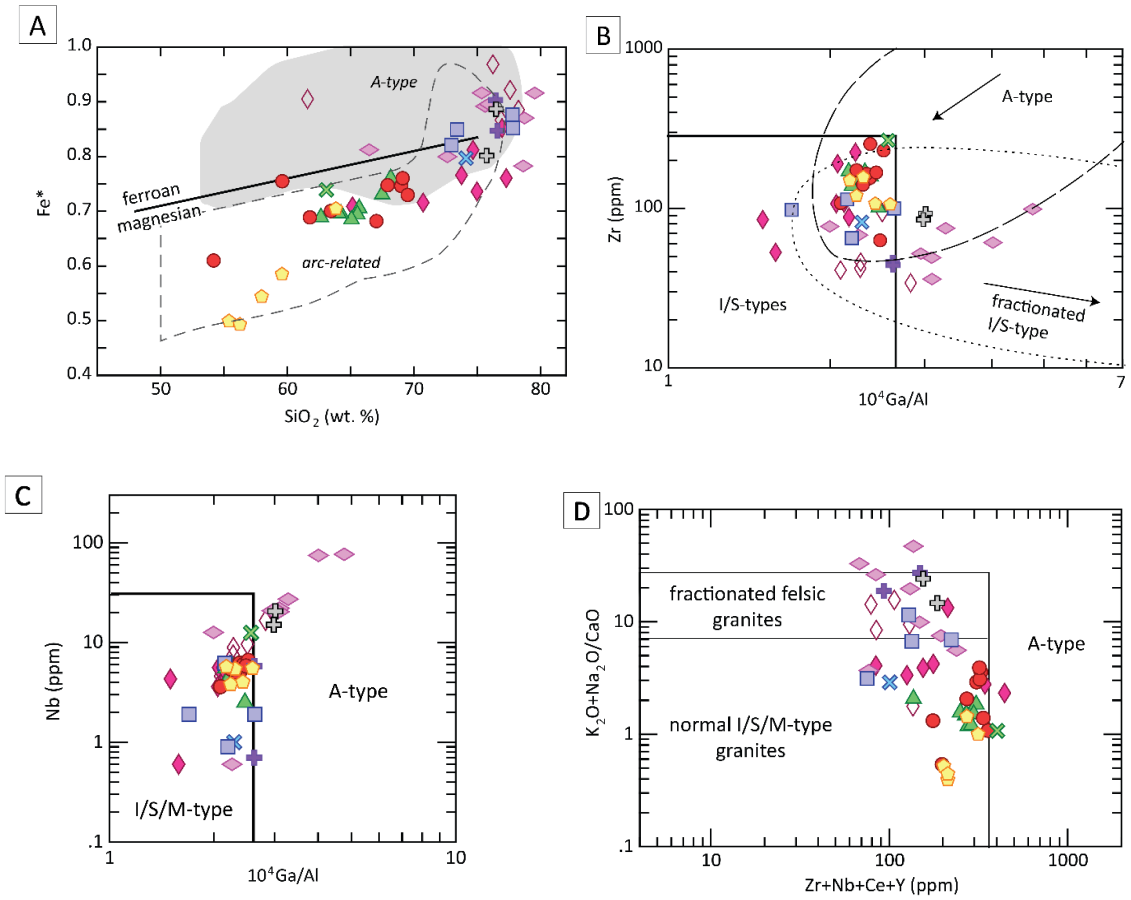


Fig. 2.14: Geochemical discrimination diagrams using major and trace elements to classify felsic and intermediate rocks of the YGB. (A) Fe* vs. SiO_2, with the addition of the A-type granite field in grey and the dashed line outlining the arc-related (Cordilleran) field (Frost et al. 2001, Frost and Frost 2008); (B) Zr vs. 10^4Ga/Al with added fields for A-type and fractionated I/S-types (Whalen et al. 1987, Wu et al. 2017, Altherr et al. 2019); (C) Nb vs. 10^4Ga/Al (Wang et al. 2020); (D) (K_2O+Na_20)/CaO vs. Zr+Nb+Ce+Y (Rutanen et al. 2011). Symbols are shown in Fig. 2.11A.

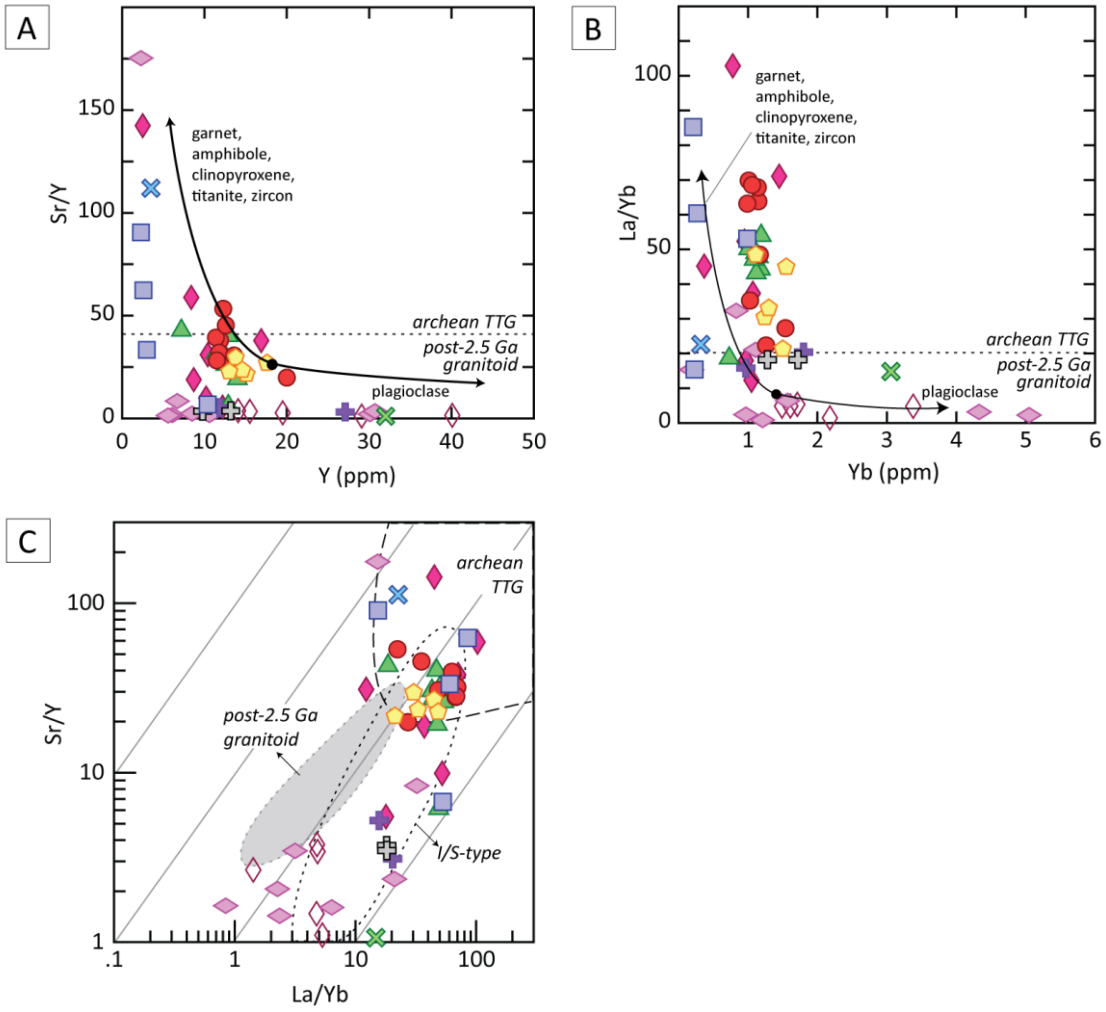


Fig. 2.15: Trace element diagrams indicating the tonalite-trondhjemite-granodiorite (TTG) and arc signatures of felsic and intermediate rocks of the YGB. (A) Sr/Y vs. Y (Moyen 2009, Arndt 2013, Altherr et al. 2019); (B) La/Yb vs. Yb (Moyen 2009, Arndt 2013, MacDonald and Piercey 2019); (C) Sr/Y vs. La/Yb, (Martin and Moyen 2002, Moyen 2009, Arndt 2013, Altherr et al. 2019, MacDonald and Piercey 2019). Typical fractionation trends for common minerals extending from an average andesite composition are shown (Richards and Kerrich 2007, and references therein). The TTG, post 2.5 Ga, and I/S-type granite fields are highlighted in Fig. 2.15C (Martin and Moyen 2002, Moyen 2009, Arndt 2013). Symbols are shown in Fig. 2.11 A.

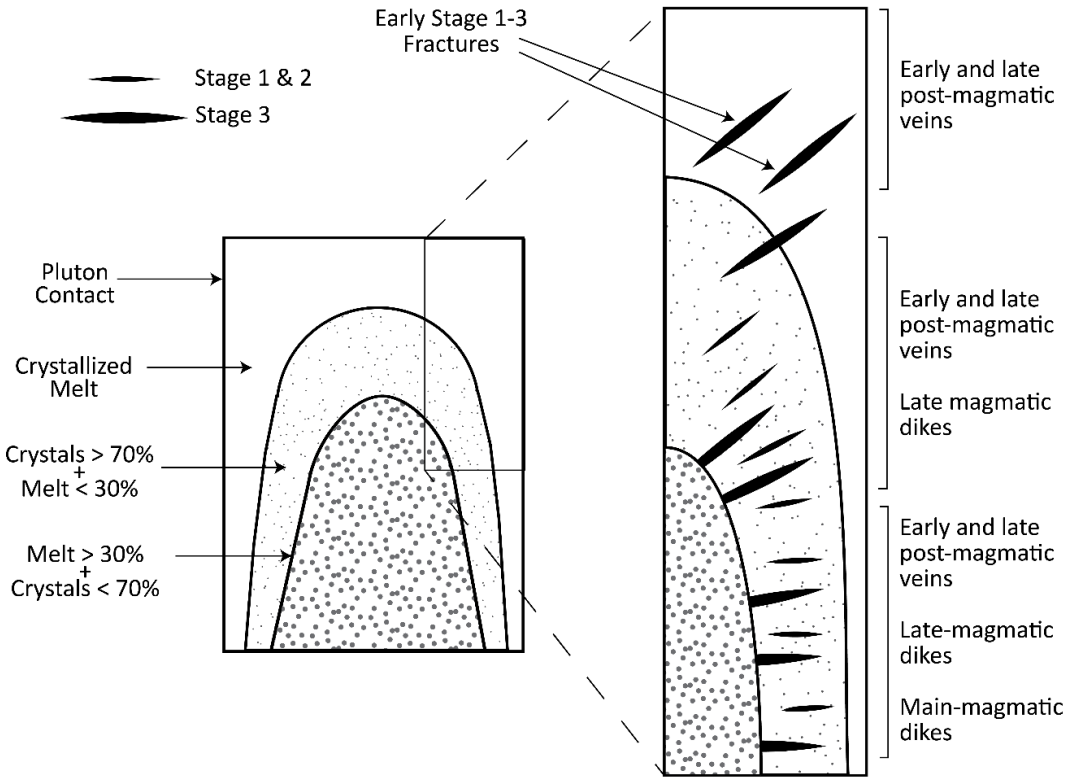


Fig. 2.16: Schematic depiction of locally-sourced dikes and their relative timing based on models by Hibbard (1980) and Hibbard and Watters (1985). The model is based on a two-feldspar granite stock with 3 wt. % H_2O for 1250 years (Hibbard 1980, and references therein). The enlarged area shows the timing of fluid emplacement from a partially crystallized pluton and the suggested method of fracturing and intrusion propagation (Hibbard and Watters 1985). Stages 1 and 2 of dike emplacement are due to fracturing of a pluton with < 30% melt followed by dilatancy pumping into the fracture. Stage 3 intrusions extend by hydraulic fracturing.

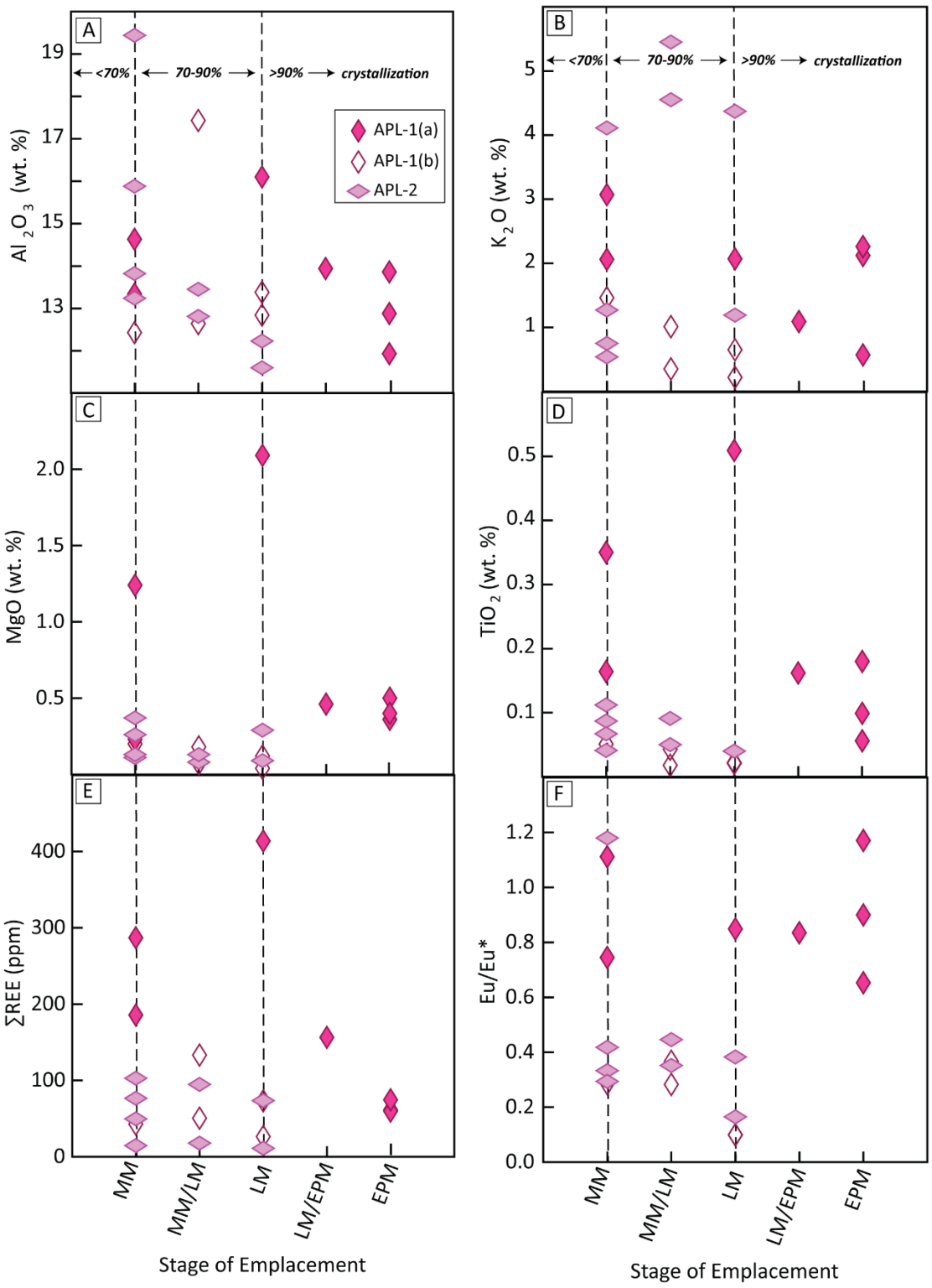


Fig. 2.17: Geochemical comparison of aplitic dikes based on their petrographically determined stage of emplacement after Hibbard (1980) and Hibbard and Watters (1985).

The dashed lines highlight the crystallization percent represented by the different stages of aplite emplacement. MM = *main magmatic* stage; MM/LM = transitional between *main* and *late magmatic* stage; LM = *late magmatic* stage; LM/EPM = transitional between *late magmatic* and *early post-magmatic* stage; EPM = *early post-magmatic* stage. Symbols shown in Fig. 2.17A.

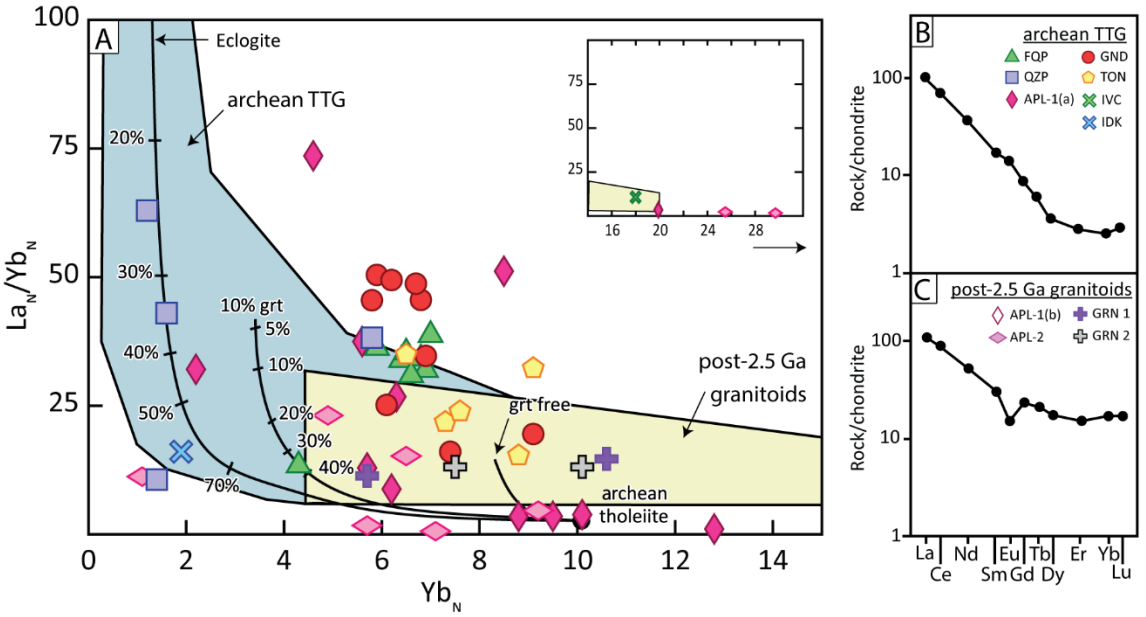


Fig. 2.18: (A) Trace element discrimination diagram comparing La_N/Yb_N vs. Yb_N (chondrite-normalized) with three Archean tholeiite partial melting curves added reflecting a garnet free, 10% garnet-bearing amphibolite, eclogite-bearing residue (de Souza et al. 2001). The tick marks along the partial melting curves reflect the percent of melting. The fields related to Archean TTG and post-2.5 Ga granitoids have been highlighted in blue and yellow, respectively (modified from Moyen and Martin 2012; Arndt 2013). Inset in Fig. 2.18A shows data that plot beyond $Yb_N = 15$. (B) Chondrite-normalized REE profile of an Archean TTG, with the corresponding YGB lithologies listed. (C) Chondrite-normalized REE profile of post-2.5 Ga granitoids, with the corresponding YGB lithologies are indicated. Symbols are shown in Fig. 2.18B-C. grt = garnet.

Table 2-1: Summary of petrographic characteristics used by Hibbard (1980) and Hibbard and Watters (1985) to determine the stage of dike emplacement.

Stage of Dike Emplacement	Typical Mineralogy	Percent Crystallized	Crystallization Characteristics
Main magmatic	Qtz, Kfs, Pl, Bt ± sodic-Pl ± myrmekite	> 70%	Crystallization prior to H_2O-saturation; no broken crystals, crystals rotate instead (Fig. 2.6C)
Late magmatic	Qtz, Kfs, Pl, sodic-Pl, mineral overgrowths, abundant myrmekite	> 90%	Crystallization from melt saturated in H_2O; some fractured crystals with minor rotation (10-15% melt) (Fig. 2.6D)
Early post-magmatic	Secondary Kfs, Qtz (± ore minerals)	> 90%	Minerals grow in an H_2O-rich environment; abundant fractured crystals (Fig. 2.6E)
Late post-magmatic	Qtz, ore minerals	> 90%	Crystallization from the last H_2O-rich fluids; abundant fractured crystals (1-2% melt; Fig. 2.6F)

Notes: Qtz: quartz; Kfs: K-feldspar; Pl: plagioclase; Bt: biotite.

Table 2-2: Petrographically determined stage of emplacement for aplite dikes in the YGB following the characteristics determined by Hibbard (1980) and Hibbard and Watters (1985). Aplite-1 samples are from the southern field area (near RLP and Defeat Suite), while aplite-2 samples are proximal to the Duckfish granite in the northern field area. See Fig. 2.6 for representative images of each stage of emplacement. APL-1(a) = aplite-1(a); APL-1(b) = aplite-1(b); APL-2 = aplite-2; X = quartz core; o = quartz pods.

Lithology	Sample	Width (m)	Qtz core/pods	Main magmatic	Late magmatic	Early post-magmatic	Late post-magmatic
APL-1(a)	SS18-055	0.3-0.4		·—·			
	UNB-1	1-1.5		·—·			
	SS18-053B	0.2	o		·—·		
	SS18-062B	0.2-0.3			·—·		
	SS18-018B	0.2-0.3			·———·		
	SS18-062A	0.3				·—·	
	SS18-067A	0.1	x			·—·	
	SS18-071	0.25				·—·	
	SS18-018A	0.4	x				·—·
APL-1(b)	UNB-2	0.3-0.5		·—·			
	SS18-005A	0.2-0.3		·———·			
	SS18-029B	0.25		·———·			
	SS18-032	0.2-1	x		·—·		
	SS18-007	0.1-0.2			·—·		
	SS18-030A	0.3	x		·———·		
	SS18-030B	0.2-0.3	x		·———·		
APL-2	SS18-075	0.1-0.2		·—·			
	SS18-087	0.4		·—·			
	SS18-105	5		·—·			
	SS18-091A	0.3-1		·—·			
	SS18-094	1	o	·———·			
	SS18-104	0.4		·———·			
	SS18-073A	0.2-0.3			·—·		
	SS18-093B	1	o		·—·		

2.8. References

Altherr, R., Hanel, M., Schwarz, W.H., and Wimmenauer, W. 2019. Petrology and U–Pb zircon age of the Variscan porphyroclastic Rand Granite at the southeastern margin of the Central Schwarzwald Gneiss Complex (Germany). International Journal of Earth Sciences, 108: 1879–1895.

Arndt, N.T. 2013. Formation and evolution of the continental crust. Geochemical Perspectives, 2: 405–533.

Bethune, K.M., Villeneuve, M.E., Bleeker, W., Bethune, K.M., Villeneuve, M.E., and Bleeker, W. 1999. Laser 40Ar/39Ar thermochronology of Archean rocks in Yellowknife Domain, southwestern Slave Province: insights into the cooling history of an Archean granite-greenstone terrane. Canadian Journal of Earth Sciences, 36: 1189–1206.

Bleeker, W., and Hall, B. 2007. The Slave Craton: Geology and Metallogenic Evolution. In Mineral Deposits of Canada: A Synthesis of Major Deposit-Types, District Metallogeny, the Evolution of Geological Provinces, and Exploration Methods: Geological Association of Canada. Edited by W.D. Goodfellow. Mineral Deposits Division. pp. 849–879.

Bleeker, W., Ketchum, J.W., Jackson, V.A., Villeneuve, M.E., Bleeker, W., Villeneuve, M., Ketchum, J., and Jackson, V. 1999a. The Central Slave Basement Complex, Part I: its structural topology and autochthonous cover. Canadian Journal of Earth Sciences, 36: 1083–1109.

Bleeker, W., Ketchum, J.W.F., and Davis, W.J. 1999b. The Central Slave Basement Complex, Part II: age and tectonic significance of high-strain zones along the basement-cover contact. Canadian Journal of Earth Sciences, 36: 1111–1130.

van Breemen, O., Davis, W.J., and King, J.E. 1992. Temporal distribution of granitoid plutonic rocks in the Archean Slave Province, northwest Canadian Shield. Canadian Journal of Earth Sciences, 29: 2186–2199.

Carter, L.C., Williamson, B.J., Tapster, S.R., Costa, C., Grime, G.W., and Rollinson, G.K. 2021. Crystal mush dykes as conduits for mineralising fluids in the Yerington porphyry copper district, Nevada. Communications Earth and Environment, 2: 1–11.

Cousens, B., Facey, K., and Falck, H. 2002. Geochemistry of the late Archean Banting Group, Yellowknife greenstone belt, Slave Province, Canada: Simultaneous melting of the upper mantle and juvenile mafic crust. Canadian Journal of Earth Sciences, 39: 1635–1656.

Cousens, B., Falck, H., Ootes, L., Jackson, V., Mueller, W., Corcoran, P., Finnigan, C., van Hees, E., Facey, C., and Alcazar, A. 2006. Regional Correlations, Tectonic Settings, and Stratigraphic Solutions in the Yellowknife Greenstone Belt and Adjacent Areas from Geochemical and Sm-Nd Isotopic Analysis of Volcanic and Plutonic Rocks. In Gold in the Yellowknife Greenstone Belt, Northwest Territories: Results of the EXTECH III Multidisciplinary Research Project. Edited by C.D. Anglin, H. Falck, D.F. Wright, and E.J. Ambrose. pp. 70–94.

Cousens, B.L. 2000. Geochemistry of the Archean Kam Group, Yellowknife Greenstone Belt, Slave Province, Canada. The Journal of Geology, 108: 181–197.

Davis, W.J., and Bleeker, W. 1999. Timing of plutonism, deformation, and metamorphism in the Yellowknife Domain, Slave Province, Canada. Canadian Journal of Earth Sciences, 36: 1169–1187.

Davis, W.J., Fryer, B.J., and King, J.E. 1994. Geochemistry and evolution of Late Archean plutonism and its significance to the tectonic development of the Slave craton. Precambrian Research, 67: 207–241.

Dutch, R.A., Werner, M.X., Krapf, C.B.E., and Rusak, T. 2013. Geology of the TIEYON 1:100 000 map sheet (5645). In Geological Survey of South Australia. Department for Manufacturing.

Finnigan, C.S. 2000. The Townsite Formation: an aborted rift setting in the Yellowknife greenstone belt, NWT. M. Sc., University of Western Ontario, London, Ontario.

Finnigan, C.S., and Duke, N.A. 2006. Geology and Geochemistry of the Townsite Formation: Recognition of Felsic Porphyritic Intrusions Adjacent to Gold-Bearing Shear Zones in the Yellowknife Greenstone Belt, NWT. In Gold in the Yellowknife Greenstone Belt, Northwest Territories: Results of the EXTECH III Multidisciplinary Research Project. Edited by C.D. Anglin, H. Falck, D.F. Wright, and E.J. Ambrose. pp. 58–69.

Frost, B.R., Barnes, C.G., Collins, W.J., Arculus, R.J., Ellis, D.J., and Frost, C.D. 2001. A geochemical classification for granitic rocks. Journal of Petrology, 42: 2033–2048. Oxford University Press. [accessed 17 August 2021].

Frost, B.R., and Frost, C.D. 2008. A geochemical classification for feldspathic igneous rocks. Journal of Petrology, 49: 1955–1969.

Frost, B.R., and Frost, C.D. 2014. Essentials of igneous and metamorphic petrology. Cambridge University Press.

Green, D.C., and Baadsgaard, H. 1971. Temporal Evolution and Petrogenesis of an Archaean Crustal Segment at Yellowknife, N.W.T., Canada. Journal of Petrology, 12: 177–217.

Helmstaedt, H., and Padgham, W.A. 1986. A new look at the stratigraphy of the Yellowknife Supergroup at Yellowknife, N.W.T. — implications for the age of gold-bearing shear zones and Archean basin evolution. Canadian Journal of Earth Sciences, 23: 454–475.

Helmstaedt, H., Padgham, W.A., and Brophy, J.A. 1986. Multiple dikes in Lower Kam Group, Yellowknife greenstone belt: Evidence for Archean sea-floor spreading? Geology, 14: 562–566.

Helmstaedt, H.H., and Pehrsson, S.J. 2012. Geology and tectonic evolution of the Slave Province-A post-LITHOPROBE perspective. In Tectonic Styles in Canada: The Lithoprobe Perspective. Edited by J.A. Percival, F.A. Cook, and R.M. Clowes. Geological Association of Canada. pp. 379–466.

Henderson, J.B. 1985. Geology of the Yellowknife-Hearne Lake Area, District of Mackenzie: A segment across an Archean Basin. Geological Survey of Canada. Memoir 414. pp. 135.

Henderson, J.F., and Brown, I.C. 1966. Geology and structure of the Yellowknife greenstone belt, District of Mackenzie. In Bulletin 141. Geological Survey of Canada.

Hibbard, M. 1980. Indigenous Source of Late-Stage Dikes and Veins in Granitic Plutons. Economic Geology, 75: 410–423.

Hibbard, M.J., and Watters, R.J. 1985. Fracturing and diking in incompletely crystallized granitic plutons. Lithos, 18: 1–12.

Hollis, S.P., Roberts, S., Earls, G., Herrington, R., Cooper, M.R., Piercey, S.J., Archibald, S.M., and Moloney, M. 2014. Petrochemistry and hydrothermal alteration within the Tyrone Igneous Complex, Northern Ireland: Implications for VMS mineralization in the British and Irish Caledonides. Mineralium Deposita, 49: 575–593. Springer Verlag.

Irvine, T.N., and Baragar, W.R.A. 1971. A Guide to the Chemical Classification of the Common Volcanic Rocks. Canadian Journal of Earth Sciences, 8: 523–548.

Isachsen, C.E. 1992. U-Pb zircon geochronology of the Yellowknife volcanic belt and subjacent rocks, N.W.T., Canada: Constraints on the timing, duration, and mechanics of greenstone belt formation. Ph. D., Washington University, St. Louis, Mo.

Isachsen, C.E., and Bowring, S.A. 1994. Evolution of the Slave craton. Geology, 22: 917–920.

Isachsen, C.E., Bowring, S.A., and Padgham, W.A. 1991. U-Pb Zircon Geochronology of the Yellowknife Volcanic Belt, NWT, Canada: New Constraints on the Timing and Duration of Greenstone Belt Magmatism. The Journal of Geology, 99: 55–67.

Jerram, D., and Petford, N. 2011. The Geological Field Guide Series: The Field Description of Igneous Rocks. Edited By R.S. Thorpe and G.C. Brown. Wiley-Blackwell, Oxford, UK.

MacDonald, P.J., and Piercey, S.J. 2019. Geology, lithogeochemistry, and significance of porphyry intrusions associated with gold mineralization within the Timmins–Porcupine gold camp, Canada. Canadian Journal of Earth Sciences, 56: 399–418. Canadian Science Publishing.

Maniar, P.D., and Piccoli, P.M. 1989. Tectonic discrimination of granitoids. Geological Society of America Bulletin, 101: 635–643.

Martel, E., and Lin, S. 2006. Structural Evolution of the Yellowknife Greenstone Belt, with Emphasis on the Yellowknife River Fault Zone and the Jackson Lake Formation. In Gold in the Yellowknife Greenstone Belt, Northwest Territories: Results of the EXTECH III Multidisciplinary Research Project, Special Pub. No. 3. Edited by C.D. Anglin, H. Falck, D.F. Wright, and E.J. Ambrose. pp. 95–115.

Martin, H., and Moyen, J.-F. 2002. Secular changes in tonalite-trondhjemite-granodiorite composition as markers of the progressive cooling of Earth. Geology, 30: 319–322.

Moyen, J.F. 2009. High Sr/Y and La/Yb ratios: The meaning of the “adakitic signature.” Lithos, 112: 556–574.

Moyen, J.F., and Martin, H. 2012. Forty years of TTG research. Lithos, 148: 312–336.

Nash, W.P., and Crecraft, H.R. 1985. Partition coefficients for trace elements in silicic magmas. Geochimica et Cosmochimica Acta, 49: 2309–2322.

Ootes, L., and Lentz, D.R. 2002. Occurrence of bleached mafic flows and their association with stockwork sulphides and banded iron-formation in the Crestaurum Formation of the late Archean Yellowknife Greenstone Belt, Northwest Territories. In Current Reseach-E5. Geological Survey of Canada.

Ootes, L., Lentz, D.R., Cabri, L.J., and Hall, D.C. 2006. Geology and Gold Mineralization in the Crestaurum Mine Area, Northern Yellowknife Greenstone Belt, N. W. T. In Gold in the Yellowknife Greenstone Belt, Northwest Territories: Results of the EXTECH III Multidisciplinary Research Project, Special Pub. No. 3. Edited by C.D. Anglin, H. Falck, D.F. Wright, and E.J. Ambrose. pp. 249–269.

Ootes, L., Lentz, D.R., Creaser, R.A., Ketchum, J.W.F., and Falck, H. 2007. Re-Os molybdenite ages from the Archean Yellowknife greenstone belt: Comparison to U-Pb ages and evidence for metal introduction at ~2675 Ma. Economic Geology, 102: 511–518.

Palmer, E.M. 2018. Petrogenesis of the Archean Prestige leucogranite and spatially associated LCT pegmatites, NWT: insights from whole-rock and muscovite trace element geochemistry and apatite U-Pb geochronology. M. Sc., University of New Brunswick, Fredericton, NB.

Pearce, J.A. 1996. A user’s guide to basalt discrimination diagrams. In Trace element geochemistry of volcanic rocks; applications for massive sulphide exploration: Geological Association of Canada, Short Course Notes. Edited by D.A. Wyman. pp. 79–113.

Pearce, J.A., Harris, N.B.W., and Tindle, A.G. 1984. Trace Element Discrimination Diagrams for the Tectonic Interpretation of Granitic Rocks. Journal of Petrology, 25: 956–983.

Richards, J.P., and Kerrich, R. 2007. Adakite-like rocks-their diverse origins and questionable role in metallogenesis. Bulletin of the Society of Economic Geologists, 102: 537–576.

Rutanen, H., Andersson, U.B., Väisänen, M., Johansson, Å., Fröjdö, S., Lahaye, Y., and Eklund, O. 2011. 1.8 Ga magmatism in southern Finland: Strongly enriched mantle and juvenile crustal sources in a post-collisional setting. International Geology Review, 53: 1622–1683.

Shau, Y.-H., Yang, H.-Y., and Peacor, D.R. 1991. On oriented titanite and rutile inclusions in sagenitic biotite. American Mineralogist, 76: 1205–1217.

Smithies, R.H., Lu, Y., Johnson, T.E., Kirkland, C.L., Cassidy, K.F., Champion, D.C., Mole, D.R., Zibra, I., Gessner, K., Sapkota, J., de Paoli, M.C., and Poujol, M. 2019. No evidence for high-pressure melting of Earth’s crust in the Archean. Nature Communications, 10: 1-12.

de Souza, Z.S., Potrel, A., Lafon, J.M., Althoff, F.J., Martins Pimentel, M., Dall'Agnol, R., and de Oliveira, C.G. 2001. Nd, Pb and Sr isotopes in the Identidade Belt, an Archaean greenstone belt of the Rio Maria region (Carajás Province, Brazil): Implications for the Archaean geodynamic evolution of the Amazonian Craton. Precambrian Research, 109: 293–315.

Speight, S.C., McFarlane, C.R.M., and Hanley, J.J. 2023. U-Pb geochronology and zircon mineral chemistry of syn-volcanic and plutonic intrusions in the Yellowknife greenstone belt, NWT, Canada: understanding an Archean magmatic plumbing system. In prep., Fredericton, N. B.

Stanley, C.R. 1998. Lithogeochemical exploration for metasomatic zones associated with hydrothermal mineral deposits using molar element ratio analysis: Advanced Topics. In Lithogeochemical Exploration Research Project, Mineral Deposit Research Unit, University of British Columbia, Short Course Notes. pp. 0–180.

Stanley, C.R. 2020. Molar element ratio analysis of lithogeochemical data: a toolbox for use in mineral exploration and mining. Geochemistry: Exploration, Environment, Analysis, 20: 233–256. Geological Society of London.

Sun, S.S., and McDonough, W.F. 1989. Chemical and isotopic systematics of oceanic basalts: Implications for mantle composition and processes. Geological Society Special Publication, 42: 313–345.

Thompson, P.H. 2006. Metamorphic Constraints on the Geological Setting, Thermal Regime, and Timing of Alteration and Gold Mineralization in the Yellowknife Greenstone Belt, NWT, Canada. In Gold in the Yellowknife Greenstone Belt, Northwest Territories: Results of the EXTECH III Multidisciplinary Research Project, Special Pub. No. 3. Edited by C.D. Anglin, H. Falck, D.F. Wright, and E.J. Ambrose. Geological Association of Canada Mineral Deposits Division. pp. 142–172.

Torró, L., Proenza, J.A., Marchesi, C., Garcia-Casco, A., and Lewis, J.F. 2017. Petrogenesis of meta-volcanic rocks from the Maimón Formation (Dominican Republic): Geochemical record of the nascent Greater Antilles paleo-arc. Lithos, 278–281: 255–273.

Wang, Y., Yang, Y.Z., Siebel, W., Zhang, H., Zhang, Y.S., and Chen, F. 2020. Geochemistry and tectonic significance of late Paleoproterozoic A-type granites along the southern margin of the North China Craton. Nature, 10: 1–15.

Were, P., and Keppler, H. 2021. Trace element fractionation between biotite, allanite, and granitic melt. Contributions to Mineralogy and Petrology, 176: 74.

Whalen, J.B., Currie, K.L., and Chappell, B.W. 1987. A-type granites: geochemical characteristics, discrimination and petrogenesis. Contributions to Mineralogy and Petrology, 95: 407–419.

Wu, F., Liu, X., Ji, W., Wang, J., and Yang, L. 2017. Highly fractionated granites: Recognition and research. Science China Press, 60: 1201–1219.

Zajacz, Z., Halter, W.E., Pettke, T., and Guillong, M. 2008. Determination of fluid/melt partition coefficients by LA-ICPMS analysis of co-existing fluid and silicate melt

inclusions: Controls on element partitioning. Geochimica et Cosmochimica Acta, 72: 2169–2197.

Zall, F., Tahmasbi, Z., Jiang, S.Y., Danyushevsky, L. v., and Harris, C. 2019. Elemental and B-O-H isotopic compositions of tourmaline and associated minerals in biotite-muscovite granite of Mashhad, NE Iran: Constraints on tourmaline genesis and element partitioning. Lithos, 324–325: 803–820.

3. U-Pb geochronology and zircon mineral chemistry of syn-volcanic and plutonic intrusions in the Yellowknife greenstone belt, NWT, Canada: understanding an Archean magmatic plumbing system

3.1. Abstract

The Yellowknife greenstone belt (YGB) is a north–south trending assemblage of metavolcanic rocks located in the Archean Slave Province of the Northwest Territories, Canada. The YGB is dominated by tholeiitic mafic metavolcanic rocks and calc-alkaline felsic metavolcanic rocks that were intruded by several intermediate to felsic plutons (Ryan Lake Pluton, Defeat Suite, and Duckfish Granite) and a series of feldspar-quartz porphyry (FQP), quartz porphyry (QZP), and aplite dikes. Representative samples from these lithologies were studied to fully characterize the petrography, U-Pb geochronology, and zircon mineral chemistry of the dikes and plutons. Laser ablation-inductively couple plasma-mass spectrometry (LA-ICP-MS) was used to obtain concordant U-Pb ages for nearly all lithologies, which provided an initial evaluation of pluton-dike relationships. High-resolution chemical abrasion-thermal ionization mass spectrometry (CA-TIMS) analysis of select samples then aided in distinguishing between closely spaced magmatic events.

The geochronological and lithogeochemical data indicate that the FQP dikes (2674 to 2662 Ma) and aplite-1(a) dikes (2663 Ma) are genetically associated with the tonalitic (2662 Ma) and granodioritic (2647 Ma) intrusions of the Ryan Lake Pluton. The aplite-1(b)

dikes (2662 Ma) were found to represent early intrusions that share geochemical traits with the Defeat Suite granite (2580 Ma). Aplite-2 dikes were only geochemically associated with the Duckfish granite (2576 Ma) but correlate with previous ages determined for a Duckfish aplite. Zircon populations record a wide range of trace element concentrations within single samples, and variable positive and negative Eu anomalies that link the FQP, tonalite, and granodiorite to a common parental magma source. The QZP dike and one FQP dike were found to be the oldest samples in this study, with ages of 2770 Ma and 2746 Ma, respectively. Although the QZP dike is geochemically like the aplites and granites, the association was inconsistent, and the age of the dike suggests it is related to an older event; this is also true for the oldest FQP dike. These samples were obtained from the base of the Kam Group and indicate that the Chan Formation may in fact be part of the Central Slave Cover Group or Basement complex.

Results were compared to historic geochemical and geochronological data from two felsic volcaniclastic units in the YGB: the Townsite Formation and Banting Group. While the FQP dikes show a range in ages and chemistry, major and trace element lithogeochemistry compared to the Banting Group and Townsite Formation suggest a geochemical connection between these subvolcanic dikes and the calc-alkaline volcaniclastics. The Zr/Hf ratio successfully groups the FQP dikes with the tonalitic and granodioritic Ryan Lake Pluton, Townsite Formation, and Banting Group, effectively separating them from the QZP, aplite dikes, and granites with only minor overlap between the groups. The spread of FQP ages (2674 to 2662 Ma) suggests that the older dikes

intruded early in the development of the Kam Group volcanic pile and were feeders to the Townsite Formation, while the younger dikes at ca. 2662 Ma were feeders to the Banting Group. Based on current data, the FQP dikes are interpreted as the only feeder dikes to the Townsite Formation and Banting Group, sourced from the multi-phase Ryan Lake Pluton, representing an ancient volcanic center and magmatic plumbing system in the YGB. The associated aplite-1(a) and FQP dikes appear to act as physical conduits for magmatic-hydrothermal fluids and not genetically related to significant mineralization. The overlapping ages of the granite aplite-1(b) dikes associated with the Defeat Suite implies that a separate magma reservoir related to this intrusion was also present at ca. 2662 Ma with the Ryan Lake Pluton.

Keywords

U-Pb geochronology, LA-ICP-MS, CA-TIMS, zircon mineral chemistry, Yellowknife greenstone belt, magmatic evolution, Archean magmatism, Banting Group, Townsite Formation

3.2. Introduction

The Yellowknife greenstone belt (YGB) is in the southwest Archean Slave province of the Northwest Territories, Canada and has been an area of considerable focus for research and exploration due to the presence of the prolific Con and Giant gold mines (Helmstaedt 2006). These mines produced roughly 13 Moz of gold between 1938–2004, and the area is still being actively explored for new deposits (Silke 2009). A prominent aspect of the YGB neglected in previous research is the connection between the plutonic

history and the origin of spatially extensive felsic dike rocks. Previous studies have suggested that these dikes represent subvolcanic feeders to the overlying volcaniclastics; however, at least three texturally distinct dikes have been observed (Green and Baadsgaard 1971, Helmstaedt and Padgham 1986, Cousens et al. 2002, Bleeker and Hall 2007). To date, the feldspar-quartz porphyry dikes (FQP), quartz porphyry dikes (QZP), and aplitic dikes are collectively lumped together in a classification referred to as the "#9" dikes (Henderson and Brown 1966). These are interpreted to have been feeders to the overlying Banting Group, but this suggestion is based on their abundance in the older Kam Group, their felsic whole-rock composition and two geochronological samples that correlate to poorly constrained "Banting ages" (Henderson and Brown 1966, Isachsen 1992, Ootes et al. 2006). Previous work by Speight et al. (2023) has established the geochemical link between some of the "#9" dikes and parental plutons based on lithogeochemical and petrographic evidence. This previous study demonstrated that the multi-phase Ryan Lake Pluton (RLP) is genetically related to the FQP, QZP, and one set of aplite dikes, the Defeat Suite granite is related to a second set of aplite dikes, and finally, the Duckfish granite is associated with a third set of aplite dikes.

To further characterize the YGB felsic dikes and plutons, reassess pluton-dike relationships, and develop a deeper understanding of their magmatic evolution, correlative geochronologic and zircon mineral chemistry data were collected. This was carried out by collecting U-Pb geochronological data by laser ablation-inductively coupled plasma-mass spectrometry (LA-ICP-MS) on a large zircon dataset and then refining the

ages of specific samples with complimentary chemical abrasion-isotope dilution thermal ionization mass spectrometry (CA-TIMS). Previous geochronology studies have examined the timing of the major plutons in the area, including the RLP, Defeat Suite granites, Duckfish Granite, and the Prosperous Suite, but the prominent felsic dikes are largely unexamined (Isachsen et al. 1991, Isachsen and Bowring 1994, Davis and Bleeker 1999). The data provided here aims to add to the current geochronologic data set using modern techniques and compare it to previous work to determine which pluton and dike suites may be related to the overlying Banting Group.

The need to better understand the felsic dikes in the YGB is more significant than merely an academic interest. A spatial correlation between felsic dikes and gold mineralization has been observed in numerous locations, but the genetic and temporal relationships have not been thoroughly examined (Finnigan and Duke 2006, Hubbard et al. 2006). For example, a spatial association is observed at the Con and Giant mines where gold mineralization overlaps with the greenschist to amphibolite facies transitional rocks; these metamorphic domains have been linked to the intrusion of the Defeat Plutonic Suite. Constraints on the age and magmatic evolution of these various intrusions, and potentially related dikes, are needed to place the magmatic events within a geologic framework that will guide the search for new mineralization targets. Therefore, a multi-analytical approach will assist in distinguishing these lithologies and establishing their timing in the current YGB magmatic history. If the dike-pluton connections can be definitively established, then this information could be used to establish the relationship between the plutons, dikes, and volcaniclastic units to define the overall plutonic-volcanic setting.

3.3. Geological setting

The YGB is a sub-vertical, north–south trending belt of dominantly metavolcanic rocks with a younging direction to the southeast. The belt is part of the Yellowknife Domain in the southwest Archean Slave Province (Fig. 1.1; Henderson and Brown 1966, Helmstaedt and Padgham 1986, Helmstaedt 2006, Martel and Lin 2006). The tonalitic and dioritic gneisses of the Central Slave Basement Complex are overlain by supracrustal rocks that include the Central Slave Cover Group and the Yellowknife Supergroup. The Yellowknife Supergroup is comprised of a series of mafic and felsic metavolcanic and metasedimentary rocks divided into the Kam Group, Banting Group, Duncan Lake Group, and Jackson Lake Formation (Henderson and Brown 1966, Helmstaedt and Padgham 1986, Helmstaedt 2006, Martel and Lin 2006). The Jackson Lake Formation is a conglomeratic unit that unconformably overlies the Kam and Banting Groups (Martel and Lin 2006).

The Kam Group is divided into a series of conformable units, including (from oldest to youngest) the Chan, Crestaurum, Townsite, and Yellowknife Bay Formations. Overall, the Kam Group consists of basaltic to intermediate metavolcanic rocks with tuffaceous felsic metavolcanic horizons and interflow metasediments. Due to the calc-alkaline signature and felsic geochemistry of the Townsite Formation, it is a distinctive unit within the Kam Group and has been used as a marker horizon to reconstruct the offset motions of Proterozoic faults throughout the YGB (Helmstaedt and Padgham 1986, Finnigan 2000, Finnigan and Duke 2006). The historic Con and Giant mines are hosted in the Yellowknife

Bay Formation, the uppermost unit of the Kam Group. The Kam Group was dated by Isachsen (1992) and Isachsen and Bowring (1994) using felsic metavolcaniclastic horizons and cherty felsic tuffs. U-Pb geochronology from these lithologies indicates a crystallization age of 2722 ± 1 to 2701 ± 4 Ma for assemblages of the Kam Group. Previous geochronology studies found some cherty, felsic volcanic rocks in the lower Kam Group to have inherited zircons as old as ca. 2820 Ma (Isachsen 1992).

The Banting Group is dominated by intermediate to felsic volcanic rocks, typically felsic tuffs, ash-flow tuffs, lesser massive and pillowed mafic flows, quartz porphyry, and volcaniclastic metasedimentary rocks (Helmstaedt and Padgham 1986, Isachsen and Bowring 1994, Martel and Lin 2006). The Banting volcaniclastics are considered unconformable with the underlying Kam Group and are typically separated by the Jackson Lake Formation (Helmstaedt and Padgham 1986, Isachsen 1992). The upper contact of the Kam Group is in faulted contact with the Banting Group, along the Yellowknife River Fault Zone (Martel and Lin 2006).

The YGB has been intruded by felsic plutons and dikes, including the previously mentioned RLP, Defeat Suite, Duckfish Granite, and the Prosperous Suite (Henderson and Brown 1966, Isachsen 1992, Isachsen and Bowring 1994, Davis and Bleeker 1999). Together with the plutonic bodies, various cross-cutting dikes have been observed, including aplitic dikes, porphyritic feldspar-quartz and porphyritic quartz dikes (FQP and QZP); all these dike variants have been referred to as the "#9" dikes (Henderson and Brown 1966). The YGB was subjected to widespread greenschist- to amphibolite-grade

metamorphism during intrusion of the Defeat Suite granites; therefore, all rock names have had the term meta- dropped in this study (Thompson 2006). Four deformation events (D_1–D_4) have affected the YGB, including folding, thrusting, and shear zone development. These events are bracketed by the deposition of volcanic and sedimentary rocks (ca. 2.62-2.60 Ga), the Defeat Suite granite emplacement (ca. 2630 Ma), and intrusion of post-collisional granites (2.59-2.56 Ga; Martel and Lin 2006).

3.4. Methods

3.4.1. Sample collection and processing

Field locations were targeted to obtain representative samples of felsic to intermediate dikes and plutons, collected from outcrops for zircon separation, U-Pb geochronology, and petrographic analysis. Sampling was guided by historic and current mapping and focused on exposures of felsic to intermediate dike and plutons in and around the RLP, Defeat Suite, and Duckfish Granite throughout the Kam Group of the YGB (Fig. 1.1; Henderson and Brown 1966, Bleeker and Hall 2007, Ootes et al. 2007). Three different dike lithologies and three plutonic bodies that represent possible parent plutons to the dikes were sampled. This study focuses on 12 samples consisting of six different lithologies, including FQP dikes, QZP dikes, aplites, tonalite and granodiorite of the RLP, Defeat Suite granite, and Duckfish granite.

Approximately 10 kg of rock from each sampled lithology was collected for heavy mineral separates; these were processed by Overburden Drilling Management Ltd.

(Nepean, Ontario). The rocks were prepared first by electric-pulse disaggregation, followed by zircon hand-picking from a final pan concentrate. Picked grains were mounted in epoxy and polished for imaging and LA-ICP-MS analysis (U-Pb, and trace element analysis). Of the 18 samples submitted for disaggregation, only 15 had appreciable amounts of zircons in the pan concentrate of the mineral separates; 12 of these were further analyzed. The grains selected were colourless and euhedral; however, samples did show evidence of more than one population of zircons. These populations differed in colour and shape; representative grains from each population were mounted separately to establish their age and chemical compositional differences.

3.4.2. Petrography

Mineralogy and textures were characterized using a Nikon Eclipse E600 polarizing microscope, and photomicrographs were taken with a Zeiss AxioImager microscope. The thin sections were also analyzed by micro-XRF (μXRF) and SEM-EDS to characterize common rock-forming minerals and accessory minerals, including zircon. The μXRF instrument used was a Bruker M4 Tornado μXRF housed at the University of New Brunswick. Each analysis, resulting in an X-ray intensity (and corresponding concentration intensity) map of the entire thin section, was obtained using a Rh tube as an excitation source, operated at 50 kV and 400 A, and utilizing a spot size of 20 μm for each spectral collection area on the sample surface. A full spectrum of elemental data was collected for each spot. SEM-EDS and accompanying BSE (back-scattered electron) imaging was done at Saint Mary's University using a TESCAN MIRA 3 LMU VPS field emission SEM equipped

with a solid-state EDS detector (Oxford Instruments X-max 80mm^2). The SEM was operated at an accelerating voltage of 25 kV, a beam current of 2 nA, and a working distance of 17 mm. The desktop computer software used for EDS spectrum collection and analysis was the INCA platform (ETAS GmbH).

The mounted zircons were imaged using a JEOL 6400 scanning electron microscope (SEM) with a BSE detector at the University of New Brunswick. The SEM was operated at a beam current of 1.5 nA and an accelerating voltage of 15 kV. The SEM-BSE imaging was utilized to avoid inclusions that would contaminate LA-ICP-MS analytical volumes and observe growth zones and inherited zircon cores. Cathodoluminescence imaging was attempted, but the zircons had no significant response.

3.4.3. U-Pb geochronology and zircon mineral chemistry

LA-ICP-MS analyses were carried out using a Resolution™ M-50 193 ArF Excimer laser ablation system coupled with an Agilent 7700X quadrupole ICP-MS at the University of New Brunswick. A Laurin Technic Pty "Squid" smoothing device was added between the ablation cell and ICP-MS torch with 4mm OD Nylon™ used for transfer tubing. Ablated materials were transported using a combination of ultra-pure He (300 mL/min) and Ar (930 mL/min) carrier gases, with ultra-pure N_2 (2 mL/min) added downstream of the ablation cell to enhance sensitivity. Oxide production (ThO^+/Th^+) was monitored and tuned to < 0.2% and doubly charged production ($^{44}Ca^{++}/^{44}Ca^+$) was monitored and restricted to < 0.3 %. The laser was operated at a repetition rate of 3 Hz with a fluence rate of 3 J/cm^2. Zircons were ablated using a 24 µm spot size, a 60-second ablation time

and 30 second washout time between ablations. Ablations were focused on the outer growth zones of zircons to avoid inherited cores and obtain magmatic crystallization ages. However, the shape and size of the zircon grains often dictated the ultimate ablation location.

The elements and isotopes quantified in zircon were ^{29}Si, ^{31}P, ^{49}Ti, ^{89}Y, ^{90}Zr, ^{139}La, ^{140}Ce, ^{141}Pr, ^{146}Nd, ^{147}Sm, ^{153}Eu, ^{157}Gd, ^{159}Tb, ^{163}Dy, ^{165}Ho, ^{166}Er, ^{169}Tm, ^{172}Yb, ^{175}Lu, ^{178}Hf, ^{202}Hg, ^{204}Hg, ^{204}Pb, ^{206}Pb, ^{207}Pb, ^{208}Pb, ^{232}Th and ^{238}U. Isotopes of the elements selected for measurement were those of the highest natural abundance to minimize potential interferences. For example, ^{49}Ti was selected instead of the more abundant ^{48}Ti to avoid an interference with $^{96}Zr^{++}$ (Lin et al. 2016). This suite of elements was chosen to obtain both geochronologic data and trace element chemistry. Measurements of reference standards (NIST-610, 91500, Plesovice, and FC-1) were interspersed throughout data collection and bracketed unknown samples to serve as analyte sensitivity calibrants to correct for instrument drift and quality control checks of the data. Plesovice and 91500 standards were used as unknowns throughout data collection. Instrument drift (automatic fit) and down-hole fractionation (automatic exponential fit) modelling and calculations were done using the program Iolite3.7^{TM} (Paton et al. 2010). There are isobaric interferences between ^{204}Hg and ^{204}Pb that must be mitigated during sample ablation; therefore, Vici Metronics Hg traps were used within all gas lines to ensure that ^{204}Hg remains under 150 cps. Correction of ^{204}Hg interference was then corrected by peak-stripping using the measured ^{202}Hg. Geochronologic data reduction was done to

minimize the effects of common lead (^{204}Pb) and inclusions, which varied from grain to grain, using the data reduction scheme VizualAge operating within Iolite3.7^{TM}; the ^{204}Pb signal was used for common Pb corrections within the data reduction scheme (Petrus and Kamber 2012). Final data filtering and ^{207}Pb/^{206}Pb age calculations were done using Isoplot3.75 software (Ludwig 2012).

The final ^{207}Pb/^{206}Pb ages obtained by LA-ICP-MS alone had errors that were too large to discern closely spaced magmatic events of these Archean intrusions, therefore, additional CA-TIMS was performed on select samples (von Quadt et al. 2014). Chemical abrasion has been shown to reduce areas affected by Pb-loss which are prevalent in Archean rocks (Crowley et al. 2014). Using these two analytical techniques in tandem offers a broad array of information regarding each sample, and an opportunity to refine each age through a high-precision technique (Schoene 2013). A detailed description of CA-TIMS methods are given in Appendix 2.1**.**

3.5. Results

3.5.1. Lithogeochemical classification

The geochemical characteristics and rock classifications of the YGB intrusions are given in a lithogeochemical analysis carried out by Speight et al. (2023) and the relevant results are summarized here and given in Appendix 1, Table A1.2. Grouping lithologies by geochemistry was done at the start and further corroborated by U-Pb geochronology and zircon mineral chemistry trends in this study. Many lithogeochemical plots were made to

establish that the genetic groupings were not just coincidental, but in fact occurred repeatedly in a variety of figures that include major, minor, and trace element data. When the lithogeochemical results were compared using major, minor, and trace element data, Speight et al. (2023) determined that the FQP, QZP, and aplite-1(a) dikes discussed here are geochemically related to the tonalite and granodiorite of the RLP, while the aplite-1(b) dikes are related to the Defeat Suite granite. A third group of aplite-2 dikes (not dated here) is associated with the Duckfish granite. These distinctions were based on the rare earth element (REE) chondrite-normalized diagrams and other trace element discrimination diagrams. The FQP, QZP, aplite-1(a), tonalite, and granodiorite were found to have smooth REE profiles that decrease from the light REE (LREE) to the heavy REE (HREE). The aplite-1(b) dikes and Defeat Suite granite were also found to have smooth REE profiles that decrease from LREE to HREE but have a moderate to strong negative Eu anomaly (average Eu/Eu* = 0.29). Finally, the Duckfish granite (and associated aplite dikes) were found to have concave up REE profiles with moderate negative Eu anomalies (average Eu/Eu* = 0.44). All these samples have a calc-alkaline signature, and the samples presented here form a linear fractionation trend from andesitic to rhyolitic composition, with one trachyte. Overall, the RLP tonalite and granodiorite are considered the least fractionated rock of the suite and have I/S-type, volcanic arc signatures, while the Defeat Suite and Duckfish granite groups which have an A-type and syn-collisional/within-plate granite signature.

3.5.2. Sample descriptions

3.5.2.1. Feldspar-Quartz Porphyries

Five FQP dikes were analyzed for this study (samples SS18-008, SS18-051, SS18-100, SS18-125, and SS18-128). The samples were taken in various locations, both near and adjacent to igneous pluton contacts. For example, sample SS18-100 was obtained 85 m from the Duckfish Granite contact, whereas sample SS18-125 was approximately 3 km away from the RLP/Defeat Suite contact. The dikes vary from 1-6 m wide and are occasionally crosscut by white quartz veins. Mafic volcanic flows host four dikes, and one crosscuts gabbroic sills is found in the Townsite Formation (SS18-125). The dikes have sharp contacts, and only one dike has a 20 cm-wide chill margin with a cherty, tuffaceous texture (SS18-128). The FQP dikes have a trend between 100 – 150°. The outcrops of FQP vary slightly in colour and have weathered surfaces varying from light pink-buff to grey-brown, with a grey-white to medium grey fresh surface (Fig. 3.1A).

The FQP dikes typically have a fine- to medium-grained matrix hosting medium- to coarse-grained prismatic feldspar phenocrysts and fine- to medium-grained subrounded quartz phenocrysts. Feldspars range from oligoclase to andesine in composition. There is very fine- to fine-grained, disseminated biotite within the matrix, variably altered to chlorite. Some FQP dikes have a more pervasive weak chloritic alteration with a weak to moderate foliation developed. Rare aggregates of chlorite grains occur in one FQP (SS18-128). There is less than 1 vol. %, very fine- to fine-grained disseminated pyrite in the FQP dikes.

3.5.2.2. Quartz Porphyry

Sample SS18-082 is from a QZP dike with a cherty texture taken near the Duckfish Granite and is hosted in massive gabbro with a trend of 172°. The outcrop exposure of this dike shows a massive QZP rock, weathered to a pink-grey colour with a grey colour on fresh surfaces and a cherty matrix (Fig. 3.1B). The cherty texture is like that in other QZP and intermediate dikes in the area. The dike has a massive texture dominated by quartz phenocrysts with fine-grained plagioclase and very fine-grained biotite relegated to the groundmass. The dike has trace amounts of very fine- to fine-grained, disseminated pyrite.

3.5.2.3. Aplite dikes

Two aplite dikes were sampled for this study, and both are hosted in mafic volcanic flows near the RLP and Defeat Suite granite. Previous geochemical analysis by Speight et al. (2023) determined distinct geochemical differences in the aplite dikes related to the RLP and Defeat Suite granite and differentiated them as aplite-1(a) dikes associated with the RLP and aplite-1(b) dikes related to the Defeat Suite granite; the same naming convention will be used here. Sample UNB-1 was obtained 300 m from the RLP contact and part of the aplite-1(a) group. Sample SS18-029 was obtained 50 m from the Defeat Suite granite contact and considered part of the aplite-1(b) group. The aplite dikes have a massive, aplitic texture and have variable geometries. Some aplites have a consistent width ranging from 0.25 to 1.5 m wide in both directions, while others can be observed narrowing down to 1cm wide (Fig. 3.1C). The aplite-1(b) dikes has a trend of 112°. Overall,

the aplite dikes have a buff pink- to pink-coloured weathered surface and a light grey-pink- to pink-coloured fresh surface with trace, weak hematite alteration, sharp contacts, and no chill margins. The dikes are cherty, microcrystalline to nearly aphanitic, equigranular, and dominated by quartz and K-feldspar, with lesser amounts of plagioclase and biotite.

3.5.2.4. Tonalite

Sample SS18-066 is from a tonalitic domain of the RLP and is finer grained with a darker matrix compared to the nearby (and coeval) granodiorite sample (SS18-058). The phaneritic tonalite is fine- to medium-grained, massive, and has a grey and white weathered surface and a fresh grey-green surface (Fig. 3.1D). It is dominated by quartz, plagioclase, biotite, chlorite, and brown-green amphibole.

3.5.2.5. Granodiorite

Sample SS18-058 is part of the RLP and was taken from an exposure of granodiorite. The outcrop is weathered to a white-pink colour and has a grey-white-pink-coloured fresh surface (Fig. 3.1E). The phaneritic granodiorite is massive, medium- to coarse-grained, and comprised of grey quartz with plagioclase, K-feldspar, and mixtures of biotite and chloritized biotite. This sample of granodiorite also contains 1 vol. % disseminated, fine-grained pyrite.

3.5.2.6. Granites

Samples were taken from two different granites, the Defeat Suite granite and the Duckfish Granite occurring north of the RLP and Defeat Suite. Samples JS18-374 and JS18-377 (GRN 1) were obtained from the Defeat Suite granite on the Eastbelt property near Mason Lake. The granite has a pink and grey-coloured weathered surface and is pink, white, and grey on a fresh surface. The granites are phaneritic, massive, equigranular, coarse-grained with quartz, K-feldspar, plagioclase, and disseminated biotite. The Defeat Suite granites have a crystalline and pegmatitic-like texture in some areas where quartz grains cluster together and coarsen.

Sample SS18-084 (GRN 2) was taken from part of the Duckfish Granite within 10 m of the contact between the pluton and mafic volcanic flows. This granite is also phaneritic and weathers to a pink colour and has a pink-coloured fresh surface. It is medium- to coarse-grained, equigranular, and massive with phenocrysts up to 5 mm in width (Fig. 3.1F). The granite is intermittently pegmatitic with quartz pods that are coarse- to very coarse-grained. The Duckfish granite is dominated by quartz, K-feldspar, and plagioclase with up to 5% fine-grained biotite. There are occasional crosscutting quartz veins that are 5 to 10 cm wide.

3.5.3. Optical petrography

Standard polished thin sections were examined to determine sample mineralogy and to obtain information on the textural context of zircon grains. This is important to determine the relative timing of zircon crystallization to interpret ages more

meaningfully. Zircons in these samples were too small to easily locate and image by optical microscopy, so SEM and μXRF mapping were carried out. Additionally, SEM-EDS was used to obtain basic compositional information for primary igneous minerals described here.

The FQP dikes have coarse-grained plagioclase phenocrysts that are variably altered to sericite and often show magmatic zoning (Fig. 3.2A-E). Sericitic alteration intensity of feldspars ranges from minimal to nearly complete alteration of the phenocrysts, often leaving behind sericite pseudomorphs after plagioclase. Fine- to medium-grained, rounded quartz phenocrysts are disseminated throughout the FQP samples and often have an embayed appearance. Interstitial biotite ranges from fine- to coarse-grained and is variably altered to chlorite. Very fine- to fine-grained opaques are spatially associated with biotite. The FQP matrix is typically a combination of recrystallized quartz and feldspars.

Petrographic analysis of the QZP dike shows a similar appearance to the FQP dikes but is more altered overall (Fig. 3.2F). The QZP dike has medium-grained, rounded, and embayed quartz phenocrysts set in a microcrystalline matrix of quartz, calcite, muscovite, and trace opaques. Quartz phenocrysts were rarely euhedral with a square to hexagonal shape. Feldspar pseudomorphed to sericite were present, as in the FQP dikes. Trace amounts of fine-grained anhedral to subhedral titanite with moderate to high relief were observed.

Aplite dikes are typically fine- to medium-grained and dominated by equigranular quartz, K-feldspar, and lesser plagioclase (Fig. 3.2G-H). The plagioclase is often altered to sericite. Myrmekite is distributed throughout the samples. Potassium-feldspar can vary in appearance, showing variable tartan twinning or a wormy, perthitic texture. Minor hematite (alteration) can be observed along quartz grain boundaries and fractures. Trace amounts of disseminated, very fine- to fine-grained biotite is present with very fine-grained opaques.

The plutonic phases sampled include tonalitic and granodioritic intrusions of the multi-phase RLP and granites from the Defeat Suite and Duckfish plutons. The tonalite sample was the only lithology with remnant (magmatic) hornblende, a fine- to medium-grained, pleochroic brown-green to green variety. The tonalite is dominated by quartz and plagioclase with minor disseminated biotite (Fig. 3.2I). Quartz is fine- to medium-grained and disseminated. Feldspars are almost completely altered to sericite. Magmatic zoning is present in some coarser-grained plagioclase crystals. Biotite grains are fine- to medium-grained and have abundant damage halos scattered throughout due to zircon inclusions. Trace amounts of fine-grained opaques are disseminated throughout.

The granodiorite sample is dominated by medium-grained, interlocking quartz and plagioclase (Fig. 3.2J). The larger quartz grains have recrystallized grain boundaries, and the grains tend to occur in clusters. The plagioclase is nearly completely altered to sericite, with sericite distribution defining a ringed pattern that follows magmatic zoning in the original plagioclase. Fine- to medium-grained biotite is disseminated throughout and is

variably altered to chlorite. Damage halos from zircon inclusions are also present in these biotite grains, as in the tonalite.

The granite samples from two different plutons share similar textures and mineralogy with very few differences. The Defeat Suite granite is dominated by coarse- to very coarse-grained quartz and K-feldspar and medium- to coarse-grained plagioclase (Fig. 3.2K). The plagioclase is variably altered to sericite; the sericite is coarser grained than in other plutons or dikes. Muscovite and biotite are fine- to medium-grained; biotite is weakly to moderately altered to chlorite. Muscovite often has a wormy or amoeboid texture and contains inclusions of quartz and feldspars. Trace amounts of myrmekite is present, and K-feldspar is perthitic.

The Duckfish Granite sample is like the Defeat Suite samples, with a few distinctions in textures observed. Weak magmatic zoning occurs in some plagioclase crystals, highlighted by preferential sericite alteration more abundant in some zones than others (Fig. 3.2L). Quartz shows extensive recrystallization and deformation textures (i.e., undulose extinction, grain bulging, sub-grain development, and the initiation of deformation bands). Rarely, K-feldspar contains inclusions of lathy, fine-grained plagioclase.

3.5.4. SEM-EDS and µXRF

Due to the small size of the zircon grains encountered in this study, SEM and µXRF scans of polished thin sections were employed to obtain details on the textural setting of zircon (Fig. 3.3A-H). The location of zircon grains are highlighted with enlarged circles to

show their position relative to other phases. Of the 13 µXRF scans of polished thin sections, five samples were found to have zircons hosted in phenocrystic quartz and feldspars. This occurs in two FQP samples and both the Defeat Suite and Duckfish granites. Several zircons in the FQP samples are included in feldspar and quartz phenocrysts (Fig. 3.3C-D) and included in coarse-grained quartz and K-feldspar in the Defeat Suite and Duckfish granites (Fig. 3.3 G-H). Zircons are scattered throughout the samples and commonly occur along phenocryst grain boundaries or are completely included within phenocrysts of quartz and feldspars. This suggests that these grains were crystallizing early in the history of the rock and became included in co-crystallizing quartz and feldspar, genetically linking them to their host rock and reducing the possibility that these zircons were entrained during crustal assimilation or emplacement. The *in-situ* mineralogical associations of zircons were investigated to corroborate the µXRF observations (Fig. 3.4A-B). SEM-BSE images show subhedral zircons hosted within a quartz-rich matrix (Fig. 3.4A) and occurring along biotite grain boundaries (Fig. 3.4B) in RLP samples.

3.5.5. U-Pb geochronology

To identify textural characteristics of the zircons to be analyzed that may be relevant to data interpretation and quality control, SEM-BSE images were obtained (Fig. 3.5). Specifically, these images allowed the internal structure of the zircons to be visualized, and certain areas with obvious mineral or melt inclusions, metamict/altered domains, sieve texture, fractures and inherited cores could be avoided during LA-ICP-MS data collection. This imaging also allowed oscillatory and irregular zoning patterns to be

identified. All zircons show oscillatory zoning in part or the entire grain or a patchy zoning pattern (Fig. 3.5). Inclusions have been identified in all populations and typically have a spherical to ovoid shape and black or red-brown colour. Overgrowths on xenocrystic cores were occasionally present, most often found in colourless and violet zircons.

Eight zircon colour populations were identified, including colourless, cloudy white, grey, violet, yellow, turbid yellow, orange, and brown. These can be grouped into three main populations of colourless, violet, and yellow, with gradational changes between them. Data reduction was completed in two stages to determine whether zircon colour subsets have different ages than an unfiltered dataset. Zircon colour and morphology have been linked to differences in chemistry, metamictization, and metamorphism; therefore, zircons were segregated by colour for comparison (Corfu et al. 2003). Each lithology contains at least two populations, all of which have colourless zircons and at least one other colour of zircon. The distribution of each colour per lithology is summarized in Table 3-1. Ages for each zircon colour subset were calculated separately. However, no significant difference was found when these data populations were compared as all ages were found to be within error. Therefore, the larger and more robust unfiltered results are presented with the corresponding Concordia diagrams shown in Fig. 3.6 and Fig. 3.7.

Data filtering protocols were employed to mitigate the effects of deformation and alteration, recent Pb-loss, ancient Pb-loss, or both. Data with no ^{204}Pb-correction were used whenever possible. The ^{204}Pb signal was used to determine if a common Pb

correction was needed, using a threshold of > 50 cps and < 98.5% radiogenic Pb for Concordia age calculations. Data were then sorted by percent concordance and limited to data with a normal and reverse discordance of < 5%. A weighted mean Concordia age was calculated with no less than three data points. When possible, data were manipulated to a mean squared weighted deviation (MSWD) of ≈ 1; however, higher MSWD values are acceptable when small data sets are considered (Wendt and Carl 1991). For example, sample JS18-377 used only four concordant points to calculate a weighted mean Concordia age with a corresponding MSWD of 1.4; according to Wendt and Carl (1991), an MSWD < 2.4 is acceptable with this smaller dataset. All ages discussed in the results below are for the weighted average $^{207}Pb/^{206}Pb$ age of near-concordant data (±5% discordant), except for three samples that produced insufficient concordant data. Where concordant data was not available, an upper intercept age was calculated using data with > 50% concordance, all of which are summarized in Table 3-2 and the entire dataset is given in Appendix 2, Table A2.1. The ages described below likely represent minimum crystallization ages as a combination of ancient and recent Pb-loss may have translated data to younger $^{207}Pb/^{206}Pb$ ages (Bauer et al. 2017). To improve the temporal resolution of this data, six samples were also analyzed by high-precision CA-TIMS. These ages are given with each corresponding sample with two errors listed, the calculated internal error and the error determined when decay constant errors are included {shown in square brackets). A summary of CA-TIMS ages are provided in Table 3-3, and the full data set used to calculate weighted mean ages is given in Appendix 2, Table A2.2.

3.5.5.1. Feldspar-Quartz Porphyry

3.5.5.1.1. SS18-008

This FQP dike contained violet, yellow, and colourless zircons ranging from 50 to 250 μm with aspect ratios of 1:2 to 1:5. The violet zircons have an elongated 'soccer-ball' shape and are doubly terminated. These zircons are clear to translucent and are the largest zircons overall. The yellow zircons are variably pale to dark yellow, the smallest observed in SS18-008, typically with a short and stubby shape, some of which have a 'soccer-ball' shape. The colourless zircons can vary to pale grey and have an extensive size range, from small and stubby to elongated and acicular. Inclusions were observed in all zircon populations. A total of 160 zircon analyses were gathered to determine the age of this FQP dike. After data filtering and analysis, a Concordia age was calculated using only three data points, giving a crystallization age of 2687 ± 8 Ma (MSWD 0.24) and a weighted mean age of 2691 ± 13 Ma (MSWD 0.062) from the same data points (Fig. 3.6A). This age is corroborated by the upper intercept age calculated using seven data points (anchored at 50 ± 50 Ma) and found to be 2688 ± 19 Ma (MSWD 3.1) (Fig. 3.6A). This sample was further analyzed by CA-TIMS, where three whole zircon grains and two fragments from one grain yielded a weighted mean age of 2662.07 ± 0.79 [2.37] Ma (MSWD 0.79). This is considered the interpreted minimum crystallization age for this FQP dike.

3.5.5.1.2. SS18-051

This FQP contained zircons that are violet, yellow, and colourless, all containing inclusions. The zircons range from 50 to 175 µm with aspect ratios of 1:2 to 1:3. The violet zircons have a 'soccer-ball shape,' are clear to translucent and are the largest zircons of all three colours. The yellow zircons are overall short and stubby, but they are larger than usual in this sample and have a similar size to the colourless zircons. The colourless to pale grey zircons are elongated and acicular with a variable size range. A total of 172 analyses were reduced to 21 concordant data points, used to calculate a Concordia age of 2674 ± 7 Ma (MSWD 0.65) for this FQP dike and a weighted mean age of 2677 ± 11 Ma (MSWD 4.6); the Concordia age is considered the age of crystallization (Fig. 3.6B).

3.5.5.1.3. SS18-100

This FQP dike was sampled proximal to the Duckfish granite and contains brown and colourless zircons ranging from 50 to 100 µm with aspect ratios of 1:2 to 1:3. Zircons were scarce in this mineral separate and included only seven colourless and one brown zircon. The brown zircon was stubby and wide with a subhedral shape and rounded tips, although the colour may be due to alteration. The colourless zircons were broken, euhedral, elongated needles that varied to a pale grey. None of the eight zircons analyzed fell along the Concordia curve and were affected by Pb-loss. Five analyses were 84–89% concordant and defined a Discordia line with an upper intercept of 2746 ± 15 Ma, anchored at a lower intercept of 50 ± 50 Ma (Fig. 3.6C).

3.5.5.1.4. SS18-125

Zircons in this FQP sample include turbid yellow, yellow, and colourless; overall, the zircons show a gradual colour change. The turbid yellow zircons have two size fractions, a population of larger and small turbid grains. The larger zircons have a grungy yellow-brown colour, they are faceted, stubby to 'soccer-ball'-shaped, and some have a pale violet hue. The yellow zircons are smaller than the turbid zircons, they are also clearer, and are typically short and stubby with few elongated grains. The colourless zircons in this sample also have a pale brown-yellow hue and typically a short and stubby shape, which contrasts with other colourless zircons, which are mainly elongated. The zircons in this FQP ranged from 50 to 175 μm with aspect ratios of 1:2 to 1:3. A total of 130 zircon analyses were performed, and data were reduced to 10 concordant points that give a calculated age of 2629 ± 10 Ma (MSWD 0.31) and a weighted mean age of 2637 ± 15 Ma (MSWD 0.55) (Fig. 3.6D). This sample was further analyzed by CA-TIMS, where five whole zircon grains yielded a weighted mean age of 2662.69 ± 0.67 [2.37] Ma (MSWD 0.46). This is considered the interpreted minimum crystallization age for this FQP dike.

3.5.5.1.5. SS18-128

This FQP sample has the same three zircon populations as SS18-125. There are turbid yellow, yellow, and colourless zircons which all have a gradational change in colour. These zircons are smaller than in SS18-125, ranging from 40 to 100 μm with similar aspect ratios of 1:2 to 1:3. A total of 139 zircon analyses were obtained, and data were reduced to 12 concordant points, giving a calculated Concordia age of 2674 ± 5 Ma (MSWD 0.67) and a

weighted mean age of 2667 ± 11 Ma (MSWD 1.03) for this FQP dike (Fig. 3.6E). These two ages overlap within error; therefore, the Concordia age is considered the minimum crystallization age for this dike.

3.5.5.2. Aplite dikes

3.5.5.2.1. UNB-1

This aplitic dike has two zircon colour populations, colourless and grey, equally abundant and the same size. The zircons in this aplite dike range from 50 to 100 µm with aspect ratios of 1:1 to 1:2. The colourless zircons are subhedral prisms, often broken and with rounded tips. Some grains have a shorter oval shape. The grey zircons have a euhedral to subhedral shape and are less broken than the colourless grains. These zircons are mainly short and stubby, with some elongated and prismatic grains. A total of 85 zircon analyses were collected to determine the age of this aplite-1(a) dike, found proximal to the RLP and Defeat Suite granite. After data filtering, 13 analyses were used to calculate a Concordia age of 2673 ± 13 Ma (MSWD 1.3) and weighted mean age of 2676 ± 15 Ma (MSWD 0.71; Fig. 3.6F). An anchored (50 ± 50 Ma) upper intercept age was calculated from the Discordia line defined by 20 analyses and found to be 2673 ± 10 Ma (Fig. 3.6F). This dike was also analyzed by CA-TIMS, where five whole zircon grains yielded a weighted mean age of 2662.75 ± 1.04 [2.42] Ma (MSWD 0.44). This is considered the interpreted minimum crystallization age for this aplite dike.

3.5.5.2.2. SS18-029

This aplitic dike contains violet and colourless zircons ranging from 50 to 175 µm with aspect ratios of 1:2 to 1:3. The violet zircons vary to a pale violet and have a 'soccer-ball' and teardrop-shaped. Some of the grains are very transparent, typically the paler grains. The violet zircons are rarely elongated and can have fractured surfaces. The colourless zircons can also be a pale violet to gray. The colourless zircons are typically euhedral to subhedral with the same 'soccer-ball' and teardrop as the violet grains. A total of 84 zircons were analyzed from this aplite-1(b) dike, also sampled proximal to the RLP and Defeat Suite granite. Only three analyses were concordant enough to determine a Concordia age of 2663 ± 19 Ma (MSWD 0.0040) and a weighted mean age of 2661 ± 32 Ma (MSWD 0.44) (Fig. 3.6G). This age was refined by calculating an anchored (50 ± 50 Ma) upper intercept age along the Discordia line defined by 43 zircon analyses with > 50% concordance, giving a $^{207}Pb/^{206}Pb$ age of 2667 ± 12 Ma (Fig. 7G). This aplite dike was further analyzed by CA-TIMS, where three whole zircon grains and two fragments from a single zircon grain yielded a weighted mean age of 2661.77 ± 0.70 [2.46] Ma (MSWD 1.3). This is considered the interpreted minimum crystallization age for this aplite dike.

3.5.5.3. Tonalite

3.5.5.3.1. SS18-066

This sample from the tonalitic RLP has two zircon populations, violet and colourless, ranging in size from 75 to 220 µm with aspect ratios of 1:2 to 1:5. The violet zircons can show a range in colour intensity, from pale violet to colourless. Nearly all the violet zircons

are fragmented with very few euhedral or subhedral grains. There are rare, smaller violet zircons with a euhedral 'soccer-ball' shape, but zircon tips were mainly picked from this mineral separate. The colourless zircons occasionally ranged to a pale grey colour. Most grains were broken but appeared to be short and stubby, with only a few elongated zircons. The violet zircons were more abundant than the colourless. A total of 107 zircons were analyzed from this tonalite sample, and data were reduced to 16 concordant analyses that give a calculated Concordia age of 2651 ± 6 Ma (MSWD 0.90) and a weighted mean age of 2657 ± 8 Ma (MSWD 1.5) (Fig. 3.6H). This sample was further analyzed by CA-TIMS, where three whole zircon grains and two fragments from a single zircon grain yielded a weighted mean age of 2662.26 ± 0.65 [2.36] Ma (MSWD 0.38). This is considered the interpreted minimum crystallization age for this aplite dike.

3.5.5.4. Granodiorite

3.5.5.4.1. SS18-058

This granodiorite from the RLP has three zircon populations: violet, yellow, and colourless. The zircons in this sample are generally smaller than those in the tonalite, ranging from 50 to 125 µm with aspect ratios of 1:1 to 1:3. The violet zircons are turbid with a somewhat 'soccer-ball' shape, and they are the largest zircons of the three populations. The yellow zircons are clear, short, and stubby grains, though some have the same 'soccer-ball' shape as the yellow-brown grains. The colourless zircons are the most variable in this sample. They are typically colourless, but occasionally, a pale grey-brown

and even pale yellow colour can be observed. The colourless zircons are elongated, but there are some shorter and stubby grains and occasionally 'soccer-ball'-shaped grains. The zircon populations are quite similar and visually look like a continuum from one colour to the next, as observed in other samples. A total of 165 zircons were analyzed from this granodiorite sample, and data were reduced to 12 concordant analyses that give a calculated Concordia age of 2647 ± 7 Ma (MSWD 0.56) and a weighted mean age of 2649 ± 9 Ma (MSWD 4.6) (Fig. 3.6I). The Concordia age is considered the minimum age of crystallization for this pluton.

3.5.5.5. Defeat Suite Granite

3.5.5.5.1. JS18-377

This sample from the Defeat Suite granite contains three zircon colours, yellow, cloudy white, and colourless. These zircons range from 100 to 200 µm with aspect ratios of 1:2 to 1:4. The yellow zircons are typically elongated with some shorter stubby crystals. The colour varies from pale yellow to dark yellow to orange, although the orange colour looks like more of a coating than the actual colour. The yellow zircons are euhedral-subhedral, and some grains have rounded points. The cloudy white and colourless zircons are larger than the yellow grains but have a larger size variation. They are colourless to pale grey and occasionally have a turbid white colour. There were rare inherited cores observed in euhedral and elongated grains, which were avoided during LA-ICP-MS analysis. A total of 139 zircons were analyzed from the Defeat Suite granite and reduced to only four

concordant points that could be used to calculate a Concordia age of 2580 ± 27 Ma (MSWD 1.4) and a weighted mean age of 2577 ± 42 Ma (MSWD 6.7) (Fig. 3.6J). To corroborate this age, an anchored (50 ± 50 Ma) upper intercept age was calculated using data that form a Discordia line. A total of seven analyses with > 84% concordance were used to calculate an upper intercept age of 2597 ± 57 Ma (Fig. 3.6 J). A probability density plot of data with > 50% concordance shows a main peak age at 2582 Ma; therefore, the calculated Concordia age of 2580 ± 27 Ma is considered the minimum crystallization age for this pluton. Despite attempting to avoid analyzing xenocrystic cores, there is evidence for some inheritance in this sample, as indicated by the peaks at ~3600 and 3800 Ma on the probability density plot (Fig. 3.6J).

3.5.5.6. Duckfish Granite

3.5.5.6.1. SS18-084

This sample is part of the Duckfish granite and contains four groups of zircons. Zircons were found to range in colour and include orange, yellow, colourless, and grey zircons. The grains found in this sample range from 50 to 200 µm with aspect ratios of 1:1 to 1:4. The orange zircons are stubby and vary in size. The orange colouring may be due to a coating, and this population of zircons could be more yellow than orange. The zircons have subrounded tips and a blocky cross-section. The yellow zircons have the same shape and size as the orange, and the orange colour is observed along with some fractures. The colourless zircons are stubby to elongated with pointed tips and minimal rounding. There

is some patchy orange colouring on the colourless zircons. Some are cloudy and larger than most colourless grains, and a few have a violet hue. The grey zircons are overall the same as the colourless but consist of a smaller size fraction and are translucent to transparent. It is rare to find the orange coating on fractures of the grey zircons. A total of 125 zircons were ablated from the Duckfish granite, and data were reduced to only five concordant analyses that give a calculated Concordia age of 2576 ± 7 Ma (MSWD 0.82) and a weighted mean age of 2596 ± 23 Ma (MSWD 9.0); the Concordia age is considered the minimum age of crystallization for this pluton (Fig. 3.6K).

3.5.5.7. Quartz Porphyry

3.5.5.7.1. SS18-082

This QZP dike contains violet, colourless, and grey zircons which all have inclusions and range from 75 to 200 µm with aspect ratios of 1:2 to 1:4. The violet zircons are dominantly elongated and prismatic grains, with fewer 'soccer-ball'-shaped grains than other samples. The violet zircons are typically translucent and larger than the colourless grains. The colourless zircons are transparent, with the colour ranging to a cloudy grey. The colourless zircons also display sizes from elongated to stubby, typically euhedral with rare, rounded tips.

A total of 138 zircons were analyzed from this QZP dike, and the data indicate a complex history. When data with > 50% concordance are plotted together on a probability density plot, two main age peaks are apparent (Fig. 3.7A). The data define peaks at 2763

Ma, 2903 Ma, and six analyses that are > 3000 Ma. A Concordia age was calculated using seven analyses and gave a $^{207}Pb/^{206}Pb$ age of 2904 ± 7 Ma (MSWD 0.090) and a corresponding weighted mean age of 2910 ± 8 Ma (MSWD 2.2; Fig. 3.7B). However, when this data is considered as part of the entire dataset, it likely reflects a mix of inherited and crystallization ages. Fig. 3.7C shows all data with > 50% concordance on a U-Pb Concordia diagram with a best-fit line through 2763 Ma, the youngest peak observed in the probability density plot. There is a spread of data from the oldest analysis at ~3400 Ma down to this younger age (2763 Ma), at which point there is evidence for recent Pb-loss as the data trend toward the origin along the best-fit line. An anchored (50 ± 50 Ma) upper intercept age was calculated, focusing on this younger age trend, and a $^{207}Pb/^{206}Pb$ age of 2770 ± 7 Ma (MSWD 0.87) was determined using ten analyses (Fig. 3.7D). When the entire dataset for this QZP sample is considered, the younger upper intercept age of 2770 ± 7 Ma is considered the minimum age of crystallization for this intrusion, rather than the mixed concordant age. This sample was also analyzed by CA-TIMS; however, the four whole grains and two fragments from one single zircon grain did not return a weighted mean age despite being >99% concordant. The ages determined by CA-TIMS for this QZP dike range from 2760.55 ± 1.52 Ma to 2895.38 ± 0.98 Ma, indicating the same inheritance observed during LA-ICP-MS analysis (Fig. 3.7D).

3.5.6. Zircon mineral chemistry

Mineral chemistry data were collected concurrently with U-Pb geochronology to characterize magma chemistry at a specific time, determine fractionation trends, and

connect YGB dikes and plutons. Although the individual ablations were manipulated to avoid Pb-rich inclusions, which may affect age results, some ablations intersected P- and Ti-rich inclusions (e.g., apatite, xenotime, and rutile). Natural zircons from a highly fractionated syenite intrusion were found to have oscillatory zoning, which corresponds to maximum P and Ti values of 2464 and 79 ppm, respectively (Yang et al. 2016). Therefore, these values were chosen as a maximum compositional limit representing P and Ti within the zircon crystal structure and not as an artifact of inclusions. Results were also filtered to only include data based on the interpreted $^{207}Pb/^{206}Pb$ crystallization age outlined in the previous U-Pb geochronology results. This data filtering of the zircon mineral chemistry, therefore, represents a snapshot of magma chemistry at the time of crystallization, and not the mineral chemistry related to a Pb-loss event. Zircons were analyzed for minor and trace elements including Ce, Dy, Er, Eu, Gd, Hf, Ho, La, Lu, Nd, P, Pb, Pr, Si, Sm, Tb, Th, Ti, Tm, and U. The minimum, maximum, and average concentrations for each element are summarized in Table 3-4, and the entire dataset can be found in Appendix 2, Table A2.3**.**

Zircon mineral chemistry data were compared to their corresponding $^{207}Pb/^{206}Pb$ age to assess geochemical changes through time (Fig. 3.8). There is an overall increase in the Th/U ratios of all samples, with the QZP dike having the oldest and lowest Th/U of 0.048 – 0.39; the oldest FQP samples overlap with the QZP with a Th/U ratio of 0.23 – 0.52 (Fig. 3.8A). Samples that fall between 2600–2700 Ma have an increasing Th/U ratio from 0.45 to 2.5 with decreasing age. Finally, the Defeat Suite granite and Duckfish granite samples

are the two youngest intrusions in this sample suite and have Th/U ratios of 0.47 – 1.6. When the Hf content of the zircons is compared to age, three clusters are observed (Fig. 3.8B). The QZP has the highest concentration of Hf, ranging from 1.1 – 1.5 wt. % Hf while the bulk of the data (including the FQP, aplites, granodiorite, and granites) have Hf concentrations ranging from 0.77 – 1.3 wt. %. The RLP tonalite has the lowest Hf concentrations, ranging from 0.71 – 0.82 wt. %. The Eu anomaly ($Eu/Eu^* = Eu_N/[Sm_N \times Gd_N]^{½}$) was also compared to the age of the zircon, and two groups that have overlapping Eu anomalies were identified (Fig. 3.8C). The QZP, Defeat Suite granite, and Duckfish granite have overlapping Eu anomalies that range from 0.14 – 0.56, with two QZP outliers at 2.2 and 3.4. The remaining intrusions have Eu anomalies that range from 0.40 – 1.72, with one granodiorite outlier at 2.47.

Zircon trace element data represents a snapshot of magma chemistry and can be used to discern fractionation trends, monitor for co-crystallizing phases and determine whether zircons are magmatic, metamorphic, or hydrothermal (Fu et al. 2008, Dilles et al. 2015, Buret et al. 2016, Rubatto 2017, Siégel et al. 2018, Sheikh et al. 2020). Therefore, the Th and U concentrations in zircons were considered in more detail and plotted to observe the Th/U ratio of each lithology; this can help assess their magmatic versus metamorphic nature. The least fractionated tonalite sample has the highest Th/U ratio range from 0.87 – 1.8, and the samples have a steadily declining Th/U ratio range from this to the FQP (0.23 – 1.6) and granodiorite (0.69 – 1.6) to the more aplitic dikes and granites (0.47 – 1.6), excluding outliers (Fig. 3.9A). The QZP has the lowest Th/U range

(0.048 – 0.39) and the highest U concentration of 3187 ppm (Fig. 3.9A). Zircons with a Th/U ratio > 0.1 are typical of magmatic zircons, while metamorphic zircons have Th/U ratios of < 0.1 (Rubatto 2017). In this case, all the YGB intrusions analyzed here fall above the Th/U of 0.1 and are considered magmatic, except two individual QZP zircons, which have Th/U ratios of 0.048 – 0.054 and could be considered metamorphic; the remaining six QZP zircons analyzed have Th/U ratios of 0.11 – 0.39 and fall in the magmatic zircon range (Rubatto 2017). These zircons are not considered hydrothermal in origin due to their REE trace element signatures and, most significantly, their Ti-in-zircon temperatures, which are all above the hydrothermal range and further described below (Fu et al. 2009). Overall, the lithologies examined here typically have Th/U ratios between 0.5 and 2 and are therefore considered magmatic in origin.

When the Th/U ratio is compared to the Hf content of the zircons, both considered elements that can be used to track fractionation, the QZP once again shows a different trend than the remaining samples (Fig. 3.9B). The QZP zircons have a much steeper negative correlation between Hf and Th/U (r = -0.74) compared to the remaining YGB intrusions. The aplites, granites, FQP, granodiorite, and tonalite follow a shallow negative trend between the Th/U ratio and Hf concentrations (r = -0.49), with the tonalite sample having the lowest Hf concentrations between 0.71 – 0.82 wt. % Hf. The FQP, granodiorite, aplites, and granites have Hf concentrations between 0.77 – 1.3 wt. % Hf while the QZP has the highest concentrations of 1.1 – 1.5 wt. % Hf. The comparison of the Hf/Y and Th/U ratios of the zircons shows similar groupings; the QZP and tonalite are distinct from the

largest population, consisting of the FQP, granodiorite, aplites, and granites (Fig. 3.9C). Closed-system fractionation trends would produce zircons with decreasing Th/U and corresponding increasing Hf/Y ratios (Large et al. 2018). This fractionation trend can be seen here, with all samples following a linear negative trend that varies in steepness. The QZP and tonalite samples have the steepest negative trend between Hf/Y and Th/U, while the remaining lithologies have shallow to flat trends. There is a broad, weak negative correlation between Hf and the calculated Eu anomaly (r = -0.16), however, the same lithologies can be observed clustering together, and following the least to most fractionated path determined by whole-rock geochemistry (i.e., from tonalite to FQP, granodiorite, aplites, and granites, finally to the QZP dike; Fig. 3.9D). Certain trace elements including Ce, Dy, La, Er, and Yb were not analyzed in every sample; thus, some samples are missing from Fig. 3.9E-F, which compare U/Yb to Hf concentrations, and chondrite-normalized Yb_N/Gd_N to Ce_N/Sm_N (Sun and McDonough 1989). The U/Yb ratio shows two clusters which include the Defeat Suite granite, aplites, and FQP, which plot together at lower U/Yb values than the QZP dike, which has a higher U/Yb ratio and no specific correlation with Hf (Fig. 3.9E). Finally, the chondrite-normalized ratios of Yb_N/Gd_N and Ce_N/Sm_N show a positive correlation for the FQP dikes, aplites, granite, and QZP, although the QZP dike extends to higher Yb_N/Gd_N values than the main population, also true for some outlying FQP dikes with elevated Ce_N/Sm_N values (Fig. 3.9F).

Chondrite-normalized REE diagrams of zircon mineral chemistry (filtered by crystallization age) have been plotted per lithology and subdivided by sample (Fig. 3.10).

Despite separating the data by lithology, there is a widespread in REE concentrations, particularly for LREE. For example, the five FQP samples with crystallization ages between 2662.1 to 2746 Ma have overlapping REE concentrations and similar REE profiles (Fig. 3.10A). Zircons from the FQP samples show variable Ce and Eu anomalies and progressively flatter REE signatures. Overall, the FQP Ce anomaly is positive at lower REE concentration, but as the REE contents increase, the Ce anomaly becomes less pronounced; overall ranging from 1.2 – 5.23, with one outlier of 51.4. The Eu anomaly in the FQP is weakly negative to weakly positive from 0.43 – 1.7, which can also be observed in other lithologies, such as the QZP (0.14 – 3.43), tonalite (0.76 – 1.6), and granodiorite (0.40 – 2.5), suggesting these intrusions crystallized in similar environments (Fig. 3.10A, B, D, E). The aplite dikes, Defeat Suite and Duckfish granites also have similar REE profiles although they only show negative Eu anomalies. The aplite dikes have Eu anomalies ranging from 0.50 – 0.73, the Defeat Suite granites range from 0.18 – 0.41, and finally, the Duckfish granite zircons range from 0.39 – 0.46. (Fig. 3.10C, F).

The Ti-in-zircon thermometer, determined by Ferry and Watson (2007), was used to calculate temperatures for each lithology (summarized in Table 3-4). These calculations were done using an $a\mathrm{TiO_2}$ of 0.7 and $a\mathrm{SiO_2}$ of 1 due to the presence of Ti-rich minerals (rutile, ilmenite) and the prevalence of quartz. The samples have a temperature range of 696 – 1039°C, with the QZP dike and tonalite zircons having the lowest temperatures (696 and 700°C, respectively). The QZP dike and tonalite also have the highest temperatures of 1029 and 1039°C, respectively, therefore representing the entire temperature range

observed in this sample set; however, this high tonalite temperature may be an outlier as the remaining concordant zircons have a lower temperature range of 700 – 826°C. When the temperatures of each lithology are compared by age; however, there is no distinct no correlation (Fig. 3.11A). There is a weak negative covariance between zircon Th/U ratios and decreasing temperature (Fig. 3.11B). As the intrusions were cooling, there was a corresponding decrease in the Th/U ratio for all samples except the QZP, which remained at a more constant Th/U ratio. The data can be segregated into three populations based on the Th/U ratio, and this can also be observed when comparing the Hf concentrations to temperature clusters that have been previously described (Fig. 3.11B, C). The least fractionated tonalite plots separately from the main group of FQP, granodiorite, aplites and granites, which also plots separately from the QZP dike (most fractionated). When the Hf concentration is compared to zircon temperature no overall correlation was observed, although Hf is expected to increase with progressive fractionation (Fig. 3.11C). The tonalite shows a weak inverse correlation between temperature and Hf concentrations (r = -0.4), while the main cluster of data (FQP, granodiorite, aplites, and granites) has a more constant Hf concentration with decreasing temperature.

The Ti-in-zircon temperature calculations were also compared to other trace element data, such as the Eu/Eu*, Ce/Ce* (Ce/Ce* = $Ce_N/[Nd_N^2/Sm_N]$), and Tm_N/Gd_N (Fig. 3.11). There is a broad correlation between the Eu anomaly and temperature, with the Eu anomaly decreasing with decreasing temperature (Fig. 3.11D). The intrusions overlap, and all samples follow the same trend, indicating decreasing Eu anomalies with decreasing

temperatures, although there is more variability at higher temperatures. When the Ce anomaly is compared to temperature, there is an overall linear, moderate negative correlation, with the Ce anomaly increasing as the temperature decreases (r = -0.49) and the data become more scattered at lower temperatures (Fig. 3.11E). Finally, the Tm_N/Gd_N ratio was compared to temperature in place of Yb_N/Gd_N due to a lack of Yb data; however, Tm can be used as a proxy for Yb, and the trends remain the same. When the Tm_N/Gd_N ratio is compared to temperature, a moderate negative correlation is observed (r = -0.5), with all lithologies overlapping and following the same path of increasing Tm_N/Gd_N with decreasing temperature (Fig. 3.11F).

3.6. Discussion

3.6.1. U-Pb geochronology of the YGB dikes and plutons

LA-ICP-MS and CA-TIMS U-Pb geochronology data of the YGB intrusive samples were obtained to help fill the geochronologic record by focusing on underrepresented lithologies. This included the FQP, QZP and aplite dikes (locally known as the "#9" dikes) and comparing them to regional plutons to ascertain the temporal connections in the YGB. Previous geochronology studies have covered a wide range of lithologies within and beyond the YGB; however, there is a consistent lack of concordant data, likely due to widespread ancient and recent Pb-loss in these Archean rocks (Isachsen et al. 1991, Isachsen 1992, Isachsen and Bowring 1994, Bleeker et al. 1999b, Davis and Bleeker 1999, Ketchum et al. 2004, Ootes et al. 2007, Reimink et al. 2016). This is problematic due to

the non-zero lower intercept ages reported for calculated upper intercept ages, confirming ancient Pb-loss and a shift in the data away from Concordia and crystallization ages (Corfu 2013). For example, the ages determined by Isachsen et al. (1991) were all upper intercept ages with non-zero lower intercepts and no concordant data; ages of this nature tend to overestimate the crystallization age. Therefore, it was the goal of this study to collect a dataset related to the FQP, QZP, aplite dikes, and parental plutons (tonalitic and granodioritic RLP, Defeat Suite granite, and Duckfish granite), use stringent filtering protocols and add to the previously documented ages. By initially collecting LA-ICP-MS U-Pb data, high-priority samples were identified for further high-resolution CA-TIMS data collection.

3.6.1.1. Origin of YGB zircons

The μXRF scans of polished thin sections and SEM-BSE analysis confirms that zircons were included in phenocrystic phases (FQP and granites), present along phenocryst grain boundaries, and disseminated throughout the groundmass (Fig. 3.3, Fig. 3.4). SEM-BSE imaging also shows characteristic concentric and oscillatory zoning in zircons, diagnostic of crystallization from a melt (Fig. 3.5). The occurrence of zircon crystals included within phenocrysts, along grain boundaries, and throughout the groundmass implies that zircons were crystallizing from the melt throughout the growth of these other crystals. Together this suggests that zircon saturation was protracted within the magma chamber and occurred early in the magmatic history. These zircons are considered magmatic in origin due to their Th/U ratios (all > 0.1 except for two QZP analyses) and their REE profiles (Fig.

3.9A, Fig. 3.10). Previous work by Hoskin (2005) describes REE profiles of magmatic zircons, which are LREE depleted relative to the HREE. These contrast with altered magmatic zircon REE profiles that tend to be enriched in LREE and have a flatter profile compared to magmatic zircons. LREE-enriched profiles are also considered to be related to zircons crystallizing from highly fractionated magmas. The data shown in Fig. 3.10 have a similar profile to those described by Hoskin (2005), particularly the FQP dikes, which have profiles that show zircon depleted in LREE with steep REE profiles, and those with flatter profiles that are relatively enriched in LREE. This suggests that these zircons are magmatic in origin, some of which either crystallized from an evolved magma or were hydrothermally altered after crystallization; in either case, the zircons are not of hydrothermal or metamorphic origin. The remaining intrusions show the same trends and are also considered magmatic (Fig. 3.10). The calculated Ti-in-zircon temperatures likewise suggest that these zircons are of magmatic origin due to their elevated crystallization temperatures of 696 – 1039°C (Hoskin 2005, Fu et al. 2009, Rubatto 2017).

A common concern in zircon U-Pb geochronology is the possibility of inheritance and inherited ages. Inherited ages are observed when ablations analyzed older zircon cores that have been entrained during partial melting, migration of magma through the crust, assimilation-contamination-mixing, and ultimate emplacement (Harrison and Watson 1983, Gagnevin et al. 2010, Claiborne et al. 2010, Dickin 2018). Depending on the magmatic processes taking place, zircon can continue to grow on the inherited cores; therefore, this new zircon outer rim would have a younger crystallization age than the

core. This is a significant concern in the YGB due to the small size of the zircons and the ensialic basement rocks that underly supracrustal and intrusive rocks, and through which magmas have passed or originated. For instance, rising magmas passing through the Central Slave Basement Complex (CSBC) could assimilate material from the CSBC and inherit zircons with ages of 3325 ± 8 Ma (Bleeker et al. 1999a). Cousens (2000) used ε_{Nd} data to determine that YGB magmas were contaminated by these gneissic basement rocks and, therefore, could endow YGB intrusions with older zircons. We endeavoured to avoid the complication of inheritance by imaging the groups of zircons by SEM-EDS, locating inherited zircon cores, and placing LA-ICP-MS ablation pits along outer growth zones to avoid any cores. After U-Pb geochronology data was collected and analyzed, data were plotted on probability density plots to monitor the overall $^{207}Pb/^{206}Pb$ age, and it was found that two samples showed inherited ages, although those data were filtered out of the final age calculations and discussed below. Xenocrystic cores were infrequently observed during BSE imaging and effectively avoided, suggesting that there was limited assimilation of the country-rock by the intruding magmas or entrained zircons were resorbed so that few xenocrystic cores remained (Harrison and Watson 1983, Watson and Harrison 1983, Boehnke et al. 2013). Experimental work by Harrison and Watson (1983) found that a 50 µm diameter zircon would take ~100 years to completely dissolve in a 750 °C hydrous (3 – 6% H_2O) granitic melt and roughly 10,000 years to dissolve a 200 µm zircon. If the melt is anhydrous, a 50 µm zircon will take more than 200 Ma to dissolve. The zircons analyzed in this study range from 50 – 175 µm, rarely reaching up to 250 µm

and based on evidence of water-saturation by Speight et al. (2023), zircons entrained in the rocks studied here would have dissolved geologically instantaneously unless they were preserved in some way (Harrison and Watson 1983, Watson and Harrison 1983, Boehnke et al. 2013).

3.6.1.2. New U-Pb geochronology of YGB dikes and plutons

For the twelve dated samples, a total of 1452 zircon ablations were performed, which were filtered down to 106 data points used to calculate concordant $^{207}Pb/^{206}Pb$ ages for nine of the intrusions and anchored upper intercept ages for the remaining three (Table 3-2). The large scale of this geochronology study enabled concordant Archean ages to be calculated and showed the complicated nature of Pb-Loss and inheritance. The samples that have a concordant $^{207}Pb/^{206}Pb$ age determined showed simple U-Pb isotopic systematics with only recent Pb-loss that could be mitigated by focusing on concordant data. The three samples with upper intercept ages lacked sufficient concordant data. The upper intercept ages use more data points (up to 43); however, they also all have non-zero lower intercept ages, indicating ancient Pb-loss. By anchoring the age calculation at a near-zero lower intercept age (i.e., 50 ± 50 Ma), the corresponding upper intercept age represents a minimum crystallization age. By taking a holistic approach to data collection and evaluation in this U-Pb geochronology study, the effects of inheritance and Pb-loss have been mitigated. This also aided in refining the samples that would be best for added CA-TIMS data collection.

The LA-ICP-MS and CA-TIMS $^{207}Pb/^{206}Pb$ ages of felsic intrusions from this study are shown graphically alongside a summary of YGB plutonic, volcanic, and geotectonic events in Fig. 3.12, modified from Bleeker and Hall (2007) and Ootes et al. (2011). The QZP dike was found to have the oldest $^{207}Pb/^{206}Pb$ age of 2770 ± 7 Ma, and the second oldest is an FQP dike with an age of 2746 ± 15 Ma (Table 3-2). The main cluster of ages falls between 2687 ± 8 Ma and 2629 ± 10 Ma, representing $^{207}Pb/^{206}Pb$ ages from FQP, aplite-1(a), aplite-1(b), RLP tonalite and granodiorite intrusions. The two youngest samples were found to be the Defeat Suite granite (2580 ± 27 Ma) and the Duckfish granite (2576 ± 7 Ma). However, of these samples, six were additionally analyzed by high-resolution CA-TIMS. This included two FQP dikes, the aplite-1(a) and -1(b) dikes, the QZP dike, and the RLP tonalite (Table 3-3). All samples resulted in concordant weighted mean $^{207}Pb/^{206}Pb$ ages except for the QZP dike, which returned six concordant inherited $^{207}Pb/^{206}Pb$ ages (two from one zircon fragment). The two FQP dikes returned weighted mean $^{207}Pb/^{206}Pb$ ages of 2662.07 ± 2.37 Ma and 2662.69 ± 2.37 Ma. The aplite-1(a) dike resulted in a CA-TIMS weighted mean $^{207}Pb/^{206}Pb$ age of 2662.75 ± 2.42 Ma, and the geochemically distinct aplite-1(b) dike returned a weighted mean $^{207}Pb/^{206}Pb$ age of 2661.77 ± 2.46 Ma (Speight et al. 2023). The RLP tonalite has a weighted mean $^{207}Pb/^{206}Pb$ age of 2662.26 ± 2.36 Ma. Finally, the QZP dike returned six CA-TIMS analyses (two from one zircon fragment) that are considered inherited concordant ages between 2760 and 2895 Ma. Except for the QZP dike, these CA-TIMS ages are considered the age of crystallization for the corresponding samples and the errors listed include decay constant propagation. The CA-TIMS ages are

also shown graphically in Fig. 3.12, highlighted and occurring in line with the corresponding LA-ICP-MS ages to depict the age shift using CA-TIMS. Therefore, this changes the crystallization age of the aplite dikes, tonalite, and the age range of the five FQP dikes from one at 2746 Ma and the remaining four from 2687 to 2629 Ma, to CA-TIMS $^{207}Pb/^{206}Pb$ ages of one FQP at 2746 Ma and the remaining FQP dikes range from 2674 to 2662 Ma.

Overall, the plutons are consistently younging from the tonalite to granodiorite to the Defeat Suite and Duckfish granites (Fig. 3.12). These plutons also show a correlated geochemical trend from the least to most fractionated (Speight et al. 2023). Previously, the RLP has been dated at 2675 Ma by Re-Os dating of molybdenite from a quartz vein that crosscuts the eastern margin of the RLP (Ootes et al. 2007). In this case, the previously determined RLP age correlates with the two FQP dike $^{207}Pb/^{206}Pb$ ages (2674 Ma) determined here (Fig. 3.12). The present CA-TIMS $^{207}Pb/^{206}Pb$ ages indicate that the RLP tonalite in this study has a younger crystallization age of 2662 Ma, compared to the Re-Os age of 2675 Ma, and correlates with the two FQP dike CA-TIMS $^{207}Pb/^{206}Pb$ ages of 2662 and 2663 Ma. The FQP dikes have previously been related, using geochemical characteristics, to the multi-phase RLP Speight et al. 2023). The zircon mineral chemistry data similarly suggest that the FQP dikes are related to the tonalite and granodiorite intrusions as they all share the variable negative and positive Eu anomalies (Fig. 3.10). The aplite-1(a) dikes have also been geochemically related to the RLP and their CA-TIMS age (2663 Ma) is within error of the RLP tonalite crystallization age (Speight et al. 2023).

Therefore, the FQP and aplite-1(a) dikes can be considered early to syn-plutonic intrusions genetically related to the RLP at ca. 2662 Ma. When this information is combined with petrographic and lithogeochemical evidence for protracted tectonic activity in the YGB, it suggests that structural mechanisms were occurring to allow for early melt injection of the FQP and aplite-1(a) dikes into the Kam Group volcanic pile (Speight et al. 2023).

The aplite dikes have overlapping CA-TIMS $^{207}Pb/^{206}Pb$ ages of 2662.75 ± 2.42 Ma and 2661.77 ± 2.46 Ma for the aplite-1(a) and -1(b) dike, respectively, despite having distinct chondrite-normalized REE signatures (Speight et al. 2023). However, the aplite-1(b) dikes were geochemically related to the Defeat Suite granite even though they have different ages. In this study, the Defeat Suite granite was sampled from an area east of Yellowknife (near Mason Lake) and found to have an imprecise concordant $^{207}Pb/^{206}Pb$ age of 2580 ± 27 Ma, which constitutes a minimum 55 Ma age gap between the time of aplite-1(b) dike crystallization (2662 Ma) and pluton emplacement. However, previous geochronology studies of the Defeat Suite granite yielded an age of 2628 ± 3 and 2624 ± 3 Ma, representing a minimum 31 Ma age gap between the crystallization of the aplite-1(b) dikes and Defeat Suite granite (Davis and Bleeker 1999). The aplite-1(b) dike examined in this study was sampled proximal to a western phase of the Defeat Suite granite, and the U-Pb data presented here came from Defeat Suite granite in the east. This aplite-1(b) dike may be geochemically related to the Defeat Suite granite, but there appear to be temporal differences in the western versus eastern Defeat Suite granite. Therefore, the Defeat Suite granite age determined here (2580 Ma) may represent a late phase of the

Defeat Suite granite in the eastern YGB or an unmapped member of the granitic Prosperous Suite, which has similar geochemical characteristics to the Defeat Suite and a closer age of 2596 to 2586 Ma (Fig. 3.12; Bethune et al. 1999, Davis and Bleeker 1999, Bleeker and Hall 2007, Palmer et al. 2018).

Finally, the Duckfish granite was found to have a younger age than the previously reported ages of 2608 ± 3 Ma (titanite age), and 2611 ± 7 Ma (proximal aplite Re-Os age), which does not overlap with the LA-ICP-MS determined $^{207}Pb/^{206}Pb$ age of 2576 ± 7 Ma presented here (van Breemen et al. 1992, Ootes et al. 2007). However, van Breemen et al. (1992) determined younger ages in plutons of similar lithology to the Duckfish granite, such as the Stagg granite at 2588 ± 7 Ma (within error) and the peraluminous Awry granite at 2560 ± 4 Ma (not within error and younger). The observation of other plutonic bodies of similar age suggests that plutonic activity was occurring at the Duckfish granite age determined here; however, higher resolution data could assist in determining the full temporal history of the pluton. Overall, when comparing previous U-Pb ages to results from this study, there is a trend in that the ages reported here are typically younger than previously reported. This may reflect the comparison of concordant $^{207}Pb/^{206}Pb$ ages to upper intercept ages with non-zero lower intercept ages, which indicates that the samples were affected by ancient Pb-loss (Corfu 2013).

One QZP dike was analyzed in this study but did not yield a concordant $^{207}Pb/^{206}Pb$ age, despite undergoing both LA-ICP-MS and CA-TIMS analysis. This sample also gave ambiguous lithogeochemical results, with the dike sharing characteristics of the

intermediate samples (e.g., RLP and FQP dikes) and the granitic samples (Defeat Suite granite, Duckfish granite, and aplite dikes; Speight et al. 2023). The age of the QZP dike reported in this study was determined by looking at all the LA-ICP-MS data and assessing which analyses were from inherited zircons, even if the data were concordant (Fig. 3.7A). From this, the youngest cluster of data was ca. 2763 Ma which also correlated to a group of analyses that experienced recent Pb-loss and a shift away from Concordia toward the origin (Fig. 3.7C). The QZP dike data around this age was then used to calculate an anchored upper intercept age of 2770 ± 7 Ma (Fig. 3.7D, Table 3-2). CA-TIMS analysis also did not produce a weighted mean $^{207}Pb/^{206}Pb$ age, instead yielding an array of ages from 2760 and 2895 Ma (Appendix 2, Table A2.2). The QZP dike reflects the oldest intrusion analyzed in this study, however, this contradicts the lithogeochemical signature (Speight et al. 2023). As the oldest dike, the QZP should exhibit the least fractionated geochemical characteristics, rather than the evolved signature observed. Thus, this QZP sample is likely related to an older magmatic event not presently analyzed and coincidently overlaps with the RLP, Defeat Suite, and Duckfish granite geochemical signatures.

The calculated $^{207}Pb/^{206}Pb$ ages presented here reflect zircon growth and the primary crystallization age of a rock. The range of ages obtained suggests an episodic intrusion of dikes and plutons, particularly between 2674 and 2662 Ma, which reflects the age range for seven of the twelve intrusions analyzed. Previous research has shown that multiple pulses of magmatism will have associated pulses of hydrothermal activity, suggesting that the YGB was subjected to prolonged magmatic-hydrothermal activity from 2674 – 2662

Ma (Cathles et al. 1997). Petrographic analysis of the aplite dikes in YGB by Speight et al. (2023) found evidence macroscopic evidence of volatile saturation textures in the aplite dikes, two of which were geochronologically dated here at ca. 2662 Ma.

3.6.1.3. Interpretation of lower intercept ages

Concordant U-Pb ages in zircon are the most reliable data for determining and interpreting crystallization ages in Archean rocks. However, discordant data is commonplace and may record post-emplacement processes or other geologic events. Data that fall along a Discordia line can be used to calculate an upper and lower intercept, typically representing the age of crystallization and timing of Pb-loss, respectively (Mezger and Krogstad 1997, Dickin 2018). A non-zero lower intercept age can indicate a geologic event that disturbed the data, such as ancient Pb-loss due to metamorphism, hydrothermal alteration, metamictization, or a combination of processes (Mezger and Krogstad 1997, Spencer et al. 2016, Dickin 2018, Andersen et al. 2019). All samples in this study record non-zero lower intercept ages that cannot be tied to a specific geologic event; therefore, they are attributed to ancient Pb-loss. When the lower intercept ages (i.e., the degree of ancient Pb-loss) are compared with the concordant or upper intercept ages, there is a correlation between samples found in the amphibolite domain proximal to the Defeat Suite (older lower intercept ages) than samples found within the greenschist domain. Samples taken from the greenschist metamorphic domain are less affected by the contact metamorphism, and therefore, the calculated upper intercept ages are more representative of a crystallization age. This metamorphic aureole has been directly linked

to the intrusion of the Defeat Suite granite (Thompson 2006). The contact metamorphism occurring at the time of Defeat Suite emplacement created conditions for Pb-loss and the recrystallization of metamict domains in zircons at 600 – 650°C, leading to localized partial Pb-loss at these conditions (Mezger and Krogstad 1997, Thompson 2006). Pb-loss below these conditions and temperatures is more likely related to hydrothermally mediated Pb-leaching from a metamict grain (Mezger and Krogstad 1997). The non-zero lower intercept ages can be explained by local hydrothermal alteration of zircon grains or, more likely, by the contact metamorphic overprint associated with intrusion of the Defeat Suite granite (Thompson 2006). Therefore, future geochronology studies should use caution when sampling within the amphibolite and transitional metamorphic domains and mitigate the effects of ancient Pb-loss.

3.6.1.4. Zircon inheritance and the Chan Formation

When inherited zircons are present within a sample, probability density plots show a multi-peak distribution of $^{207}Pb/^{206}Pb$ ages, aiding in the data filtering process. These ages can then be avoided during the data analysis and calculation of a concordant crystallization age. Of the 1452 LA-ICP-MS zircon analyses, zircon inheritance was only observed in two samples, the Defeat Suite granite and QZP dike, with ages older than 2800 Ma (Fig. 3.6J and Fig. 3.7A). The Defeat Suite granite contained zircons indicating inheritance, with only two analyses having $^{207}Pb/^{206}Pb$ ages >3000 Ma after data were filtered to > 50% concordance. The two inherited age peaks are located at ca. 3600 and 3800 Ma (Fig. 3.6J, inset). These ages either reflect zircons entrained during magma

ascent through the CSBC (ca. 3325 Ma), assimilated from the CSBC after emplacement of the Defeat Suite granite, or zircons were sourced from the nearby Acasta Gneiss Complex (Bleeker et al. 1999a, Bauer et al. 2017). The Acasta gneiss was found to have zircon ages older than 4000 Ma, and material from these basement rocks may have been assimilated and entrained in the Defeat Suite (Reimink et al. 2016, Bauer et al. 2017).

The probability density plot of the QZP dike LA-ICP-MS data showed three ages peaks at 2763 Ma, 2903 Ma, and >3000 Ma (Fig. 3.7A). The first age is considered most representative of the crystallization age, while the second age represents a mixture between the youngest and oldest peaks and correlates with the calculated concordant age of 2909 Ma (Fig. 3.7B). The concordant age calculated from the QZP represents a mixed-age calculation from the 3398 Ma inheritance to the younger age cluster of 2763 Ma. The CA-TIMS data yielded six ages for the QZP dike from four zircons and two from fragments of one zircon (Table 3-3 and Appendix 2, Table A2.2). Of the CA-TIMS data, five of the ages are considered inherited, including 2822, 2842, 2887, 2894, and 2895 Ma (Fig. 3.7D). When these ages are considered within the context of the larger LA-ICP-MS dataset, it becomes clear that they are inherited ages. The youngest CA-TIMS age was 2761 Ma, which correlates with the youngest age peak observed in the LA-ICP-MS data (2763 Ma) and supports the interpretation that data around this age peak can be used to calculate an upper intercept age, in this case, 2770 Ma (Fig. 3.7D).

The abundant concordant inherited ages observed in the QZP dike suggests an interaction with the underlying basement rocks. The CSBC, dated at 3325 ± 8 Ma, and the

Central Slave Cover Group (CSCG) ranging from 2743–2924 Ma, overlaps with the inherited ages observed and the age of the QZP and oldest FQP dike from this study (Isachsen and Bowring 1994, Bleeker et al. 1999a, 1999b, 2004, Ketchum and Bleeker 2000). The QZP dike upper intercept age of 2770 ± 7 Ma and the FQP dike age of 2746 ± 15 Ma are considered minimum ages of crystallization and broadly overlap with the age of the CSCG, between 2743 and 2924 Ma. Both dikes were sampled from the base of the Kam Group within the Chan Formation, and proximal to the Duckfish granite. The QZP and FQP dike were sampled 660 and <100 m from the Duckfish granite, respectively. The Chan Formation was previously considered to have no datable lithologies present, however, these cross-cutting dikes may provide an opportunity to obtain a minimum age for the Chan Formation (Isachsen and Bowring 1997). The Kam Group is interpreted to have an age of 2722 to 2710 Ma, corresponding to an age of 2722 Ma for the Chan Formation as it is the lowermost member of the Kam Group (Isachsen 1992). The QZP and FQP dikes are both older (2770 and 2746 Ma) than this by at least 21 Ma. This suggests that there was either a significant period of volcanic inactivity between the deposition of the Chan and Crestaurum Formations of the Kam Group, or these dikes are related to an older magmatic event. Previous research has debated whether the Chan Formation should instead be a member of the CSCG; the age of the cross-cutting QZP and FQP dikes suggests this as well (Cousens et al. 2006b).

3.6.2. Zircon mineral chemistry link between YGB dikes and plutons

Data collection in this study focused on maintaining the temporal context of zircon mineral chemistry by collecting data alongside U-Pb geochronology. Therefore, we can compare zircon mineral chemistry to the age of a sample and evaluate geochemical changes through time. This was facilitated by filtering the zircon mineral chemistry by crystallization age, in this case using the age and error determined by LA-ICP-MS or CA-TIMS when available (Table 3-4). Zircon mineral chemistry reflects the magma as zircons were crystallizing and record changes in the magmatic evolution of an intrusion (Watson and Harrison 1983, Hoskin and Ireland 2000, Poller et al. 2001, Ballard et al. 2002, Hoskin and Schaltegger 2003, Hoskin 2005, Fu et al. 2009, Gagnevin et al. 2010, Claiborne et al. 2010, Trail et al. 2012, Boehnke et al. 2013, Dilles et al. 2015, Smythe and Brenan 2016, Rubatto 2017, Buret et al. 2017, Siégel et al. 2018, Ni et al. 2020, Sheikh et al. 2020, Chen et al. 2021). For example, an evolving magmatic system would show systematic changes in Th/U, Hf, and Eu/Eu* due to fractionation processes. Zircon mineral chemistry from this study is shown with respect to age, and these changes can be observed (Fig. 3.8).

The zircon mineral chemistry of the QZP is found as an outlying group compared to the remaining samples. For instance, the QZP Th/U ratio is lower (<0.39), and the Hf concentration (1.1 – 1.5 wt. %) is higher than the rest of the suite, which have Th/U of 0.23 – 2.5 and 0.71 – 1.3 wt. % Hf (Fig. 3.8A-B). As the oldest sample in the group, the QZP should have the highest Th/U ratio and the lowest Hf concentrations if it were part of the same magmatic suite as the RLP, Defeat Suite or Duckfish granite. The lithogeochemical

data also suggests that the QZP dikes are some of the most evolved samples in this data set (Speight et al. 2023). However, if the QZP dike is from a different and older magmatic system, this could explain the evolved Hf signature. When comparing the REE concentrations, the FQP, QZP, tonalite, and granodiorite were found to have similar profiles with negative and positive Eu anomalies while the aplites and granites show corresponding REE profiles and only negative Eu anomalies; these groupings are also found in the whole-rock geochemistry of Speight et al. (2023). This once again suggests that there is a relationship between the FQP, tonalite, granodiorite and, in this case, the coincidental similarity of the QZP dike.

The expected zircon REE profile would consist of a steeply increasing REE signature where the HREE >>LREE and possible Ce and Eu anomalies (Hoskin and Schaltegger 2003). There are several reasons why zircon mineral chemistry may show a positive Eu anomaly on a chondrite-normalized REE diagram. A positive Eu anomaly could be explained by: 1) zircon saturation occurring before plagioclase crystallization; 2) the melting and assimilation of plagioclase crystals; 3) the alteration of zircons and addition of LREE (Hoskin and Ireland 2000, Poller et al. 2001, Hoskin and Schaltegger 2003). In this case, the variable positive Eu anomalies may be due to local changes in magma chemistry, due to crustal assimilation or zircon saturation occurring before plagioclase crystallization since the mineral chemistry data were collected from the least altered and inclusion-free parts of the zircons and zircon temperatures are above the hydrothermal threshold.

Therefore, caution should be taken when analyzing small zircon datasets as they may underrepresent the range in mineral chemistry values.

3.6.3. FQP connection to the Banting Group and Townsite Formation

A previous study by Cousens et al. (2002) focused on the geochemistry of the Banting Group and attempted to establish a connection between the calc-alkaline Banting Group volcaniclastics and the multiple generations of porphyritic dikes that crosscut the Kam Group. The unconformable contact between the Kam and Banting Group is an obstacle to observing the relationship directly. Previous work by Cousens et al. (2002) determined that the "#9" dikes were of Banting Group age and geochemically and isotopically the same as the Banting Group felsic volcaniclastics. The multiple generations of "#9" dikes represent the FQP, QZP, and aplite dikes examine in this study. The question that remained was whether all generations of "#9" dikes are related to the Banting Group and confirming whether they are sourced from a marginal phase of the Defeat Suite granite in the Ryan Lake area. The current work by Speight et al. (2023) determined that the FQP and aplite-1(a) dikes are geochemically related to the tonalitic and granodioritic RLP, the aplite-1(b) dikes are related to the Defeat Suite granite, and the aplite-2 dikes are related to the Duckfish granite. The QZP dikes geochemically overlap with the RLP and Defeat Suite granite, however, they are geochronologically associated with an unknown older magmatic phase. The two ages determined for the Banting Group are 2662 ± 3 Ma and 2664 ± 1 Ma, with one sample containing zircons with inherited cores of more than 2700 Ma (Isachsen 1992, Isachsen and Bowring 1994). These ages fall within the ages provided

here and most closely link to four of the FQP and aplite-1(a) ages of 2674-2662 Ma and 2663 Ma, respectively.

When the geochemistry of these samples is compared to the Banting volcaniclastics and RLP samples from Cousens et al. (2002), the Banting Group consistently plots with the intermediate rocks (FQP, tonalite, granodiorite) of this study (Fig. 3.13; Speight et al. 2023). Specifically, there is a geochemical correlation between the calc-alkaline Banting Group rocks and the FQP dikes, tonalite, and granodiorite of this study. For example, when plotted together on an AFM diagram, the Banting Group mafic flows and gabbros plot in the tholeiitic field and trend towards the intermediate rocks of this study, which overlap with the Banting volcaniclastics and all but one RLP sample (Fig. 3.13A; Cousens et al. 2002). The Defeat Suite and Duckfish granite samples, along with the aplites and QZP, plot in a separate group and are the most evolved of this sample set. Although the samples follow a linear path on the AFM diagram, the Zr/Hf ratio can be used to discern two populations of samples; one with the Banting volcaniclastics (highlighted in yellow) and the intermediate samples of this study which plot separately from the granitic samples and QZP dikes (highlighted in grey; Fig. 3.13). Various trace elements that typically show linear fractionation trends, such as TiO_2, Th/U, Ce/Ce*, and Eu/Eu*, were plotted against the whole-rock Zr/Hf ratio of the samples (Fig. 3.13B-E). The Banting Group samples are highlighted in each plot and show the geochemical correlation between the FQP, tonalite, granodiorite, and the overlying Banting Group volcaniclastics. Combined with the geochronologic data presented in this study, the Banting Group

volcaniclastics can be geochemically and geochronologically linked specifically to FQP feeder dikes and the tonalite and granodiorite phases of the RLP. Although the aplite-1(a) dikes were also found to have the same age as the younger FQP dikes, the RLP tonalite, and the Banting Group volcaniclastics, they are not considered to be feeder dikes to the Banting Group based on their spatial extent within the YGB. At this time, aplite dikes were only observed at the base of the Kam Group, up to 780 m from the margin of the RLP and Defeat Suite granite (Speight et al. 2023).

Cousens et al. (2002) determined that the Townsite Formation, a calc-alkaline felsic volcaniclastic unit within the Kam Group, formed by assimilation and fractional crystallization compared to the Banting Group felsic volcaniclastics, which they considered to have a depleted upper mantle signature with signs of crustal contamination. Their suggestion that the RLP, "#9" dikes, and Banting volcaniclastics are related is confirmed here and refined with the presentation of this data, indicating that only the FQP dikes are feeders to the Banting Group. The FQP dikes may also be feeders to the Townsite Formation within the Kam Group, a unit dominated by calc-alkaline felsic to intermediate volcaniclastics (Cousens 2000, Finnigan 2000). Fig. 3.13 also shows data related to the Townsite Formation, and it is found to consistently overlap with the FQP and RLP samples from this study and the historic Banting Group geochemistry (Cousens 2000, Finnigan 2000, Cousens et al. 2002). The FQP dikes have a range of ages, and one sample has an age of 2746 ± 15 Ma, which is within error of the Kam Group at 2722–2710 Ma (Isachsen 1992). Field relationships also indicate that the FQP dikes are feeders to the

Townsite Formation as one dike was observed cross-cutting mafic volcanic flows and transitioning to a felsic volcaniclastic tuff of the Townsite Formation (Fig. 3.14, inset). Therefore, the FQP dikes could represent an early suite of dikes that were feeders to the Townsite Formation as the supracrustal rocks of the Kam Group were deposited. There are geochemical and petrographic similarities in the Townsite and Banting volcaniclastics, and the data presented here suggests that the FQP dikes are feeders to both units at different times (i.e., ca. 2674 Ma and 2662 Ma). Thus, the calc-alkaline Townsite Formation represents an older precursor of the Banting Group (Cousens 2000, Finnigan 2000, Finnigan and Duke 2006).

3.6.4. The magmatic plumbing system of the YGB dikes, plutons, and related volcaniclastic rocks

The FQP dikes represent feeders from a rising magma, the RLP, that was impeded during ascent at the base of the Kam Group (Fig. 3.14). This is schematically depicted in Fig. 3.14, which illustrates the emplacement of the RLP, FQP dikes, aplite-1(a) dikes and their relationships to the Townsite Formation and Banting Group at ca. 2662 Ma. This may have caused melting and assimilation of either basaltic rocks of the Kam Group and/or feldspars from the CSBC; assimilation of feldspars from these rocks would have added Eu to the RLP magmatic system. This Eu addition is observed in the variably positive Eu anomalies in the zircon mineral chemistry of the FQP dikes, tonalite, and granodiorite (Fig. 3.14). The FQP dikes were periodically emplaced during the development of the YGB volcanic pile between 2746 Ma (one sample) and 2674 to 2662 Ma (four samples). The

geochemical and age correlations between the dikes and both the Townsite Formation and Banting Group suggests that this magmatic system was evolving with little to no new magma input, and the FQP dikes are feeders to both units (Fig. 3.14; Speight et al. 2023). The aplite-1(a) and -1(b) dikes were observed proximal to the RLP and Defeat Suite granite margins, although only the aplite-1(a) dikes were observed crosscutting the tonalite and granodiorite of the RLP (Fig. 3.14). Both sets of aplite dikes have CA-TIMS ages within error at 2663 and 2662 Ma. The geochronologic and lithogeochemical evidence of the aplite-1(b) dike infers that the related parental pluton, the Defeat Suite granite, was present and active as a separate magmatic body at that time (ca. 2662 Ma). This has been depicted in Fig. 3.14, with the corresponding field relationships shown. The previously reported geochemical links between the respective dikes and plutons by Speight et al. (2023), as well as the new U-Pb geochronology presented here, suggest that two distinct plutonic bodies were emplaced at the base of the Kam Group (Fig. 3.14). Solidifying the relationship between the multi-phase RLP, FQP dikes, and Banting Group establishes this area as an ancient volcanic center. Banting Group-related volcanism is now temporally associated with the onset of tectonic activity linked with D_1 deformation, which has been bracketed between 2660 and 2630 Ma, based on the intrusion and age of the Defeat Suite granite (Davis and Bleeker 1999, Martel and Lin 2006, Bleeker and Hall 2007). The onset of D_1 deformation at ca. 2660 Ma correlates with the ages of the FQP dikes, aplite-1(a) and -1(b) dikes, and RLP tonalite from this study. This early deformation event could have

structurally initiated emplacement of the syn-volcanic aplite dikes and FQP feeders to the overlying volcaniclastic rocks.

The active magmatic plumbing system of these plutons and dikes at 2662 Ma suggests that both the RLP and Defeat Suite granite were present as crystal mushes with >70 % crystallization (Hibbard 1980, Carter et al. 2021, Speight et al. 2023). The previous petrographic analysis of the aplite dikes by Speight et al. (2023) showed evidence of aplite dike emplacement at various stages of pluton crystallization, although all dikes must have emplaced after 70% crystallization of the parental pluton. The results also indicated that many of the aplite-1(a) and -1(b) dikes showed textural evidence of volatile-saturation, based on observed quartz cores and pods noted throughout the aplite dikes (Speight et al. 2023). Since the aplite-1(a) dikes have been geochemically and geochronologically linked to the multi-phase RLP, it suggests that the RLP itself was also volatile-saturated at the time of emplacement. These aplite dikes, along with the FQP dikes, showed a lack of sulfide or ore minerals during petrographic analysis, despite being locally spatially associated with gold mineralization (Finnigan and Duke 2006, Hubbard et al. 2006). Therefore, we suggest that the FQP and aplite dike magmatic plumbing system reflects only physical conduits for magmatic-hydrothermal fluids, based on data available at this time (Carter et al. 2021, Speight et al. 2023).

3.7. Conclusions

This study aimed to contribute to the overall understanding of the magmatic history in the YGB by taking a multi-analytical approach to examining the geochemical and

geochronological relationships of YGB dikes and plutons. The multi-generational "#9" dikes were examined to distinguish them and identify their parental plutons in a regional context temporally and geochemically. This investigation has led to the following conclusions:

I. Evaluating larger LA-ICP-MS datasets of Archean magmatic zircons helps provide sufficient data to assess the degree of Pb-loss and inheritance in a sample, while still obtaining meaningful ages. However, when closely timed intrusions are being examined, higher resolution CA-TIMS can yield the temporal resolution necessary for determining dike-pluton relationships. In this case, half of the CA-TIMS ages were within error of initial LA-ICP-MS ages. Therefore, this technique can be utilized as a first pass to determine general timing relationships, with the later addition of CA-TIMS data to fully resolve magmatic events. Future geochronology studies in the YGB should avoid or take caution when sampling within the amphibolite domain near the Defeat Suite granite due to increased ancient Pb-loss, compared to rocks from the greenschist domain.

II. The LA-ICP-MS data indicates that the YGB was subjected to the frequent intrusion of magmatic bodies from 2770 to 2576 Ma. The main group of intrusions related to the RLP were emplaced between 2674 to 2662 Ma, with a pronounced age peak at 2662 Ma obtained from high-resolution CA-TIMS analysis. The FQP dikes of this study show a broad range of ages from 2746 to 2662 Ma.

III. The “#9” dikes were effectively distinguished and linked to a parental pluton using geochemical and geochronological data. The QZP dikes were geochronologically distinguished, however, the geochemical data was ambiguous and could not be linked with a regional pluton from this study. The results indicate there is a genetic link between the FQP, aplite-1(a) dikes, tonalitic and granodioritic RLP, between the aplite-1(b) dikes and Defeat Suite granite, and the aplite-2 dikes and Duckfish granite. These dikes represent early to syn-volcanic intrusions of their respective parental plutons. This interpretation is also supported by the zircon mineral chemistry signatures of each group.

IV. The U-Pb geochronology data of the Defeat Suite granite presented here suggests that there may be differences in the timing between Defeat Suite found in the western area of the YGB versus the eastern portion of the belt. However, this may reflect the available LA-ICP-MS data, as the age determined for the Defeat Suite granite was 2580 ± 27 Ma. Further CA-TIMS data on Defeat Suite granite samples from the east and west could be compared to establish this relationship and determine whether different phases of the Defeat Suite granite are present.

V. The QZP dike sampled in the northern area of the YGB is the oldest dike identified in this study, with an interpreted crystallization age of 2770 ± 7 Ma, but also geochemically evolved. This dike likely reflects magmatism older than the Kam Group that was not examined in this study. It has been suggested that the Chan Formation, the lowermost member of the Kam Group, may be part of the CSBC.

The QZP dike discussed here was sampled from the Chan Formation, has a different geochemical trend compared to the YGB intrusions studied here, and is the oldest sample dated. The oldest FQP dike (2746 Ma) was also sampled from this area, which together suggests that this area could be related to the Central Slave Cover Group instead of the Kam Group.

VI. Local variations in magma chemistry were recorded as zircons crystallized and are reflected in the wide range of trace element data, particularly the REE and the Eu anomaly. The Eu anomaly was found to be both positive and negative in the FQP dikes, QZP dike, tonalite, and granodiorite, reflecting either zircon saturation before plagioclase crystallization or assimilation of the plagioclase-rich mafic volcanic flows of the Kam Group.

VII. The CA-TIMS ages indicate that two sets of dikes, those related to the RLP (FQP and aplite-1(a) dikes) and the Defeat Suite granite (aplite-1(b) dikes) share a crystallization age of 2662-2663 Ma. This suggests that a magma reservoir related to the RLP, and Defeat Suite granite were present at this time, approximately 30 Ma before the oldest Defeat Suite granite age. These intrusions may have led to sustained magmatic-hydrothermal activity initiated at the onset of D_1 deformation that has been previously bracketed to 2660 and 2630 Ma. The U-Pb ages, lithogeochemistry, and field relationship data presented here shows that the FQP dikes are feeders to both the calc-alkaline Townsite Formation within the Kam Group and the overlying calc-alkaline Banting Group. Therefore, the RLP and

associated magmatic plumbing system established an ancient volcanic center related to the Banting Group within the YGB. The FQP and aplites dikes associated with this magmatic plumbing system reflect fluid conduits for magmatic-hydrothermal activity.

The data presented here indicate that at least two magma chambers related to the RLP, and Defeat Suite granite were present at ca. 2662 Ma. Further radiogenic isotope analysis of zircons could shed light on these magma reservoirs. *In-situ* analysis of zircons would provide added textural context to future geochronological studies and interpretations. Further exploration for the older FQP dikes would assist in clarifying their relationship to the Townsite Formation. High-resolution CA-TIMS data could refine the apparent temporal disagreement between Defeat Suite granite found in the western versus eastern YGB. Finally, a more extensive study of the rocks proximal to the Duckfish granite, including the QZP dikes, could assist in determining their relationship to the CSBC and CSCG, which would add to our understanding of the YGB stratigraphy.

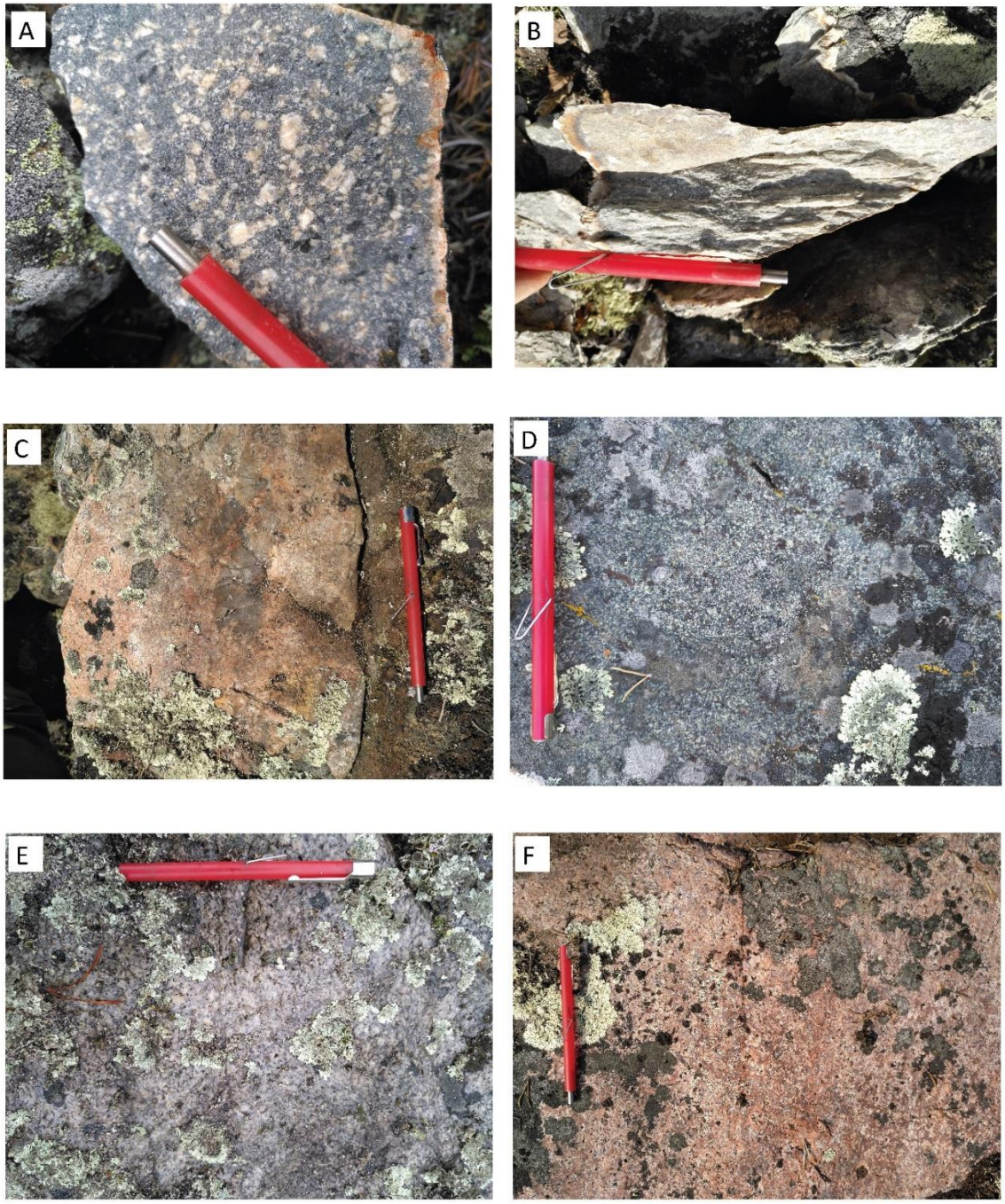
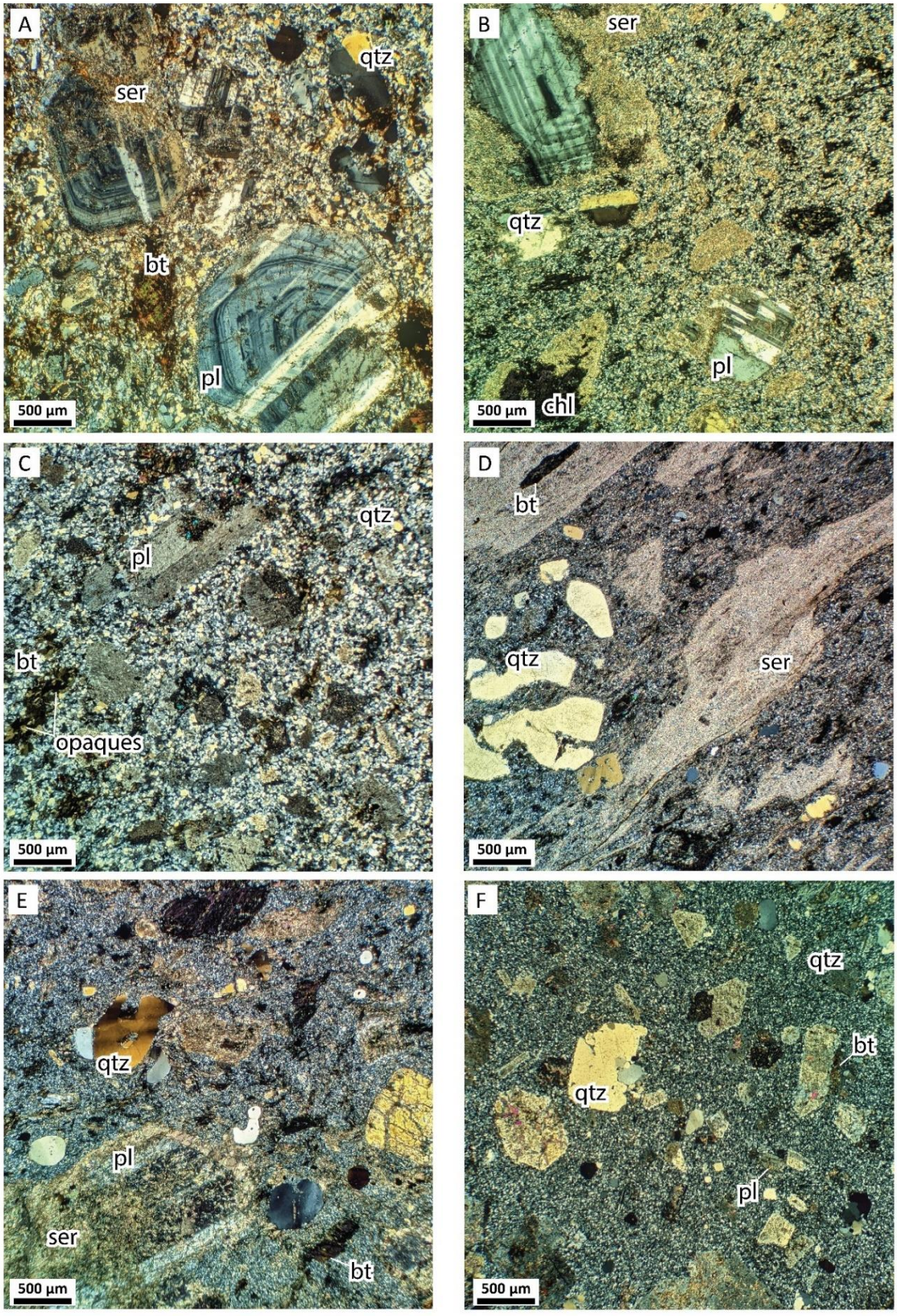
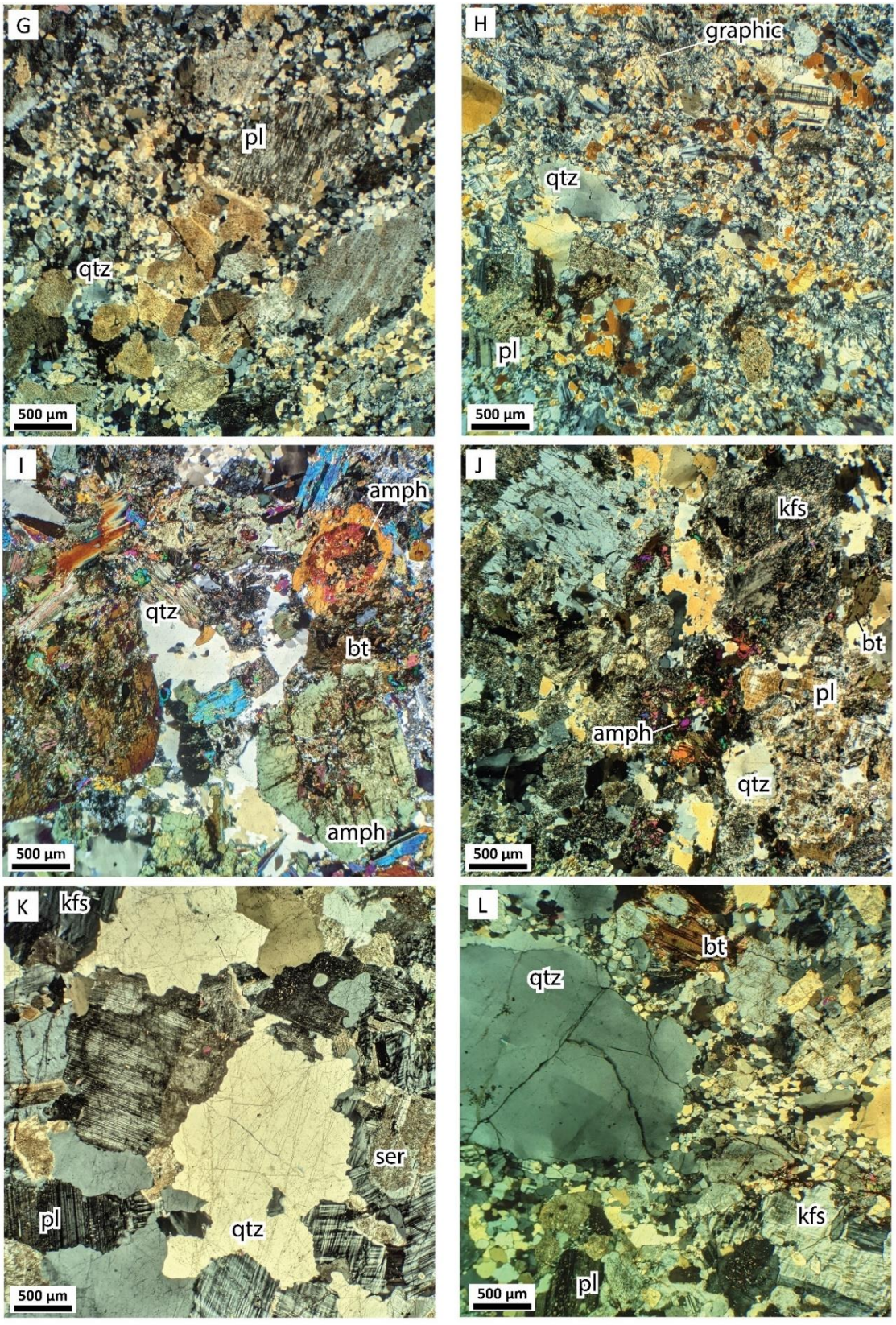


Fig. 3.1: Field and hand sample images of representative lithologies, including (A) feldspar-quartz porphyry, (B) quartz porphyry, (C) aplite-1(a) dike (mineralogically similar to aplite-1(b), (D) tonalite, (E) granodiorite, and (F) granite (Duckfish Granite shown here, comparable to Defeat Suite). See text for description of each lithology. Pen magnet for scale.

Fig. 3.2: *Following two pages*. Petrographic images of polished thin sections from each lithology, including (A-E) feldspar-quartz porphyry, (F) quartz porphyry, (G-H) aplite-1(a), (I) tonalite, (J) granodiorite, (K) Defeat Suite granite, (L) Duckfish granite. An image from each sample is shown to illustrate the variety of textures observed, varying degrees of alteration, dominant mineralogy, and magmatic textures. Amph = amphibole, bt = biotite, chl = chlorite, kfs = K-feldspar, graphic = graphic texture, opaques, pl = plagioclase, qtz = quartz, ser = sericite.


A
qtz
ser
bt
pl
500 µm
B
ser
qtz
pl
chl
500 µm
C
qtz
pl
bt
opaques
500 µm
D
bt
qtz
ser
500 µm
E
qtz
pl
ser
bt
500 µm
F
qtz
bt
qtz
pl
500 µm


G
pl
qtz
500 µm
H
graphic
qtz
pl
500 µm
I
amph
qtz
bt
amph
500 µm
J
kfs
bt
pl
amph
qtz
500 µm
K
kfs
ser
pl
qtz
500 µm
L
bt
qtz
kfs
pl
500 µm

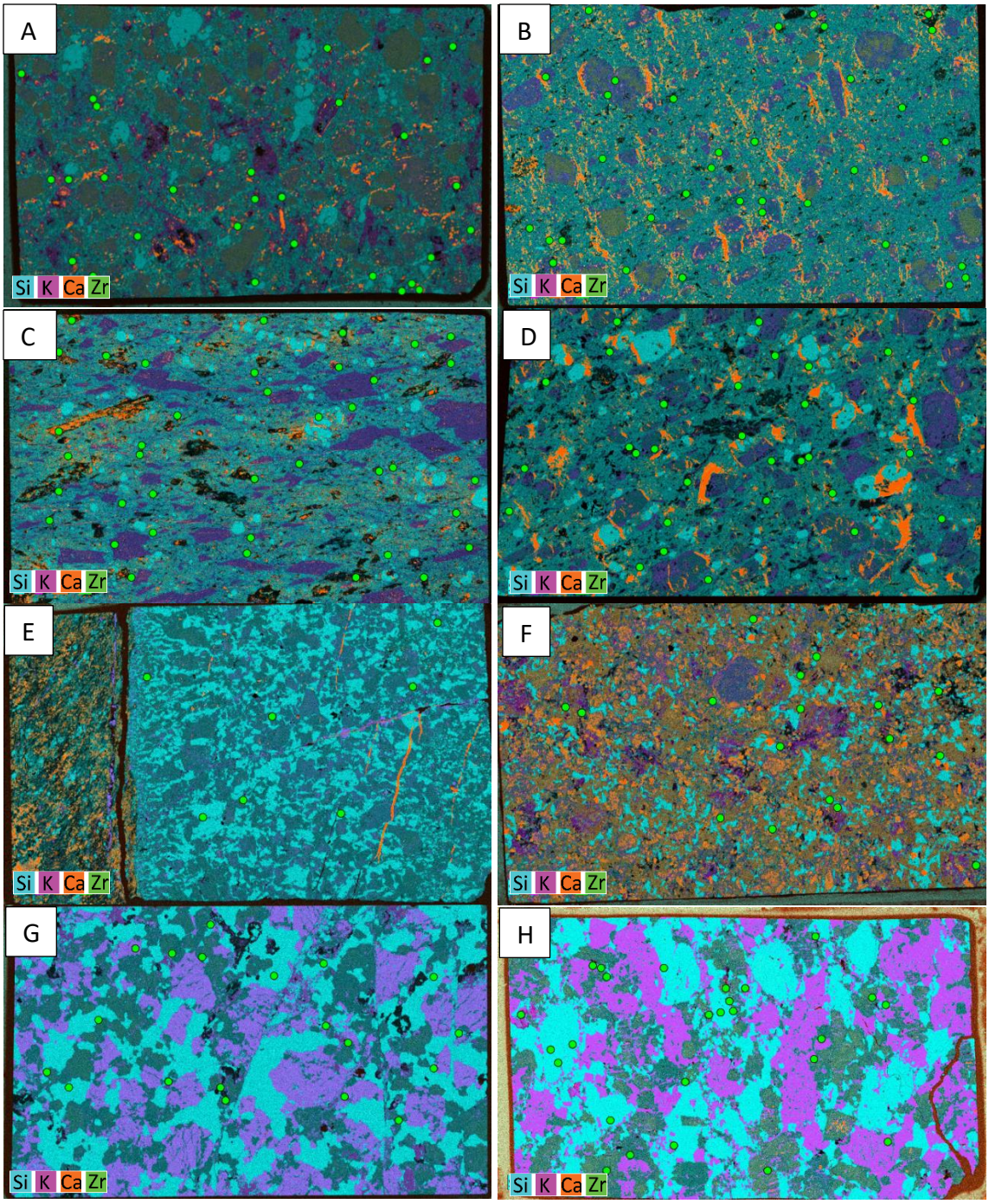


Fig. 3.3: Multi-element µXRF images of standard polished thin sections that are 27x46 mm. A-D) feldspar-quartz porphyry, E) aplite-1(a), F) tonalite, G) Defeat Suite granite, H) Duckfish granite. The corresponding colour and element and image colour are shown in the bottom left of each image, with zircon locations highlighted by enlarged green circles. Where more than one element is present in a mineral, the colours shown are additive.

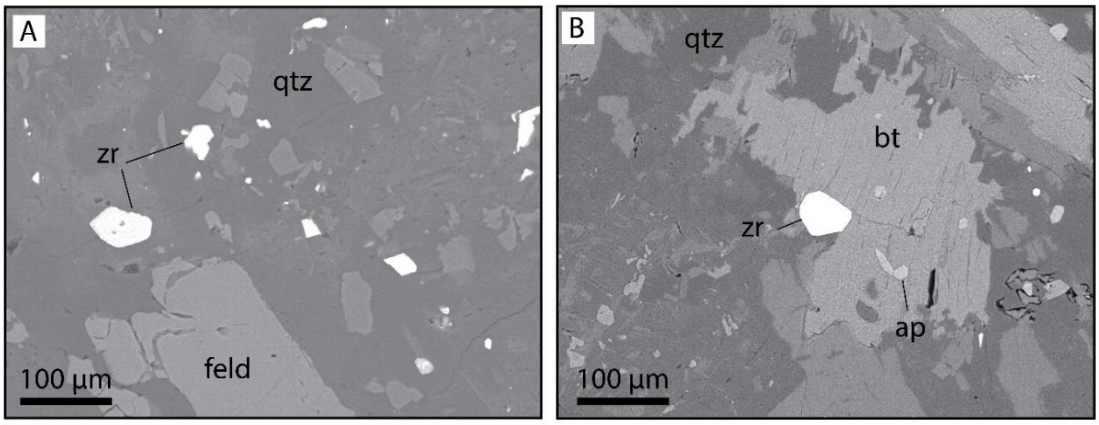


Fig. 3.4: SEM-BSE of *in-situ* zircon grains in polished thin sections, showing their relative locations and associated mineralogy. Both examples shown are from the RLP, however (A) shows the inclusion of subhedral zircons in quartz, while (B) shows anhedral, rounded zircon along the margin of biotite. Ap = apatite, bt = biotite, feld = feldspar, qtz = quartz, zr = zircon.

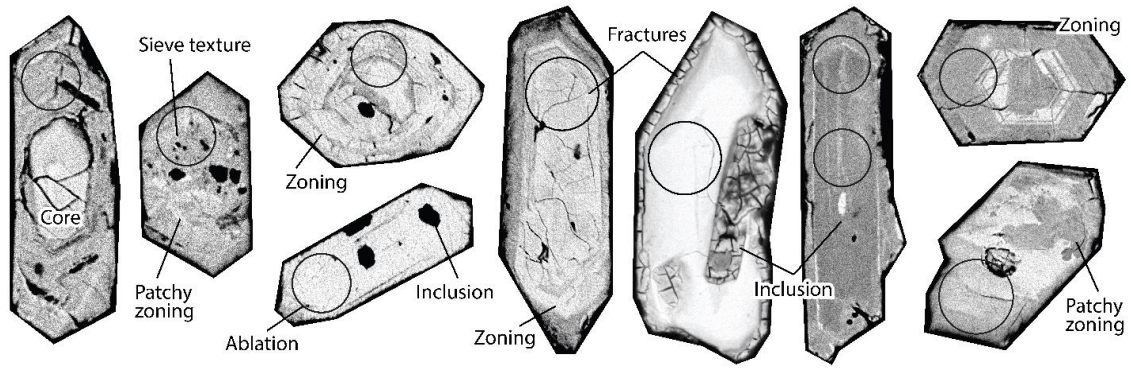


Fig. 3.5: A selection of SEM-EDS back-scatter electron images that have been contrast-adjusted to highlight the internal structures of zircons, including oscillatory zoning, irregular and patchy zoning, fractures, inclusions, inherited zircon cores, and sieve texture. These zircons also show the corresponding 24 µm ablation for scale and illustrate the challenges of analyzing undisturbed domains.

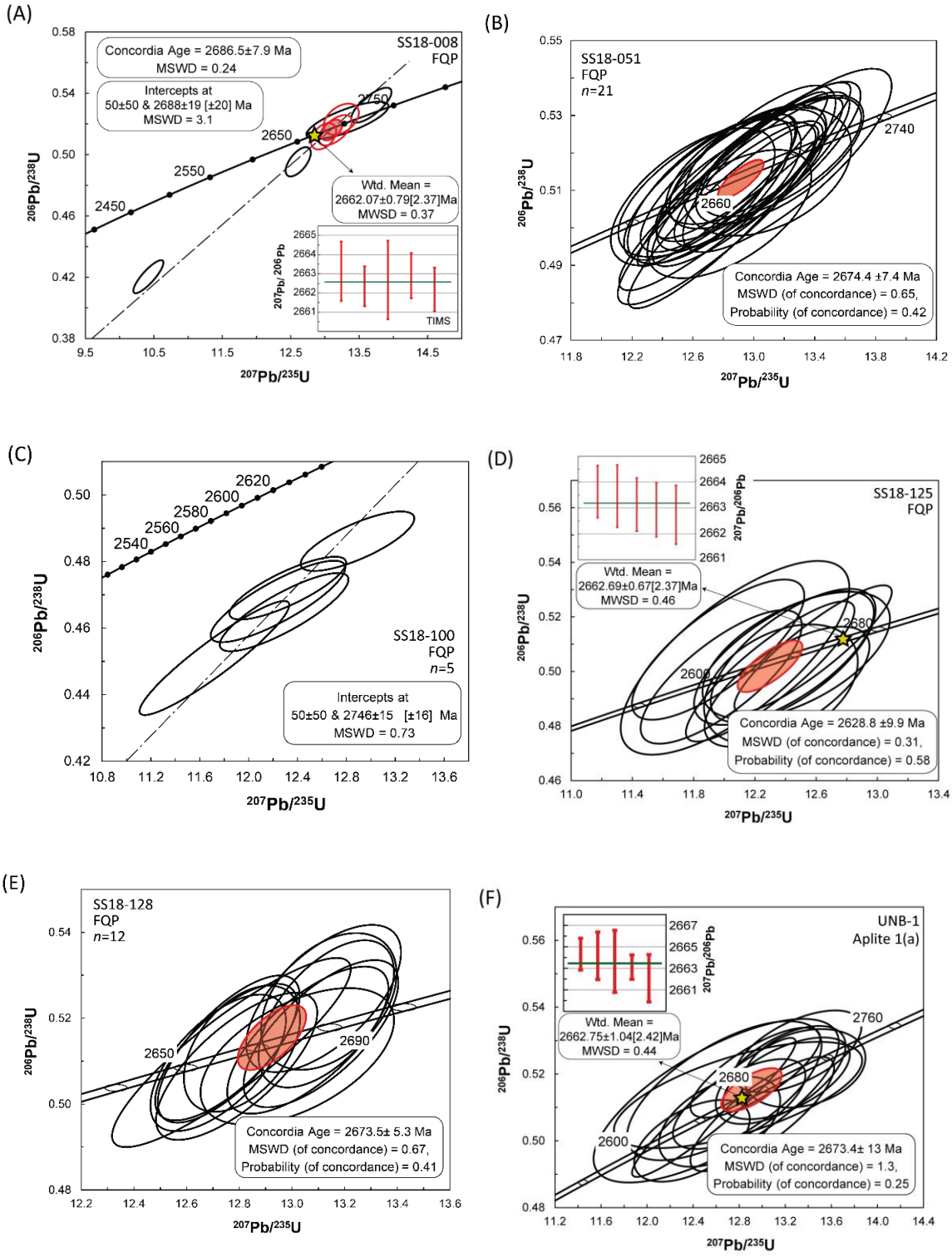


Fig. 3.6: Concordia diagrams of U-Pb data from YGB intrusions. Each figure indicates the sample's calculated age, using data with no ^{204}Pb-correction, <5% normal and reverse

discordance for Concordia ages, and >50% concordance for upper intercept ages (anchored at 50 ± 50 Ma). A-E) Feldspar-quartz porphyry, F) aplite-1(a), G) aplite-1(b), H) tonalite, I) granodiorite, J) Defeat Suite granite, K) Duckfish granite. Probability density plot insets are shown for samples with inheritance; the main age and inherited age peaks are indicated. *n* = the number of data points. Red ellipses indicate LA-ICP-MS data used to calculate the concordant age shown in A, F, G, and J (compared to the upper intercept age calculation); errors are 2σ and include decay-constant errors. CA-TIMS data were collected for select samples and weighted mean $^{207}Pb/^{206}Pb$ ages (Wtd. Mean) were calculated and added to the corresponding Concordia diagram; errors are 2σ and also shown with the propagation of decay constant errors in brackets.

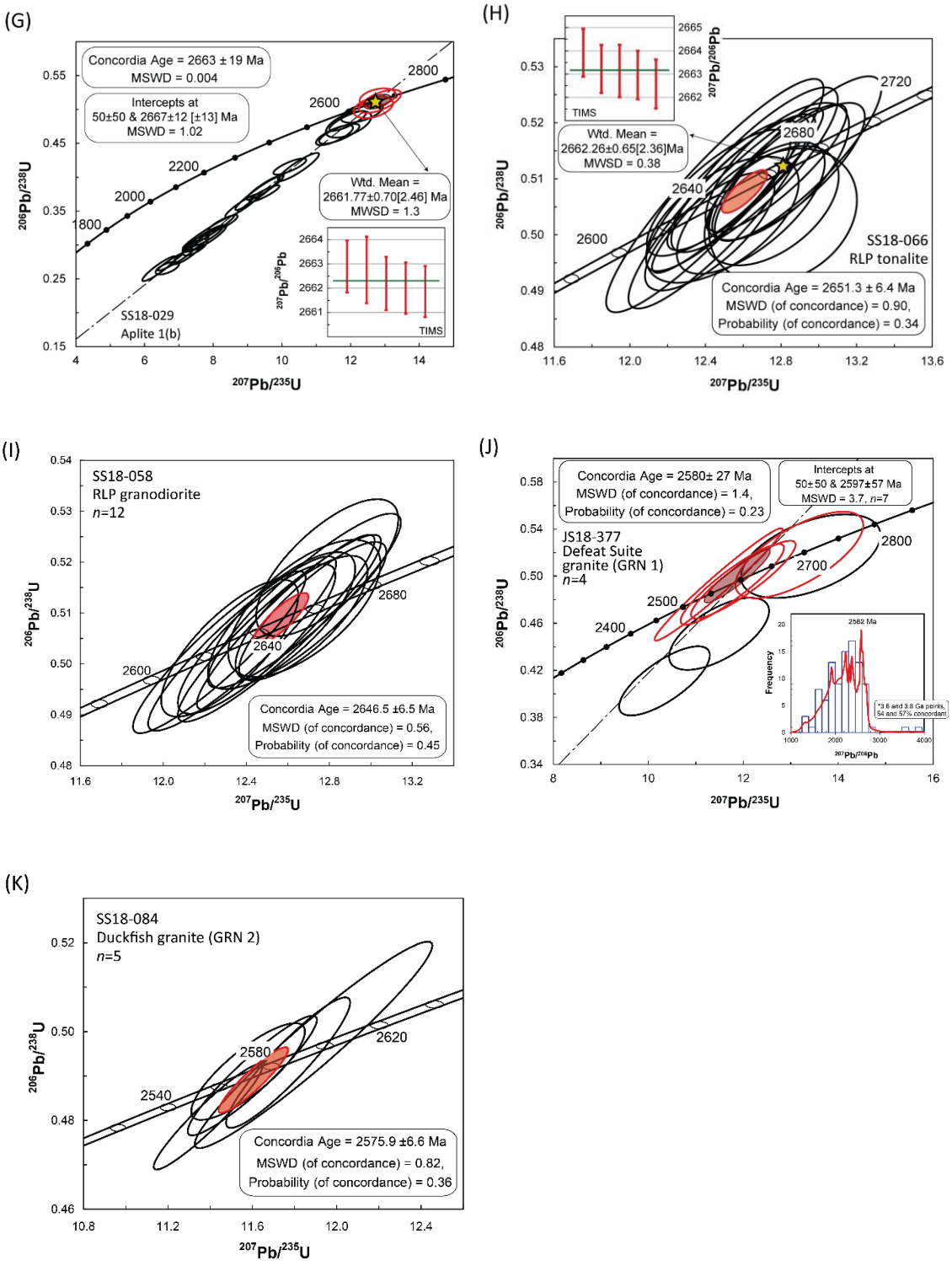


Fig. 3.6: *Continued*.

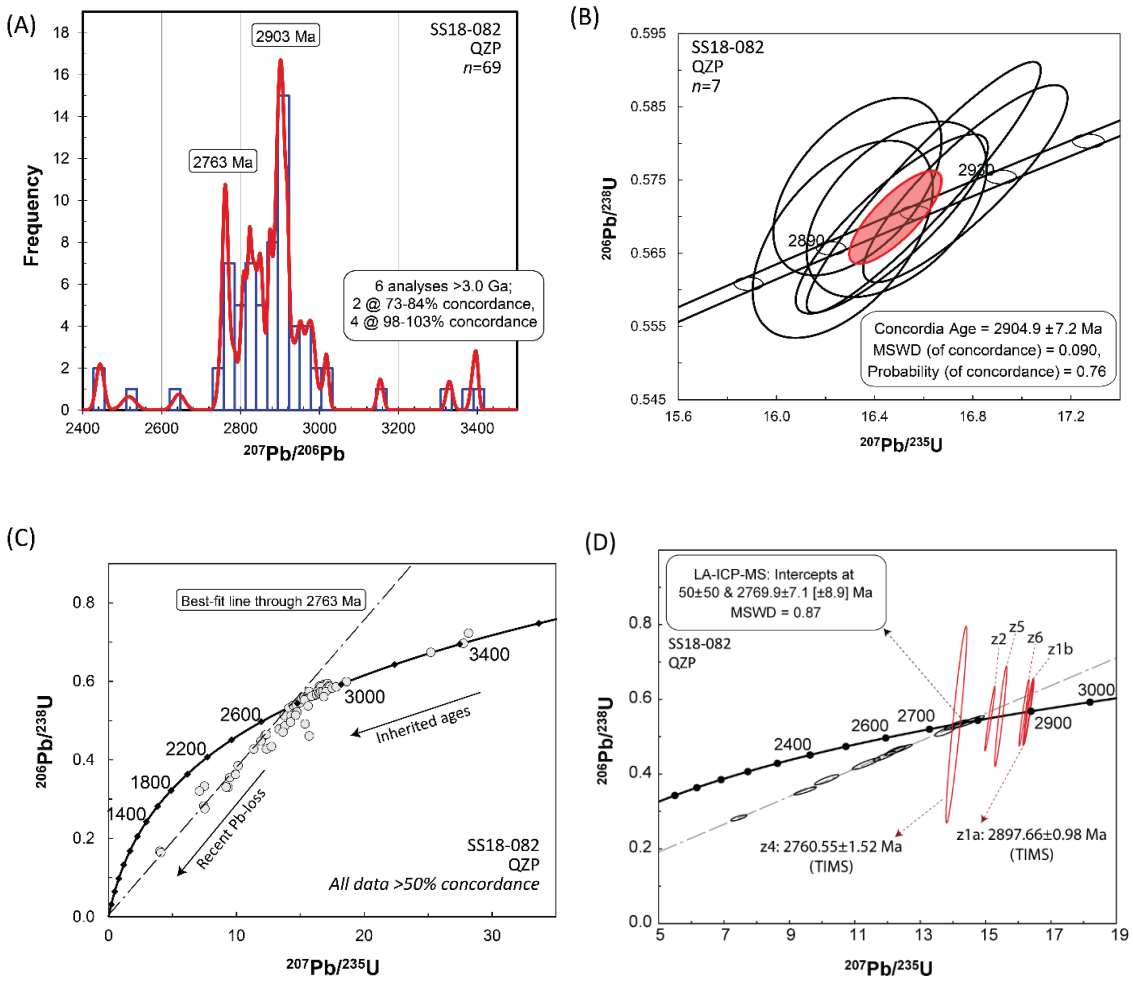


Fig. 3.7: U-Pb isotopic data for QZP sample SS18-082. All ages were calculated with data that required no ^{204}Pb-correction and have > 50% concordance. A) Probability density plot showing the dominant age peaks at 2763 and 2903 Ma, and 6 inherited ages > 3.0 Ga. B) Concordia diagram showing a concordant age reflecting one age cluster representing a mix between inherited and crystallization ages. C) Concordia diagram showing all data with > 50% concordance and a best-fit line through 2763 Ma, representing the interpreted crystallization age. D) Concordia diagram showing the upper intercept age calculation related to the age cluster around 2763 Ma, anchored at 50 ± 50 Ma with additional TIMS data added; red ellipses represent individual zircon fragment analyses where z1a and z1b are fragments from the same grain. The youngest and oldest TIMS weighted mean ^{207}Pb/^{206}Pb ages are given for z4 and z1a, respectively.

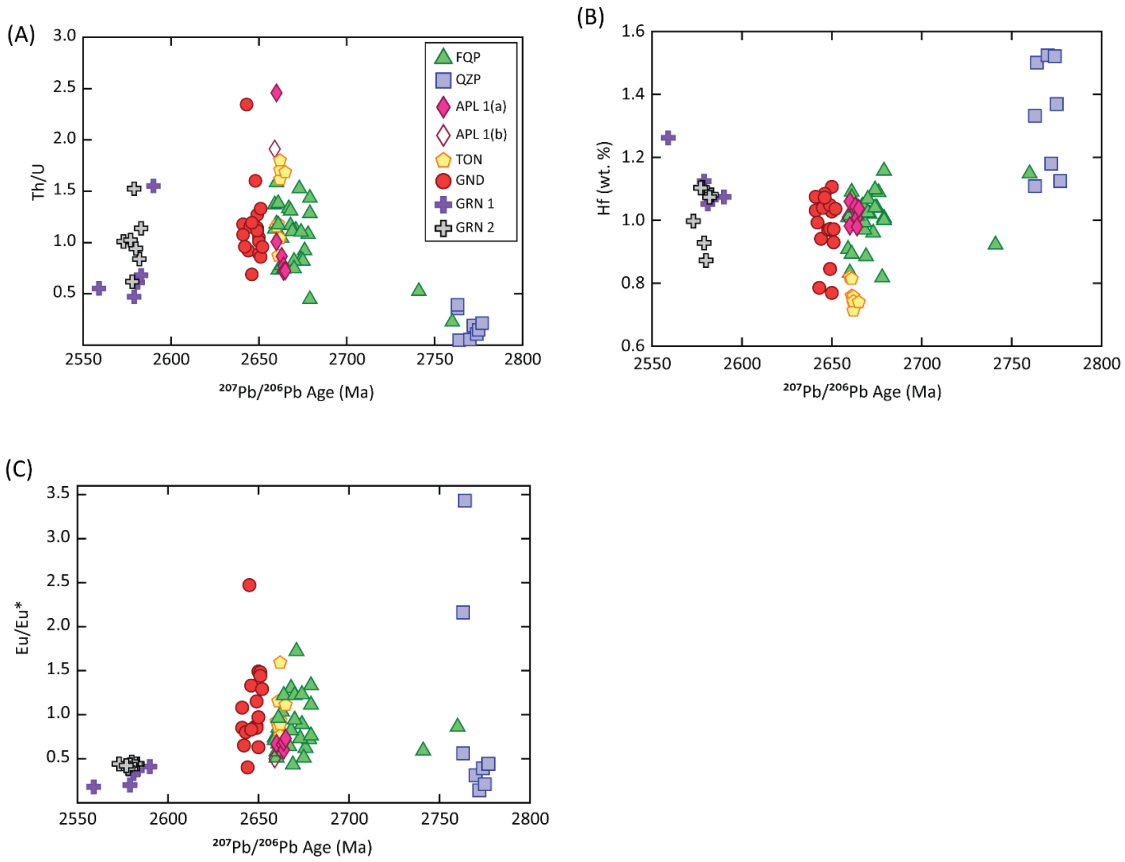


Fig. 3.8: Comparison of zircon mineral chemistry data through time. (A) Th/U, (B) Hf (C) Eu/Eu*. The legend for each graph can be found in Fig. 3.8A. Data have been filtered to only include analysis within the calculated crystallization ages described in the U-Pb geochronology results and summarized in Table 3-2 and Table 3-3.

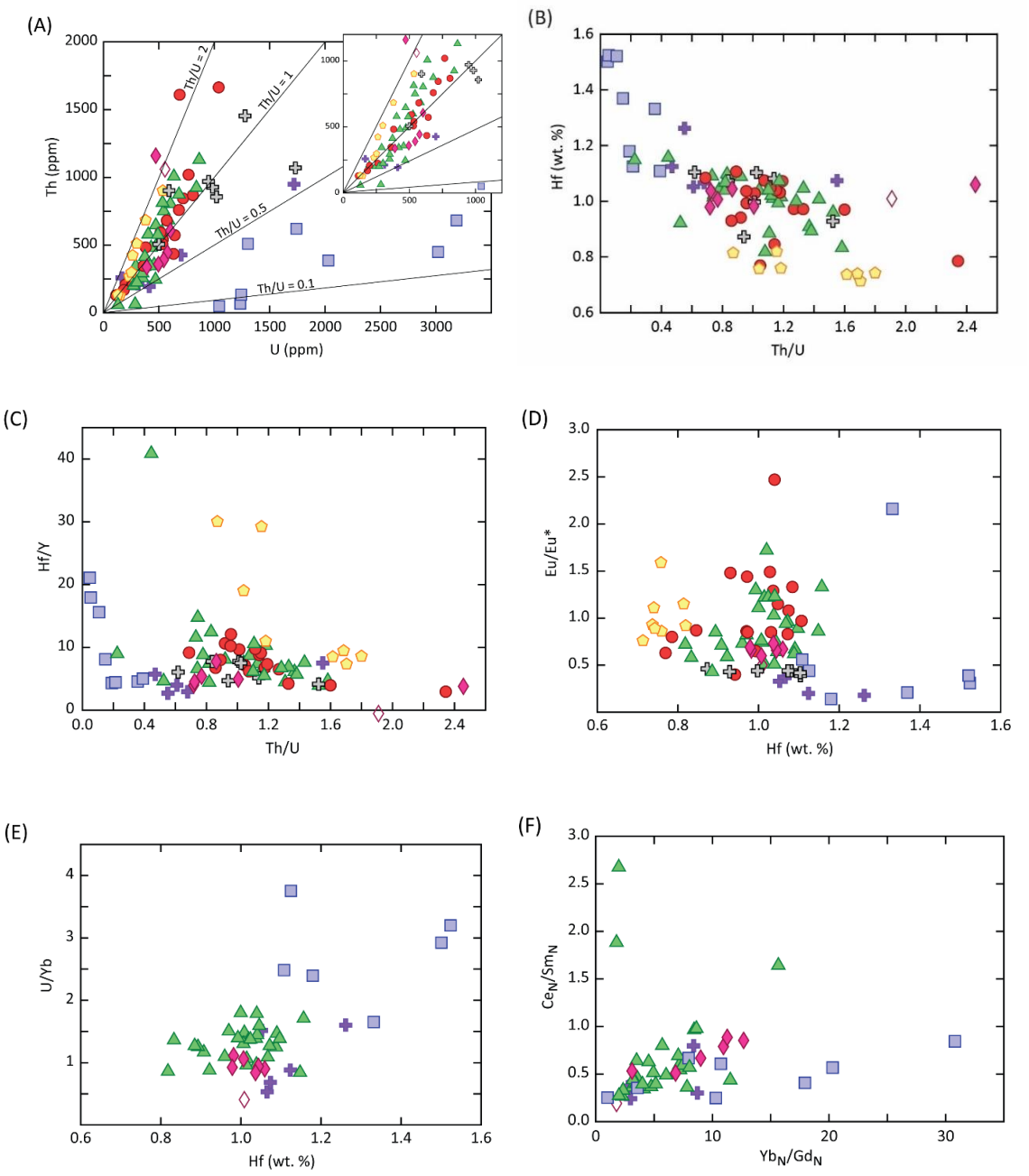


Fig. 3.9: Comparison of zircon trace element data for concordant analyses. (A) Th vs. U, the inset shows a narrower range for the bulk of the data, (B) Th/U vs. Hf, and (C) Th/U vs. Hf/Y. (D) Hf vs. Eu/Eu*, (E) Hf vs. U/Yb, (F) Yb_N/Gd_N vs. Ce_N/Sm_N. Ce and Yb were only collected for FQP, QZP, aplite, and Defeat Suite samples; the FQP and aplite samples have been found to plot together with the tonalite and granodiorite in other diagrams and are considered a reasonable proxy, which is also true for the granite samples. The legend can be found in Fig. 3.8A.

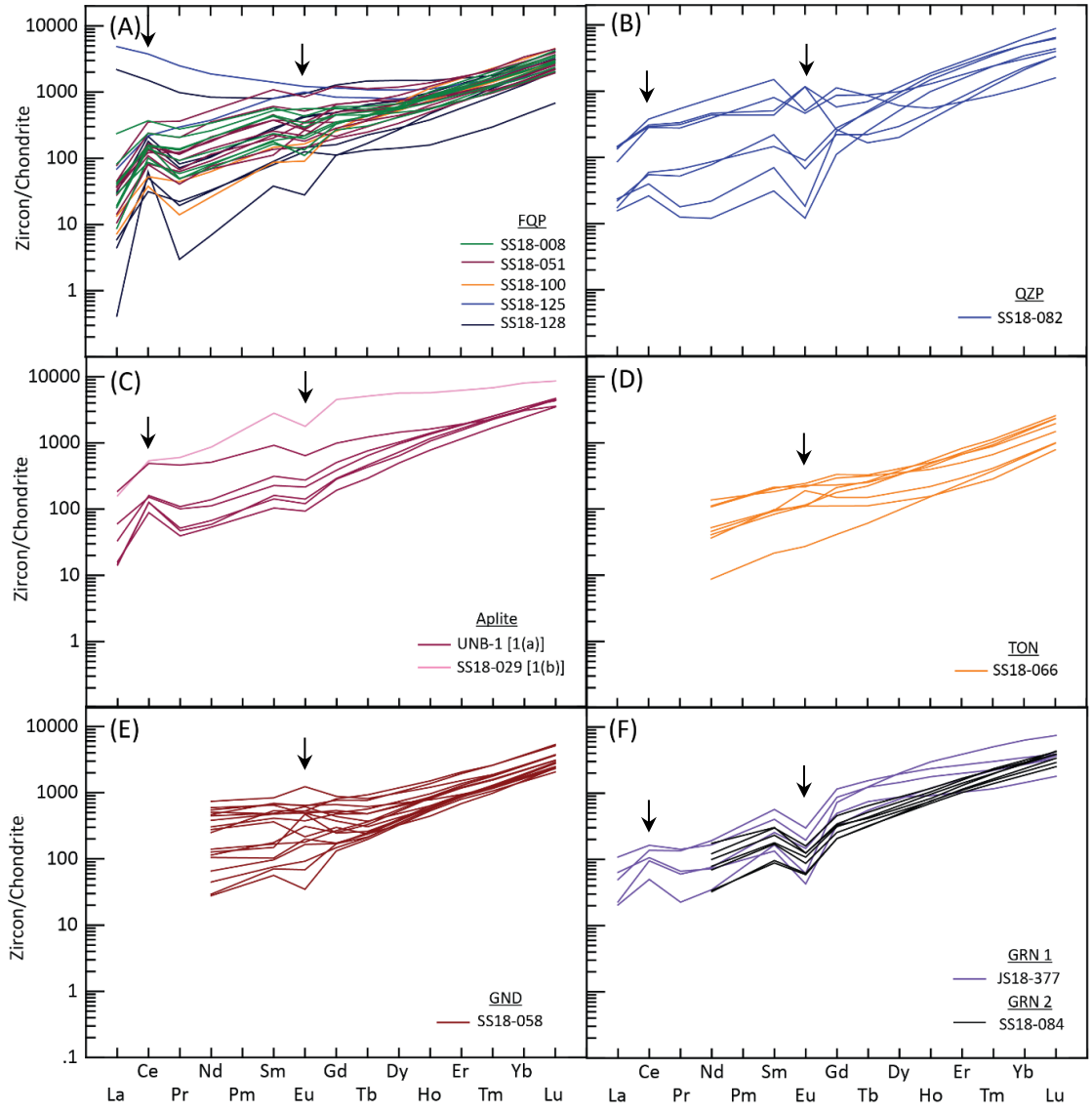


Fig. 3.10: Chondrite-normalized REE diagrams showing zircon mineral chemistry for each sample, grouped by lithology and filtered by the crystallization age of each sample (Sun and McDonough 1989). Black arrows highlight the Ce and Eu anomalies.

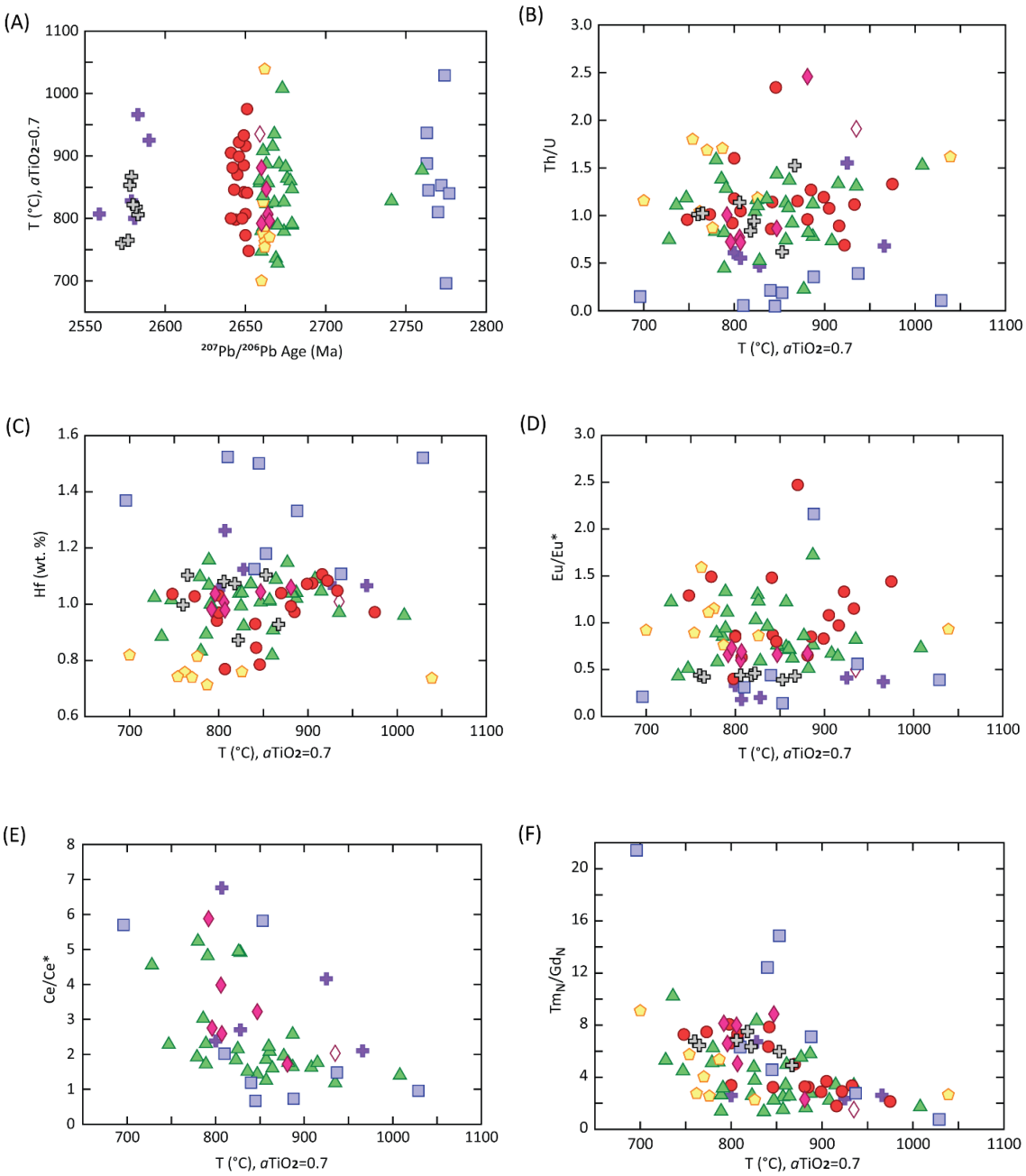


Fig. 3.11: Comparison of zircon trace element data to the calculated Ti-in-zircon temperatures. (A) Age (Ma), (B) Th/U ratio, (C) Hf concentration, (D) Eu/Eu*, (E) Ce/Ce*, (F) Tm_N/Gd_N (Watson et al. 2006, Ferry and Watson 2007). The Ti-in-zircon temperatures were calculated using $aTiO_2 = 0.7$ and $aSiO_2 = 1$. Ce was only collected for FQP, QZP, aplite, and Defeat Suite samples; the FQP and aplite are considered reasonable proxies for the tonalite and granodiorite samples and Defeat Suite granites plot with the Duckfish granite. The legend can be found in Fig. 3.8A.

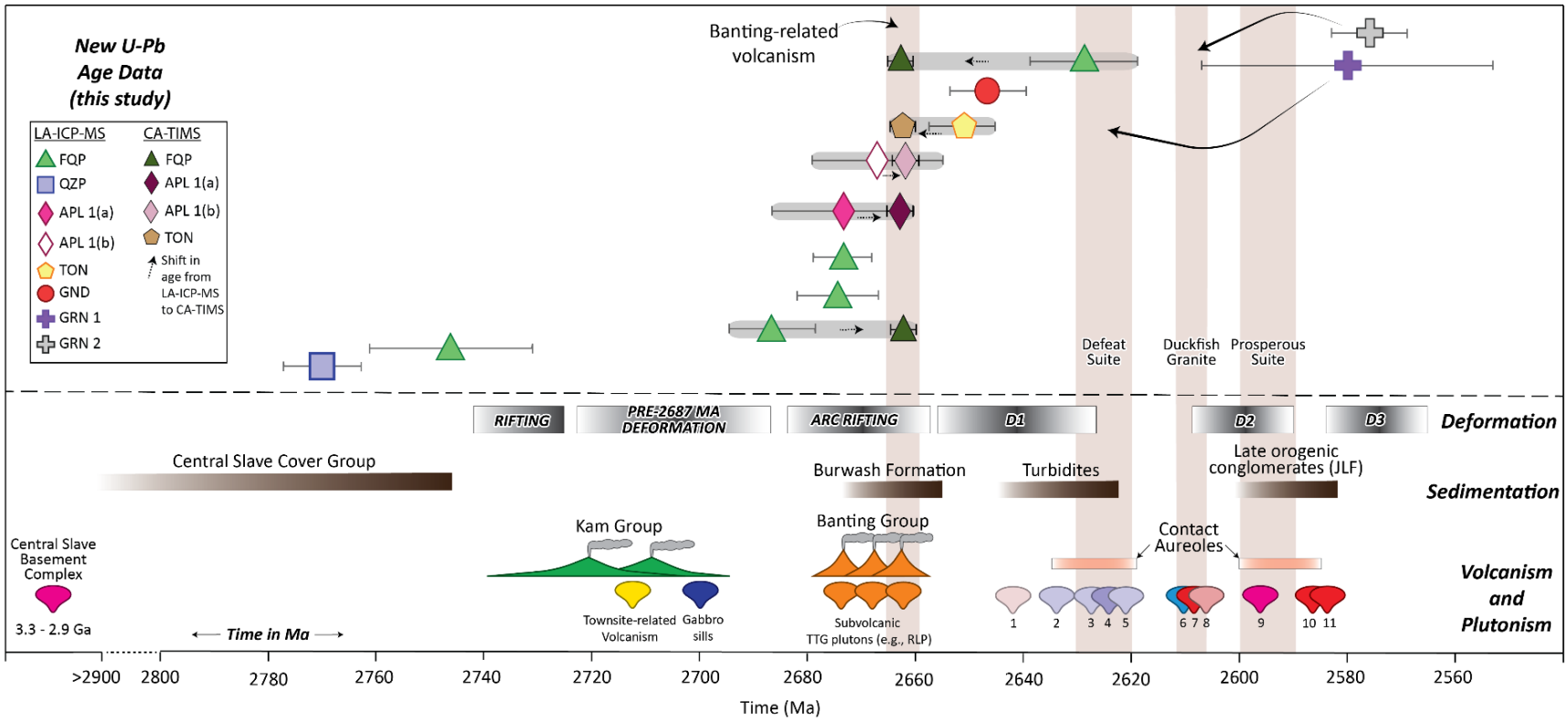


Fig. 3.12: Summary of events within the Slave craton, focusing on those related to the formation of the YGB, as they relate to the new U-Pb ages presented in this study [modified from Bleeker and Hall (2007) and Ootes et al. (2011)]. The diagram shows a schematic representation of volcanism, plutonism, sedimentation, and deformation related to the YGB, concerning previous ages determined by Bleeker and Hall (2007; and references therein). CA-TIMS ages have been placed in line with the corresponding sample analyzed by LA-ICP-MS, highlighted with a grey box and small, dashed arrows to indicate the shift in age from LA-ICP-MS to CA-TIMS (Table 3-2, Table 3-3). Black arrows indicate the previously determined age ranges for the Defeat Suite and Duckfish granites compared to this

study and the presently confirmed Banting-related volcanism. 1: Suse Lake granite; 2: Early Defeat Suite plutons; 3: Wool Bay; 4: U Watta Lake; 5: Western Defeat Suite pluton; 6: Concession Suite; 7: Duckfish granite; 8: Hidden Lake pluton; 9: Prosperous Suite; 10: Morose Lake granite; 11: Agassiz Lake. JLF: Jackson Lake Formation. RLP: Ryan Lake Pluton. APL 1(a) = aplite-1(a);, APL 1(b) = aplite-1(b); TON = tonalite; GND = granodiorite; GRN 1 = Defeat Suite granite; GRN 2 = Duckfish granite.

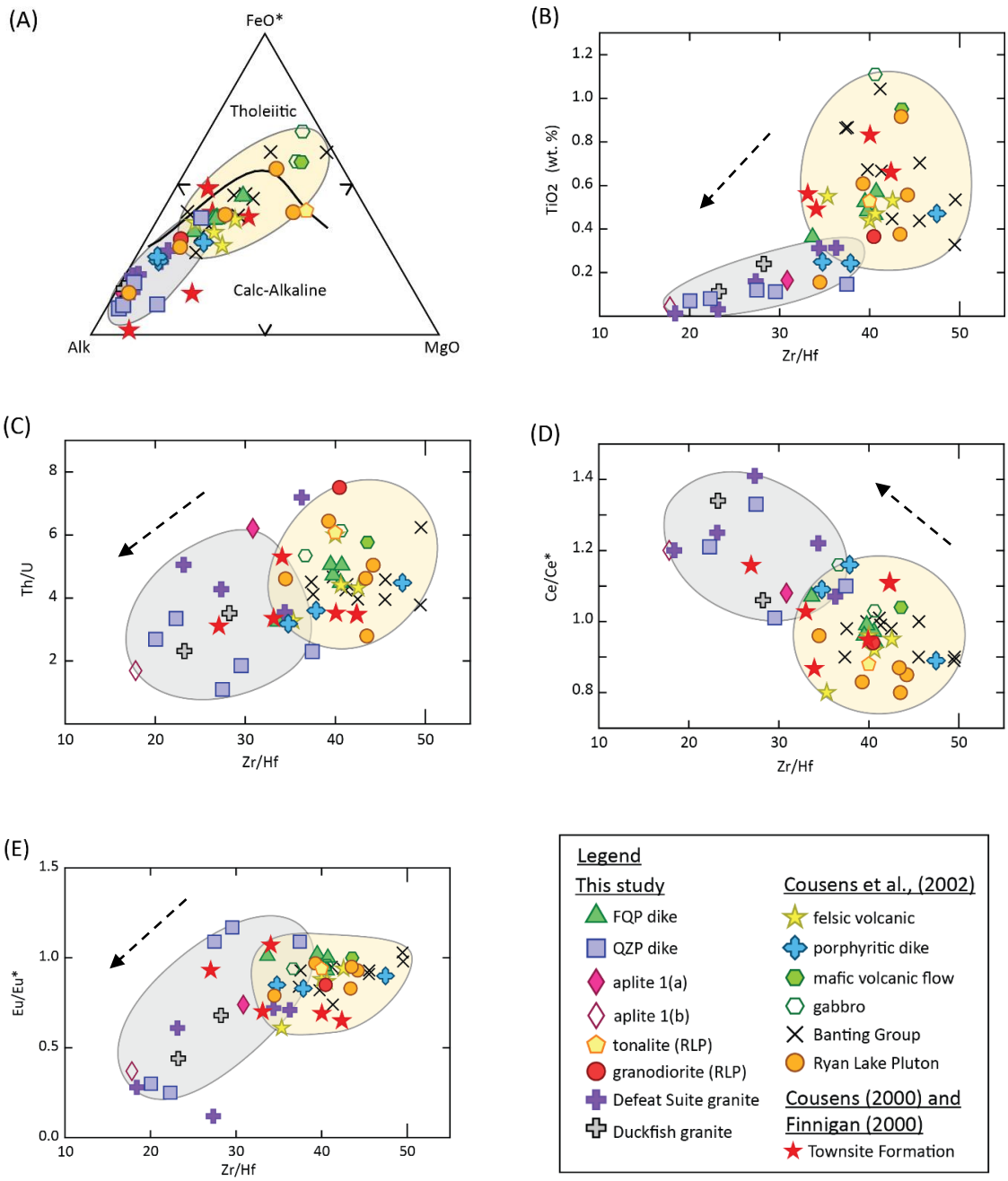


Fig. 3.13: Comparison of whole-rock geochemistry data from this study and the data presented by Cousens et al. (2002) for the Banting Group and Cousens (2000) and Finnigan (2000) for the Townsite Formation. (A) Alkali-FeO*-MgO (Irvine and Baragar 1971), Zr/Hf ratio versus (B) TiO_2, (C) Th/U, (D) Ce/Ce*, and (E) Eu/Eu*. Two groups of data have been highlighted in these figures; the yellow circle encompasses the Banting Group and Townsite Formation data, and the grey circle highlights the granitic units. The dashed arrows show the expected fractionation trends.

Fig. 3.14: *Following page*. Schematic depiction (not to scale) of tonalitic and granodioritic intrusion (Ryan Lake Pluton) at ca. 2662 Ma. The RLP emplaced through the Central Slave Basement Complex and Central Slave Cover Group (CSBC and CSCG) to the base of the Kam Group mafic volcanics (MVF). FQP dikes intruded at various times during the development of the volcanic pile and were feeders to both the Townsite Formation (Fm) and the younger Banting Group. Aplite-1(a) dikes associated with the RLP, and aplite-1(b) dikes associated with the Defeat Suite granite are also shown. A melt zone along the margin of the RLP incorporated older zircons and assimilated the mafic volcanics of the Kam Group, including feldspars that added Eu to the magma, recorded in the zircon mineral chemistry. Photomicrographs shown are from Fig. 3.2 and are shown with the corresponding feeder dike and intrusion (black arrows). Field image from the base of the Townsite Fm showing an FQP dike that crosscuts the Kam Group mafic volcanic rocks and turns parallel to stratigraphy, gaining a tuffaceous texture as in the Townsite Fm (hammer for scale).

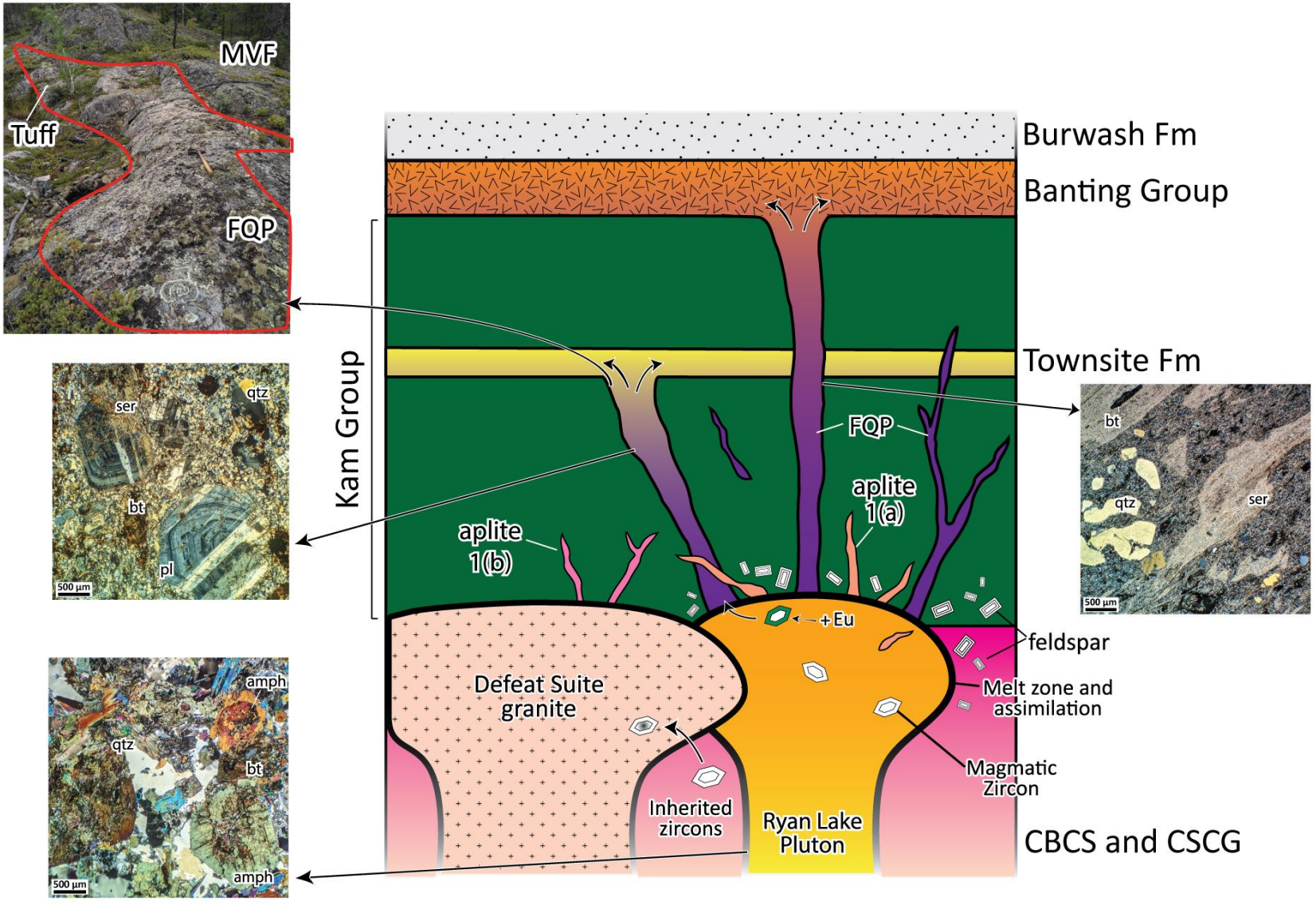

MVF
Tuff
FQP
ser
qtz
bt
pl
500 µm
amph
qtz
bt
amph
500 µm
Kam Group
Burwash Fm
Banting Group
Townsite Fm
FQP
aplite 1(a)
aplite 1(b)
+Eu
Defeat Suite granite
Inherited zircons
Ryan Lake Pluton
feldspar
Melt zone and assimilation
Magmatic Zircon
CBCS and CSCG
bt
qtz
ser
500 µm

Table 3-1: A summary of the distribution of each zircon colour population as they relate to each sample and lithology. APL 1(a) = aplite-1(a); APL 1(b) = aplite-1(b); TON = tonalite; GND = granodiorite; GRN 1 = Defeat Suite granite; GRN 2 = Duckfish granite.

		Zircon Colour						
Sample	Lithology	Colourless	Grey	Yellow	Turbid yellow	Orange	Brown	Violet
SS18-008	FQP	X		X				X
SS18-051	FQP	X		X				X
SS18-100	FQP	X					X	
SS18-125	FQP	X		X	X			
SS18-128	FQP	X		X	X			
SS18-082	QZP	X	X					X
UNB-1	APL 1(a)	X	X					
SS18-029	APL 1(b)	X						X
SS18-066	TON	X						X
SS18-058	GND	X		X				X
JS18-377	GRN 1	X		X				
SS18-084	GRN 2	X	X	X		X		

Table 3-2: Summary of U-Pb geochronology ages separated by type of age calculation. Samples with a lack of concordant data also had an upper intercept age calculated, which include SS18-100, SS18-082, SS18-029, and JS18-377. Upper intercept ages were anchored at 50 ± 50 Ma to mitigate the effects of ancient Pb-loss. Weighted mean ages were calculated for corresponding Concordia ages. The zircon standard Plesovice (337 Ma) was treated as an unknown during analysis and corresponding Concordia ages are also listed. P. o. F.: Probability of fit; Wtd. M.: Weighted mean age; n: number of analyses (number rejected from weighted mean age); *: samples showed inherited ages.

Concordia ages

Sample	Lithology	Easting (UTM)	Northing (UTM)	Concordia Age (Ma)	2σ	MSWD	P.o.F.	Wtd. M. Age (Ma)	2σ	MSWD	P.o.F.	*n*	Concordia Age (Ma) for Standard	2σ	MSWD	P.o.F.
SS18-008	FQP	636212	6943602	2687	8	0.24	0.63	2691	13	0.062	0.94	3	336	1.9	0.16	0.69
SS18-051	FQP	636643	6942621	2674	7	0.65	0.42	2677	11	4.6	0.00	21(1)	340	3.0	0.93	0.34
SS18-125	FQP	637429	6940080	2629	10	0.31	0.58	2637	15	0.55	0.84	10	337	4.0	0.80	0.37
SS18-128	FQP	636508	6942271	2674	5	0.67	0.41	2667	11	1.03	0.41	12	340	2.9	0.046	0.83
SS18-082*	QZP	635733	6947690	2905	7	0.090	0.76	2910	8	2.2	0.036	7	338	2.0	0.11	0.74
UNB-1	APL 1(a)	635871	6942769	2673	13	1.3	0.25	2676	15	0.71	0.74	13	334	2.5	0.28	0.60
SS18-029	APL 1(b)	635767	6943376	2663	19	0.0040	0.95	2661	32	0.44	0.64	3	334	2.5	0.28	0.60
SS18-066	TON	635470	6942487	2651	6	0.90	0.34	2657	8	1.5	0.11	16	338	1.8	0.36	0.55
SS18-058	GND	635490	6942293	2647	7	0.56	0.45	2649	9	4.6	0.00	12	335	2.1	0.059	0.81
JS18-377*	GRN 1	644112	6924245	2580	27	1.4	0.23	2577	42	6.7	0.00	4	335	6.7	0.051	0.82
SS18-084	GRN 2	634968	6947860	2576	7	0.82	0.36	2596	23	9.0	0.00	5	337	2.2	0.27	0.60

Table 3-2: *Continued*.

Upper intercept ages

Sample	Lithology	Easting (UTM)	Northing (UTM)	Upper Intercept Age (Ma)	2σ	Lower Intercept Age (Ma)	2σ	MSWD	*n*	Concordia Age (Ma) for Standard	2σ	MSWD	P.o.F.
SS18-100	FQP	634514	6947212	2746	15	50	50	0.73	5	335	1.9	1.2	0.28
SS18-082	QZP	635733	6947690	2770	7	50	50	0.87	10	338	2.0	0.11	0.74
SS18-029	APL 1(b)	635767	6943376	2667	12	50	50	1.0	43	334	2.5	0.28	0.60
JS18-377	GRN 1	644112	6924245	2597	57	50	50	3.7	7	335	6.7	0.051	0.82

Table 3-3: Summary of CA-TIMS calculated weighted mean ages for 5 of 6 samples selected for analysis chosen to refine the Concordia ages determined by LA-ICP-MS. 2σ error given along with the error including propagated decay constant errors given in brackets. The single QZP dike (SS18-082) did not render a weighted mean age but did give 5 concordant analyses which are depicted in Fig. 3.7D. The full data set used to calculate the weighted mean ages and individual QZP dike ages are given in Appendix 2**,** Table A2.2**.**

CA-TIMS

Sample	Lithology	Easting (UTM)	Northing (UTM)	Weighted mean age (Ma)	2σ error [incl. decay constant]	MSWD	Probability of fit	*n*
SS18-008	FQP	636212	6943602	2662.07	0.79 [2.37]	0.37	0.83	5
SS18-125	FQP	637429	6940080	2662.69	0.67 [2.37]	0.46	0.76	5
SS18-082	QZP	635733	6947690	-	-	-	-	5
UNB-1	APL 1(a)	635871	6942769	2662.75	1.04 [2.42]	0.44	0.78	5
SS18-029	APL 1(b)	635767	6943376	2661.77	0.70 [2.46]	1.3	0.25	5
SS18-066	TON	635470	6942487	2662.26	0.65 [2.36]	0.38	0.82	5

n = number of analyses.

Table 3-4: Summary of minimum, maximum, and average zircon trace element chemistry; see Appendix 2, Table A2.3 for the full dataset. Data has been filtered for P, Ti, and Si to avoid analyses that ablated inclusions. The Pb_T shown is a calculated total Pb based on isotopic abundances. - = not analyzed.

		SS18-008	SS18-051	SS18-100	SS18-125	SS18-128	SS18-082	UNB-1	SS18-029	SS18-066	SS18-058	JS18-377	SS18-084
	(ppm)	FQP	FQP	FQP	FQP	FQP	QZP	APL 1(a)	APL 1(b)	TON	GND	GRN 1	GRN 2
Ce	Min	53.0	49.4	23.2	134	19.2	16.1	54.3	330	-	-	30.5	-
	Max	226	217	32.3	2310	922	232	300	330	-	-	99.8	-
	Avg	107	96.6	27.8	1222	209	110	121	330	-	-	67.5	-
Dy	Min	105	85.5	133	200	36.2	50.9	126	1440	-	-	207	-
	Max	170	302	177	273	381	291	368	1440	-	-	509	-
	Avg	142	165	155	237	156	175	221	1440	-	-	360	-
Er	Min	-	-	-	-	-	-	-	-	34.8	114	-	169
	Max	-	-	-	-	-	-	-	-	136	339	-	278
	Avg	-	-	-	-	-	-	-	-	85.0	187	-	219
Eu	Min	6.40	8.50	5.26	58.0	1.62	0.700	5.41	103	1.58	2.01	2.47	3.42
	Max	32.5	49.1	9.60	70.7	55.2	67.8	37.2	103	14.1	71.6	17.3	9.27
	Avg	16.6	19.9	7.43	64.4	20.4	25.3	14.7	103	8.98	23.4	8.63	6.00
Gd	Min	54.9	41.2	52.5	172	22.7	22.8	39.6	930	8.47	27.1	67.6	42.3
	Max	123	252	56.2	237	262	231	204	930	68.3	181	238	93.8
	Avg	85.9	105	54.4	205	90.3	94.7	93.2	930	39.7	83.3	147	61.8
Hf	Min	8330	8180	9218	10140	8848	11080	9790	10090	7131	7690	10520	8725
	Max	10900	10970	11480	10720	11569	15240	10600	10090	8190	11064	12620	11040
	Avg	9784	10038	10349	10430	10288	13325	10144	10090	7603	9832	11156	10227
Ho	Min	31.2	28.2	42.1	47.9	8.96	21.1	44.2	324	8.64	25.1	52.0	39.8
	Max	56.9	78.2	64.4	62.9	84.6	106	92.0	324	31.1	85.3	168	67.0
	Avg	43.6	47.5	53.3	55.4	41.4	61.8	68.5	324	20.6	45.0	104	50.6
La	Min	2.07	2.53	1.71	16.3	0.0980	3.70	3.38	37.7	-	-	4.85	-
	Max	56.0	18.5	3.20	1153	517	34.9	44.0	37.7	-	-	25.7	-
	Avg	14.1	8.69	2.46	585	88.5	17.5	12.5	37.7	-	-	12.6	-

Table 3-4: *Continued*.

		SS18-008	SS18-051	SS18-100	SS18-125	SS18-128	SS18-082	UNB-1	SS18-029	SS18-066	SS18-058	JS18-377	SS18-084
	(ppm)	FQP	FQP	FQP	FQP	FQP	QZP	APL 1(a)	APL 1(b)	TON	GND	GRN 1	GRN 2
Lu	Min	52.0	49.4	70.7	57.6	17.3	40.4	88.8	219	19.9	52.1	45.6	63.8
	Max	108	114	115	77.4	103	223	120	219	65.1	136	189	109
	Avg	76.9	75.2	93.0	67.5	67.0	121.0	106	219	42.5	79.8	102.3	90.9
Nd	Min	32.9	32.2	12.1	175	3.18	5.60	25.0	404	4.07	13.0	16.3	15.2
	Max	158	245	29.4	878	391	359	239	404	64.0	346	90.0	81.8
	Avg	79.9	90.7	20.8	527	87.2	132	77.6	404	31.5	134	50.7	40.8
P	Min	0.00	146	237	229	40.0	60.0	298	760	73.0	184	509	176
	Max	1830	810	567	1464	2350	2230	539	760	174	1230	1410	762
	Avg	545	287	402	847	677	628	469	760	136	539	778	402
Pb_T	Min	372	143	159	128	66.5	619	240	285	97.4	95.3	123	352
	Max	674	537	313	372	561	2118	469	285	453	819	1181	1004
	Avg	519	340	236	250	335	1112	401	285	237	395	435	680
^{204}Pb	Min	24.7	0.800	0.500	2.20	1.10	0.300	5.40	4.00	0.100	0.200	10.7	0.100
	Max	164	6.80	3.40	24.2	18.8	153	245	4.00	2.20	4.00	28.0	5.50
	Avg	86.3	3.00	1.95	13.2	7.73	35.3	63.9	4.00	1.00	2.01	20.3	2.30
^{206}Pb	Min	828	393	533	379	203	2121	699	771	274	265	331	996
	Max	1559	1413	976	982	1482	6930	1347	771	1130	2084	3800	3166
	Avg	1228	922	754	681	921	3611	1064	771	608	1075	1340	2015
^{207}Pb	Min	236	80.0	111	77.3	41.9	449	144	153	54.2	52.7	74.7	191
	Max	420	290	201	216	304	1474	341	153	223	411	736	594
	Avg	311	188	156	147	188	785	256	153	120	213	272	381
^{208}Pb	Min	221	58.1	11.6	37.7	15.9	15.9	76.6	126	37.0	38.0	40.6	135
	Max	433	256	63.5	168	262	233	309	126	253	434	197	297
	Avg	294	146	37.6	103	137	130	168	126	122	171	99.4	211

Table 3-4: *Continued*.

		SS18-008	SS18-051	SS18-100	SS18-125	SS18-128	SS18-082	UNB-1	SS18-029	SS18-066	SS18-058	JS18-377	SS18-084
	(ppm)	FQP	FQP	FQP	FQP	FQP	QZP	APL 1(a)	APL 1(b)	TON	GND	GRN 1	GRN 2
	Min	4.62	3.87	1.33	28.2	0.282	1.19	3.75	57.4	-	-	2.14	-
Pr	Max	26.3	34.4	4.22	238	93.5	51.6	44.0	57.4	-	-	13.5	-
	Avg	12.0	11.7	2.78	133	18.7	19.2	13.5	57.4	-	-	8.09	-
	Min	160600	158300	155700	157000	152600	147300	147800	176200	-	-	151900	-
Si	Max	177500	193400	166700	175100	181000	187600	172100	176200	-	-	182900	-
	Avg	168200	173540	161200	166050	169017	169388	161680	176200	-	-	168620	-
	Min	25.1	17.1	13.3	123	5.83	4.77	15.9	431	3.29	8.62	20.4	13.5
Sm	Max	88.1	166	22.4	216	122	230	141	431	32.7	128	87.0	46.3
	Avg	52.6	58.8	17.9	170	39.9	71.1	50.3	431	18.9	55.2	46.7	29.8
	Min	11.5	9.29	13.8	30.8	4.95	6.20	11.0	190	2.28	7.36	20.7	11.7
Tb	Max	22.8	42.2	16.4	40.7	54.9	32.8	46.0	190	12.2	34.7	58.0	24.2
	Avg	17.5	20.5	15.1	35.8	20.5	18.9	23.8	190	7.93	15.8	39.9	16.2
	Min	257	199	64.2	201	58.1	49.8	338	1060	128	130	194	506
Th	Max	1007	1130	246	576	924	682	1160	1060	902	1664	950	1454
	Avg	556	553	155	389	473	362	588	1060	419	648	408	955
	Min	7.10	9.90	15.7	16.9	5.80	4.00	11.2	38.4	4.19	7.20	12.1	8.10
Ti	Max	31.1	64.4	24.2	20.3	15.5	74.0	24.9	38.4	79.0	51.3	48.0	22.2
	Avg	17.7	27.3	20.0	18.6	10.1	26.6	16.1	38.4	18.0	22.7	24.9	14.4
	Min	25.3	24.6	35.9	32.2	7.56	21.9	43.5	174	7.25	25.0	29.7	35.5
Tm	Max	52.0	56.5	58.1	39.5	46.5	105	65.0	174	28.7	66.4	128	59.6
	Avg	38.0	36.6	47.0	35.9	31.5	62.0	57.0	174	18.1	38.6	69.7	47.7
	Min	291	197	285	271	131	1044	391	555	128	114	167	501
U	Max	636	864	470	491	839	3187	604	555	535	1040	1720	1732
	Avg	469	458	377	381	458	1851	518	555	280	535	662	1008

Table 3-4: *Continued*.

		SS18-008	SS18-051	SS18-100	SS18-125	SS18-128	SS18-082	UNB-1	SS18-029	SS18-066	SS18-058	JS18-377	SS18-084
	(ppm)	FQP	FQP	FQP	FQP	FQP	QZP	APL 1(a)	APL 1(b)	TON	GND	GRN 1	GRN 2
Y	Min	941	883	1280	1540	283	712	1349	10100	271	822	1430	1285
	Max	1779	2450	1989	1959	2430	2920	2800	10100	973	2680	4690	2241
	Avg	1338	1468	1635	1750	1239	1830	2091	10100	641	1425	2872	1740
Yb	Min	239	230	340	283	76.5	193	415	1370	-	-	245	-
	Max	467	574	537	387	470	1054	589	1370	-	-	1074	-
	Avg	354	352	438	335	304	599	523	1370	-	-	567	-
T (°C)	Min	747	779	828	836	728	696	792	935	700	748	800	760
	Max	908	1008	877	857	826	1029	881	935	1039	975	966	867
	Avg	831	880	853	846	777	862	826	935	802	858	865	813

3.8. References

Andersen, T., Elburg, M.A., and Magwaza, B.N. 2019. Sources of bias in detrital zircon geochronology: Discordance, concealed lead loss and common lead correction. Earth-Science Reviews, **197**: 1–15.

Ballard, J.R., Palin, J.M., and Campbell, I.H. 2002. Relative oxidation states of magmas inferred from Ce“IV”/Ce“III” in zircon: Application to porphyry copper deposits of northern Chile. Contributions to Mineralogy and Petrology, **144**: 347–364.

Bauer, A.M., Fisher, C.M., Vervoort, J.D., and Bowring, S.A. 2017. Coupled zircon Lu–Hf and U–Pb isotopic analyses of the oldest terrestrial crust, the >4.03 Ga Acasta Gneiss Complex. Earth and Planetary Science Letters, **458**: 37–48. Elsevier B.V.

Bethune, K.M., Villeneuve, M.E., Bleeker, W., Bethune, K.M., Villeneuve, M.E., and Bleeker, W. 1999. Laser 40Ar/39Ar thermochronology of Archean rocks in Yellowknife Domain, southwestern Slave Province: insights into the cooling history of an Archean granite-greenstone terrane. Canadian Journal of Earth Sciences, **36**: 1189–1206.

Bleeker, W., and Hall, B. 2007. The Slave Craton: Geology and Metallogenic Evolution. *In* Mineral Deposits of Canada: A Synthesis of Major Deposit-Types, District Metallogeny, the Evolution of Geological Provinces, and Exploration Methods: Geological Association of Canada. *Edited by* W.D. Goodfellow. Mineral Deposits Division. pp. 849–879.

Bleeker, W., Ketchum, J., Davis, B., Sircombe, K., Stern, R., and Waldron, J. 2004. The Slave Craton From On Top: The Crustal View. *In* The Lithoprobe Celebratory Conference. Toronto. pp. 1–5.

Bleeker, W., Ketchum, J.W.F., and Davis, W.J. 1999a. The Central Slave Basement Complex, Part II: age and tectonic significance of high-strain zones along the basement-cover contact. Canadian Journal of Earth Sciences, **36**: 1111–1130.

Bleeker, W., Ketchum, J.W.F., Jackson, V.A., and Villeneuve, M.E. 1999b. The Central Slave Basement Complex, Part I: its structural topology and autochthonous cover. Canadian Journal of Earth Sciences, **36**: 1083–1109.

Boehnke, P., Watson, E.B., Trail, D., Harrison, T.M., and Schmitt, A.K. 2013. Zircon saturation re-revisited. Chemical Geology, **351**: 324–334.

van Breemen, O., Davis, W.J., and King, J.E. 1992. Temporal distribution of granitoid plutonic rocks in the Archean Slave Province, northwest Canadian Shield. Canadian Journal of Earth Sciences, **29**: 2186–2199.

Brown, M., and Johnson, T. 2018. Secular change in metamorphism and the onset of global plate tectonics. American Mineralogist, **103**: 181–196.

Buret, Y., von Quadt, A., Heinrich, C., Selby, D., Wälle, M., and Peytcheva, I. 2016. From a long-lived upper-crustal magma chamber to rapid porphyry copper emplacement: Reading the geochemistry of zircon crystals at Bajo de la Alumbrera (NW Argentina). Earth and Planetary Science Letters, **450**: 120–131.

Buret, Y., Wotzlaw, J.F., Roozen, S., Guillong, M., von Quadt, A., and Heinrich, C.A. 2017. Zircon petrochronological evidence for a plutonic-volcanic connection in porphyry copper deposits. Geology, **45**: 623–626.

Burke, K., and Kidd, W.S.F. 1978. Were Archean continental geothermal gradients much steeper than those of today. Nature, **272**: 240–241.

Carter, L.C., Williamson, B.J., Tapster, S.R., Costa, C., Grime, G.W., and Rollinson, G.K. 2021. Crystal mush dykes as conduits for mineralising fluids in the Yerington porphyry copper district, Nevada. Communications Earth and Environment, **2**: 1–11.

Cathles, L.M., Erendi, A.H.J., and Barrie, T. 1997. How Long Can a Hydrothermal System Be Sustained by a Single Intrusive Event? Economic Geology, **92**: 766–771.

Chen, S.R., Wang, Q., Zhu, D.C., Weinberg, R.F., Zhang, L.L., and Zhao, Z.D. 2021. Reheating and magma mixing recorded by zircon and quartz from high-silica rhyolite in the Coqen region, southern Tibet. American Mineralogist, **106**: 112–122.

Claiborne, L.L., Miller, C.F., Flanagan, D.M., Clynne, M.A., and Wooden, J.L. 2010. Zircon reveals protracted magma storage and recycling beneath Mount St. Helens. Geology, **38**: 1011–1014.

Corfu, F. 2013. A century of U-Pb geochronology: The long quest towards concordance. Bulletin of the Geological Society of America, **125**: 33–47.

Corfu, F., Hanchar, J.M., Hoskin, P.W.O., and Kinny, P. 2003. Atlas of Zircon Textures. Reviews in Mineralogy and Geochemistry, **53**: 469–500.

Cousens, B., Facey, K., and Falck, H. 2002. Geochemistry of the late Archean Banting Group, Yellowknife greenstone belt, Slave Province, Canada: Simultaneous melting of the upper mantle and juvenile mafic crust. Canadian Journal of Earth Sciences, **39**: 1635–1656.

Cousens, B., Falck, H., Ootes, L., Jackson, V., Mueller, W., Corcoran, P., Finnigan, C., van Hees, E., Facey, C., and Alcazar, A. 2006. Regional Correlations, Tectonic Settings, and Stratigraphic Solutions in the Yellowknife Greenstone Belt and Adjacent Areas from Geochemical and Sm-Nd Isotopic Analysis of Volcanic and Plutonic Rocks. *In* Gold in the Yellowknife Greenstone Belt, Northwest Territories: Results of the EXTECH III Multidisciplinary Research Project. *Edited by* C.D. Anglin, H. Falck, D.F. Wright, and E.J. Ambrose. pp. 70–94.

Cousens, B.L. 2000. Geochemistry of the Archean Kam Group, Yellowknife Greenstone Belt, Slave Province, Canada. The Journal of Geology, **108**: 181–197.

Crowley, Q.G., Heron, K., Riggs, N., Kamber, B., Chew, D., McConnell, B., and Benn, K. 2014. Chemical Abrasion Applied to LA-ICP-MS U-Pb Zircon Geochronology. **4**: 503–518.

Crowley, J.L., Schoene, B., and Bowring, S.A. 2007. U-Pb dating of zircon in the Bishop Tuff at the millennial scale. Geology, **35**: 1123–1126.

Davis, W.J., and Bleeker, W. 1999. Timing of plutonism, deformation, and metamorphism in the Yellowknife Domain, Slave Province, Canada. Canadian Journal of Earth Sciences, **36**: 1169–1187.

Dickin, A.P. 2018. Radiogenic Isotope Geology. *In* Third edition. Cambridge University Press.

Dilles, J.H., Kent, A.J.R., Wooden, J.L., Tosdal, R.M., Koleszar, A., Lee, R.G., and Farmer, L.P. 2015. Zircon compositional evidence for sulfur-degassing from ore-forming arc magmas. Economic Geology, **110**: 241–251.

Ferry, J.M., and Watson, E.B. 2007. New thermodynamic models and revised calibrations for the Ti-in-zircon and Zr-in-rutile thermometers. Contributions to Mineralogy and Petrology, **154**: 429–437.

Finnigan, C.S. 2000. The Townsite Formation: an aborted rift setting in the Yellowknife greenstone belt, NWT. M. Sc., University of Western Ontario, London, Ontario.

Finnigan, C.S., and Duke, N.A. 2006. Geology and Geochemistry of the Townsite Formation: Recognition of Felsic Porphyritic Intrusions Adjacent to Gold-Bearing Shear Zones in the Yellowknife Greenstone Belt, NWT. *In* Gold in the Yellowknife Greenstone Belt, Northwest Territories: Results of the EXTECH III Multidisciplinary Research Project. *Edited by* C.D. Anglin, H. Falck, D.F. Wright, and E.J. Ambrose. pp. 58–69.

Fu, B., Mernagh, T.P., Kita, N.T., Kemp, A.I.S., and Valley, J.W. 2009. Distinguishing magmatic zircon from hydrothermal zircon: A case study from the Gidginbung high-sulphidation Au-Ag-(Cu) deposit, SE Australia. Chemical Geology, **259**: 131–142.

Fu, B., Page, F.Z., Cavosie, A.J., Fournelle, J., Kita, N.T., Lackey, J.S., Wilde, S.A., and Valley, J.W. 2008. Ti-in-zircon thermometry: Applications and limitations. Contributions to Mineralogy and Petrology, **156**: 197–215.

Gagnevin, D., Daly, J.S., and Kronz, A. 2010. Zircon texture and chemical composition as a guide to magmatic processes and mixing in a granitic environment and coeval volcanic system. Contributions to Mineralogy and Petrology, **159**: 579–596.

Gerstenberger, H., and Haase, G. 1997. A highly effective emitter substance for mass spectrometric Pb isotope ratio determinations. Chemical Geology, **136**: 309–312. Elsevier.

Green, D.C., and Baadsgaard, H. 1971. Temporal Evolution and Petrogenesis of an Archaean Crustal Segment at Yellowknife, N.W.T., Canada. Journal of Petrology, **12**: 177–217.

Harrison, T.M., and Watson, E.B. 1983. Kinetics of Zircon Dissolution and Zirconium Diffusion in Granitic Melts of Variable Water Content. Contributions to Mineralogy and Petrology, **84**: 66–72.

Helmstaedt, H., and Padgham, W.A. 1986. A new look at the stratigraphy of the Yellowknife Supergroup at Yellowknife, N.W.T. — implications for the age of gold-bearing shear zones and Archean basin evolution. Canadian Journal of Earth Sciences, **23**: 454–475.

Helmstaedt, H.H. 2006. Evolution of geological understanding of the Yellowknife Domain. *In* Gold in the Yellowknife Greenstone Belt, Northwest Territories: Results of the EXTECH III Multidisciplinary Research Project, Special Pub. No. 3. *Edited by* C.D.

Anglin, H. Falck, D.F. Wright, and E.J. Ambrose. Geological Association of Canada Mineral Deposits Division. pp. 29–37.

Henderson, J.F., and Brown, I.C. 1966. Geology and structure of the Yellowknife greenstone belt, District of Mackenzie. *In* Bulletin 141. Geological Survey of Canada.

Hibbard, M. 1980. Indigenous Source of Late-Stage Dikes and Veins in Granitic Plutons. Economic Geology, **75**: 410–423.

Hiess, J., Condon, D.J., Mclean, N., and Noble, S.R. 2012. 238U/235U systematics in terrestrial U-bearing minerals. Science, **335**: 1610–1614.

Hoskin, P.W.O. 2005. Trace-element composition of hydrothermal zircon and the alteration of Hadean zircon from the Jack Hills, Australia. Geochimica et Cosmochimica Acta, **69**: 637–648.

Hoskin, P.W.O., and Ireland, T.R. 2000. Rare earth element chemistry of zircon and its use as a provenance indicator. Geology, **28**: 627–630.

Hoskin, P.W.O., and Schaltegger, U. 2003. The Composition of Zircon and Igneous and Metamorphic Petrogenesis. Reviews in Mineralogy and Geochemistry, **53**: 27–62.

Hubbard, L.J., Marshall, D.D., Anglin, C.D., Thorkelson, D., and Robinson, M.H. 2006. Giant Mine: Alteration, Mineralization, and Ore-Zone Structures with an Emphasis on the Supercrest Zone. *In* Gold in the Yellowknife Greenstone Belt, Northwest Territories: Results of the EXTECH III Multidisciplinary Research Project. *Edited by* C.D. Anglin, H. Falck, D.F. Wright, and E.J. Ambrose. pp. 197–212.

Irvine, T.N., and Baragar, W.R.A. 1971. A Guide to the Chemical Classification of the Common Volcanic Rocks. Canadian Journal of Earth Sciences, **8**: 523–548.

Isachsen, C.E. 1992. U-Pb zircon geochronology of the Yellowknife volcanic belt and subjacent rocks, N.W.T., Canada: Constraints on the timing, duration, and mechanics of greenstone belt formation. Ph. D., Washington University, St. Louis, Mo.

Isachsen, C.E., and Bowring, S.A. 1994. Evolution of the Slave craton. Geology, **22**: 917–920.

Isachsen, C.E., and Bowring, S.A. 1997. The Bell Lake group and Anton Complex: a basement – cover sequence beneath the Archean Yellowknife greenstone belt revealed and implicated in greenstone belt formation. Canadian Journal of Earth Sciences, **34**: 169–189.

Isachsen, C.E., Bowring, S.A., and Padgham, W.A. 1991. U-Pb Zircon Geochronology of the Yellowknife Volcanic Belt, NWT, Canada: New Constraints on the Timing and Duration of Greenstone Belt Magmatism. The Journal of Geology, **99**: 55–67.

Jaffey, A.H., Flynn, K.F., Glendenin, L.E., Bentley, W.C., and Essling, A.M. 1971. Precision Measurement of Half-Lives and Specific Activities of 235U and 238U. Physical Review C, **4**: 1889–1906.

Ketchum, J.W.F., and Bleeker, W. 2000. New field and U-Pb data from the Central Slave Cover Group near Yellowknife and the Central Slave Basement Complex at Point Lake. *In* Slave-Northern Cordillera Lithospheric Experiment (SNORCLE) Transect Meeting. *Edited by* F. Cook and P. Erdmer. pp. 27–31.

Ketchum, J.W.F., Bleeker, W., and Stern, R.A. 2004. Evolution of an Archean basement complex and its autochthonous cover, southern Slave Province, Canada. Precambrian Research, **135**: 149–176.

Krogh, T.E. 1973. A low-contamination method for hydrothermal decomposition of zircon and extraction of U and Pb for isotopic age determinations. Geochimica et Cosmochimica Acta, **37**: 485–494.

Large, S.J.E., von Quadt, A., Wotzlaw, J.F., Guillong, M., and Heinrich, C.A. 2018. Magma evolution leading to porphyry Au-Cu mineralization at the Ok Tedi deposit, Papua New Guinea: Trace element geochemistry and high-precision geochronology of igneous zircon. Economic Geology, **113**: 39–61.

Lin, J., Liu, Y., Yang, Y., and Hu, Z. 2016. Calibration and correction of LA-ICP-MS and LA-MC-ICP-MS analyses for element contents and isotopic ratios. Solid Earth Sciences, **1**: 5–27.

Ludwig, K.R. 2003. User's Manual for Isoplot 3.00: A Geochronological Toolkit for Microsoft Excel. Berkeley Geochronology Center, Berkeley, CA.

Ludwig, K.R. 2012. Isoplot 3.75: A geochronological toolkit for Microsoft Excel. Berkeley Geochronology Center Special Publication, **5**: 0–75.

Martel, E., and Lin, S. 2006. Structural Evolution of the Yellowknife Greenstone Belt, with Emphasis on the Yellowknife River Fault Zone and the Jackson Lake Formation. *In* Gold in the Yellowknife Greenstone Belt, Northwest Territories: Results of the EXTECH III Multidisciplinary Research Project, Special Pub. No. 3. *Edited by* C.D. Anglin, H. Falck, D.F. Wright, and E.J. Ambrose. pp. 95–115.

Mattinson, J.M. 2005. Zircon U-Pb chemical abrasion ("CA-TIMS") method: Combined annealing and multi-step partial dissolution analysis for improved precision and accuracy of zircon ages. Chemical Geology, **220**: 47–66.

Mezger, K., and Krogstad, E.J. 1997. Interpretation of discordant U-Pb zircon ages: An evaluation. Journal of Metamorphic Geology, **15**: 127–140. Blackwell Publishing Inc.

Moyen, J.F. 2011. The composite Archaean grey gneisses: Petrological significance, and evidence for a non-unique tectonic setting for Archaean crustal growth. Lithos, **123**: 21–36.

Ni, Z., Arevalo, R., Piccoli, P., and Reno, B.L. 2020. A Novel Approach to Identifying Mantle-Equilibrated Zircon by Using Trace Element Chemistry. Geochemistry, Geophysics, Geosystems, **21**: 1–22.

Ootes, L., Lentz, D.R., Cabri, L.J., and Hall, D.C. 2006. Geology and Gold Mineralization in the Crestaurum Mine Area, Northern Yellowknife Greenstone Belt, N. W. T. *In* Gold in the Yellowknife Greenstone Belt, Northwest Territories: Results of the EXTECH III Multidisciplinary Research Project, Special Pub. No. 3. *Edited by* C.D. Anglin, H. Falck, D.F. Wright, and E.J. Ambrose. pp. 249–269.

Ootes, L., Lentz, D.R., Creaser, R.A., Ketchum, J.W.F., and Falck, H. 2007. Re-Os molybdenite ages from the Archean Yellowknife greenstone belt: Comparison to U-Pb ages and evidence for metal introduction at ~2675 Ma. Economic Geology, **102**: 511–518.

Ootes, L., Morelli, R.M., Creaser, R.A., Lentz, D.R., Falck, H., and Davis, W.J. 2011. The timing of Yellowknife gold mineralization: a temporal relationship with crustal anatexis? Economic Geology, **106**: 713–720.

Palmer, E.M. 2018. Petrogenesis of the Archean Prestige leucogranite and spatially associated LCT pegmatites, NWT: insights from whole-rock and muscovite trace element geochemistry and apatite U-Pb geochronology. M. Sc., University of New Brunswick, Fredericton, NB.

Paton, C., Woodhead, J.D., Hellstrom, J.C., Hergt, J.M., Greig, A., and Maas, R. 2010. Improved laser ablation U-Pb zircon geochronology through robust downhole fractionation correction. Geochemistry, Geophysics, Geosystems, **11**: 1–36.

Petrus, J.A., and Kamber, B.S. 2012. VizualAge: A Novel Approach to Laser Ablation ICP-MS U-Pb Geochronology Data Reduction. Geostandards and Geoanalytical Research, **36**: 247–270.

Poller, U., Huth, J., Hoppe, P., and Williams, I.S. 2001. REE, U, Th, and Hf distribution in zircon from western Carpathian Variscan granitoids: a combined cathodoluminescence and ion microprobe study. American Journal of Science, **301**: 858–876.

von Quadt, A., Gallhofer, D., Guillong, M., Peytcheva, I., Waelle, M., and Sakata, S. 2014. U-Pb dating of CA/non-CA treated zircons obtained by LA-ICP-MS and CA-TIMS techniques: impact for their geological interpretation. Journal of Analytical Atomic Spectrometry, **29**: 1618–1629.

Reimink, J.R., Chacko, T., Stern, R.A., and Heaman, L.M. 2016. The birth of a cratonic nucleus: Lithogeochemical evolution of the 4.02-2.94 Ga Acasta Gneiss Complex. Precambrian Research, **281**: 453–472.

Reiners, P.W. 2005. Zircon (U-TH)/He thermochronometry. Reviews in Mineralogy and Geochemistry, **58**: 151–179.

Rozel, A.B., Golabek, G.J., Jain, C., Tackley, P.J., and Gerya, T. 2017. Continental crust formation on early Earth controlled by intrusive magmatism. Nature 2017 545:7654, **545**: 332–335. Nature Publishing Group.

Rubatto, D. 2017. Zircon: The Metamorphic Mineral. Reviews in Mineralogy and Geochemistry, **83**: 261–295.

Sandiford, M., Hand, M., and McLaren, S. 1998. High geothermal gradient metamorphism during thermal subsidence. Earth and Planetary Science Letters, **163**: 149–165.

Sandiford, M., Mclaren, S., and Neumann, N. 2002. Long-term thermal consequences of the redistribution of heat-producing elements associated with large-scale granitic complexes. Journal of Metamorphic Geology, **20**: 87–98.

Schoene, B. 2013. U-Th-Pb Geochronology. *In* Treatise on Geochemistry: Second Edition. Elsevier Inc. pp. 341–378.

Sheikh, L., Lutfi, W., Zhao, Z., and Awais, M. 2020. Geochronology, trace elements and hf isotopic geochemistry of zircons from swat orthogneisses, northern Pakistan. Open Geosciences, **12**: 148–162.

Siégel, C., Bryan, S.E., Allen, C.M., and Gust, D.A. 2018. Use and abuse of zircon-based thermometers: A critical review and a recommended approach to identify antecrystic zircons. Earth-Science Reviews, **176**: 87–116.

Silke, R. 2009. The Operational History of Mines in the Northwest Territories, Canada. Northwest Territories Geologic Survey. Available from www.nwtgeoscience.ca.

Sizova, E., Gerya, T., Stüwe, K., and Brown, M. 2015. Generation of felsic crust in the Archean: A geodynamic modeling perspective. Precambrian Research, **271**: 198–224.

Smythe, D.J., and Brenan, J.M. 2016. Magmatic oxygen fugacity estimated using zircon-melt partitioning of cerium. Earth and Planetary Science Letters, **453**: 260–266.

Speight, S.C., Hanley, J.J., and McFarlane, C.R.M. 2023. Geodynamic evolution of felsic magmatism in the Yellowknife greenstone belt, N.W.T., Canada: evidence for Archean magmatism in a volatile-saturated environment. In prep., Fredericton, N.B.

Spencer, C.J., Kirkland, C.L., and Taylor, R.J.M. 2016. Strategies towards statistically robust interpretations of in situ U–Pb zircon geochronology. Geoscience Frontiers, **7**: 581–589.

Sun, S.S., and McDonough, W.F. 1989. Chemical and isotopic systematics of oceanic basalts: Implications for mantle composition and processes. Geological Society Special Publication, **42**: 313–345.

Thompson, P.H. 2006. Metamorphic Constraints on the Geological Setting, Thermal Regime, and Timing of Alteration and Gold Mineralization in the Yellowknife Greenstone Belt, NWT, Canada. *In* Gold in the Yellowknife Greenstone Belt, Northwest Territories: Results of the EXTECH III Multidisciplinary Research Project, Special Pub. No. 3. *Edited by* C.D. Anglin, H. Falck, D.F. Wright, and E.J. Ambrose. Geological Association of Canada Mineral Deposits Division. pp. 142–172.

Trail, D., Bruce Watson, E., and Tailby, N.D. 2012. Ce and Eu anomalies in zircon as proxies for the oxidation state of magmas. Geochimica et Cosmochimica Acta, **97**: 70–87.

Vanderhaeghe, O., Guergouz, C., Fabre, C., Duchêne, S., and Baratoux, D. 2019. Secular cooling and crystallization of partially molten Archaean continental crust over 1 Ga. Comptes Rendus Geoscience, **351**: 562–573.

Watson, E.B., and Harrison, T.M. 1983. Zircon saturation revisited: temperature and composition effects in a variety of crustal magma types. Earth and Planetary Science Letters, **64**: 295–304.

Watson, E.B., Wark, D.A., and Thomas, J.B. 2006. Crystallization thermometers for zircon and rutile. Contributions to Mineralogy and Petrology, **151**: 413–433.

Wendt, I., and Carl, C. 1991. The statistical distribution of the mean squared weighted deviation. Chemical Geology (Isotope Geoscience Section), **86**: 275–285.

Yang, W., Lin, Y., Hao, J., Zhang, J., Hu, S., and Ni, H. 2016. Phosphorus-controlled trace element distribution in zircon revealed by NanoSIMS. Contributions to Mineralogy and Petrology, **171**: 1–16.

4. Preliminary zircon-hosted silicate melt and mineral inclusion data from plutonic rocks of the Yellowknife greenstone belt, NWT: insights into pre-eruptive Archean magmas

4.1. Abstract

The Yellowknife greenstone belt (YGB) is in the Archean Slave Province of the Northwest Territories, Canada. The belt hosts two historic, high-grade gold deposits (the Con and Giant mines) that together produced ~13 Moz gold. Zircon-hosted silicate melt inclusions (SMI) from four lithologies in the YGB were analyzed to assess aspects of the quality of Archean SMI data (e.g., degree of preservation), identify saturated mineral phases at the time of MI entrapment, and evaluate the pre-eruptive metal characteristics of the YGB intrusions. This study focuses on samples from the Defeat Suite granite, quartz porphyry dikes, and the genetically related feldspar-quartz porphyry dikes and Ryan Lake Pluton tonalite. A systematic data filtering protocol was applied to semi-quantitative laser ablation-inductively coupled plasma-mass spectrometry (LA-ICP-MS) MI data to obtain a small dataset representing bulk SMI compositions. The evaluation of 50 inclusions from 47 zircon grains resulted in 7 MI representing primary magma compositions from the YGB intrusions. The remaining 43 analyses represent mixed mineral and melt inclusion (MMI) compositions that were examined separately.

The SMI data were compared to average YGB whole rock lithogeochemical data and show evidence of a less evolved tholeiitic affinity and metal enrichment, relative to the

whole rock data. Metals found to be relatively enriched in the SMI include Ag, As, Sb, Cu, Sn, W, Pb, and Bi which also showed higher concentrations in more fractionated melt compositions resulting from suspected metal-rich particles trapped together with more metal-rich melt. The mixed MMI were categorized based on the major, minor, and trace element data. The mixed MMI data provide direct evidence of mineral phases that were saturated and co-entrapped in zircon with silicate melt. The accessory phases identified include quartz, feldspars, apatite, biotite, amphibole, Fe-(Ti)-oxides, and suspected sulfides. This mineralogical evidence suggests that the studied FQP dike and related Ryan Lake Pluton tonalite magmas were H_2O-saturated and metal-enriched at their time of emplacement, ca. 2662 Ma. The SMI and mixed MMI Au concentrations show a moderate to strong positive covariance with Ag, As, Bi, Pb, Sn, W, and Mo and no correlation with Co, Cu, Sb, or Ta. Zircon-hosted SMI data from YGB dikes and plutons shows the preservation of an intrusion-related Au mineralization signature, and in general, demonstrates that MI studies may provide some insight into Archean systems despite their age and relatively poor preservation.

Keywords

Zircon-hosted melt inclusions, Archean silicate melt inclusions, Yellowknife greenstone belt, gold mineralization, intrusion-related gold, H_2O-saturation in Archean magmas

4.2. Introduction

Silicate melt inclusions (SMI) occur in a wide range of plutonic rocks (ultramafic to felsic) and represent an opportunity to study related magma compositions at different times

during pluton evolution (Thomas et al. 2003). Throughout mineral crystallization, droplets of melt and/or saturated mineral phases can become trapped along crystal growth zones or syn-magmatic fractures. This entrapment effectively removes the magma sample from the crystallizing intrusion and reflects magma chemistry at that point in time. The melt is trapped in a growing crystal or along healed fractures, along with possible accidentally entrapped solid (mineral) inclusions (Lowenstern 2003, Thomas et al. 2003, Chupin et al. 2006, Audétat and Lowenstern 2014, Lecumberri-Sanchez et al. 2021). When host phases trap primary melt and co-crystallizing mineral phases together, it changes the final inclusion composition and have been henceforth termed mixed mineral-melt inclusions (MMI).

Zircon-hosted SMI obtained from dikes and plutons may provide direct geochemical data related to a magma chamber and subvolcanic system, while the host also provides constraints on the age of the rock (Sobolev 1996, Thomas et al. 2003, Chupin et al. 2006, Mason et al. 2008, Hanley et al. 2020, Morales et al. 2022). Zircons are an ideal host to study due to their robust nature, resistance to alteration, and therefore post-emplacement modification, and have been shown to have very slow diffusions rates between host and inclusion, especially when compared to other rock-forming minerals (e.g., olivine, plagioclase) that are typically studied (Audétat and Lowenstern 2014, Hanley et al. 2020, Chang and Audétat 2021). Melt inclusion data record magmatic processes over a much smaller time scale compared to studying the whole rock geochemistry of a sample, which is the culmination of multiple processes and likely multiple episodes of

deformation and metamorphism (Audétat and Lowenstern 2014). Despite this small-time scale and the small size of zircon-hosted MI compared to MI hosted in other phases, evidence suggests that MI >15 um gives data representative of the bulk melt (Audétat and Lowenstern 2014).

SMI are composed of single or multiple phases, such as glass, crystals, and vapour bubbles (Sobolev 1996, Thomas et al. 2003). When SMI escape post-entrapment modification after dike or pluton emplacement, they can provide pre-emplacement compositional data (Audétat and Lowenstern 2014, Meagher 2020, Chang and Audétat 2021, Lecumberri-Sanchez et al. 2021). Incompatible elements that are often lost during devolatilization and segregation of magmatic fluids can then be measured (Sobolev 1996, Heinrich et al. 2003, Thomas et al. 2003, Mason et al. 2008, Audétat and Lowenstern 2014, Hanley et al. 2020, Lecumberri-Sanchez et al. 2021). These elements, potentially related to metallic mineralization, can provide a deeper understanding of the ore tenor in an evolving magmatic system (Audétat and Pettke 2003, Zajacz et al. 2008, Zhang and Audétat 2017, Hanley et al. 2020, Neyedley et al. 2020). SMI compositions and other trace element characteristics can also be used to reconstruct magmatic systems and identify intrusions with the same source. When studying magmatic systems that have an unknown relationship to mineralization, MI data and chemistry can be particularly useful for identifying a metal signature that may aid mineral exploration. There are several types of melt inclusions, and corresponding information, that may be encountered in a study such as SMI, sulfide melt or mineral inclusions, oxide minerals, or mixed silicate/sulfide/oxide

melt inclusions (MMI; Fig. 4.1). Sulfide melt (or mineral) inclusions are indicative of chalcophile metal collectors present early in the magmatic system. Oxide minerals that occur as inclusions (representing a saturated Fe-oxide) can be qualitatively used as a proxy for fO_2 and to indicate aTiO2 during early crystallization used for temperature calculations (Berry et al. 2008, Hanley et al. 2020). MMI provide the same types of information although in a more qualitative sense and cannot be used to directly comment on primary magma compositions.

Zircon-hosted SMI from intrusions are often subjected to multiple episodes of metamorphism, deformation, and post-solidus and hydrothermal alteration. Resulting post-entrapment modifications may limit the whole rock geochemical data obtained from SMI (Chang and Audétat 2021). The Yellowknife greenstone belt (YGB) has been subjected to four deformational events and extensive regional and contact metamorphism that has altered the host rocks (Martel and Lin 2006, Thompson 2006). However, the genetic association between mineralization and magmatism remains poorly understood and there is a spatial association between gold mineralization, intermediate and felsic dikes, regional plutons, and shear zones that crosscut these lithologies (Finnigan and Duke 2006, Ootes et al. 2006, Thompson 2006, Speight et al. 2023b). Very few studies focus on zircon-hosted inclusions in a granitic plutonic setting and there are no previous studies regarding Archean zircon-hosted MI in the YGB (Hanley et al. 2020).

The SMI and zircon hosts were analyzed to assess the quality of melt inclusion data obtained from zircons of this age. The results may reflect bulk silicate melt or mixed

mineral and melt inclusions, which could then be used to make inferences on the possible co-crystallizing phases and primary magma chemistry. This data would provide a greater understanding of magmatic-hydrothermal processes in the YGB, and potentially clarify the dike-pluton relationships to mineralization. Therefore, this pilot study aims to: (1) assess the quality of zircon-hosted SMI data from an Archean setting, (2) explore pre-emplacement metal-enrichment in YGB magmas, and (3) identify phases that were entrapped with silicate melt in zircon.

4.3. Regional Geology

The YGB is in the southwestern portion of the Archean Slave province in the NWT, Canada. The belt is part of the Yellowknife Domain and consists of supracrustal rocks that unconformably overlie the Central Slave Basement Complex and Central Slave Cover Group (Fig. 1.1; Henderson and Brown, 1966; Helmstaedt and Padgham, 1986; Bleeker et al., 1999b; Bleeker et al., 1999a). The belt trends north-south and consists of mafic and felsic metavolcanic sequences that have been intruded by calc-alkaline plutonic and synvolcanic intrusions (Henderson and Brown 1966, Isachsen and Bowring 1994, Helmstaedt 2006, Speight et al. 2023a).

The mafic and felsic metavolcanic sequences are sub-vertical with a southeast younging direction and are part of the Kam and Banting Groups. The Kam Group consists of four members, including the Chan, Crestaurum, Townsite, and Yellowknife Bay Formations. These units all have a mafic and tholeiitic signature, except for the Townsite Formation which is a calc-alkaline volcaniclastic sequence used as a marker horizon

throughout the YGB (Cousens 2000). The Banting Group unconformably overlies the Kam Group and consists of dominantly calc-alkaline, intermediate to siliceous volcaniclastic rocks with lesser tholeiitic mafic flows (Isachsen and Bowring 1994, Cousens et al. 2002). The YGB is overlain by conformable sediments of the Duncan Lake Group and an unconformable conglomeratic unit known as the Jackson Lake Formation (Helmstaedt and Padgham 1986, Cousens et al. 2006b, Martel and Lin 2006).

The YGB is intruded and surrounded by four major plutonic phases which include (from oldest to youngest) the Ryan Lake Pluton (RLP), the Defeat Suite granite, the Duckfish granite, and the Prosperous Suite (Bethune et al. 1999, Davis and Bleeker 1999, Ootes et al. 2007, Palmer 2018). The RLP is a tonalitic and granodioritic, multi-phases pluton with associated episodic magmatism between 2687 and 2647 Ma (Ootes et al. 2007, Speight et al. 2023a). The RLP is mostly obscured by the widespread Defeat Suite granite which consists of tonalite, granodiorite, diorite, and granite found on both the eastern and western margins of the YGB (Fig. 1.1; Davis and Bleeker, 1999; Bleeker and Hall, 2007). The Defeat Suite was intruded from 2630 – 2615 Ma and was followed by the intrusion of the Duckfish granite between 2608 and 2576 Ma (Isachsen 1992, Isachsen and Bowring 1994, Davis and Bleeker 1999, Bleeker and Hall 2007, Speight et al. 2023a). Finally, the Prosperous Suite is considered a late-orogenic granitic suite that intruded between 2608 and 2588 Ma (Palmer et al., 2018, and references therein). Extensive regional and contact metamorphism, due to the Defeat Suite, along with local seafloor and hydrothermal metamorphism, is prevalent throughout the YGB (Ootes and Lentz

2002, Thompson 2006). The belt was tilted and deformed before the deposition of the Jackson Lake Formation, after which the belt was subjected to further deformation, folding, and thrusting events before the intrusion of late-stage granites (Isachsen and Bowring 1994, Martel and Lin 2006).

4.3.1. YGB mineralization

The YGB is host to two historic gold mines which produced a total of ~13 Moz gold from the Con and Giant mines (Siddorn et al. 2006). The Con mine closed in 2003 after producing 5.8 Moz gold at 0.48 oz/ton while the Giant mine produced 7.1 Moz gold until 2004 at 0.45 oz/ton (Siddorn et al. 2006). Refractory ore, occurring as extremely fine-grained gold in arsenopyrite and arsenian pyrite, and free-milling native gold, can be found at both mines in varying proportions (Armstrong 1997, Siddorn et al. 2006). Previous research has suggested that mineralization occurred in multiple stages, which have been related to orogenesis, crustal anatexis, metamorphism, and spatial association with porphyritic dikes (van Hees et al. 1999, Finnigan and Duke 2006, Ootes et al. 2007, 2011).

In the YGB, refractory ore is associated with paragonitic muscovite, Al-rich chlorite, and Fe-Mg carbonate, while free-milling ore is associated with phengitic muscovite, chlorite, calcite, pyrite, and pyrrhotite (Armstrong 1997). The alteration observed at the mines is zoned from propylitic to phyllic alteration with silicification and carbonatization (or ankeritization) at the core. Previous research into mineralization has suggested that the ore at the Giant mine was enriched by fluids derived from proximal metasedimentary

units, including an associated enrichment in As, S, and Sb that correlates with gold ore bodies (van Hees et al. 1999, 2006a). The mineralization at the Con mine has been linked to the late-stage granite boom (ca. 2590 Ma) and the associated metamorphism (Ootes et al. 2011). Currently, the YGB is being extensively explored for new economically viable gold deposits in the vicinity of the Con and Giant mines, but also within the lower Kam and Banting Groups.

4.4. Methods

Dikes and plutons of interest were sampled for whole rock geochemical, petrography, and geochronologic studies, for which detailed descriptions and results can be found in Speight et al. (2023a; 2023b). Twelve samples for geochronology from six different lithologies were processed for heavy mineral separates, at Overburden Drilling Management Limited (Nepean, ON). Silicate melt inclusions were observed in zircons from all lithologies, but six samples were chosen for this preliminary study including: three FQP (SS18-008, SS18-125, SS18-128), one QZP (SS18-082), one tonalite (SS18-129), and one Defeat Suite granite (JS18-377). A subset of inclusion-rich zircons were handpicked using a binocular microscope, grouped by size and mounted in epoxy. Zircon mounts were polished until representative inclusions were near the crystal surface, but not exposed; sorting of zircon grains into two size fractions helped with this. Zircon-hosted SMI were imaged using a Nikon Eclipse E600 polarizing microscope beforehand, and photomicrographs were taken with a Zeiss AxioImager microscope at the University of New Brunswick. Exposed inclusions were identified during other imaging of zircons for

geochronologic analysis. These exposed inclusions were imaged and qualitatively characterized with a JOEL 6400 scanning electron microscope with energy dispersive spectrometer (SEM-EDS) operated at a beam current of 1.5 nA and an accelerating voltage of 15 kV.

Laser ablation-inductively coupled plasma-mass spectrometry (LA-ICP-MS) is an effective approach for analyzing unhomogenized, multiphase SMI as it is relatively insensitive to matrix effects and involves ablation of the entire inclusion and host phase (Audétat and Lowenstern 2014). Inclusions were not homogenized due to the risk of decrepitation and a subset of the zircon grain mount was also used for U-Pb geochronology, therefore heating and homogenization experiments would have risked damage to the entire grain mount. Zircon-hosted melt inclusions were analyzed in their entirety, along with the host, by LA-ICP-MS at the Magmatic and Ore-Forming Processes Research Laboratory at the University of Toronto. These data were collected using an NWR-193 UC laser ablation system equipped with an Agilent 7900 quadrupole mass spectrometer. The instrument was tuned to ThO/Th and mass-21/mass-42 ratios of <0.2 %, U/Th = 115-120 % using NIST 610 glass for in-house tuning together with rutile and 91500 zircon were used as standards to calibrate analyte sensitivities and monitor some interfering oxide production rates. Gas flow rates were 0.84 L/min and 0.16 L/min for He and Ar, respectively, and dwell times of 10 ms were used. A fluence of 7 J/cm^2, a repetition rate of 10 Hz, and a spot size of 40 µm were used for each ablation. Inclusion ablations were bracketed by standards, each ablation involved 40 seconds of background (laser-off)

prior to ablation. A total of 47 inclusions were ablated and laser drilling of three zircon grains revealed two MI in each, which returned 50 inclusion analyses total. The isotopes measured were ^{11}B, ^{23}Na, ^{25}Mg, ^{27}Al, ^{29}Si, ^{31}P, ^{39}K, ^{44}Ca, ^{49}Ti, ^{51}V, ^{55}Mn, ^{56}Fe, ^{59}Co, ^{65}Cu, ^{75}As, ^{85}Rb, ^{88}Sr, ^{89}Y, ^{91}Zr, ^{93}Nb, ^{95}Mo, ^{107}Ag, ^{118}Sn, ^{121}Sb, ^{133}Cs, ^{137}Ba, ^{139}La, ^{140}Ce, ^{141}Pr, ^{146}Nd, ^{147}Sm, ^{153}Eu, ^{157}Gd, ^{159}Tb, ^{163}Dy, ^{165}Ho, ^{166}Er, ^{169}Tm, ^{172}Yb, ^{175}Lu, ^{178}Hf, ^{181}Ta, ^{182}W, ^{197}Au, ^{208}Pb, ^{209}Bi, ^{232}Th and ^{238}U.

The resulting mixed zircon SMI raw data were quantified using the software SILLS (Guillong et al. 2008). Transient LA-ICP-MS profiles were visually evaluated for inclusion intersection (indicated by an increase in melt-compatible, zircon-incompatible major and minor trace elements) and integrations were set to yield background, inclusion (occasionally more than one), and host phase compositions via deconvolution-corrected within the SILLS program (Fig. 4.2). Inclusions were intersected after 5-10 seconds of ablating the host zircon. Inclusions were quantified using a total oxide value of 95 wt. %, Zr exclusion (from the host-phase only) of 47 wt. %, and internal standardization was done using the Al_2O_3 concentrations from the individual sample (ranging from 12.98 – 14.76 wt. %).

4.5. Results

4.5.1. Petrography

4.5.1.1. Sample descriptions

Zircon-hosted melt inclusions were evaluated from six samples from the YGB, including 3 FQP dikes, a QZP dike, a RLP tonalite, and a Defeat Suite granite sample (Fig. 4.3). A detailed description of each lithology can be found in Speight et al. (2023a; 2023b). The samples were initially collected for whole-rock geochemistry and U-Pb geochronology of zircons obtained from mineral separates. The FQP dikes are 1 to 5 m wide with sharp contacts, porphyritic with medium- to coarse-grain, blocky feldspar phenocrysts and fine- to medium-grained subrounded quartz phenocrysts set in a quartz, feldspar, and biotite-rich groundmass. These dikes show variability in the degree of alteration and deformation, particularly concerning the preservation of feldspar phenocrysts. Two of the FQP samples (SS18-125 and SS18-128) show a higher degree of sericitic alteration, typically distinguished by the differential weathering of phenocryst observed in the field and examination of polished thin sections. The QZP dikes are 2 to 5m wide with sharp contacts, fine- to medium-grain, rounded quartz phenocrysts set in a microcrystalline groundmass. The RLP tonalite sample has a grey to dark grey weathered surface and dark grey and white fresh surface. The tonalite is inequigranular and dominated by medium- to coarse-grained blocky feldspars and sub-rounded fine- to medium-grained quartz, with

fine-grained interstitial biotite. The Defeat Suite granite is equigranular, coarse-grained, and dominated by K-feldspar and quartz, with lesser amounts of plagioclase and biotite.

4.5.1.2. Zircon-hosted inclusion descriptions

The zircon-hosted melt inclusions analyzed in this pilot study were first identified in a U-Pb geochronology study of zircons by Speight et al. (2023b); a summary of the host zircons is given here. Zircons range in size from 40 to 250 µm, with aspect ratios mainly from 1:1 to 1:3, and some acicular grains with ratios up to 1:5. Three dominant grain colour populations were recognized colourless, violet, and yellow (Fig. 4.4; Speight et al., 2023b). Melt inclusions were observed in all three colour variants of zircon. The zircon host grains are subhedral to euhedral, translucent to cloudy. Colourless grains are typically acicular, while the violet grains have a faceted 'soccer-ball' shaped. Yellow zircons are the smallest with a smaller aspect ratio (1:1 – 1:2) and are more "pill"-shaped. Colourless zircons are the most abundant, whereas violet grains are second in abundance, and yellow zircons are the least abundant.

Zircon-hosted melt inclusions are spherical to ovoid, with most ranging from 7 to 25 µm in long dimension, and typically with a 1:1 to 1:2 aspect ratio unless the inclusion has a tubular shape parallel to the zircon c-axis, in which case the aspect ratios are ~1:8 (9 x 78 um). The inclusions are variably opaque with a dark grey-black to red-brown colour. The inclusions can be found anywhere from the cores of zircons to outer growth zones, and there are typically only one to two inclusions in a grain. Zircons from the YGB dikes and intrusions are considered magmatic based on their Th/U ratios (all > 0.1 except for

two QZP analyses) and their REE profiles (Speight et al. 2023b). Therefore, any chemistry obtained from the inclusions can be considered primary, barring any post-entrapment modifications which are mitigated by the study of robust zircons and abundant data filtering (Speight et al. 2023b).

4.5.1.3. SEM-BSE imaging of exposed inclusions

Although exposed melt inclusions are small, a qualitative chemical analysis was obtained to attempt to identify the solid inclusion contents (Fig. 4.5). The inclusions show finely crystallized daughter products that do not cross inclusion boundaries and are likely the product of cooling and crystallization of the entrapped melt. By looking at the nature of the exposed inclusions (their occurrence within the inclusion versus minerals that cross the inclusion boundaries) and the LA-ICP-MS ablation profiles (looking for the nugget effect and co-varying elements that indicate a mineral) we can infer that some phases were accidentally trapped with melt during zircon growth. Accidental inclusions of apatite were identified during SEM-BSE imaging of exposed zircons (Ca-P; Fig. 4.5A-C), and in one instance the apatite is enriched in REE. One zircon has two inclusions that do not appear to be crystallized (Fig. 4.5A). However, these inclusions show gradational changes in the chemistry, with areas enriched in Si, Si-Al-K, Si-Al-Na, and Si-Al-Mg-Fe, suggesting it is finely recrystallized with mineralogically distinct domains. One polycrystalline inclusion contains a phase rich in Si-Al-Mg-K-Fe with a platy texture, possibly a daughter biotite crystal or accidentally entrapped biotite (Fig. 4.5B). The zircon-hosted inclusions are

typically spherical to ovoid; however, tubular inclusions have also been observed (Fig. 4.5C).

4.5.2. LA-ICP-MS results for zircon-hosted SMI and mixed MMI

4.5.2.1. LA-ICP-MS ablation profiles

The method yields complex, transient ablation profiles that can be used to determine the composition of the inclusion in the zircon-host (Fig. 4.6). For example, when the signals showed a complex pattern that suggests an accidentally trapped phase in the inclusion (e.g., by high-count intensity Ca-P indicating accidental apatite), it was noted since these analyses couldn't be used to represent primary magma composition. It is often challenging to differentiate trapped melt from mixtures of melt and small, accidentally trapped crystals. Therefore, various levels of data filtering and grouping were used to assess and categorize the inclusions. For instance, contaminated SMI typically show a smooth ablation profile with several co-varying elements (Fig. 4.6A). Co-entrapped phases can be identified when a smooth and coincident signal involving major and trace elements in melt interpreted by separate higher intensity features related to entrapped phases, such as sulfides (e.g., Fe, and metals such as Pb, Cu, As, Sb), oxides (e.g., Fe, Ti, V, Cr), or phosphates (Fig. 4.6B). The related elements tied to the mineral inclusions co-vary separately from the main melt phase (e.g., Ca and P in Fig. 4.6B), which suggests an apatite grain. Some ablation profiles show more chaotic signals for which it is harder to

distinguish individual phases in; these may represent mixed MMI containing melt and more than one accidental phase (Fig. 4.6C).

4.5.2.2. Data filtering of semi-quantitative analyses

To determine which inclusions are representative of primary magmas that do not contain accidentally trapped phases, the major, minor, and trace element data exported from SILLS was examined via a flow sheet discrimination approach (Fig. 4.7). This data filtering approach chemically identifies trapped mineral phases but does not resolve the effects of post-entrapment modification of the bulk SMI chemistry. An inclusion with silicate melt plus a mineral phase indicates co-entrapment, which causes overall changes to the resulting LA-ICP-MS chemical data due to inclusions being ablated in their entirety by laser drilling. To remove these analyses from the dataset, data were filtered first to select analyses with > 40 wt. % SiO_2, then the subset was filtered to select data with < 50 wt. % FeO_T, then < 5 wt. % TiO_2, and finally < 5 wt. % P_2O_5. Each value was chosen to represent a common mineral phase or chemical parameter. For example, to capture SMI that have alkali basalt compositions (SiO_2 between 46 and 48 wt. %), SMI data with less than 40 wt. % SiO_2 were excluded from the final SMI dataset (Frost and Frost 2014). Three phases observed during SEM-EDS imaging of exposed inclusions and considered possible accidentally trapped phases include Fe-Mg-silicates, Ti-oxides, and apatite and were considered during the development of this flow-sheet discrimination protocol, along with Fe-oxides and sulfides. To exclude data that may have altered chemistry due to accidentally trapped phases, FeO_T, TiO_2, and P_2O_5 were included (Fig. 4.7). LA-ICP-MS SMI

ablation data with a composition > 50 wt. % FeO_T were excluded to account for Fe-Mg silicates, Fe-oxide, and/or sulfides that were trapped along with silicate melt. The remaining data were also filtered to remove results with > 5 wt. % TiO_2 and P_2O_5 to account for Ti-oxides and apatite contamination of SMI. The lithogeochemical results for the corresponding samples indicate that the studied YGB lithologies have > 54 wt. % SiO_2, < 10 wt. % FeO_T, < 1 wt. % TiO_2, and < 0.4 wt. % P_2O_5, therefore, the chosen data filtering values remove contaminated analyses while preserving potential SMI analyses that can be further evaluated.

This data filtering protocol narrowed the inclusion dataset down from 50 inclusions to 13 inclusions that represent possible SMI; these analyses were looked at individually and further narrowed down to seven bulk SMI with the least amount of contamination and best qualitative data; this categorization is listed in Table 4-1 and Table 4-2. Evaluation of only the inclusions classified as silicate melt inclusions leads to a much more limited dataset. However, we can comment more directly on pre-eruptive magma entrapped in crystallizing zircon. Filtering the data in this way was found to remove analyses with oxide (Fe or Ti) and phosphate solid inclusions.

4.5.2.3. Classification of inclusions

An initial semi-quantitative export of zircon-hosted MI data from the SILLS program was done to evaluate which inclusions represent primary silicate melts, once complete the seven SMI analyses were further quantified and a second export was done. The remaining 43 inclusion analyses are therefore semi-quantitative. A qualitative analysis of the MI data

indicates that most MI are heterogeneous and multi-phase (e.g., silicate melt plus Fe-Ti oxide). Of the 50 zircon-hosted heterogeneous inclusions, 31 show evidence of silicates or silicate melt, representing 62% of the data (Fig. 4.8). These include inclusions of SMI, silicates and apatite, silicates and sulfides, silicate minerals, silicate minerals and other phases (oxides, sulfides, phosphates). The categories of inclusions observed are given in Table 4-1, along with an accounting of which inclusion types were present in each sample.

The four main groups that make up 52% of the inclusions are silicates and apatite (18%), SMI (14%), silicates and sulfides (12%), and sulfides ad oxides (8%; Fig. 4.8). The remaining categories consist of different combinations of minerals, such as apatite, silicates, sulfides, oxides, and unknowns. These other inclusions which appear to have accidentally trapped phases or mixtures of mineral inclusions are considered mixed and have been termed melt and mineral inclusions (MMI). Only the analyses identified as SMI should be considered the most representative of trapped primary magmas.

4.5.3. SMI and mixed MMI chemistry

4.5.3.1. Major and trace elements vs. SiO_2 for SMI and MMI

Data from both the SMI and mixed MMI are summarized in Table 4-2 and plotted together in Fig. 4.9 to observe the behaviour of major and trace elements during progressive fractionation. In these figures, SiO_2 is used as a proxy for fractionation, since SiO_2 increases with fractionation (i.e., higher SiO_2 values relate to increased fractionation). Zircon-hosted SMI have between 40.4 and 74.7 SiO_2 wt. %, whereas the mixed MMI have

a wider range from below detection to 79.5 wt. % SiO_2 (Table 4-2; Fig. 4.9). When the Na_2O, K_2O, CaO, Mg #, TiO_2, Cs, and As are plotted against SiO_2, the SMI consistently have a smaller range of data compared to the mixed MMI which have accidentally trapped phases that change the overall chemistry of the inclusions. The SMI shows a range from below detection to 0.591 wt. % Na_2O with no correlation to increasing SiO_2, and the mixed MMI range from below detection to 9.57 wt. % Na_2O (Fig. 4.9A). The SMI show decreasing K_2O concentrations from 11.7 to 1.86 wt. % with increasing SiO_2, and therefore progressive fractionation; the MMI range from below detection to 37.5 wt. % K_2O (Fig. 4.9B). The SMI from FQP dikes also shows a linear relationship between decreasing K_2O and increasing SiO_2. The CaO concentration of the SMI shows a range from 0.481 to 7.79 wt. % CaO and data decrease with increasing SiO_2 (Fig. 4.9C). There is also a break in the SMI, where two FQP dike analyses have CaO between 4.34 to 7.79 wt. % and the tonalite and Defeat Suite granite data have CaO between 0.481 to 0.873 wt. % (Table 4-2). The mixed MMI data show a large range in CaO values from below detection to 66.6 wt. %, corresponding to the abundant apatite minerals within the inclusions.

The Mg # (molar $MgO/(MgO+FeO_T)*100$) of the SMI effectively separates the FQP dike and Defeat Suite granite from the tonalite samples and shows two different trends concerning increasing SiO_2 (Fig. 4.9D). The FQP dike SMI have Mg # of 1.7 to 35 and the Defeat Suite granite SMI has an Mg # of 15, whereas the tonalite SMI have Mg # between 39 and 56. The FQP dike SMI also shows a linear relationship between increasing Mg # and SiO_2, and the tonalite samples do not. The Mg # of the mixed MMI shows that the

tonalite samples overlap with FQP dike MMI (Mg # = 0.25 – 84); however, the tonalite overall have a narrower range in Mg # from 1.0 to 50 (Fig. 4.9D). The TiO_2 concentration of SMI has a narrow range from 0.0187 to 0.494 wt. % and have a linear, negative relationship with increasing SiO_2; the MMI data range from below detection to 47.1 wt. % TiO_2 (Fig. 4.9E). The Cs concentration of the SMI ranges from 2.13 to 6.79 ppm and can be further subdivided by lithology (Fig. 4.9F). The FQP dike inclusions have Cs values of 2.13 to 4.08 ppm while the tonalite and Defeat Suite granite have Cs values of 4.38 to 6.79 ppm. Only 24 of the mixed MMI have Cs concentrations above detection, ranging from 0.289 to 136 ppm, although most of these (18 of the 24 MMI) have Cs values between 0.289 and 6.52 ppm. Finally, the As concentrations were compared to SiO_2 since As is often a proxy for other precious metals (including Ag, and Au) and it was found that the SMI have variable As concentrations from 15.7 to 1692 ppm (Fig. 4.9G). The mixed MMI have a broader range in As values, with 32 inclusions having As values between 16.1 and 6676 ppm, and two inclusions have As concentrations of 14,719 and 116,843 ppm.

4.5.3.2. Comparison of SMI and lithogeochemical data

To evaluate whether the primary SMI have a less evolved signature than the final lithologies, the SMI data were plotted together with average lithogeochemical data from previous research in the YGB (Speight et al. 2023a). In the AFM diagram, we can see that the FQP dikes are depleted in MgO relative to the tonalite samples, which makes sense since they are considered to be sourced from the tonalite, although both lithologies show a progressive shift to the more alkali-rich endmember and their final whole-rock

geochemical composition (Fig. 4.10A; Irvine and Baragar, 1971; Speight et al. 2023a, b). Of the SMI data, five of the seven inclusions plots in the tholeiitic field, compared to nearly all the average lithogeochemical data which plot in the calc-alkaline field, except for the average Slave Province basalt which plots in the tholeiitic field as well. When the data are plotted together on a TAS diagram, the SMI have a range in compositions from basaltic andesite to trachydacite and dacite (Fig. 4.10B). However, the average lithogeochemical data have a more evolved signature from basalt to rhyolite, despite overlapping with the SMI data.

4.5.3.3. Comparison of SMI metals vs. Mg

The Mg # effectively separates the tonalite SMI from the FQP dike SMI and was compared to various metals, including As, Sb, Cu, Mo, Sn, W, Pb, and Bi (Fig. 4.11). These data were also plotted with average lithogeochemical data from the corresponding lithologies from Speight et al., (2023a), and upper continental crust data for comparison (Rudnick and Gao 2003). All the silicate mount inclusion As data are enriched relative to the average lithogeochemistry except for one FQP dike analysis, which overlaps with the lithogeochemical data; with the exception of that one point, there is a strong negative covariance between decreasing As concentrations and the increasing Mg # of SMI (Fig. 4.11A). The SMI have As concentrations of 15.7 to 1692 ppm (Table 4-2). The Sb concentrations of the SMI are all at least one order of magnitude higher than the average whole rock data and show a weak negative covariance between decreasing Sb and increasing Mg # (Fig. 4.11B). The SMI have Sb concentrations of 14.6 to 1635 ppm. The Cu

values of the bulk SMI data are also all enriched relative to the whole rock data, however, there is no consistent covariance with increasing Mg # (Fig. 4.11C). The SMI have Cu concentrations of 106 to 834 ppm. Only two SMI had Mo concentrations above the detection limit, however, one of these values Is the least enriched in Mo (Defeat Suite granite) and the other analysis (tonalite) overlaps with the average whole rock data (Fig. 4.11D). The SMI have Mo values of 0.622 and 2.28 ppm. The Sn values of the SMI are all elevated compared to the lithogeochemical data and show a negative covariance between decreasing Sn and increasing Mg # (Fig. 4.11E). The SMI have Sn concentrations of 3.46 to 55.7 ppm. The W concentrations of the SMI are slightly more variable although they are typically more enriched in W than the average whole rock data; 2 of the SMI analysis overlap with the full rock data (Fig. 4.11F). The SMI have W concentrations of 1.66 to 176 ppm. Of the 7 SMI analyses, only three showed Pb data above the detection limit and all three analyses are enriched in Pb compared to the average lithogeochemistry (Fig. 4.11G). The SMI have Pb concentrations of 493 to 4194 ppm. Finally, the Bi concentrations of SMI were compared to the Mg # and show an enrichment of Bi compared to the whole rock data; the Bi values also show a negative covariance between decreasing Bi and increasing Mg # (Fig. 4.11H). The SMI have Bi concentrations of 1.14 to 102 ppm. In all cases except one, the SMI are enriched in metals compared to the whole rock data (i.e., As, Sb, Cu, Sn, W, Pb, and Bi). The only metal that does not follow this trend is Mo, which is relatively depleted compared to the whole rock data (Fig. 4.11D). Despite the efforts to limit analyses identified as primary SMI that may be contaminated, the

elevated metal concentrations suggest that nanocrystals of metal-rich alloys and/or sulfides were accidentally entrapped in some of these inclusions.

4.5.3.4. Mixed MMI metal concentrations

Although the mixed MMI data contain accidentally trapped phases that are mixed with primary melt, the data obtained from them can still give valuable information regarding saturated phases that may have been present at the time of zircon crystallization (Table 4-2). Many of these inclusions contain metals that may be occurring as alloys, therefore various metals were plotted together to characterize their trends and compare them with the LA-ICP-MS ablation profiles. Of the 50 zircon-hosted inclusions that were encountered, 28 % of inclusions contained sulfides and overall, 60 % were categorized as having a combination of sulfides, oxides, or unknown phases (Fig. 4.8). The complete list of metals encountered in the inclusions consists of Ag, As, Au, Bi, Co, Cu, Mo, Pb, Sb, Sn, Ta, and W, although not every metal was noted in each inclusion. The raw LA-ICP-MS ablation profiles were also examined for peaks related to these metals, to confirm their presence.

4.5.3.4.1. Ag vs. As concentrations

The Ag and As concentrations of mixed MMI were plotted together and found to have a strong, co-varying positive relationship (Fig. 4.12A). The Ag and As values from the upper continental crust were also shown with the MMI data from this study; all MMI data plotted above the Ag and As values of the upper continental crust (Rudnick and Gao 2003). Fig. 4.12 also shows raw LA-ICP-MS ablation profiles for the most Ag and As

enriched inclusion, highlighted in Fig. 4.12A. A select element list has been shown in each LA-ICP-MS ablation profile, consisting of Zr, Al, K, Na, Fe, Cs, Rb, Sr, and As with various metals shown in subsequent figures. The LA-ICP-MS raw counts indicate that Al, Fe, Sr, As, Sb, Au, and Ag are all enriched and generally co-vary in the zircon-hosted inclusion (Fig. 4.12B). The ablation profile also suggests that As, Ag, and Au are co-varying since they share a similar profile shape, in contrast to Sb. The raw LA-ICP-MS counts for Cu and Mo were also shown and Cu values increase within the inclusion while Mo counts remain low (Fig. 4.12C). Finally, Sn, W, Pb, and Bi ablation profiles were plotted and Pb and Bi can be observed co-varying (with Fe-Al-Sr) and increasing within the inclusion, while Sn and W counts remain low (Fig. 4.12D).

4.5.3.4.2. Mo vs. Cu concentrations

The Mo and Cu concentrations of mixed MMI were plotted together and found to have a strong, co-varying positive relationship (Fig. 4.13A). The Mo and Cu values from granite melt inclusions of Audétat and Pettke, (2003) are also shown from samples with comparable Cs concentrations, indicating approximately the same degree of fractionation as the rocks in this study. Of the 26 mixed MMI with Mo and Cu data, 58 % are found to have Mo and Cu values above the MI data from barren granites (Audétat and Pettke 2003). Fig. 4.13 also shows raw LA-ICP-MS ablation profiles for the most Mo and Cu enriched inclusion, highlighted in Fig. 4.13A. A select element list has been shown in each LA-ICP-MS ablation profile, consisting of Zr, Al, K, Na, Fe, Cs, Rb, Sr, and As with various metals shown in subsequent figures. The LA-ICP-MS raw counts indicate that Al, K, Fe, Rb,

Sr, As, Sb and Ag are all enriched in the zircon-hosted inclusion (Fig. 4.13B). The ablation profile also suggests that As, Ag, and Sb co-vary within the inclusion as they have similar profile shapes, which is also the case for K, and Rb. The raw LA-ICP-MS counts for Cu and Mo were also shown and both Cu and Mo counts increased within the inclusion (Fig. 4.13C). Finally, Sn, W, Pb, and Bi ablation profiles were also plotted and Pb and Bi can be seen co-varying and increasing within the inclusion, while Sn and W counts remain low (Fig. 4.13D).

4.5.3.4.3. W vs. Sn concentrations

The W and Sn concentrations of mixed MMI were plotted together and found to have a strong, co-varying positive relationship (Fig. 4.14A). The W and Sn values from granite melt inclusions of Audétat and Pettke, (2003) are also shown from samples with comparable Cs concentrations, indicating approximately the same degree of fractionation as in this study. Of the 23 mixed MMI with W and Sn data, 83 % are found to have W and Sn values above the MI data from barren granites (Audétat and Pettke 2003). Fig. 4.14 also shows raw LA-ICP-MS ablation profiles for the most W-enriched inclusion, highlighted in Fig. 4.14A. A select element list has been shown in each LA-ICP-MS ablation profile, consisting of Zr, Al, K, Na, Fe, Cs, Rb, Sr, and As with various metals shown in successive figures. The LA-ICP-MS raw counts indicate that Al, K, Na, Fe, Cs, Rb, As, and Sb are all enriched in the zircon-hosted inclusion (Fig. 4.14B). The ablation profile also suggests that Fe, As, Sb, and Na co-vary within the inclusion as they have similar profile shapes, which differs from the co-varying profiles of Al, K, Cs, and Rb. The raw LA-ICP-MS counts for Cu

and Mo were also shown and Cu counts increase and co-vary with Fe and As, although Mo counts remain low within the inclusion (Fig. 4.14C). Finally, Sn, W, Pb, and Bi ablation profiles were also plotted and W, Pb and Bi have increasing counts within the inclusion, while Sn counts remain low (Fig. 4.14D). The Pb and W signals share a similar shape with Fe and As, while Bi has a similar ablation profile to the K and Al-rich areas of the inclusion. Sn has some small increases in counts that suggest the Sn may co-vary with Fe and As within the inclusion.

4.6. Discussion

This preliminary study of zircon-hosted melt inclusions in the Archean YGB aimed to assess the quality of semi-quantitative MI data obtained from a setting of this age, identify co-crystallizing phases with zircon, and determine pre-emplacement metal characteristics. Archean greenstone belts typically undergo multiple stages of deformation and metamorphism, which can cause post-entrapment modification of inclusions (Chang and Audétat 2021). Therefore, one of the goals of this study was to ascertain whether meaningful and useful data could still be obtained. This data could then be used to give insight into the YGB intrusions as possible sources of mineralization (van Hees et al. 1999, 2006b, Shelton et al. 2004, Siddorn et al. 2006). Despite the qualitative nature of these melt inclusion results, they provide an opportunity to add to the information about these magmatic and synvolcanic intrusions that cannot be obtained by petrography or lithogeochemistry alone. Zircons from four lithologies were examined in this study, including FQP dikes, a QZP dike, RLP tonalite, and Defeat Suite granite. The

tonalitic RLP sample in this study is from a previously unmapped outcropping of the RLP. Previous work has established that the FQP dikes are genetically related to and part of the magmatic plumbing system of the multi-phase RLP, represented here by the tonalite (Speight et al. 2023a, 2023b). The QZP dikes are related to an older unknown source and the Defeat Suite granite is the youngest in this sample set. Since the FQP dikes and RLP tonalite are genetically related intrusions, their results can be directly compared. Melt inclusions in zircons obtained from these mineral separates were analyzed due to the robust nature of zircon and its ability to resist alteration (Neyedley et al. 2020, Chang and Audétat 2021). Examination of the hand samples and corresponding thin sections for the YGB dikes and plutons show variable hydrothermal alteration, occurring as sericitization and chloritization of primary minerals (Fig. 4.3; Speight et al., 2023a; Speight et al., 2023b).

4.6.1. Implications of SMI and mixed MMI mineralogy

The zircon-hosted MI data were categorized based on the major, minor, and trace elements observed (Table 4-1). The raw LA-ICP-MS ablation profiles were also examined to identify co-varying elements that are indicative of accidentally trapped minerals in the MI (e.g., Fig. 4.6). For example, when Ca and P are observed with rising counts at the same time interval in an ablation profile, it suggests that an apatite crystal is present; this can then be confirmed in the exported data. Although this is limited qualitative data, valuable information regarding saturated minerals in the Archean YGB intrusions can still be obtained. Based on the categories identified in these samples for the 50 inclusions

encountered, the SMI and mixed MMI data from these intrusions indicate that they are rich in accessory phases (Table 4-1). The inclusion data were qualitatively compared to the ideal mineral chemistry of common rock-forming minerals that may be found in a crystallizing Archean magma system (e.g., quartz, feldspars, biotite, amphibole, apatite, Fe-(Ti)-oxides, sulfides). A total of 14 combinations of melt and minerals were observed in the inclusion data and their relative proportions are shown in Fig. 4.8 and summarized in Table 4-1. Early accessory phases (apatite, ilmenite, rutile) could have sequestered metals. Apatite was encountered in 48 % of inclusions and silicate minerals were present in 54% of the inclusions. The minerals were also observed in exposed zircon-hosted MI during SEM-BSE imaging (Fig. 4.5). Minerals consistent with quartz, feldspars, biotite, amphibole, and apatite were all semi-quantitatively identified during SEM-BSE imaging, which corresponds to silicate mineralogy observed in the YGB MI data (Table 4-2). Despite the limited data, the identification of hydrous minerals (i.e., biotite, amphibole) in these primary melts suggests that these phases were co-crystallizing with zircon at the time of entrapment and the related magmas contained dissolved H_2O. Primary amphibole have also been identified during petrographic analysis of the RLP tonalite and magmatic plagioclase was observed in both the tonalite and the FQP dikes (Speight et al. 2023a, 2023b). Speight et al., (2023a) determined that the YGB dikes and plutons were crystallizing primary amphibole and plagioclase from a garnet-bearing source, based on a comparison of lithogeochemical data. The SMI and mixed MMI data presented here confirms the presence of these primary co-crystallizing phases.

4.6.2. SMI composition compared to lithogeochemistry

Of the 50 zircon-hosted inclusions encountered in this study, the dataset was progressively narrowed down to seven analyses which are considered to represent trapped primary melts from the YGB tonalite, FQP dikes, and Defeat Suite granite. This was accomplished by initially evaluating the major and minor elements in each analysis and filtering out data that contained < 40 wt. % SiO_2, > 50 wt. % FeO_T, > 5 wt. % TiO_2, and > 5 wt. % P_2O_5 (Fig. 4.7). This first pass at data filtering effectively removed analyses that encountered accidentally trapped phases of Fe-, Ti-, or P-rich minerals. Each remaining analysis was then evaluated for contamination from accidentally trapped solid phases, which yielded seven SMI (Table 4-2). These seven SMI are considered the most representative of primary magma compositions for each corresponding lithology; no SMI were identified from the QZP dike.

The SMI data were plotted on traditional geochemical plots including Harker-style diagrams, an AFM diagram, and a TAS diagram to observe chemical changes during progressive fractionation (Fig. 4.9 -Fig. 4.11; Irvine and Baragar, 1971; le Bas et al., 1986). Average lithogeochemical data from the corresponding lithologies, Slave Province basalt, and the upper continental crust were also plotted for comparison (Rudnick and Gao 2003, Speight et al. 2023a). The Harker-style bivariant plots indicate that K_2O, CaO, and TiO_2 were decreasing with fractionation, interpreted here to be represented by increasing SiO_2 (Fig. 4.9B, C, E). The Mg # was found to effectively separate the FQP dike and tonalite data, indicating that the tonalite SMI are less evolved (i.e., higher Mg #) than the FQP dike

SMI which have lower Mg # (Fig. 4.9D). This is to be expected since the multi-phase RLP is considered the magmatic source of the FQP dikes (Speight et al. 2023b, 2023a). The Mg # of the Defeat Suite granite overlaps with the FQP dikes.

The SMI have a narrow range in Cs concentrations, from 2.13 to 6.79 ppm, which suggests that they have a similar degree of fractionation (Fig. 4.9F). When the data are considered per lithology, the FQP dikes SMI have a lower range in Cs concentrations, from 2.13-4.08 ppm, while the tonalite and Defeat Suite granite SMI have Cs values of 4.38 to 6.79 ppm. This is not the expected trend, considering the SMI Mg # and parental nature of the tonalite to the FQP, the least evolved tonalite SMI should have the lower Cs values compared to the more fractionated FQP dike SMI (Audétat and Pettke 2003, Zajacz et al. 2008). This unexpected Cs trend was also observed in the lithogeochemical data, where the least fractionated tonalites had the most enriched Cs concentrations compared to the more evolved FQP dikes (Speight et al. 2023a).

When the SMI are compared to average lithogeochemical data from the corresponding lithologies and Slave Province basalt, the SMI nearly always show a less evolved signature concerning major elements and are more enriched in metals (Fig. 4.10; Irvine and Baragar, 1971; le Bas et al., 1986; Speight et al., 2023a). The AFM diagram shows that the SMI have a more tholeiitic signature, and therefore, they do represent less evolved primary melts of the rocks (Fig. 4.10A). The Mg # and various metals from the SMI were also compared with average lithogeochemical data and the upper continental crust to determine whether primary enrichment of metals can be observed in these

Archean zircon-hosted inclusions. Of the eight metals (As, Sb, Cu, Mo, Sn, W, Pb, and Bi) that were plotted against the SMI Mg #, they were all enriched relative to the average lithogeochemical data except for Mo (Fig. 4.11). Only two SMI have Mo concentrations above detection, and they overlap with average whole rock data at lower concentrations (Fig. 4.11). Despite the overlapping data, the Mo concentrations of one tonalite SMI is enriched relative to the upper continental crust value (Rudnick and Gao 2003).

The Mg # also relates to the degree of fractionation that a sample has undergone, therefore metals that show a negative relationship with the Mg # were becoming more enriched as crystallization and fractionation progressed. All the metals examined here (As, Sb, Cu, Sn, W, Pb, and Bi) except Mo have this negative relationship with the SMI Mg # (Fig. 4.11). The fact that the SMI were enriched by one to two orders of magnitude in metals (e.g., Sb, Sn, Pb) suggests that nanocrystals of sulfides may be accidentally trapped within the SMI and not identified during preliminary data filtering. However, Mustard et al. (2006) found that melt inclusions from natural granitic magmas also showed metal-enrichment (Sn, Mo, W, Bi, As, Sb, Cu, Pb, Zn, and Au) when compared to the whole rock data and attributed this enrichment to crystal fractionation; this could also be the situation in the YGB. In either case, there is still evidence that these metals and their associated mineral and/or alloy phases were saturated in the magma chamber at the time of zircon crystallization and melt entrapment. Moreover, the As, Sb, Cu, Mo, Sn, W, Pb, and Bi concentrations for all SMI (except Mo one analyses) are enriched compared to the

upper continental crust values. This suggests that the magmas may have been pre-enriched in metals to generate SMI with these metal concentrations (Mustard et al. 2006).

4.6.3. Metal characteristics of YGB magmas: insights into mineralization

Overall, the YGB dikes and plutons hand samples were minimally mineralized in sulfides and petrographic analysis of each lithology showed only trace sulfides and opaques (Fig. 4.3; Speight et al., 2023a; Speight et al., 2023b). In contrast, the MI analysis indicates that accidentally trapped sulfides are present in at least 36 % of inclusions (Fig. 4.8, Table 4-1). The mixed MMI inclusions represent silicate melt with accidentally trapped phases that were co-crystallizing at the time that zircons were growing and are therefore saturated in the magma. Several metals in the mixed MMI data were found to have strong positive relationships, including Ag versus As, Mo versus Cu, and W versus Sn (Fig. 4.12-Fig. 4.14). The strong co-varying relationships between these metals suggest that they may be occurring in the mixed MMI as alloys, sulfides, or oxides. When considering the inclusion with the highest Ag/As value, this analysis also correlates to the one LA-ICP-MS profile that shows a definite Au peak within the MI (Fig. 4.12B). The same analysis of an FQP dike MMI also correlated to the highest Pb, Bi, Co, Ba, Ag, As, and Mg. This dike is located 790 m from the RLP (from which it is sourced) and 615 m from the Crestaurum mine site (Speight et al. 2023a). The sample that was found to have the only defined Au peak also has the highest W concentration but was found in different zircon-hosted MMI (Fig. 4.14A). This FQP dike was previously found to have a $^{207}Pb/^{206}Pb$ Concordia age of 2674 ± 5 Ma and a weighted mean $^{207}Pb/^{206}Pb$ age of 2667 ± 11 Ma (Speight et al. 2023b).

The weighted average $^{207}Pb/^{206}Pb$ age of the FQP dike age is within error of a major intrusive event at ca. 2662 Ma. This suggests that these metal-rich melts were present within the magmatic plumbing system (i.e., FQP dikes and related RLP tonalite) just before the main dike and RLP emplacement or at the same time. Metal-enrichment of the YGB dikes and plutons may have pre-dated this since the mixed MMI with the highest Mo/Cu value is from the QZP dike, which is the oldest dike (2770 ± 7 Ma) from the previous U-Pb geochronology work by Speight et al. (2023b; Fig. 4.13A).

To assess whether these intrusions contributed to mineralization in the YGB, the common metal associations concerning Au in the inclusion data were evaluated. When the semi-quantitative data are compared, Au concentrations show a moderate to strong positive covariance with Ag, As, Bi, Pb, Sn, W, and Mo but showed no correlation with Co, Cu, Sb, or Ta. Although the data are considered semi-quantitative, and the Au concentrations may be artificially inflated, of the 50 SMI and mixed MMI, 50 % have Au concentrations above detection and a total of 42 % of inclusions have Au concentrations > 1 ppm (Table 4-2). Concentrations > 1 ppm Au are considered high by Mustard et al. (2006), and suggestive of an immiscible melt phase that is metal-enriched and occurs heterogeneously throughout the melt. This could give rise to a 'nugget effect' in the magma, evidenced by the variable SMI and mixed MMI data from a single sample such as the FQP dikes (e.g., SS18-128; Mustard et al. 2006). These variable compositions may not be solely due to differences in fractionation trends but related to a heterogeneous magma

that is variably sampled by crystallizing zircon grains, and therefore, traps melt of different compositions and various co-crystallizing phases.

Mustard et al. (2006) found that Au mineralization could progress to economic levels by fractional crystallization alone if accessory oxides and sulfides remain low, there is a lack of a Cl-bearing fluid, volatiles in the melt, and prolonged crystallization of the intrusion. Although the YGB and the intrusions examined here show evidence of Au mineralization and the relationship between Au and magmatic intrusions have been postulated, no significant intrusion-related Au deposit has been found to date. The MI data presented here shows evidence of abundant accessory oxide and suspected sulfide phases that were saturated in the RLP tonalite, FQP dikes, QZP dikes, and Defeat Suite granite. It is therefore possible that these accessory phases inhibited the Au enrichment of the YGB intrusions by sequestering precious metals and preventing a significant Au occurrence from developing (Candela 1997, Halter et al. 2002, Mustard et al. 2006). Further investigation into the magmatic fluid characteristics of YGB intrusions would help determine what role fluid exsolution had on Au mineralization in the YGB.

The zircon-hosted MI presented here show evidence for an intrusion-related Au mineralization signature; however, an intrusion-related Au deposit has yet to be identified proximal to the RLP or FQP dikes. The Crestaurum deposit is considered a shear-zone hosted Au deposit, although it is located roughly 500 m from the RLP margin (Fig. 1.1). Enrichments in Mo (and Cu) can be observed within and around the RLP. The lack of mineralization directly associated with the RLP or FQP could be because metal-rich

exsolved fluids at the end of the pluton's crystallization were degassed at the time of FQP (and aplite) dike emplacement. The FQP dikes were found to be related to the Banting Group volcaniclastic rocks and therefore breached the surface at that time (ca. 2662 Ma). This event may have led to the loss of considerable incompatible elements in the degassing magmatic fluids. The dikes could have remained conduits for further exsolving fluids during deposition of the Banting Group volcaniclastics as the RLP and FQP completed crystallizing. This type of magmatic plumbing system beneath the Banting Group would leave behind traces of metal enrichment without any significant deposits.

The SMI and mixed MMI data from this study suggests that the multi-phase RLP was saturated in metals, Ti, Fe, and H_2O before or close to the time of emplacement at 2662 Ma, the age of the tonalite, FQP dikes, and one aplite-1(a) dike from a previous geochronology study (Speight et al. 2023b). It is therefore possible that the RLP and associated dikes (FQP and aplite-1(a)) contributed to Au mineralization in the YGB, although possibly only indirectly. The summary metal list and associated Ag, As, and Au concentration ranges of MI from the FQP and tonalite samples are shown schematically in Fig. 4.15. Also shown are the relative locations of the MI samples and the stratigraphic level of the historic, Con, Giant, and Crestaurum mines (Armstrong 1997, Siddorn et al. 2006, Siddorn 2011). The past-producing Con and Giant mines are located within the Yellowknife Bay Formation, stratigraphically above the Townsite Formation and below the Banting Group and Burwash metasedimentary unit (Fig. 4.15).

Speight et al. (2023b) provided evidence that the Defeat Suite granite, responsible for regional metamorphism and thought to be related to the development of Au mineralization, was present in the YGB as early as 2662 Ma (van Hees et al. 1999, 2006a, Cousens et al. 2006c, Ootes et al. 2011). This major dike and pluton emplacement event at ca. 2662 Ma is now considered the initial event that instigated mineralization in the YGB, roughly 30 Ma before the oldest Defeat Suite granite ages (Davis and Bleeker 1999, Speight et al. 2023b). The previously studied aplite dikes by Speight et al. (2023a) showed textural evidence of H_2O-saturation and here the MI-hosted accidentally trapped hydrous phases (e.g., biotite, amphibole) provide further evidence of H_2O-saturation in the FQP dikes, QZP dikes, RLP tonalite, and Defeat Suite granite (Fig. 4.15). Not only were these dikes and plutons H_2O-saturation at the time of zircon growth, and the magma was also saturated in metal-rich oxide and sulfide phases. Therefore, these intrusions, specifically regarding the genetically related FQP dikes and RLP tonalite, may have led to sustained magmatic-hydrothermal activity initiated at ca. 2662 Ma. The initial emplacement of FQP and aplite dikes may have led to a pre-fertilization of the Kam Group mafic volcanic flows due to metal-enriched magmatic fluids. These metals may have been later remobilized by metamorphic fluids and deposited within shear zones, or the dikes acted as crystal-mush conduits for magmatic fluids, which were transported through the system to the genetically related subaerial Banting Group volcaniclastics(van Hees et al. 1999, Speight et al. 2023b, 2023a).

4.7. Conclusions

The YGB is host to multiple generations of crosscutting felsic to intermediate dikes and regional plutons, which have been the focus of recent petrographic, lithogeochemical, and U-Pb geochronology studies (Speight et al. 2023b, 2023a). The data presented here aimed to assess the quality of Archean zircon-hosted MI from the YGB, identify phases that were co-crystallizing with zircon, and consider the pre-emplacement metal-enrichment of the YGB intrusions using SMI and mixed MMI data. This preliminary MI study from the Archean YGB yielded the following conclusions:

I. Systematic data filtering of semi-quantitative zircon-hosted MI data limited the results from 50 inclusions in 47 zircons down to 7 inclusions that best represent primary SMI data. This SMI data showed a less evolved tholeiitic signature compared to average lithogeochemical data from the same lithologies. The remaining 43 inclusions represent data that were contaminated to varying degrees by accidentally trapped mineral phases (i.e., mixed MMI).

II. The bulk SMI showed evidence of metal enrichment relative to lithogeochemical data from the YGB and upper continental crust. In this case, As, Sb, Cu, Sn, W, Pb, and Bi all show a negative relationship with the SMI Mg #, suggesting that these metals were increasing with progressive crystal fractionation. This may be the result of unidentified nanocrystals of metal-rich alloys that are enriching the SMI data, or from crystal fractionation alone.

III. Although the dataset is limited, categorization of the mixed MMI identified co-crystallizing accessory phases including, quartz, feldspars, apatite, biotite, amphibole, Fe-(Ti)-oxides, and suspected sulfides. These phases must have been saturated in the melt to occur as accidentally entrapped solid inclusions with silicate melt. This provides direct evidence of Ti-saturation in the magmas, as well as H_2O-saturation based on the presence of hydrous minerals.

IV. The $^{207}Pb/^{206}Pb$ ages of the FQP dikes and genetically related RLP tonalite (ca. 2662 Ma) suggests that these hydrous and metal-rich mixed zircon-hosted MMI were present within the magmatic plumbing system of the YGB at or close to their time of emplacement.

V. An evaluation of the semi-quantitative inclusion data concerning Au concentrations compared to various metals shows a moderate to a strong positive covariance between Au and Ag, As, Bi, Pb, Sn, W, and Mo and no correlation with Co, Cu, Sb, or Ta. Of the fifty inclusions analyzed, 42 % have Au concentrations above 1 ppm, indicative of an immiscible metal-enriched melt phase throughout the magma. This shows that the zircon-hosted MI have preserved evidence of an intrusion-related Au signature in the YGB dikes and plutons analyzed here.

4.8. Future work

Obtaining a larger and more comprehensive data set would allow SMI and corresponding metal concentrations to be correlated and compared across lithologies and stratigraphic

units. If this inclusion data is collected concurrently with U-Pb geochronology data, the precise timing of precious metal saturation could be determined. Combining this type of MI study with an analysis of zircon-hosted fluid inclusions would provide further information related to pre-emplacement and pre-eruptive magmas and any associated fluids (e.g., salinity, temperature, composition). Focusing on lithologies in and around the multi-phase RLP and the Crestaurum deposit could assist in determining the mineralization relationship. The addition of inclusion-free zircons to the initial data collection would assist in obtaining more quantitative data and the corresponding zircon mineral chemistry could be quantified and used as an internal standard.

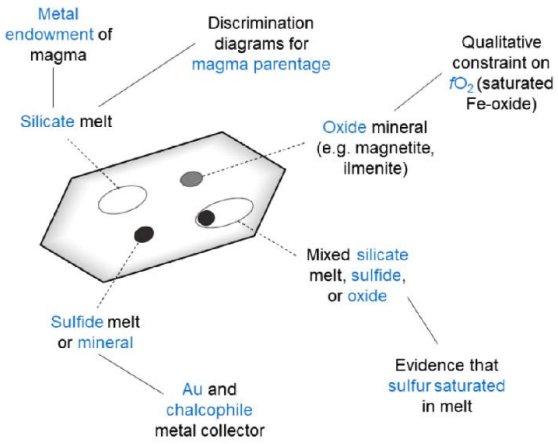


Fig. 4.1: Schematic diagram of zircon with four types of inclusions, including silicate melt, sulfide melt or mineral, oxide mineral, and a mixed silicate and mineral inclusion. Also indicated are the different types of data and information that can be garnered from these types of inclusions, barring post-entrapment modification.

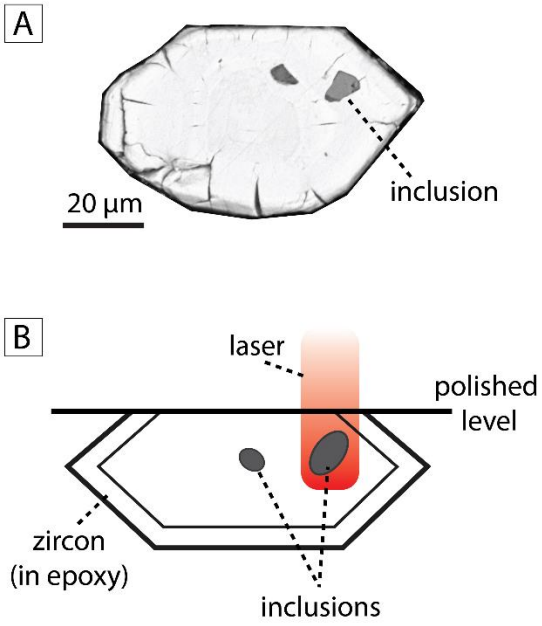


Fig. 4.2: (A) Scanning electron microscope backscatter electron image of a polished zircon with exposed inclusions and fractures along the exterior of the grain. (B) Cartoon illustration of laser-drilling for zircon-hosted melt inclusions that are encapsulated in the host phase.

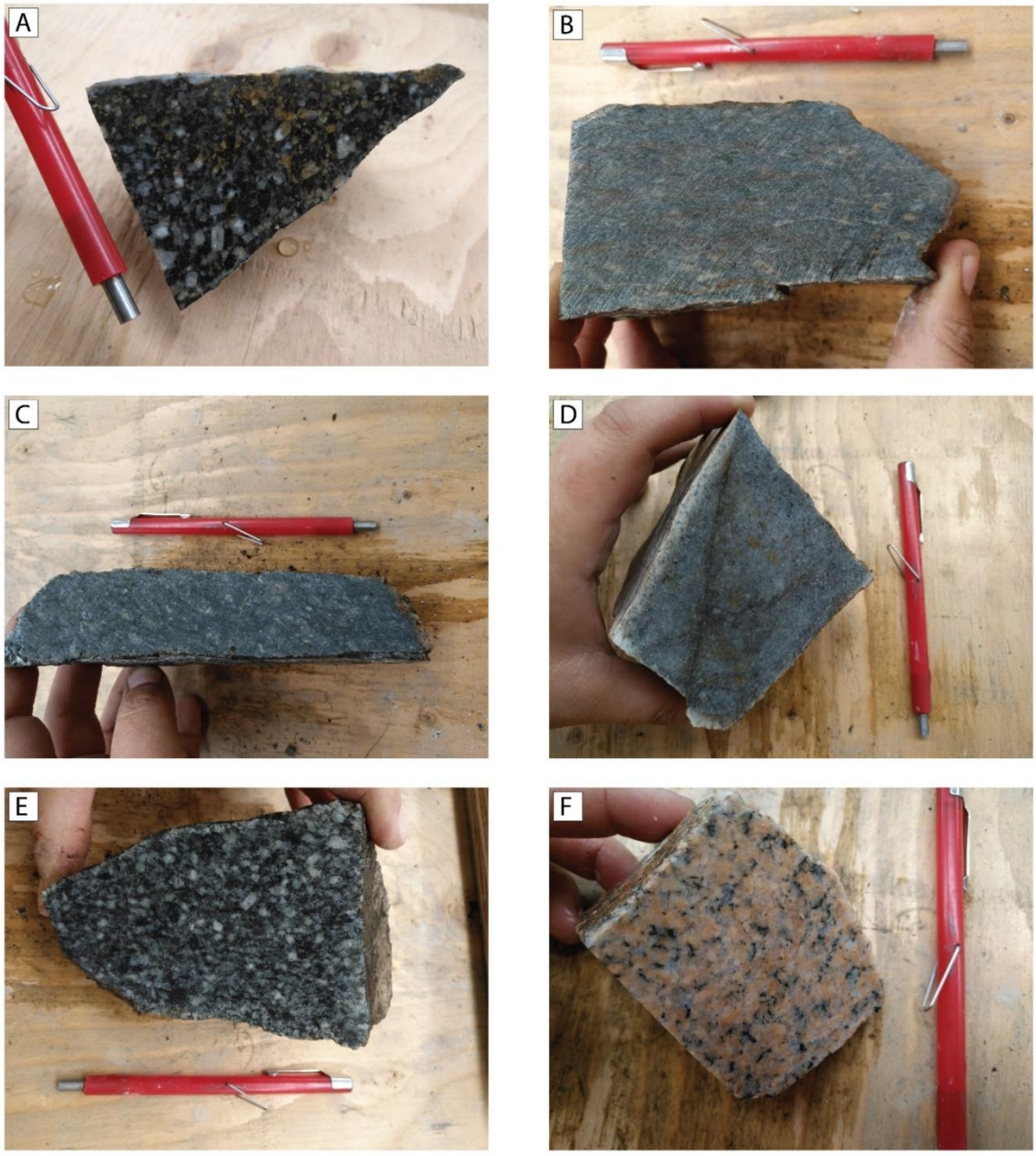


Fig. 4.3: Hand sample images of each sample selected for melt inclusion analysis. (A) feldspar-quartz porphyry (SS18-008), (B) feldspar-quartz porphyry (SS18-125), (C) feldspar-quartz porphyry (SS18-128), (D) quartz porphyry (SS18-082), (E) tonalite (SS18-129), and (F) Defeat Suite granite (JS18-377). Pen magnet for scale.

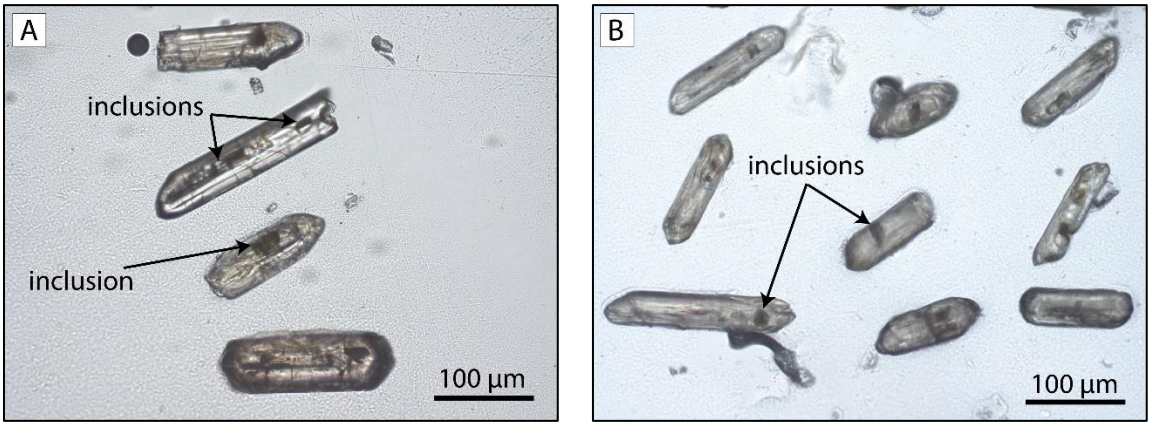


Fig. 4.4: Transmitted light photomicrographs of zircon-hosted melt inclusions from (A) Defeat Suite granite, and (B) FQP dike. Zircons typically host one (or two) inclusions that are spherical to ovoid, rarely elongated parallel to the c-axis, and have a dark grey to reddish-brown opaque colour.

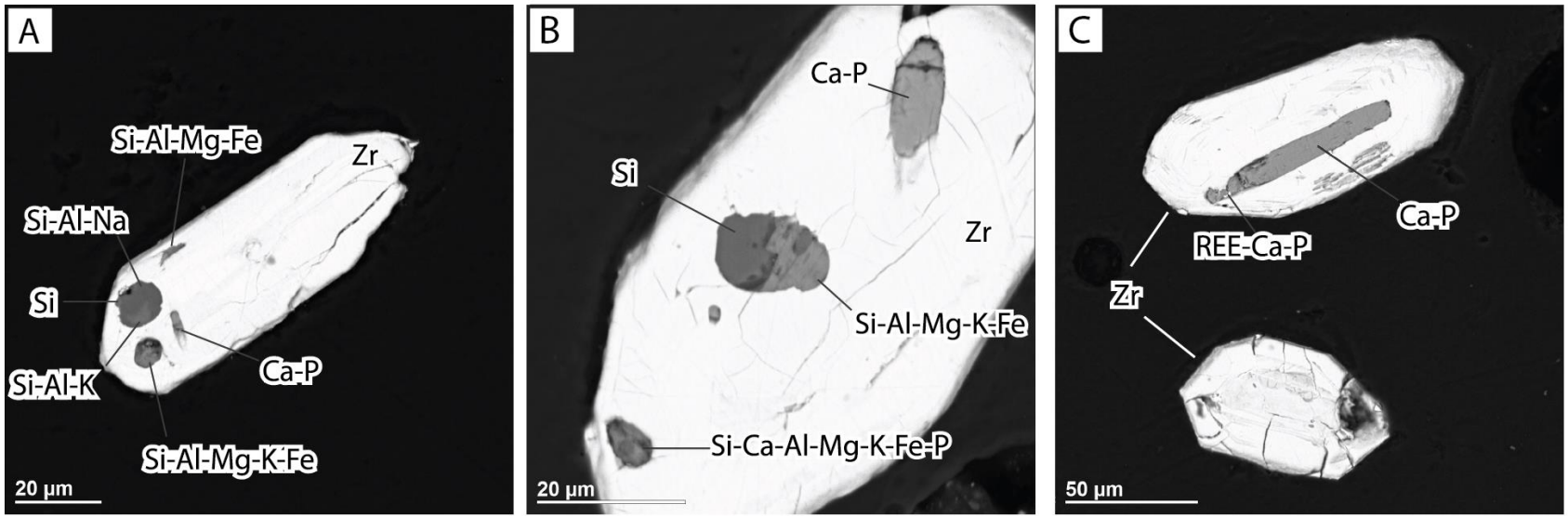


Fig. 4.5: Scanning electron microscope-backscatter electron images of exposed zircon-hosted inclusions. Qualitative analyses of the inclusions were done to determine their overall chemical characteristics, which have been indicated in each figure. REE: rare earth elements; Zr: zircon.

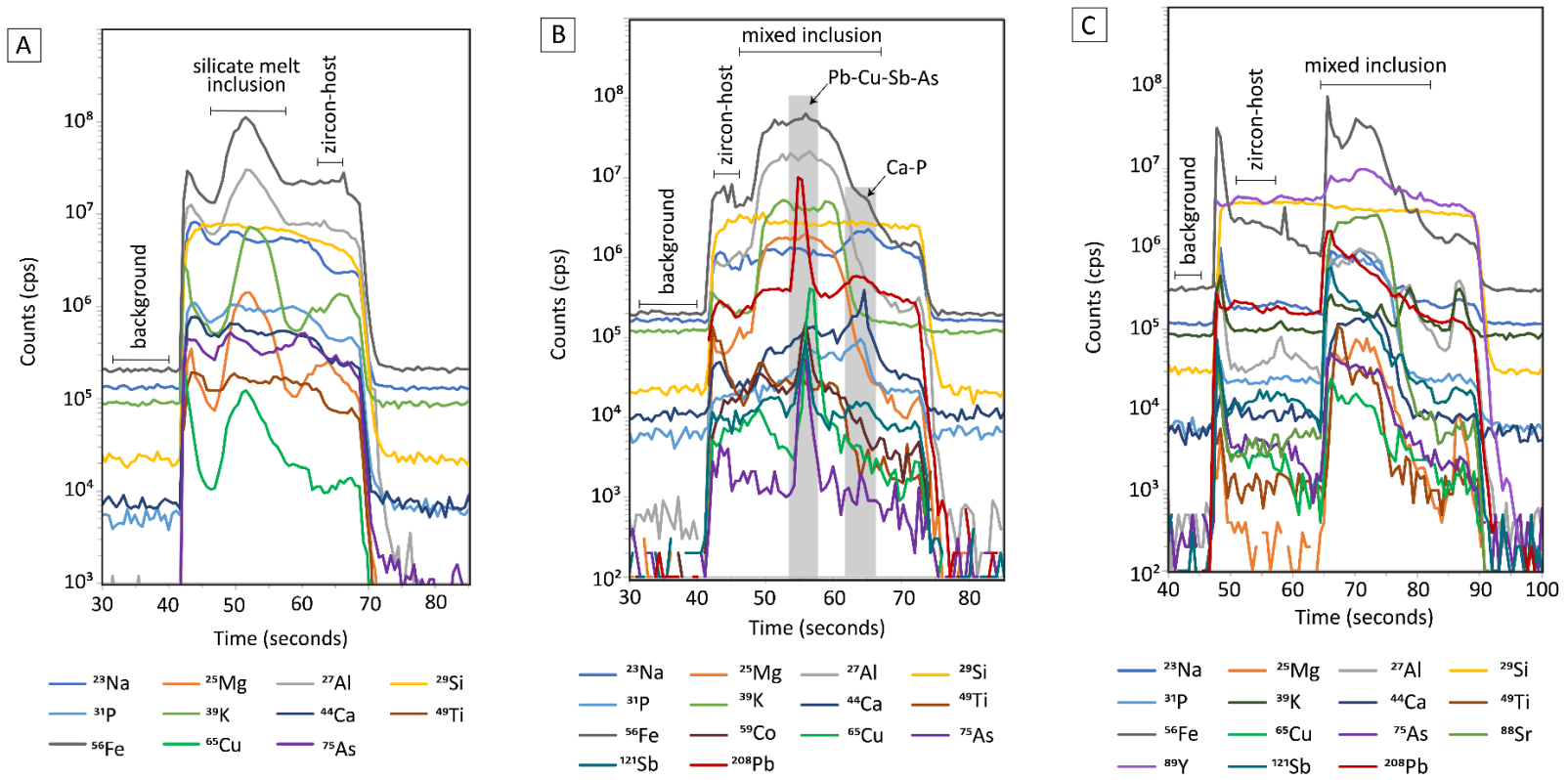


Fig. 4.6: Raw LA-ICP-MS signals from three different zircon-hosted inclusions, all with different chemical characteristics. Each ablation begins and ends in the zircon host phase, however, the areas used to deconvolute the inclusion-host signal has been indicated. (A) Smooth silicate melt inclusion showing various covarying elements, (B) a mixed inclusion with a defined sulfide mineral (Pb-Cu-Sb-As) and apatite (Ca-P) peak, and (C) a mixed inclusion with no well-defined mineral peaks.

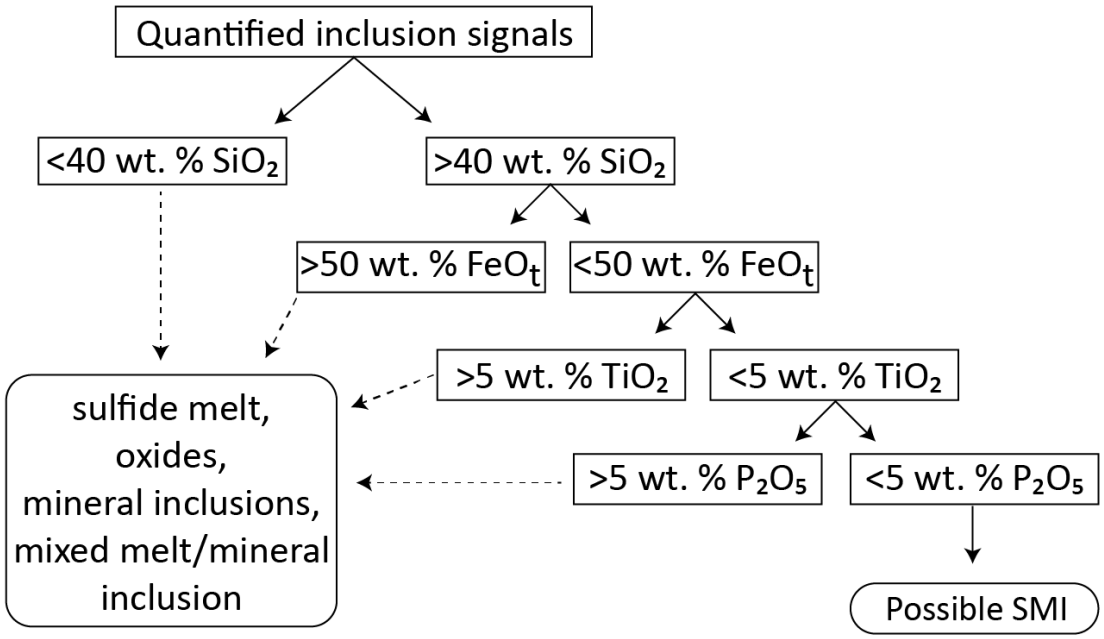


Fig. 4.7: Flow chart illustrating the data filtering protocol used to isolate data representing bulk silicate melt inclusions. The values shown here will remove analyses that may have encountered sulfide melt or minerals, oxides, mineral inclusions, or mixed melt and mineral inclusions (e.g., rutile, apatite). SMI: silicate melt inclusion.

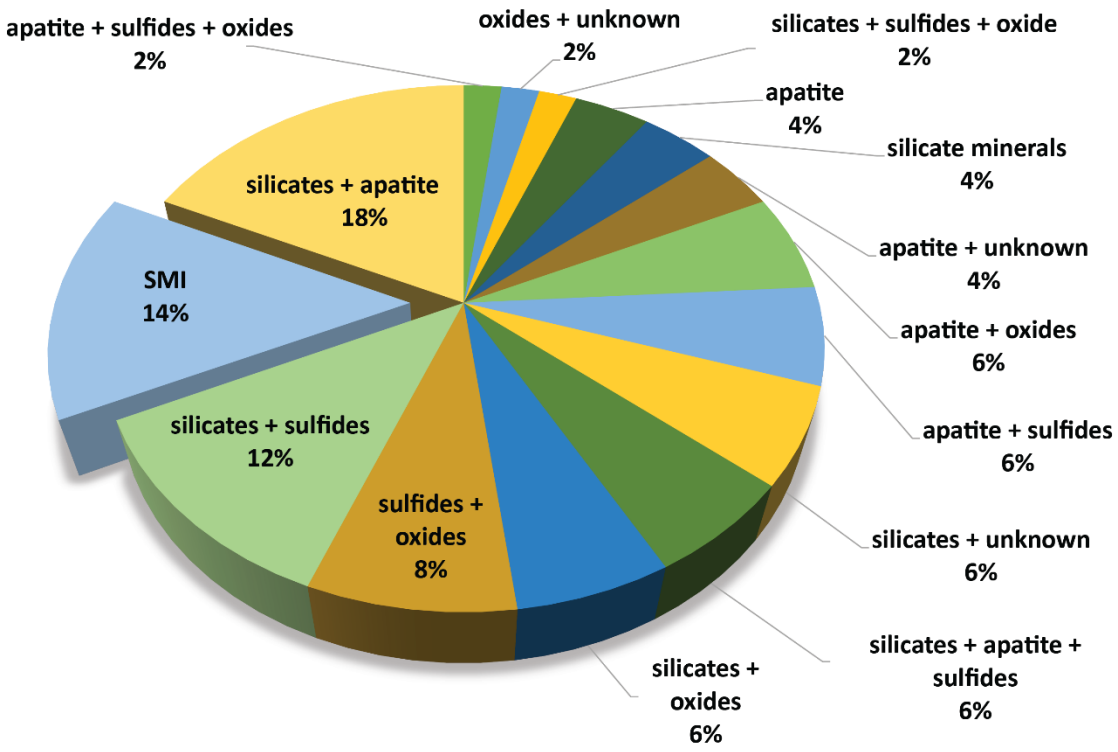


Fig. 4.8: Illustration indicating the types of inclusions encountered in this study from four different lithologies. A total of 50 inclusions from 47 analyses were categorized based on the elemental assemblages observed and the comparison of the respective LA-ICP-MS signals. This chart indicates the categories observed and their relative abundance within the YGB zircon-hosted inclusions.

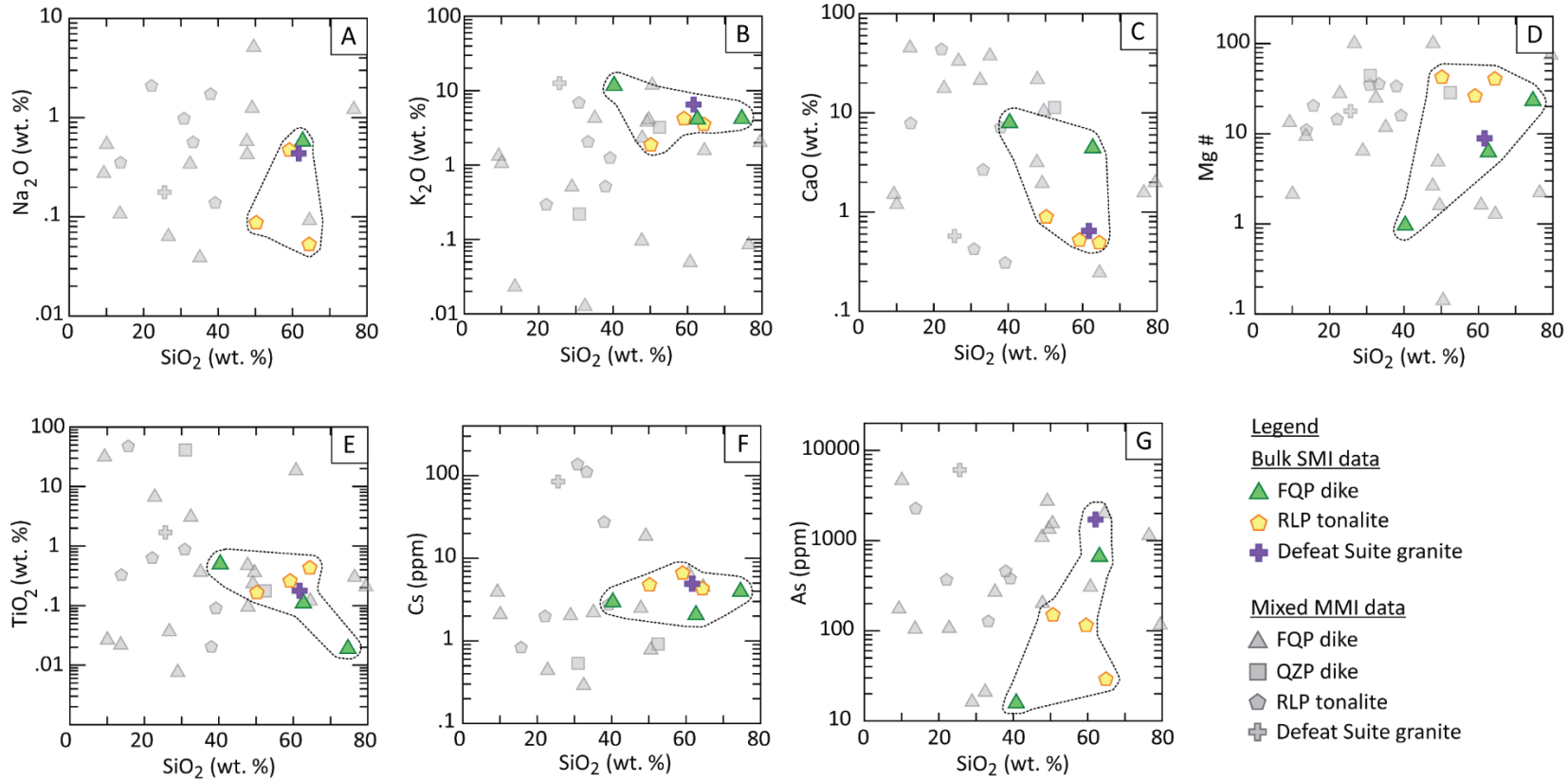


Fig. 4.9: Comparison of major and trace element data to SiO_2 for SMI and MMI of the YGB, including A) Na_2O, B) K_2O, C) CaO, D) Mg #, E) TiO_2, F) Cs, and G) As. The data determined to represent SMI are shown in colour and highlighted with a dashed line, while the MMI data has been shown in grey. The MMI data present inclusions with accidentally entrapped phases that have changed the overall chemistry of the inclusions, making them unrepresentative of primary melts.

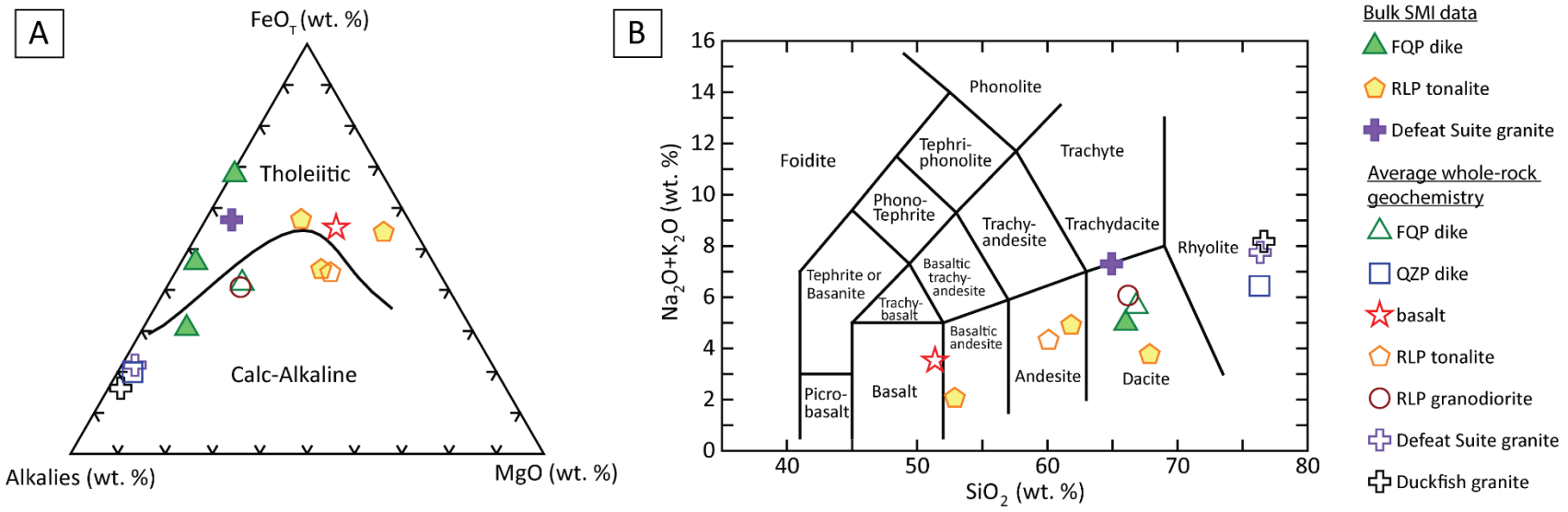


Fig. 4.10: Comparison of SMI (filled symbols) from this study to average lithogeochemistry of Speight et al., (2023a) shown on (A) Alkali-FeO$_T$-MgO (AFM) and (B) Total Alkalis versus SiO$_2$ (TAS) diagrams (Irvine and Baragar 1971, le Bas et al. 1986). The basalt chemistry shown is from the GeoRoc database for the Slave Province.

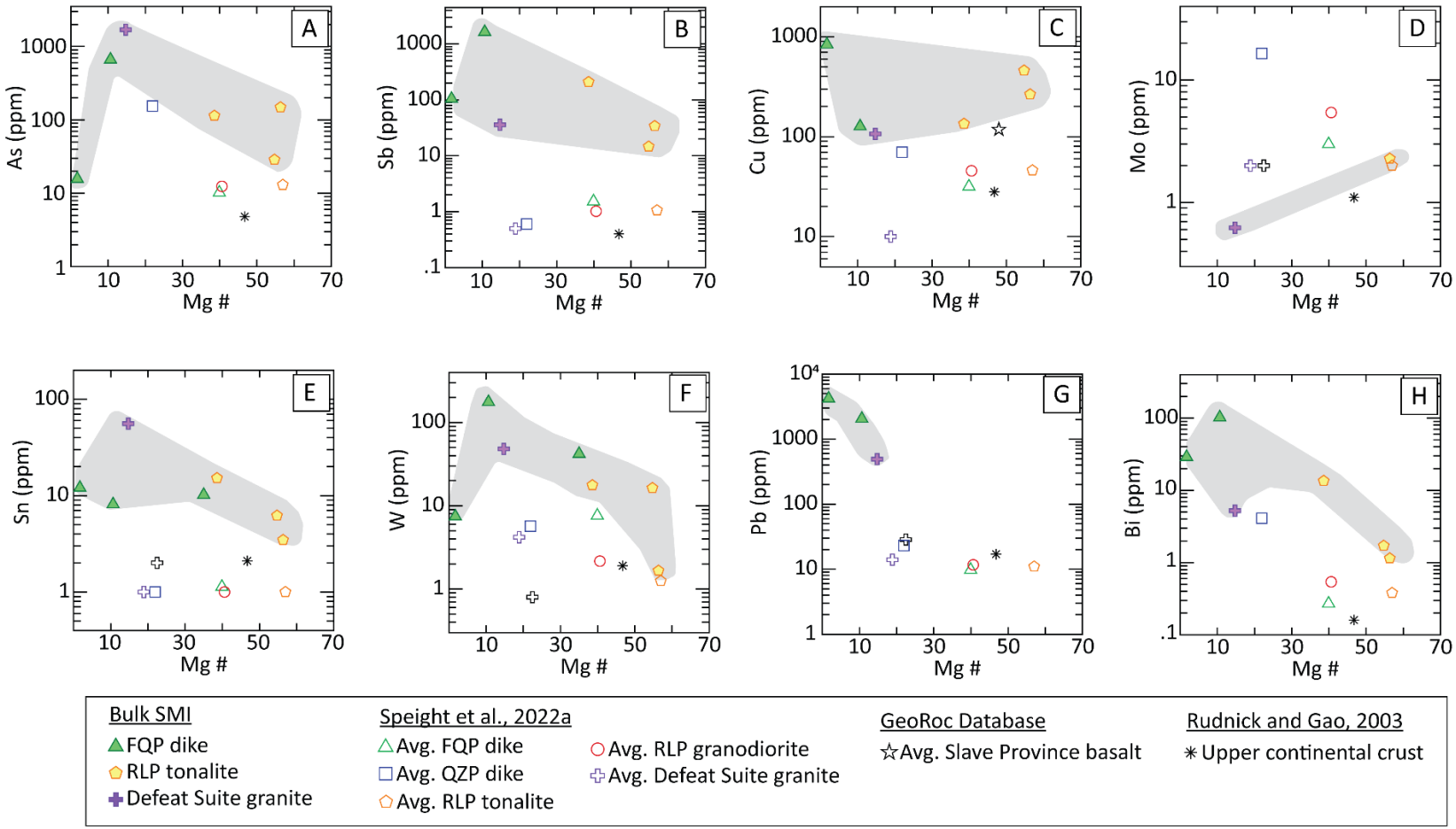


Fig. 4.11: Comparison of metal concentrations to the Mg # of SMI and average lithogeochemical data and the upper continental crust, including A) As, B) Sb, C) Cu, D) Mo, E) Sn, F) W, G) Pb, and H) Bi (Rudnick and Gao 2003, Speight et al. 2023a). The SMI from this study have been highlighted in grey.

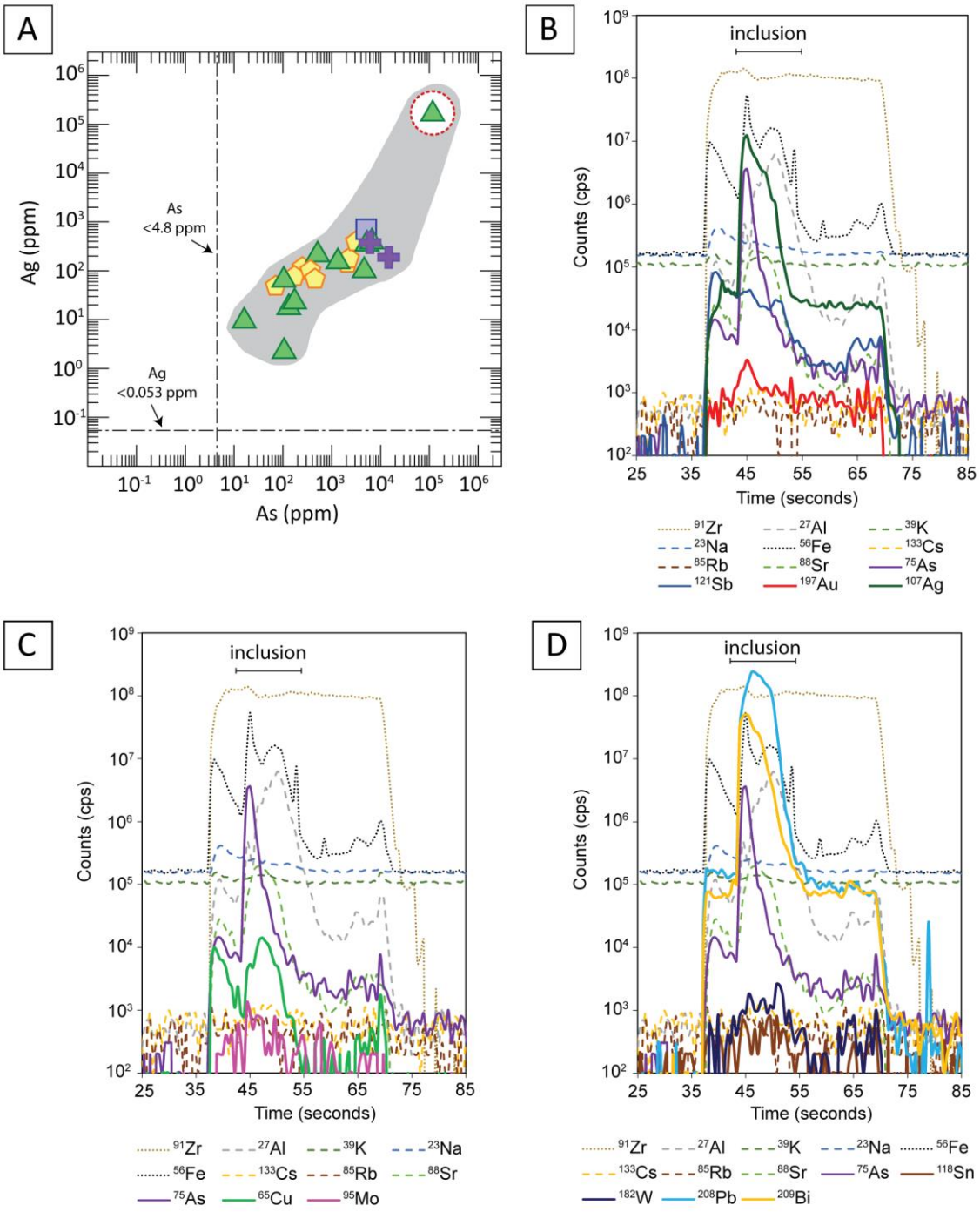


Fig. 4.12: A) Comparison of Ag and As concentrations in mixed melt and mineral inclusion (MMI) data from this study. The Ag and As values from the upper continental crust with comparable Cs concentrations (Cs = 4.9 ppm) have also been indicated (Rudnick and Gao 2003). Data that fall above these values are highlighted in grey and represent accidentally trapped saturated phases. B-D) Graphs showing the raw LA-ICP-MS counts for select

major and trace elements in the most enriched inclusions, circled (dashed red line) in Fig. 4.12A.

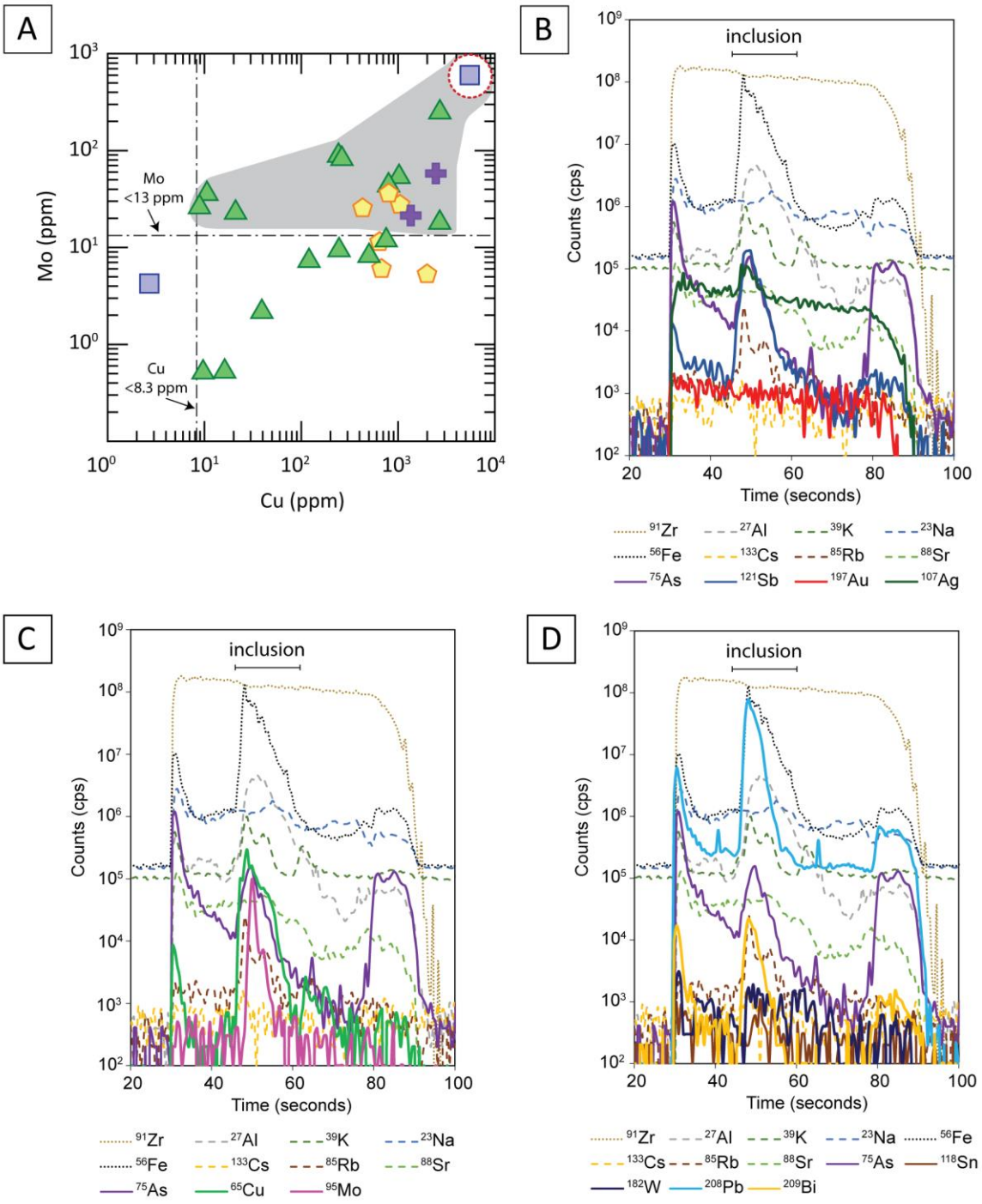


Fig. 4.13: A) Comparison of Mo and Cu concentrations in mixed melt and mineral inclusion (MMI) data from this study. The Mo and Cu values from the granite-hosted MI with comparable Cs concentrations (Cs = 0.9-13 ppm) have also been indicated (Audétat and

Pettke 2003). Data that fall above these values are highlighted in grey and represent accidentally trapped saturated phases. B-D) Graphs showing the raw LA-ICP-MS counts for select major and trace elements in the most enriched inclusions, circled (dashed red line) in Fig. 4.13A.

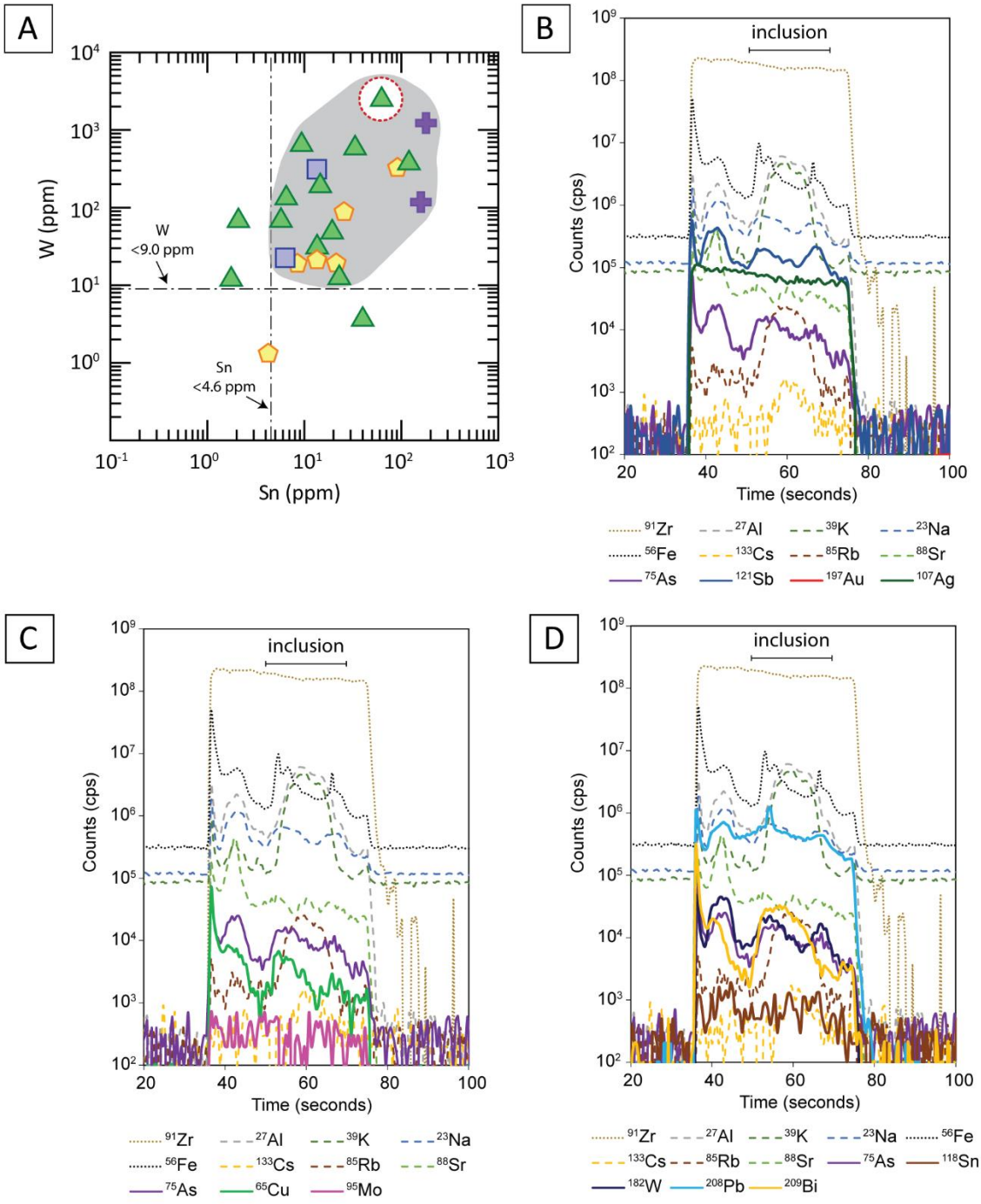


Fig. 4.14: A) Comparison of W and Sn concentrations in mixed melt and mineral inclusion (MMI) data from this study. The W and Sn values from the granite-hosted MI with comparable Cs concentrations (Cs = 0.9-13 ppm) have also been indicated (Audétat and Pettke 2003). Data that fall above these values are highlighted in grey and represent

accidentally trapped saturated phases. B-D) Graphs showing the raw LA-ICP-MS counts for select major and trace elements in the most enriched inclusions, circled (dashed red line) in Fig. 4.14A.

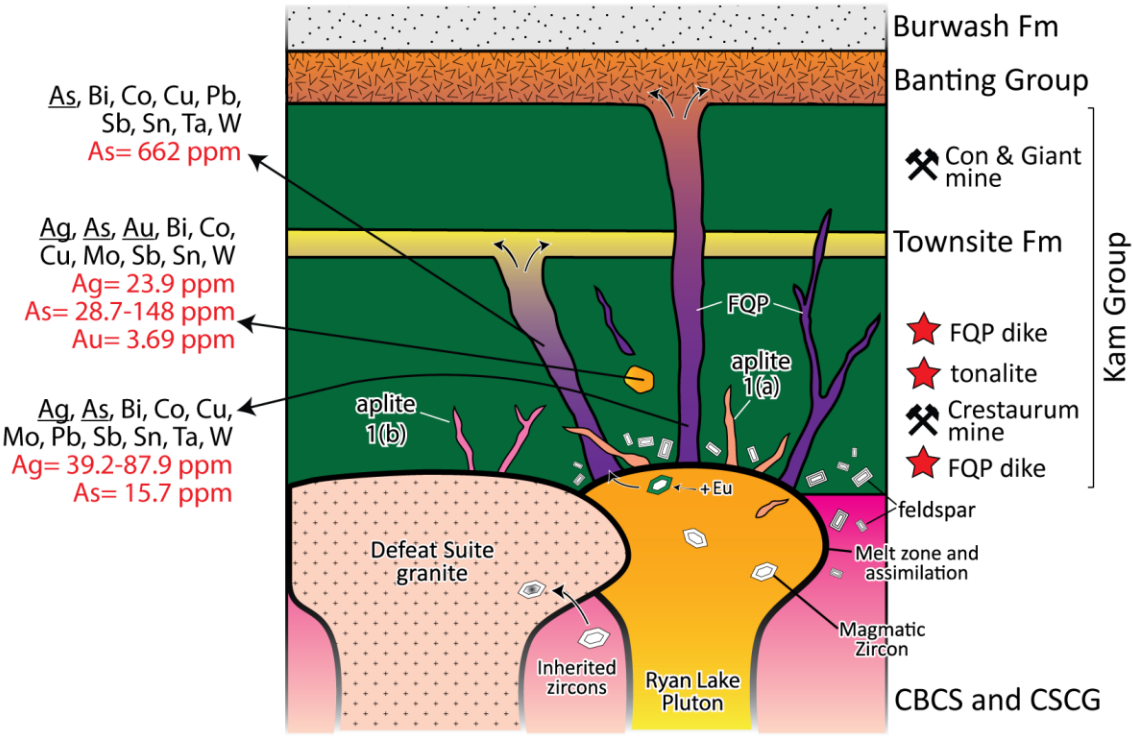


Fig. 4.15: Schematic depiction of RLP magmatic plumping system within the YGB, showing the relative location of aplite dikes 1(a) and 1(b) and the Defeat Suite granite (Speight et al. 2023b). The approximate stratigraphic positions of samples with SMI (red stars) and the Crestaurum, Con, and Giant mines are indicated. The general metal list for three samples with SMI (two FQP dikes and one RLP tonalite) are given on the left, along with the Ag, As, and Au concentrations when available; the full dataset is given in Table 4-2.

Table 4-1: Summary of the type of inclusion encountered in each sample analyzed by LA-ICP-MS, from 50 inclusions from 47 analyses. *n* = number of analyses, Lith. = lithology, SMI = silicate melt inclusion, Ap = apatite, sulf. = sulfides, unkn. = unknown, min. = minerals.

Sample	Lith.	*n*	SMI	Ap	Ap + oxides	Ap + sulf.	Ap + sulf. + oxides	Ap + unkn.	Oxides + unkn.	Silicate min.	Silicates + ap	Silicates + unkn.
SS18-008	FQP	17	X		X	X	X		X	X	X	X
SS18-125	FQP	2									X	
SS18-128	FQP	7	X	X		X					X	
SS18-082	QZP	3									X	
SS18-129	tonalite	14	X	X	X			X		X		X
JS18-377	granite	4	X		X	X						

Table 4-1: *Continued*.

Sample	Lith.	Silicates + ap + sulf.	Silicates + oxides	Silicates + sulf.	Silicates + sulf. + oxides
SS18-008	FQP	X	X	X	X
SS18-125	FQP				
SS18-128	FQP	X		X	X
SS18-082	QZP		X		X
SS18-129	tonalite	X	X	X	X
JS18-377	granite			X	

Table 4-2: Zircon-hosted melt and mineral inclusion data from four lithologies from the YGB, including three FQP dikes, a QZP dike, tonalitic RLP, and Defeat Suite granite (GRN 1). Each analysis was categorized by the most likely combination of melt +/- minerals.

Sample	Lithology	Inclusion category	SiO_2 (wt. %)	TiO_2	Al_2O_3	FeO_T	MnO	MgO	CaO	Na_2O	K_2O	P_2O_5
SS18-008	FQP	Ap + oxides	-	27.8	1.17	1.72	0.277	0.200	62.2	0.0899	0.0399	1.48
SS18-008	FQP	Ap + sulfides	-	2.06	17.8	33.6	3.05	0.780	19.6	6.94	-	11.1
SS18-008	FQP	Ap + sulfides + oxides	-	6.90	13.6	-	-	1.28	44.1	-	3.52	25.7
SS18-008	FQP	Oxides + unkn.	-	6.19	47.3	-	-	3.35	0.640	-	37.5	-
SS18-008	FQP	Silicate min.	29.0	0.00755	22.1	40.5	0.157	2.78	-	-	0.506	-
SS18-008	FQP	Silicates + ap	32.5	3.07	6.07	10.8	0.271	3.58	21.2	0.340	0.0126	17.2
SS18-008	FQP	Silicates + ap	22.8	6.63	15.2	21.6	-	8.34	17.6	-	-	2.77
SS18-008	FQP	Silicates + ap	79.5	0.207	5.90	0.0926	-	0.273	1.97	-	2.01	5.02
SS18-008	FQP	Silicates + ap + sulfides	49.6	0.357	6.87	13.6	1.98	0.220	10.3	5.11	4.07	2.89
SS18-008	FQP	Silicates + oxides	60.7	18.4	1.24	13.2	1.16	0.215	-	-	0.0488	-
SS18-008	FQP	Silicates + sulfides	64.5	0.119	5.55	21.7	0.0566	0.281	0.244	0.0918	1.56	0.895

Notes: wt. % = weight percent, ppm = parts per million, Ap = apatite, unkn. = unknown, min. = minerals, SMI = silicate melt inclusions, - = below detection.

Table 4-2: *Continued.*

Sample	Ag (ppm)	As	Au	B	Ba	Bi	Ce	Co	Cs	Cu	Dy	Er	Eu	Gd	Hf
SS18-008	17.4	132	-	109	145	4.91	2176	62.9	1.00	405	710	-	245	1194	-
SS18-008	386	6676	73.7	3758	1583	266	55602	285	14.6	2709	40465	33974	14233	50535	562673
SS18-008	210	517	16.5	1392	1035	88.3	8991	198	-	690	3439	-	1451	7568	102066
SS18-008	-	-	-	-	1696	-	-	-	-	-	-	-	-	-	-
SS18-008	9.22	16.1	2.14	-	-	-	100940	287	2.02	-	-	-	-	-	6945
SS18-008	-	20.8	0.611	16.2	19.7	6.34	942	29.5	0.289	16.2	155	486	-	-	144
SS18-008	2.21	106	0.509	-	-	0.859	-	429	0.439	501	-	-	-	-	1824
SS18-008	-	115	-	-	214	-	4305	-	-	120	1303	-	434	1690	27635
SS18-008	152	1336	1.52	4448	1073	4.25	9911	29.7	-	246	7949	6957	2000	8054	-
SS18-008	-	305	-	-	152	4.98	69.2	175	6.52	242	-	-	634	-	33317
SS18-008	-	1994	-	41.7	242	95.5	384.45	75.1	4.48	1026	800	839	80.6	439	-

Table 4-2: *Continued.*

Sample	Ho (ppm)	La	Lu	Mo	Nb	Nd	Pb	Pr	Rb	Sb	Sm	Sn	Sr	Ta	Tb	Th	Tm
SS18-008	56.2	672	-	-	317	2457	8582	401	-	109	1165	9.39	705	5.91	154	1192	-
SS18-008	9872	7834	5958	247	380	102098	218099	13588	-	784	50888	120	2483	122	6439	-	5799
SS18-008	170	2909	-	-	386	11784	11511	1953	204	135	7217	33.3	671	14.1	965	-	-
SS18-008	-	-	-	-	-	-	-	-	348	-	-	-	109	-	-	33265	-
SS18-008	-	62345	-	-	-	25186	-	8869	30.3	-	-	-	40.5	-	-	-	-
SS18-008	96.9	290	201	0.523	7.27	202	7.71	80.9	1.35	60.8	-	0.89	308	1.65	-	5733	103
SS18-008	-	130	-	8.14	2.69	-	-	-	-	-	-	1.77	-	-	-	-	-
SS18-008	53.1	2453	-	7.23	73.3	2920	-	695	95.7	-	1464	22.9	-	-	203	-	-
SS18-008	1906	796	2031	9.36	103	12731	18816	1675	88.1	1245	7599	14.6	1678	27.3	1181	54384	1335
SS18-008	-	211	-	88.1	-	401	4542	72.9	16.2	82.6	31.3	13.6	224	-	-	-	-
SS18-008	216	74.8	228	53.2	11.8	415	374	67.4	80.6	47.1	252	-	16.3	0.608	93.7	1117	174

Table 4-2: *Continued.*

Sample	U (ppm)	V	W	Y	Yb	Analysis
SS18-008	-	221	641	163	-	a22
SS18-008	33365	1302	371	238634	43944	a43
SS18-008	-	235	579	-	-	a20
SS18-008	-	-	125	-	-	a42
SS18-008	-	59.8	-	-	-	a24
SS18-008	2223	427	-	2487	962	a44
SS18-008	-	3709	11.8	-	-	a47
SS18-008	-	-	12.4	761	-	a48
SS18-008	26221	246	189	52727	11895	a46
SS18-008	-	451	30.6	-	-	a17
SS18-008	324	193	12.3	5488	1264	a18

Table 4-2: *Continued.*

Sample	Lithology	Inclusion category	SiO_2 (wt. %)	TiO_2	Al_2O_3	FeO_T	MnO	MgO	CaO	Na_2O	K_2O	P_2O_5
SS18-008	FQP	Silicates + sulfides + oxides	9.31	31.5	9.44	35.3	0.801	5.39	1.50	0.273	1.32	0.177
SS18-008	FQP	Silicates + sulfides + oxides	-	43.5	-	33.2	3.12	0.569	7.40	7.18	0.0266	-
SS18-008	FQP	Silicates + unkn.	35.1	0.363	12.3	4.85	0.0208	0.642	37.4	0.0387	4.24	0.0775
JS18-377	GRN 1	Ap + sulfides	-	2.02	16.1	20.6	1.77	1.24	16.0	5.85	0.421	31.0
JS18-377	GRN 1	Silicates + sulfides	25.6	1.68	38.1	12.2	0.0777	2.65	0.572	0.177	12.6	1.32
JS18-377	GRN 1	SMI	61.7	0.174	13.0	10.6	0.162	1.03	0.631	0.442	6.49	0.807
SS18-129	Tonalite	SMI	50.3	0.163	14.8	15.5	0.312	11.2	0.873	0.0888	1.86	-
SS18-129	Tonalite	SMI	59.1	0.256	14.8	11.8	0.318	4.16	0.510	0.480	4.21	-

Table 4-2: *Continued.*

Sample	Ag (ppm)	As	Au	B	Ba	Bi	Ce	Co	Cs	Cu	Dy	Er	Eu	Gd	Hf
SS18-008	22.9	174	-	133	286	1.40	2276	351	3.88	754	825	680	189	777	15828
SS18-008	871	-	-	1281	661	-	-	34.3	-	-	3227	8089	-	-	-
SS18-008	-	267	-	18.8	688	2.25	-	97.1	2.21	1139	-	-	-	-	-
JS18-377	187	14719	3.57	17147	1182	57.3	22820	6.31	-	1357	119209	77746	4808	54999	39411
JS18-377	377	6074	11.2	1013	2147	4.17	1300	-	84.8	212	-	-	40.2	-	171147
JS18-377	-	1692	0.205	465	697	5.21	1086	1.27	5.03	106	5184	3958	208	2317	-
SS18-129	-	148	-	85.4	441	1.14	180	57.9	4.90	265	-	-	-	-	-
SS18-129	23.9	114	3.69	82.6	941	13.5	1952	129	6.79	135	798	-	180	902	28658

Table 4-2: *Continued.*

Sample	Ho (ppm)	La	Lu	Mo	Nb	Nd	Pb	Pr	Rb	Sb	Sm	Sn	Sr	Ta	Tb	Th	Tm
SS18-008	185	689	71.6	11.8	27.2	1808	11027	354	46.4	17.6	683	40.0	104	-	125	717	96.4
SS18-008	1295	-	2962	6.68	212	-	-	-	18.5	-	-	-	1645	37.5	-	58171	1912
SS18-008	-	225	25.3	-	10.5	-	-	2.94	193	2.47	-	-	876	1.05	-	701	-
JS18-377	25810	3113	10076	21.3	32709	24325	3687	3910	76.6	707	24513	180	3375	407	15103	28521	11783
JS18-377	-	414	-	-	3498	1174	-	255	632	30.1	781	159	143	29.9	-	-	-
JS18-377	1227	214	623	0.622	1442	1063	493	172	181	35.8	966	56	166	24.9	634	1756	595
SS18-129	-	313	-	2.28	7.21	51.7	-	13.6	85.4	34.0	-	3.46	79.5	-	-	116	-
SS18-129	95.5	600	-	-	37.9	1890	-	332	193	209	771	15.2	259	-	133	-	-

Table 4-2: *Continued.*

Sample	U (ppm)	V	W	Y	Yb	Analysis
SS18-008	1267	6764	3.59	4694	596	a23
SS18-008	30664	1492	243	35782	19993	a45
SS18-008	-	19.2	8.58	-	-	a49
JS18-377	43606	2089	1226	671834	81388	a53
JS18-377	-	763	118	-	-	a54
JS18-377	2757	195	48.1	32527	4003	a51
SS18-129	-	44.2	1.66	-	-	a39
SS18-129	-	64.3	17.7	2209	-	a41

Table 4-2: *Continued.*

Sample	Lithology	Inclusion category	SiO_2 (wt. %)	TiO_2	Al_2O_3	FeO_T	MnO	MgO	CaO	Na_2O	K_2O	P_2O_5
SS18-008	FQP	Silicates + unkn.	50.5	-	11.8	20.4	-	0.0289	-	-	11.8	0.465
SS18-008	FQP	SMI	74.7	0.0187	14.6	2.14	-	0.646	-	-	4.20	0.199
SS18-008	FQP	SMI	40.4	0.494	14.6	25.6	-	0.248	7.79	-	11.7	-
SS18-125	FQP	Silicates + ap	49.2	0.233	22.1	7.22	0.160	0.368	1.94	1.24	3.77	8.86
SS18-125	FQP	Silicates + ap	76.5	0.297	3.70	3.43	0.156	0.0772	1.56	1.21	0.0842	8.01
SS18-128	FQP	Ap	-	-	-	-	0.120	0.0626	50.5	0.0973	-	44.2
SS18-128	FQP	Ap + sulfides	-	0.536	22.4	29.9	0.444	0.412	13.1	6.01	0.865	21.4
SS18-128	FQP	Silicates + ap	13.6	0.0218	0.219	1.28	0.107	0.132	45.1	0.107	0.0229	34.4
SS18-128	FQP	Silicates + ap	26.7	0.0365	-	-	0.0988	0.0114	33.1	0.0634	-	35.0
SS18-128	FQP	Silicates + ap	47.8	0.0950	4.20	-	0.0925	0.164	21.7	0.423	2.31	18.2
SS18-128	FQP	Silicates + ap + sulfides	10.1	0.0265	5.75	73.1	0.0966	1.59	1.19	0.537	1.06	1.58
SS18-128	FQP	Silicates + sulfides	47.7	0.474	1.48	20.6	0.158	0.556	3.16	0.575	0.0955	20.2
SS18-128	FQP	Silicates + sulfides +	-	0.0810	25.0	55.0	0.203	13.4	0.792	0.463	0.0713	-
SS18-128	FQP	SMI	62.7	0.109	14.6	4.39	0.0699	0.293	4.34	0.591	4.13	3.70
JS18-377	GRN 1	Ap + oxides	-	1.08	22.4	32.5	0.728	9.63	9.48	3.60	2.19	13.3

Table 4-2: *Continued.*

Sample	Ag (ppm)	As	Au	B	Ba	Bi	Ce	Co	Cs	Cu	Dy	Er	Eu	Gd	Hf
SS18-008	-	1540	-	-	508	27.0	-	25.2	0.776	1564	892	248	-	-	-
SS18-008	39.2	-	-	-	120	-	-	259	4.08	-	-	-	-	-	-
SS18-008	87.9	15.7	-	-	2219	29.0	-	428	3.04	834	-	-	-	-	9079
SS18-125	-	2721	-	1163	550	-	10624	16.9	18.5	10.6	10663	5563	3776	11675	5712
SS18-125	-	1134	-	798	428	2.79	38499	13.2	-	8.89	6754	4057	2484	8133	-
SS18-128	440	-	9.01	-	-	-	3762	-	-	21.0	1002	2420	-	-	-
SS18-128	349	5293	17.5	8446	3452	237	172923	36.7	-	1460	98125	34035	36241	108156	91260
SS18-128	63.6	104	-	47.4	38.0	9.35	5629	11.1	-	39.3	311	344	104	319	299
SS18-128	-	-	2.38	-	-	-	2925	-	-	-	1267	2162	42.3	442	-
SS18-128	-	200	1.08	274	528	122	28987	-	2.47	9.7	3384	1516	1226	3700	-
SS18-128	100	4638	2.96	66.4	951	606	16415	2970	2.07	2692	61.1	259	153	393	875
SS18-128	-	1086	-	308	233	48.5	199892	83.1	-	263	3828	2293	2455	6968	-
SS18-128	159800	116843	26.1	500	33808	246741	1342	69898	-	798	2599	1275	592	2315	32341
SS18-128	-	662	-	797	479	102	2834	7.19	2.13	127	1796	692	1108	3497	-
JS18-377	435	-	2.16	6774	541	6.56	12966	14.5	4.22	2458	98011	63483	3302	45246	9432

Table 4-2: *Continued.*

Sample	Ho (ppm)	La	Lu	Mo	Nb	Nd	Pb	Pr	Rb	Sb	Sm	Sn	Sr	Ta	Tb	Th	Tm
SS18-008	188	-	96.7	-	-	-	585	-	43.3	-	-	-	-	-	74.9	-	42.6
SS18-008	-	-	-	-	4.64	-	-	-	150	-	-	10.2	-	0.916	-	-	-
SS18-008	-	-	-	-	-	-	4194	-	357	105	-	12.0	-	-	-	-	-
SS18-125	2052	1771	917	35.5	25.5	13188	634	2164	154	3025	8522	6.52	188	0.920	1812	9227	784
SS18-125	1368	17873	777	25.9	14.3	19072	1671	4584	4.81	2024	6612	5.74	1999	-	1170	11590	603
SS18-128	539	1848	192	22.8	10.4	1293	-	399	-	-	-	-	462	0.733	34.7	-	398
SS18-128	15545	70920	1678	-	75.7	132542	5724	25314	17.0	20423	66877	62.8	5657	11.3	18751	-	4210
SS18-128	79.1	2733	133	2.16	3.09	2432	298	662	1.32	75.3	396	-	519	0.717	45.6	961	67.6
SS18-128	476	1267	608	6.00	21.4	1263	342	333	4.27	-	293	-	295	8.05	124	1059	354
SS18-128	576	14887	224	0.513	11.8	14131	1504	3528	26.6	757	3303	2.09	1251	1.66	601	7046	228
SS18-128	49.5	8241	148	17.9	10.2	6511	4184	1762	42.3	460	849	1.32	967	3.31	9.8	5271	51.2
SS18-128	738	100787	524	81.6	9.93	89305	2600	23751	4.79	1885	13009	-	7004	2.28	730	857	382
SS18-128	427	692	121	43.6	-	1445	2277144	243	-	1284	1236	19.4	1732	1.85	410	1233	165
SS18-128	347	468	82.1	-	-	4062	2054	630	129	1635	2343	8.10	82.4	2.94	493	4556	79.2
JS18-377	21755	1630	7969	58.1	29193	16040	2149	2176	152	242	18563	-	2939	621	12439	42912	9319

Table 4-2: *Continued.*

Sample	U (ppm)	V	W	Y	Yb	Analysis
SS18-008	-	-	-	1035	405	a50
SS18-008	-	25.5	42.0	-	-	a19
SS18-008	-	9.55	7.44	-	-	a21
SS18-125	3307	148	131	65518	5653	a30
SS18-125	3820	89.9	67.4	44300	4482	a31
SS18-128	-	27.4	-	10455	3502	a35
SS18-128	-	16.8	2446	353738	25952	a33
SS18-128	1186	11.8	1.79	2122	787	a34_A
SS18-128	811	10.7	-	10759	3118	a34_B
SS18-128	3696	17.1	67.0	13500	1618	a36
SS18-128	1872	61.2	-	1744	507	a26
SS18-128	3427	67.8	84.0	17242	2960	a32
SS18-128	2389	291	47.8	12688	793	a25
SS18-128	1500	17.4	176	9070	474	a33
JS18-377	39168	908	1630	502682	62185	a52

Table 4-2**:** *Continued.*

Sample	Lithology	Inclusion category	SiO_2 (wt. %)	TiO_2	Al_2O_3	FeO_T	MnO	MgO	CaO	Na_2O	K_2O	P_2O_5
SS18-082	QZP	Silicates + ap	52.5	0.176	13.7	5.28	-	2.11	11.3	-	3.21	6.78
SS18-082	QZP	Silicates + oxides	31.0	41.3	8.68	7.46	-	5.93	-	-	0.220	0.432
SS18-082	QZP	Silicates + sulfides + oxides	-	0.00790	12.9	70.9	0.368	4.73	4.53	0.968	0.652	-
SS18-129	Tonalite	Ap	-	0.127	1.90	1.66	0.486	0.197	66.6	1.44	0.235	22.4
SS18-129	Tonalite	Ap + oxides	-	3.28	17.1	30.8	0.797	7.76	19.4	9.57	-	6.32
SS18-129	Tonalite	Ap + unkn.	-	0.158	4.87	3.54	0.0737	0.599	57.4	-	1.30	27.0
SS18-129	Tonalite	Ap + unkn.	-	0.168	9.67	4.00	0.332	2.12	48.1	2.06	2.72	25.8
SS18-129	Tonalite	Silicate min.	22.1	0.627	7.72	15.5	0.628	2.60	43.5	2.09	0.293	-
SS18-129	Tonalite	Silicates + ap + sulfides	13.8	0.324	10.0	53.6	0.885	6.61	7.80	0.350	-	1.69
SS18-129	Tonalite	Silicates + oxides	15.7	47.1	5.44	14.9	7.66	3.82	-	-	-	0.360
SS18-129	Tonalite	Silicates + sulfides	33.3	-	20.8	22.0	0.395	12.1	2.65	0.562	2.04	1.11
SS18-129	Tonalite	Silicates + sulfides	39.2	0.0897	11.8	35.0	0.362	6.60	0.306	0.138	1.24	0.279
SS18-129	Tonalite	Silicates + sulfides	38.0	0.0202	12.2	21.4	0.706	10.8	7.08	1.72	0.512	2.64
SS18-129	Tonalite	Silicates + sulfides + oxides	-	0.0403	9.50	69.1	0.616	0.40	6.53	3.07	5.77	-
SS18-129	Tonalite	Silicates + unkn.	30.8	0.871	22.0	21.0	0.477	11.1	0.420	0.974	6.83	0.469
SS18-129	Tonalite	SMI	64.5	0.427	14.8	6.54	0.226	4.43	0.481	0.0537	3.51	0.0870

Table 4-2: *Continued.*

Sample	Ag (ppm)	As	Au	B	Ba	Bi	Ce	Co	Cs	Cu	Dy	Er	Eu	Gd	Hf
SS18-082	-	-	-	-	2091	13.3	32.1	6.22	0.917	48.8	-	-	-	119	-
SS18-082	3.03	-	-	26.0	31.4	21.2	783	67.7	0.533	2.70	382	-	52.9	528	-
SS18-082	707	5110	1.72	431	83.2	36.9	1917	2659	-	5509	68.7	-	102	620	-
SS18-129	76.4	172	29.8	462	229	-	9008	28.8	-	-	-	139	1256	646	5763
SS18-129	389	3147	15.8	1985	924	104	19982	224	2.72	1050	14986	9363	4064	13564	18060
SS18-129	116	251	10.2	154	167	-	3118	15.1	-	86.2	609	-	466	964	18758
SS18-129	48.0	71.0	-	307	878	47.3	5441	8.81	-	77.2	2560	2079	460	1680	-
SS18-129	100	365	1.55	306	620	27.5	1306	432	1.97	802	1770	1736	365	939	-
SS18-129	176	2262	4.21	142	10.8	283	13559	1991	-	645	2133	1296	221	1829	18150
SS18-129	-	-	-	-	35.5	-	-	12.7	0.825	-	-	-	-	-	2591
SS18-129	-	127	-	9.31	28.1	-	268	99.5	110	861	345	730	-	83.8	-
SS18-129	-	378	0.271	109	348	3.62	402	783	2.74	1989	-	-	49.9	-	-
SS18-129	67.2	455	1.75	224	201	86.7	950	709	27.3	675	763	1358	-	111	-
SS18-129	143	2107	-	400	1371	787	510	2881	-	430	777	918	1.87	225	1640
SS18-129	-	-	-	32.9	875	-	509	41.6	136	-	934	1007	84.7	525	-
SS18-129	-	28.7	-	-	270	1.71	263	41.9	4.38	459	88.3	-	57.5	49.9	-

Table 4-2: *Continued.*

Sample	Ho (ppm)	La	Lu	Mo	Nb	Nd	Pb	Pr	Rb	Sb	Sm	Sn	Sr	Ta	Tb	Th	Tm
SS18-082	-	-	-	-	-	291	-	10.6	124	-	257	2.46	4.84	1.65	-	-	-
SS18-082	14.6	255	-	4.25	1458	643	623	119	13.7	3.10	364	13.5	-	68.9	77.9	1145	-
SS18-082	-	241	-	600	-	2825	183898	473	58.6	1474	860	6.37	366	-	55.2	463	-
SS18-129	279	2790	-	-	191	3992	3567	901	-	-	838	-	653	28.7	86.0	30589	238
SS18-129	3120	3769	1258	27.6	240	19478	6225	3135	-	2192	8391	91.5	1055	68.2	2118	41912	1385
SS18-129	56.7	1201	-	-	21.5	2789	-	536	41.8	-	849	-	369	0.560	182	-	-
SS18-129	639	1890	305	-	36.0	3181	1186	672	90.9	199	1063	21.3	740	3.67	305	4145	307
SS18-129	478	212	543	36.0	28.8	1140	2518	181	12.6	461	520	13.5	229	6.05	194	6055	333
SS18-129	429	598	176	11.4	23.0	2648	808	510	-	259	1317	25.6	47.6	-	285	481	190
SS18-129	-	-	-	-	346	-	-	-	-	-	-	8.50	-	14.5	-	-	-
SS18-129	157	25.1	350	-	-	-	3850	-	445	86.1	-	-	65.6	1.84	28.7	3661	158
SS18-129	-	126	-	5.29	7.79	389	760	87.1	49.5	4386	22.5	4.25	36.9	1.30	-	-	-
SS18-129	283	64.4	510	6.00	24.3	-	2670	-	53.6	659	-	-	351	7.64	62.3	13275	297
SS18-129	267	57.8	117	25.4	57.4	224	2282	12.1	172	800	-	25.6	637	17.3	56.5	-	110
SS18-129	287	-	133	-	19.6	171	551	19.3	414	39.8	144	-	42.1	3.11	114	2084	143
SS18-129	-	211	-	-	10.1	271	-	50.4	295	14.6	127	6.20	106	-	10.6	304	-

Table 4-2: *Continued.*

Sample	U (ppm)	V	W	Y	Yb	Analysis
SS18-082	-	63.0	-	-	-	a27
SS18-082	-	300	312	-	-	a29
SS18-082	-	8.91	22.6	-	-	a28
SS18-129	20545	56.8	27.3	6373	1069	a13_A
SS18-129	22102	1537	325	109498	9748	a14
SS18-129	-	44.7	18.7	905	-	a13_B
SS18-129	3374	64.7	19.1	21305	2156	a15
SS18-129	6552	54.0	20.9	12218	3192	a38
SS18-129	-	2372	87.5	10461	1180	a11
SS18-129	-	1105	18.9	-	-	a09
SS18-129	2647	199	-	5006	1392	a10
SS18-129	-	44.6	1.31	-	-	a37
SS18-129	6659	122	2.27	6983	2842	a40
SS18-129	8577	-	-	5258	1141	a08
SS18-129	2052	374	5.04	9462	943	a07
SS18-129	-	130	16.3	498	-	a12

4.9. References

Armstrong, J.P. 1997. Variations in silicate and sulphide mineral chemistry between free-milling “metallic” and refractory “invisible” gold ores, Con Mine, Yellowknife, N.W.T. Ph. D., University of Western Ontario, London, Ontario.

Audétat, A., and Lowenstern, J.B. 2014. Melt Inclusions. *In* Treatise on Geochemistry: Second Edition. Elsevier Inc. pp. 143–173.

Audétat, A., and Pettke, T. 2003. The magmatic-hydrothermal evolution of two barren granites: A melt and fluid inclusion study of the Rito del Medio and Cañada Pinabete plutons in northern New Mexico (USA). Geochimica et Cosmochimica Acta, **67**: 97–121.

le Bas, M.J., le Maitre, R.W., Streckeisen, A., and Zanettin, B. 1986. A Chemical Classification of Volcanic Rocks Based on the Total Alkali-Silica Diagram. Journal of Petrology, **27**: 745–750.

Berry, A.J., Danyushevsky, L. v., O’Neill, H.S.C., Newville, M., and Sutton, S.R. 2008. Oxidation state of iron in komatiitic melt inclusions indicates hot Archaean mantle. Nature, **455**: 960–963. Nature Publishing Group.

Bethune, K.M., Villeneuve, M.E., Bleeker, W., Bethune, K.M., Villeneuve, M.E., and Bleeker, W. 1999. Laser 40Ar/39Ar thermochronology of Archean rocks in Yellowknife Domain, southwestern Slave Province: insights into the cooling history of an Archean granite-greenstone terrane. Canadian Journal of Earth Sciences, **36**: 1189–1206.

Bleeker, W., and Hall, B. 2007. The Slave Craton: Geology and Metallogenic Evolution. *In* Mineral Deposits of Canada: A Synthesis of Major Deposit-Types, District Metallogeny, the Evolution of Geological Provinces, and Exploration Methods: Geological Association of Canada. *Edited by* W.D. Goodfellow. Mineral Deposits Division. pp. 849–879.

Bleeker, W., Ketchum, J.W., Jackson, V.A., Villeneuve, M.E., Bleeker, W., Villeneuve, M., Ketchum, J., and Jackson, V. 1999a. The Central Slave Basement Complex, Part I: its structural topology and autochthonous cover. Canadian Journal of Earth Sciences, **36**: 1083–1109.

Bleeker, W., Ketchum, J.W.F., and Davis, W.J. 1999b. The Central Slave Basement Complex, Part II: age and tectonic significance of high-strain zones along the basement-cover contact. Canadian Journal of Earth Sciences, **36**: 1111–1130.

Candela, P.A. 1997. A Review of Shallow, Ore-related Granites: Textures, Volatiles, and Ore Metals. Journal of Petrology, **38**: 1619–1633.

Chang, J., and Audétat, A. 2021. LA-ICP-MS Analysis of Crystallized Melt Inclusions in Olivine, Plagioclase, Apatite and Pyroxene: Quantification Strategies and

Effects of Post-Entrapment Modifications. Journal of Petrology, **62**: 1–23. Oxford University Press.

Chupin, V.P., Vetrin, V.R., Rodionov, N. v, Matukov, D.I., Berezhnaya, N.G., and Sergeev, S.A. 2006. Composition of melt inclusions and age of zircons of plagiogneisses from the Kola Superdeep Borehole, Baltic Shield. Doklady Earth Sciences, **406**: 153–157.

Cousens, B., Facey, K., and Falck, H. 2002. Geochemistry of the late Archean Banting Group, Yellowknife greenstone belt, Slave Province, Canada: Simultaneous melting of the upper mantle and juvenile mafic crust. Canadian Journal of Earth Sciences, **39**: 1635–1656.

Cousens, B., Falck, H., Ootes, L., Jackson, V., Mueller, W., Corcoran, P., Finnigan, C., van Hees, E., Facey, C., and Alcazar, A. 2006a. Regional Correlations, Tectonic Settings, and Stratigraphic Solutions in the Yellowknife Greenstone Belt and Adjacent Areas from Geochemical and Sm-Nd Isotopic Analysis of Volcanic and Plutonic Rocks. *In* Gold in the Yellowknife Greenstone Belt, Northwest Territories: Results of the EXTECH III Multidisciplinary Research Project. *Edited by* C.D. Anglin, H. Falck, D.F. Wright, and E.J. Ambrose. pp. 70–94.

Cousens, B.L. 2000. Geochemistry of the Archean Kam Group, Yellowknife Greenstone Belt, Slave Province, Canada. The Journal of Geology, **108**: 181–197.

Cousens, B.L., Falck, H., van Hees, E.H., Farrell, S., and Ootes, L. 2006b. Pb isotopic compositions of sulphide minerals from the Yellowknife gold camp: metal sources and timing of mineralization. *In* Gold in the Yellowknife Greenstone Belt, Northwest Territories: Results of the EXTECH III Multidisciplinary Research Project, Special Pub. No. 3. *Edited by* C.D. Anglin, H. Falck, D.F. Wright, and E.J. Ambrose. Geological Association of Canada Mineral Deposits Division. pp. 286–300.

Davis, W.J., and Bleeker, W. 1999. Timing of plutonism, deformation, and metamorphism in the Yellowknife Domain, Slave Province, Canada. Canadian Journal of Earth Sciences, **36**: 1169–1187.

Finnigan, C.S., and Duke, N.A. 2006. Geology and Geochemistry of the Townsite Formation: Recognition of Felsic Porphyritic Intrusions Adjacent to Gold-Bearing Shear Zones in the Yellowknife Greenstone Belt, NWT. *In* Gold in the Yellowknife Greenstone Belt, Northwest Territories: Results of the EXTECH III Multidisciplinary Research Project. *Edited by* C.D. Anglin, H. Falck, D.F. Wright, and E.J. Ambrose. pp. 58–69.

Frost, B.R., and Frost, C.D. 2014. Essentials of igneous and metamorphic petrology. Cambridge University Press.

Guillong, M., Meier, D.L., Allan, M.M., Heinrich, C.A., and Yardley, B.W.D. 2008. SILLS: A MATLAB-based program for the reduction of laser ablation ICP-MS

data of homogeneous materials and inclusions. *In* Mineralogical Association of Canada Short Course 40. Vancouver, B. C. pp. 328–333.

Halter, W.E., Pettke, T., Heinrich, C.A., and Rothen-Rutishauser, B. 2002. Major to trace element analysis of melt inclusions by laser-ablation ICP-MS: methods of quantification. Chemical Geology, **183**: 63–86.

Hanley, J., Neyedley, K., and Tweedale, F. 2020. A review of silicate and sulfide melt inclusions in felsic and mafic plutons: examples and practical aspects of study. *In* Fluid and Melt Inclusions: Applications to Geologic Processes. *Edited by* P. Lecumberri-Sanchez, M. Steele-MacInnins, and D. Kontak. Mineralogical Association of Canada. pp. 123–162.

van Hees, E.H., Kirkham, G.D., Sirbescu, M.-L., Shelton, K.L., Hauser, R.L., and Falck, H. 2006a. Large lithogeochemical alteration halos around Yellowknife gold deposits and implications for fluid pathways. *In* Gold in the Yellowknife Greenstone Belt, Northwest Territories: Results of the EXTECH III Multidisciplinary Research Project, Special Pub. No. 3. *Edited by* C.D. Anglin, H. Falck, D.F. Wright, and F. Ambrose. Geological Association of Canada Mineral Deposits Division. pp. 232–248.

van Hees, E.H., Shelton, K.L., McMenamy, T.A., Ross Jr., L.M., Cousens, B.L., Falck, H., Robb, M.E., and Canam, T.W. 1999. Metasedimentary influence on metavolcanic-rock-hosted greenstone gold deposits-Geochemistry of the Giant mine, Yellowknife, NWT. Geology, **1**: 71–74.

van Hees, E.H., Sirbescu, M.-L.C., Washington, G.D., Benda, K.J., Shelton, K.L., Falck, H., and Trenaman, R.T. 2006b. Genesis of the Ptarmigan gold deposit: is it of magmatic affinity? *In* Gold in the Yellowknife Greenstone Belt, Northwest Territories: Results of the EXTECH III Multidisciplinary Research Project, Special Pub. No. 3. *Edited by* C.D. Anglin, H. Falck, D.F. Wright, and E.J. Ambrose. Geological Association of Canada Mineral Deposits Division. pp. 270–285.

Heinrich, C.A., Pettke, T., Halter, W.E., Aigner-Torres, M., Audétat, A., Günther, D., Hattendorf, B., Bleiner, D., Guillong, ǂ M, and Horn, I. 2003. Quantitative multi-element analysis of minerals, fluid and melt inclusions by laser-ablation inductively-coupled-plasma mass-spectrometry. Geochimica et Cosmochimica Acta, **67**: 3473–3496.

Helmstaedt, H., and Padgham, W.A. 1986. A new look at the stratigraphy of the Yellowknife Supergroup at Yellowknife, N.W.T. — implications for the age of gold-bearing shear zones and Archean basin evolution. Canadian Journal of Earth Sciences, **23**: 454–475. Available from www.nrcresearchpress.com.

Helmstaedt, H.H. 2006. Evolution of geological understanding of the Yellowknife Domain. *In* Gold in the Yellowknife Greenstone Belt, Northwest Territories: Results of the EXTECH III Multidisciplinary Research Project, Special Pub. No. 3. *Edited by* C.D. Anglin, H. Falck, D.F. Wright, and E.J. Ambrose. Geological Association of Canada Mineral Deposits Division. pp. 29–37.

Henderson, J.F., and Brown, I.C. 1966. Geology and structure of the Yellowknife greenstone belt, District of Mackenzie. *In* Bulletin 141. Geological Survey of Canada.

Irvine, T.N., and Baragar, W.R.A. 1971. A Guide to the Chemical Classification of the Common Volcanic Rocks. Canadian Journal of Earth Sciences, **8**: 523–548.

Isachsen, C.E. 1992. U-Pb zircon geochronology of the Yellowknife volcanic belt and subjacent rocks, N.W.T., Canada: Constraints on the timing, duration, and mechanics of greenstone belt formation. Ph. D., Washington University, St. Louis, Mo.

Isachsen, C.E., and Bowring, S.A. 1994. Evolution of the Slave craton. Geology, **22**: 917–920.

Lecumberri-Sanchez, P., Steele-MacInnis, M., and Kontak, D. 2021. Fluid and Melt Inclusions: Applications to Geologic Processes. *Edited By* R. Raeside. Mineralogical Association of Canada, London, Ontario.

Lowenstern, J.B. 2003. Melt Inclusions Come of Age: Volatiles, Volcanoes, and Sorby's Legacy.

Martel, E., and Lin, S. 2006. Structural Evolution of the Yellowknife Greenstone Belt, with Emphasis on the Yellowknife River Fault Zone and the Jackson Lake Formation. *In* Gold in the Yellowknife Greenstone Belt, Northwest Territories: Results of the EXTECH III Multidisciplinary Research Project, Special Pub. No. 3. *Edited by* C.D. Anglin, H. Falck, D.F. Wright, and E.J. Ambrose. pp. 95–115.

Mason, P.R.D., Nikogosian, I., and van Bergen, M.J. 2008. Major and trace element analysis of melt inclusions by laser ablation ICP-MS. *In* Laser ablation ICP-MS in the Earth Sciences: Current practices and outstanding issues. *Edited by* P. Sylvester. Mineralogical Association of Canada. pp. 219–239.

Meagher, D.J. 2020. A melt inclusion study of rhyolitic volcanics in the Bousquet Formation, Doyon-Bousquet-LaRonde district, Abitibi Subprovince, Québec: Insight into Archean magmatic processes. M. Sc. Applied Science, Saint Mary's University, Halifax.

Morales, I., Molina, J.F., Cambeses, A., Montero, P., and Bea, F. 2022. Experimental Annealing of Zircon: Influence of Inclusions on Stability, Intracrystalline Melt Migration, Common Lead Leaching, and Permeability to Fluids. ACS Earth and Space Chemistry, **6**: 288–307.

Mustard, R., Ulrich, T., Kamenetsky, V.S., and Mernagh, T. 2006. Gold and metal enrichment in natural granitic melts during fractional crystallization. Geology, **34**: 85–88.

Neyedley, K., Hanley, J.J., Zajacz, Z., and Tsay, A. 2020. Metal Tenor and Volatile Content of the Folly Lake Diorite, Eastern Cobequid Highlands, Nova Scotia: Insights into Magma Fertility from Zircon-hosted Silicate Melt Inclusions. Nova Scotia Department of Energy and Mines.

Ootes, L., and Lentz, D.R. 2002. Occurrence of bleached mafic flows and their association with stockwork sulphides and banded iron-formation in the Crestaurum Formation of the late Archean Yellowknife Greenstone Belt, Northwest Territories. *In* Current Research-E5. Geological Survey of Canada.

Ootes, L., Lentz, D.R., Cabri, L.J., and Hall, D.C. 2006. Geology and Gold Mineralization in the Crestaurum Mine Area, Northern Yellowknife Greenstone Belt, N. W. T. *In* Gold in the Yellowknife Greenstone Belt, Northwest Territories: Results of the EXTECH III Multidisciplinary Research Project, Special Pub. No. 3. *Edited by* C.D. Anglin, H. Falck, D.F. Wright, and E.J. Ambrose. pp. 249–269.

Ootes, L., Lentz, D.R., Creaser, R.A., Ketchum, J.W.F., and Falck, H. 2007. Re-Os molybdenite ages from the Archean Yellowknife greenstone belt: Comparison to U-Pb ages and evidence for metal introduction at ~2675 Ma. Economic Geology, **102**: 511–518.

Ootes, L., Morelli, R.M., Creaser, R.A., Lentz, D.R., Falck, H., and Davis, W.J. 2011. The timing of Yellowknife gold mineralization: a temporal relationship with crustal anatexis? Economic Geology, **106**: 713–720.

Palmer, E.M. 2018. Petrogenesis of the Archean Prestige leucogranite and spatially associated LCT pegmatites, NWT: insights from whole-rock and muscovite trace element geochemistry and apatite U-Pb geochronology. M. Sc., University of New Brunswick, Fredericton, NB.

Rudnick, R.L., and Gao, S. 2003. Composition of the Continental Crust. *In* Treatise on Geochemistry. *Edited by* H.D. Holland and K.K. Turekian. pp. 1–64.

Shelton, K.L., McMenamy, T.A., van Hees, E.H.P., and Falck, H. 2004. Deciphering the Complex Fluid History of a Greenstone-Hosted Gold Deposit: Fluid Inclusion and Stable Isotope Studies of the Giant Mine, Yellowknife, Northwest Territories, Canada. Economic Geology, **99**: 1643–1663.

Siddorn, J.P. 2011. The Giant-Con gold deposit: a once-linked Archean lode-gold system. Ph. D., University of Toronto, Toronto, ON.

Siddorn, J.P., Cruden, A.R., Hauser, R.L., Armstrong, J.P., and Kirkham, G. 2006. The Giant-Con gold deposits: Preliminary integrated structural and mineralization history. *In* Gold in the Yellowknife Greenstone Belt, Northwest Territories: Results of the EXTECH III Multidisciplinary Research Project, Special Pub. No. 3. *Edited by* C.D. Anglin, H. Falck, D.F. Wright, and E.J. Ambrose. Geological Association of Canada Mineral Deposits Division. pp. 213–231.

Sobolev, A.V. 1996. Melt inclusions in minerals as a source of principle petrological information. Petrology, **4**: 228–239.

Speight, S.C., Hanley, J.J., and McFarlane, C.R.M. 2023a. Geodynamic evolution of felsic magmatism in the Yellowknife greenstone belt, N.W.T., Canada: evidence for Archean magmatism in a volatile-saturated environment. In prep., Fredericton, N. B.

Speight, S.C., McFarlane, C.R.M., and Hanley, J.J. 2023b. U-Pb geochronology and zircon mineral chemistry of syn-volcanic and plutonic intrusions in the Yellowknife greenstone belt, NWT, Canada: understanding an Archean magmatic plumbing system. In prep., Fredericton, N. B.

Thomas, J.B., Bodnar, R.J., Shimizu, N., and Chesner, C.A. 2003. Melt Inclusions in Zircon. Reviews in Mineralogy and Geochemistry, **53**: 63–67.

Thompson, P.H. 2006. Metamorphic Constraints on the Geological Setting, Thermal Regime, and Timing of Alteration and Gold Mineralization in the Yellowknife Greenstone Belt, NWT, Canada. *In* Gold in the Yellowknife Greenstone Belt, Northwest Territories: Results of the EXTECH III Multidisciplinary Research Project, Special Pub. No. 3. *Edited by* C.D. Anglin, H. Falck, D.F. Wright, and E.J. Ambrose. Geological Association of Canada Mineral Deposits Division. pp. 142–172.

Zajacz, Z., Halter, W.E., Pettke, T., and Guillong, M. 2008. Determination of fluid/melt partition coefficients by LA-ICPMS analysis of co-existing fluid and silicate melt inclusions: Controls on element partitioning. Geochimica et Cosmochimica Acta, **72**: 2169–2197.

Zhang, D., and Audétat, A. 2017. What Caused the Formation of the Giant Bingham Canyon Porphyry Cu-Mo-Au Deposit? Insights from Melt Inclusions and Magmatic Sulfides. Economic Geology, **112**: 221–244.

5. Conclusions

This dissertation focused on expanding our understanding of the magmatic history in the YGB. The project used a multi-analytical approach to examine the geochemical evolution, emplacement, timing and metallogenic characteristics of dikes and plutons in the belt. The YGB is host to multiple generations of dikes ("#9" dikes) and regional plutons that have not been the focus of a comprehensive investigation until this time. A spatial relationship between gold mineralization and dikes that crosscut the Kam Group has been previously noted, therefore the pre-emplacement metal characteristics were also studied via zircon-hosted melt inclusions. This investigation yielded the following conclusions:

I. A broad lithogeochemical dataset was obtained for dikes and plutons in the YGB. The major, minor, and trace element data were evaluated to determine the genetic relationships between multiple generations of dikes and their possible parental plutons. The data presented here effectively discriminates the "#9" dikes in the belt using REE geochemistry. Three dike-pluton relationships were observed based on the Eu anomaly, or lack thereof, observed in the REE profiles and LREE-HREE signature. The FQP and aplite-1(a) from this study were geochemically and genetically associated with the multi-phase RLP. The aplite-1(b) dikes have been linked to the Defeat Suite granite, and finally the aplite-2 dikes to the Duckfish granite. These dikes represent early- to synvolcanic intrusions that are genetically related to their parental plutons. This interpretation is also supported by the U-Pb geochronology and zircon mineral chemistry data.

II. Petrographic and textural analysis of aplitic dikes proximal to the RLP, Defeat Suite granite, and Duckfish granite indicate that the dikes were emplaced at various stages of pluton crystallization. All three plutons showed evidence of late magmatic to late post-magmatic stage dike emplacement, signifying crystallization > 90 % and related volatile-saturated fluids. Only the RLP and aplite-1(a) dikes showed evidence of emplacement during all four stages of dike emplacement, including the main magmatic stage. Macroscopic evidence of volatile saturation was also observed in the field as quartz cores within the aplite dikes and discontinuous quartz pods.

III. The evaluation of a large dataset of Archean zircons proved to be an effective method of determining concordant $^{207}Pb/^{206}Pb$ ages when Pb-loss and inheritance are a great concern. The determination of $^{207}Pb/^{206}Pb$ ages for dikes and plutons in the YGB by LA-ICP-MS provided an initial dataset to determine general timing relationships between dikes and plutons, then samples were subsequently analyzed by CA-TIMS. Closely spaced magmatic events require the use of high-precision analytical techniques, in this case, CA-TIMS, to fully resolve the magmatic history. The FQP dikes in this study showed a broad range of ages from 2746 to 2662 Ma, however, four of the five samples had ages between 2674 and 2662 Ma. These ages correlate with the geochemically related RLP tonalite, which yielded a CA-TIMS age of 2662 Ma. Overall, the main group of intrusions related

to the RLP, including two FQP dikes, an aplite-1(a) dike, and one tonalite sample yielded CA-TIMS ages of 2662-2663 Ma.

IV. One aplite-1(b) dike was also analyzed by CA-TIMS and yielded an age of 2662 Ma, correlating with the ages obtained for the RLP and related rocks. This dike has been geochemically linked to the Defeat Suite granite. This suggests that early intrusion of the aplite-1(b) from the Defeat Suite granite magma chamber occurred while FQP and aplite-1(a) dikes and tonalites were being emplaced at ca. 2662-2663 Ma. Together these results indicate that two distinct magma chambers were present at this time, despite the earliest ages obtained for the Defeat Suite granite from previous research (i.e., 2630 Ma).

V. Results related to the QZP dikes did not yield a genetic relationship with a parental pluton from this study. The QZP dike geochemical signature has traits common to both the multi-phase RLP and the younger Defeat Suite granite. One QZP dike was sampled for U-Pb geochronologic analysis from an area proximal to the Duckfish granite. Both LA-ICP-MS and CA-TIMS data yielded correlating ages, and the QZP dike is interpreted to have a crystallization age of 2770 ± 7 Ma. Despite this older age, the QZP dike has a more evolved geochemical signature compared to other lithologies in this study. Therefore, this QZP dike is interpreted to reflect an older magmatic event not presently studied that may be part of the underlying CSBC. The oldest FQP dike was also sampled from this northern field area and yielded an interpreted age of crystallization of 2746 ± 15 Ma; together this suggests that this

domain of the Kam Group and Chan Formation may be related to the underlying basement complex.

VI. Zircon mineral chemistry mimics the groupings observed in the whole rock geochemical data. The zircons record local variations in magma chemistry as the grains crystallized in an evolving magma chamber. This is reflected in the overall wide range of zircon REE concentrations and Eu anomaly. The Eu anomaly in the zircons of YGB intrusions was found to be variably positive and negative in the FQP dikes, QZP dikes, tonalite, and granodiorite. This variable Eu signature is interpreted to reflect either zircon saturation in the RLP magma chamber before plagioclase crystallization, assimilation of the plagioclase-rich mafic volcanic flows at the base of the Kam Group, or some combination of these processes. The identification of these differing REE profiles in the lithogeochemical data and zircon mineral chemistry provides an exploration tool for future characterization of dikes and plutons during mineral exploration within the YGB.

VII. The magmatic history of the YGB is refined using a multi-analytical approach to evaluate the genetic relationships between dikes and plutons in the YGB combining U-Pb geochronology, lithogeochemistry, zircon mineral chemistry, and field observations. This combination of data confirmed that the FQP dikes alone are related to the RLP and calc-alkaline Townsite Formation and Banting Group felsic volcaniclastic, and not all “#9” dikes. These results established that FQP dikes and related multi-phase RLP form the magmatic plumbing system to the felsic

volcaniclastic units and provide effective conduits for magmatic-hydrothermal fluids.

VIII. A preliminary analysis of zircon-hosted MI determined that semi-quantitative results can still provide data that represent SMI if sufficient data filtering is done. In this case, results from 50 YGB zircon-hosted MI were narrowed down to seven inclusions that were considered to best represent primary melt data. The remaining data were classified as mixed MMI that were thought to be contaminated, often by accidentally trapped phases.

IX. The mixed MMI showed evidence of accidently trapped phases that include quartz, feldspars, apatite, biotite, amphibole, Fe-(Ti)-oxides, and sulfides. For these phases to become trapped in the zircon-host, these minerals must have been saturated in the melt and co-crystallizing with zircon. This provides direct evidence from Archean zircon-hosted MI regarding Ti-saturation and H_2O-saturation in these primary magmas.

X. When the SMI data are compared to lithogeochemistry from the same samples in the YGB and upper continental crust values, evidence of metal enrichment is observed. The data presented here indicate that As, Sb, Cu, Sn, W, Pb, and Bi were increasing in the primary magmas during fractional crystallization. Some metal concentrations are several orders of magnitude higher than the lithogeochemistry or upper continental crustal values, which may be due to unidentified metal-rich nanocrystals in the inclusions, or from fractional crystallization processes.

XI. The semi-quantitative zircon-hosted MI data indicates that there is a positive relationship between Au and various metals, including Ag, As, Bi, Pb, Sn, W, and Mo. In contrast, no correlation was observed between Au and Co, Cu, Sb, or Ta. This suggests that these Archean MI preserved evidence of an early intrusion-related Au signature in the YGB dikes and plutons.

5.1. Dissertation contributions

This dissertation provides a systematic evaluation of dikes and plutons in the YGB after preliminary field work and a thorough literature review. This has resulted in an improved understanding of the magmatic history in the belt and depiction of the ancient magmatic plumbing system ca. 2662 Ma. The results and conclusions presented here provided lithogeochemical and geochronological insights into the dike-pluton relationships of multiple generations of dikes and parental plutons. Previous work has presented data related to the regional plutons and some generations of dikes but did not evaluate their genetic connections. This dissertation provides several levels of evidence, including lithogeochemistry, U-Pb geochronology, and mineral chemistry, to establish the parental plutons of YGB dikes. The multi-analytical and stepwise approach of this dissertation contributed to the overall understanding of the Archean YGB magmatic plumbing system and placed the intrusions within the geotectonic framework of past research. This thesis also provides the first zircon-hosted SMI dataset in the YGB and contributes to the global dataset of Archean MI in general. Zircon-hosted SMI provides evidence of metal-enrichment in YGB intrusions that pre-date currently reported mineralization events. The

results and interpretations in this dissertation also provide further avenues of research, outlined below.

5.2. Future work

Future research initiatives should focus on three general areas of study in the YGB, which include field work, geochronologic studies, and melt inclusion analysis with the following goals:

I. Mapping and sampling programs that focus on expanding the spatial extent of the RLP, as it was found in an unidentified area near Milner Lake. Increased sampling around Ryan Lake would advance the lithogeochemical database and identify other domains of the RLP and potential mineralization. Exploration and mapping could also focus on identifying the older generation of FQP dikes to refine their connection to the Townsite Formation. The area proximal to the 2770 Ma QZP dike and Duckfish granite should also be further explored to determine its relationship with the underlying CSCG. Assessing this area of the Chan Formation could shed light on the overall YGB stratigraphy.

II. Future U-Pb geochronology studies could offer expanded geologic interpretations by obtaining polished thick sections to perform *in-situ* analysis of zircons and accessory phases. A more extensive analysis of the QZP dikes throughout the YGB would provide clarity regarding their timing and plutonic source. Further sampling of the Defeat Suite granite in the western and eastern YGB, and subsequent

analysis by high-resolution CA-TIMS, could clarify the crystallization history of this plutonic suite.

III. A more in-depth analysis of melt inclusions from dikes and plutons in the YGB would continue to characterize early metal enrichments in the belt. Future studies should focus on expanding the database to include different lithologies to compare their precious metal signatures. This data could be collected concurrently with U-Pb geochronology to determine the timing of metal saturation. Finally, melt inclusion samples could also be examined for complimentary fluid inclusions that would provide pre-emplacement and pre-eruptive information related to Archean magmatic-hydrothermal fluids.

Appendix 1: Geodynamic evolution of felsic magmatism in the Yellowknife greenstone belt, N.W.T., Canada: evidence for Archean magmatism in a volatile-saturated environment

Table A1.1: Summary of sample locations, lithology and associated host rock (where applicable).

Lithology	Sample	Easting	Northing	Host rock
aplite-1(a)	SS18-018A	635848	6942541	mafic volcanic flow
	SS18-018B	635844	6942536	mafic volcanic flow
	SS18-053B	635489	6942208	tonalite
	SS18-055	635471	6942257	tonalite
	SS18-062A	635584	6942562	granodiorite
	SS18-062B	635584	6942562	granodiorite
	SS18-067	635471	6942485	tonalite
	SS18-071	635431	6942614	granodiorite
	UNB-1	635871	6942769	mafic volcanic flow
aplite-1(b)	SS18-005A	636004	6943495	mafic volcanic flow
	SS18-007	636153	6943613	mafic volcanic flow
	SS18-029	635767	6943376	mafic volcanic flow
	SS18-030A	635758	6943276	mafic volcanic flow
	SS18-030B	635758	6943276	mafic volcanic flow
	SS18-032	635516	6943632	mafic volcanic flow
	UNB-2	635765	6943469	mafic volcanic flow
aplite-2	SS18-073	635621	6948032	gabbro
	SS18-075	635618	6947975	gabbro
	SS18-087	634947	6947825	mafic volcanic flow
	SS18-091A	634889	6947723	mafic volcanic flow
	SS18-093	634887	6947692	mafic volcanic flow
	SS18-094	634484	6947197	mafic volcanic flow
	SS18-104	634603	6947325	mafic volcanic flow
	SS18-105	634657	6947347	mafic volcanic flow
FQP	SS18-008	636212	6943602	mafic volcanic flow
	SS18-013	636022	6943787	mafic volcanic flow
	SS18-017	635878	6942557	mafic volcanic flow
	SS18-035	635654	6943892	mafic volcanic flow
	SS18-051	636643	6942621	mafic volcanic flow
	SS18-100	634514	6947212	mafic volcanic flow
	SS18-125	637429	6940080	gabbro
	SS18-128A	636508	6942271	gabbro
QZP	SS18-011	636206	6943929	mafic volcanic flow
	SS18-039	637082	6942955	mafic volcanic flow
	SS18-042	637124	6942814	mafic volcanic flow
	SS18-082	635733	6947690	mafic volcanic flow

Table A1.1: *Continued.*

Lithology	Sample	Easting	Northing	Host rock
Intermediate dike	SS18-109	635121	6946972	mafic volcanic flow
Intermediate volcanic tuff	SS18-118	637437	6940366	-
granodiorite (RLP)	SS18-020	635798	6942574	-
	SS18-021	635826	6942756	-
	SS18-054	635446	6942233	-
	SS18-057	635462	6942293	-
	SS18-058	635490	6942293	-
	SS18-061	635704	6942434	-
	SS18-063	635589	6942561	-
	SS18-065	635537	6942496	-
	SS18-072	635431	6942614	-
Defeat Suite granite	JS18-374	643840	6924097	-
	JS18-377	644112	6924245	-
Duckfish granite	SS18-084	634968	6947860	-
	SS18-085	634929	6947869	-
tonalite (RLP)	SS18-053A	635486	6942197	-
	SS18-066	635470	6942487	-
	SS18-069	635495	6942572	-
	SS18-070	635485	6942546	-
	SS18-129	636274	6942523	-

Table A1.2: Major and trace element lithogeochemistry for representative samples from the YGB, including dikes, plutons, and one volcanic tuff.

			SS18-008	SS18-013	SS18-017	SS18-035	SS18-051	SS18-100
	Detection Limit	Analysis method	FQP	FQP	FQP	FQP	FQP	FQP
SiO_2 (wt. %)	0.01	FUS-ICP	65.7	65.5	68.2	65.1	64.2	67.5
Al_2O_3	0.01	FUS-ICP	14.6	15.1	14.7	15.3	14.8	16.1
FeO_T	0.01	FUS-ICP	5.11	5.59	4.44	5.65	5.46	4.4
MnO	0.001	FUS-ICP	0.0610	0.0600	0.0660	0.0800	0.0540	0.0760
MgO	0.01	FUS-ICP	1.92	2.22	1.26	2.34	2.15	1.46
CaO	0.01	FUS-ICP	3.53	4.31	3.33	3.96	3.75	2.99
Na_2O	0.01	FUS-ICP	3.65	3.84	3.68	3.88	3.74	4.85
K_2O	0.01	FUS-ICP	1.86	1.26	2.41	1.91	1.90	1.31
TiO_2	0.001	FUS-ICP	0.465	0.520	0.443	0.529	0.481	0.362
P_2O_5	0.01	FUS-ICP	0.180	0.190	0.160	0.190	0.200	0.0600
LOI		GRAV	2.15	1.67	0.91	1.14	4.08	1.28
Total	0.01	FUS-ICP	99.2	100	99.5	100	101	100
Ag (ppm)	0.5	FUS-MS	0.600	0.600	0.600	0.500	0.600	*< 0.500*
As	5	FUS-MS	6.00	6.00	12.0	17.0	10.0	*< 5.00*
Ba	2	FUS-ICP	599	337	925	577	763	390
Be	1	FUS-ICP	2.00	2.00	2.00	2.00	2.00	1.00
Bi	0.1	FUS-MS	1.30	0.100	0.100	0.100	0.100	0.100
Ce	0.05	FUS-MS	96.9	100	119	92.9	107	26.1
Co	1	FUS-MS	12.0	13.0	8.00	14.0	12.0	7.00
Cr	20	FUS-MS	50.0	60.0	20.0	50.0	40.0	20.0
Cs	0.1	FUS-MS	10.2	2.90	2.30	9.70	2.30	1.20
Cu	10	FUS-MS	60.0	20.0	*< 10.0*	30.0	30.0	20.0
Dy	0.01	FUS-MS	2.21	2.54	2.44	2.38	2.58	1.30
Er	0.01	FUS-MS	1.12	1.37	1.26	1.30	1.33	0.740
Eu	0.005	FUS-MS	1.37	1.53	1.35	1.38	1.55	0.555
Ga	1	FUS-MS	17.0	19.0	18.0	18.0	17.0	21.0
Gd	0.01	FUS-MS	3.62	4.08	3.73	3.83	4.09	1.57
Ge	0.5	FUS-MS	1.10	1.20	1.10	1.00	1.00	0.900
Hf	0.1	FUS-MS	3.40	4.20	4.20	3.90	4.30	3.00
Ho	0.01	FUS-MS	0.400	0.470	0.450	0.450	0.490	0.250
In	0.1	FUS-MS	*< 0.100*	*< 0.100*	*< 0.100*	*< 0.100*	*< 0.100*	*< 0.100*

Table A1.2: *Continued*.

			SS18-008	SS18-013	SS18-017	SS18-035	SS18-051	SS18-100
	Detection Limit	Analysis method	FQP	FQP	FQP	FQP	FQP	FQP
La (ppm)	0.05	FUS-MS	50.6	52.2	64.2	48.3	55.0	13.6
Lu	0.002	FUS-MS	0.158	0.175	0.173	0.170	0.175	0.116
Mo	2	FUS-MS	3.00	*< 2.00*	*< 2.00*	*< 2.00*	*< 2.00*	*< 2.00*
Nb	0.2	FUS-MS	4.20	5.60	5.60	5.70	5.50	2.50
Nd	0.05	FUS-MS	36.2	38.2	39.3	34.0000	38.7	10.1
Ni	20	FUS-MS	30.0	30.0	30.0	40.0	30.0	*< 20.0*
Pb	5	FUS-MS	9.00	11.0	13.0	13.0	9.00	8.00
Pr	0.01	FUS-MS	10.5	10.9	12.2	10.1	11.4	2.74
Rb	1	FUS-MS	83.0	56.0	67.0	90.0	56.0	39.0
Sb	0.2	FUS-MS	0.300	0.600	3.20	0.600	0.700	*< 0.200*
Sc	1	FUS-ICP	8.00	10.0	7.00	10.0	10.0	7.00
Sm	0.01	FUS-MS	5.64	5.86	5.80	5.47	5.95	1.80
Sn	1	FUS-MS	2.00	1.00	1.00	1.00	1.00	1.00
Sr	2	FUS-ICP	362	368	329	380	269	308
Ta	0.01	FUS-MS	0.540	0.610	0.640	0.580	0.580	0.210
Tb	0.01	FUS-MS	0.490	0.540	0.490	0.480	0.560	0.220
Th	0.05	FUS-MS	15.0	15.4	22.3	13.8	16.1	3.87
Tl	0.05	FUS-MS	0.290	0.100	0.160	0.410	0.190	0.600
Tm	0.005	FUS-MS	0.163	0.199	0.186	0.180	0.188	0.105
U	0.01	FUS-MS	3.35	3.58	4.28	2.81	3.41	1.19
V	5	FUS-ICP	78.0	85.0	61.0	90.0	80.0	60.0
W	0.5	FUS-MS	32.3	0.500	2.10	*< 0.500*	2.20	*< 0.500*
Y	0.5	FUS-MS	11.4	13.5	12.6	12.5	14.0	7.20
Yb	0.01	FUS-MS	1.01	1.18	1.19	1.12	1.15	0.730
Zn	30	FUS-MS	50.0	30.0	40.0	60.0	40.0	50.0
Zr	1	FUS-ICP	138	158	170	156	171	101
Eu/Eu*			0.927	0.957	0.887	0.922	0.961	1.01
Ce/Ce*			0.971	0.935	1.04	1.02	0.990	1.07
T_{ZrSat} (°C)			1026	1165	1127	1025	920	1205

Table A1.2: *Continued*.

			SS18-125	SS18-128A	SS18-011	SS18-039	SS18-042	SS18-082
	Detection Limit	Analysis method	FQP	FQP	QZP	QZP	QZP	QZP
SiO_2 (wt. %)	0.01	FUS-ICP	64.0	62.7	77.8	73.4	77.8	73.0
Al_2O_3	0.01	FUS-ICP	15.2	15.9	12.3	14.4	13.2	15.5
FeO_T	0.01	FUS-ICP	5.61	5.91	1.42	1.94	1.47	1.63
MnO	0.001	FUS-ICP	0.0740	0.0980	0.0200	0.0550	0.0250	0.0240
MgO	0.01	FUS-ICP	2.20	2.40	0.180	0.310	0.230	0.320
CaO	0.01	FUS-ICP	3.95	3.22	0.590	0.990	0.780	2.14
Na_2O	0.01	FUS-ICP	3.73	0.600	6.63	4.95	3.38	4.95
K_2O	0.01	FUS-ICP	2.18	3.25	0.12	1.68	2.02	1.73
TiO_2	0.001	FUS-ICP	0.524	0.570	0.171	0.194	0.155	0.112
P_2O_5	0.01	FUS-ICP	0.210	0.220	0.0300	0.0500	0.0200	0.0200
LOI		GRAV	2.11	5.85	0.550	1.69	1.43	0.68
Total	0.01	FUS-ICP	99.8	101	99.8	99.6	101	100
Ag (ppm)	0.5	FUS-MS	0.600	0.600	0.600	*< 0.500*	*< 0.500*	*< 0.500*
As	5	FUS-MS	*< 5.00*	*< 5.00*	146	432	25.0	13.0
Ba	2	FUS-ICP	706	525	34.0	484	785	432
Be	1	FUS-ICP	2.00	2.00	2.00	1.00	2.00	1.00
Bi	0.1	FUS-MS	0.100	*< 0.100*	8.00	0.200	*< 0.100*	*< 0.100*
Ce	0.05	FUS-MS	98.3	103	26.0	29.8	92.7	7.04
Co	1	FUS-MS	15.0	24.0	3.00	3.00	1.00	2.00
Cr	20	FUS-MS	40.0	40.0	*< 20.0*	*< 20.0*	*< 20.0*	40.0
Cs	0.1	FUS-MS	14.0	3.20	0.100	1.60	2.10	1.50
Cu	10	FUS-MS	30.0	*< 10.0*	170	10.0	*< 10.0*	30.0
Dy	0.01	FUS-MS	2.27	2.48	0.740	0.540	1.82	0.440
Er	0.01	FUS-MS	1.22	1.33	0.280	0.240	1.08	0.210
Eu	0.005	FUS-MS	1.59	1.60	0.465	0.433	0.854	0.222
Ga	1	FUS-MS	18.0	19.0	11.0	20.0	15.0	18.0
Gd	0.01	FUS-MS	3.85	3.99	1.12	0.96	2.66	0.53
Ge	0.5	FUS-MS	1.00	0.900	0.600	0.700	0.700	0.800
Hf	0.1	FUS-MS	3.90	4.10	2.60	2.80	2.80	2.20
Ho	0.01	FUS-MS	0.430	0.450	0.120	0.0900	0.370	0.0800
In	0.1	FUS-MS	*< 0.100*	*< 0.100*	*< 0.100*	*< 0.100*	*< 0.100*	*< 0.100*

Table A1.2: *Continued*.

			SS18-125	SS18-128A	SS18-011	SS18-039	SS18-042	SS18-082
	Detection Limit	Analysis method	FQP	FQP	QZP	QZP	QZP	QZP
La (ppm)	0.05	FUS-MS	51.3	54.4	16.3	17.9	52.5	3.53
Lu	0.002	FUS-MS	0.171	0.173	0.0450	0.0350	0.159	0.0310
Mo	2	FUS-MS	*< 2.00*	*< 2.00*	27.0	*< 2.00*	*< 2.00*	6.00
Nb	0.2	FUS-MS	5.70	5.90	1.90	1.90	6.20	0.900
Nd	0.05	FUS-MS	37.4	39.0	8.81	9.25	28.8	3.20
Ni	20	FUS-MS	20.0	30.0	30.0	*< 20.0*	20.0	*< 20.0*
Pb	5	FUS-MS	10.0	5.00	47.0	8.00	*< 5.00*	14.0
Pr	0.01	FUS-MS	10.5	11.0	2.48	2.93	9.34	0.830
Rb	1	FUS-MS	87.0	86.0	3.00	45.0	60.0	52.0
Sb	0.2	FUS-MS	1.80	3.50	0.400	1.20	0.600	0.200
Sc	1	FUS-ICP	9.00	11.0	1.00	2.00	2.00	1.00
Sm	0.01	FUS-MS	5.87	5.98	1.74	1.52	4.19	0.630
Sn	1	FUS-MS	1.00	1.00	1.00	*< 1.00*	1.00	*< 1.00*
Sr	2	FUS-ICP	517	79.0	100	162	70.0	208
Ta	0.01	FUS-MS	0.480	0.490	0.330	0.320	0.730	0.140
Tb	0.01	FUS-MS	0.460	0.480	0.140	0.130	0.340	0.0800
Th	0.05	FUS-MS	15.2	16.5	5.79	5.23	21.9	1.91
Tl	0.05	FUS-MS	0.840	0.630	*< 0.0500*	0.250	0.370	0.280
Tm	0.005	FUS-MS	0.171	0.191	0.0400	0.0340	0.150	0.035
U	0.01	FUS-MS	3.01	3.28	1.98	1.56	3.92	1.03
V	5	FUS-ICP	85.0	96.0	12.0	19.0	8.00	9.00
W	0.5	FUS-MS	0.90	*< 0.500*	5.40	9.60	7.00	0.800
Y	0.5	FUS-MS	12.9	12.9	3.00	2.60	10.4	2.30
Yb	0.01	FUS-MS	1.09	1.11	0.270	0.210	0.990	0.230
Zn	30	FUS-MS	60.0	60.0	*< 30.0*	*< 30.0*	*< 30.0*	*< 30.0*
Zr	1	FUS-ICP	154	167	98.0	100	114	65.0
Eu/Eu*			1.02	1.00	1.02	1.10	0.782	1.17
Ce/Ce*			0.961	0.943	1.36	1.23	1.09	1.01
T_{ZrSat} (°C)			976	1061	1035	1016	1009	961

Table A1.2: *Continued*.

			SS18-005A	SS18-007	SS18-018B	SS18-029	SS18-032	SS18-053B
	Detection Limit	Analysis method	APL 1	APL 1	APL 1	APL 1	APL 1	APL 1
SiO_2 (wt. %)	0.01	FUS-ICP	61.6	77.6	73.8	76.9	76.2	65.2
Al_2O_3	0.01	FUS-ICP	17.4	13.4	13.9	12.6	12.8	16.1
FeO_T	0.01	FUS-ICP	0.740	1.57	1.67	1.30	1.36	5.65
MnO	0.001	FUS-ICP	0.0570	0.0840	0.0190	0.0240	0.0120	0.0470
MgO	0.01	FUS-ICP	0.0700	0.120	0.460	0.180	0.0400	2.09
CaO	0.01	FUS-ICP	5.61	0.470	1.55	0.500	0.730	2.48
Na_2O	0.01	FUS-ICP	9.55	7.12	5.45	6.12	6.26	3.69
K_2O	0.01	FUS-ICP	0.350	0.220	1.09	1.01	0.650	2.07
TiO_2	0.001	FUS-ICP	0.0180	0.0210	0.162	0.0430	0.0220	0.509
P_2O_5	0.01	FUS-ICP	*< 0.0100*	0.0200	0.0300	*< 0.0100*	*< 0.0100*	0.220
LOI		GRAV	4.33	0.270	0.770	0.460	0.440	2.51
Total	0.01	FUS-ICP	99.8	101	98.9	99.2	98.6	101
Ag (ppm)	0.5	FUS-MS	*< 0.500*	*< 0.500*	*< 0.500*	*< 0.500*	0.500	0.800
As	5	FUS-MS	*< 5.00*	*< 5.00*	10.0	12.0	*< 5.00*	13.0
Ba	2	FUS-ICP	28.0	30.0	325	85.0	69.0	998
Be	1	FUS-ICP	5.00	6.00	3.00	3.00	3.00	4.00
Bi	0.1	FUS-MS	*< 0.100*	*< 0.100*	*< 0.100*	*< 0.100*	0.300	0.800
Ce	0.05	FUS-MS	46.3	27.2	75.5	18.0	6.81	196
Co	1	FUS-MS	*< 1.00*	3.00	6.00	5.00	*< 1.00*	12.0
Cr	20	FUS-MS	*< 20.0*	*< 20.0*	30.0	30.0	20.0	30.0
Cs	0.1	FUS-MS	0.100	0.300	0.600	0.200	0.200	3.70
Cu	10	FUS-MS	*< 10.0*	30.0	40.0	40.0	50.0	210
Dy	0.01	FUS-MS	8.38	5.75	1.36	2.72	2.77	3.54
Er	0.01	FUS-MS	3.77	2.14	0.84	1.54	1.95	1.66
Eu	0.005	FUS-MS	0.814	0.144	0.672	0.306	0.054	2.08
Ga	1	FUS-MS	21.0	20.0	16.0	14.0	17.0	19.0
Gd	0.01	FUS-MS	8.67	4.61	1.93	2.49	1.94	5.89
Ge	0.5	FUS-MS	2.10	1.40	1.10	1.20	1.10	1.30
Hf	0.1	FUS-MS	3.40	2.30	2.90	2.30	5.30	5.20
Ho	0.01	FUS-MS	1.44	0.910	0.270	0.540	0.630	0.580
In	0.1	FUS-MS	*< 0.100*	*< 0.100*	*< 0.100*	*< 0.100*	0.100	*< 0.100*

Table A1.2: *Continued*.

			SS18-005A	SS18-007	SS18-018B	SS18-029	SS18-032	SS18-053B
	Detection Limit	Analysis method	APL 1	APL 1	APL 1	APL 1	APL 1	APL 1
La (ppm)	0.05	FUS-MS	16.1	9.11	39.9	7.84	3.11	103
Lu	0.002	FUS-MS	0.508	0.227	0.156	0.261	0.361	0.216
Mo	2	FUS-MS	*< 2.00*	2.00	4.00	2.00	2.00	*< 2.00*
Nb	0.2	FUS-MS	7.50	16.6	4.50	4.60	9.60	5.90
Nd	0.05	FUS-MS	26.5	12.6	23.4	9.56	3.49	68.3
Ni	20	FUS-MS	*< 20.0*	*< 20.0*	*< 20.0*	*< 20.0*	*< 20.0*	30.0
Pb	5	FUS-MS	16.0	7.00	18.0	14.0	84.0	7.00
Pr	0.01	FUS-MS	6.39	3.35	7.72	2.37	0.870	20.4
Rb	1	FUS-MS	2.00	4.00	31.0	8.00	6.00	84.0
Sb	0.2	FUS-MS	0.200	*< 0.200*	1.30	0.600	0.200	1.00
Sc	1	FUS-ICP	3.00	5.00	3.00	2.00	2.00	8.00
Sm	0.01	FUS-MS	8.95	4.17	3.14	2.61	1.43	9.52
Sn	1	FUS-MS	*< 1.00*	1.00	*< 1.00*	*< 1.00*	*< 1.00*	2.00
Sr	2	FUS-ICP	59.0	32.0	164	53.0	52.0	639
Ta	0.01	FUS-MS	3.43	3.07	0.660	1.44	1.48	0.600
Tb	0.01	FUS-MS	1.52	0.940	0.260	0.480	0.420	0.750
Th	0.05	FUS-MS	13.2	13.7	34.0	17.1	28.1	30.8
Tl	0.05	FUS-MS	*< 0.0500*	*< 0.0500*	*< 0.0500*	*< 0.0500*	*< 0.0500*	0.440
Tm	0.005	FUS-MS	0.508	0.290	0.144	0.221	0.303	0.247
U	0.01	FUS-MS	11.2	6.72	6.88	10.1	11.7	4.63
V	5	FUS-ICP	6.00	6.00	20.0	9.00	*< 5.00*	63.0
W	0.5	FUS-MS	1.10	0.500	89.7	0.800	*< 0.500*	1.00
Y	0.5	FUS-MS	40.1	29.1	8.70	15.5	19.5	16.9
Yb	0.01	FUS-MS	3.38	1.71	1.07	1.61	2.18	1.45
Zn	30	FUS-MS	*< 30.0*	60.0	*< 30.0*	160	*< 30.0*	50.0
Zr	1	FUS-ICP	42.0	34.0	88.0	41.0	94.0	225
Eu/Eu*			0.283	0.100	0.835	0.367	0.099	0.849
Ce/Ce*			1.37	1.66	1.01	1.20	1.86	0.932
T_{ZrSat} (°C)			871	914	1062	948	983	963

Table A1.2: *Continued*.

			SS18-055	SS18-062A	SS18-067	SS18-071	UNB-1	UNB-2
	Detection Limit	Analysis method	APL 1	APL 1	APL 1	APL 1	APL 1	APL 1
SiO_2 (wt. %)	0.01	FUS-ICP	70.7	74.7	77.3	75.0	77.0	78.3
Al_2O_3	0.01	FUS-ICP	14.6	12.9	11.9	13.9	13.3	12.4
FeO_T	0.01	FUS-ICP	3.47	1.92	1.27	1.55	1.47	1.72
MnO	0.001	FUS-ICP	0.0460	0.0300	0.0180	0.0220	0.0240	0.0180
MgO	0.01	FUS-ICP	1.24	0.400	0.360	0.500	0.230	0.200
CaO	0.01	FUS-ICP	2.42	1.47	1.48	1.77	0.540	0.820
Na_2O	0.01	FUS-ICP	4.64	3.45	3.90	5.34	4.11	5.46
K_2O	0.01	FUS-ICP	2.06	2.26	2.12	0.570	3.07	1.46
TiO_2	0.001	FUS-ICP	0.350	0.180	0.0560	0.0990	0.164	0.0510
P_2O_5	0.01	FUS-ICP	0.140	0.0400	*< 0.0100*	0.0100	0.0400	0.0200
LOI		GRAV	1.04	1.87	0.330	0.740	0.600	0.500
Total	0.01	FUS-ICP	101	99.2	98.7	99.5	101	101
Ag (ppm)	0.5	FUS-MS	0.600	0.500	*< 0.500*	*< 0.500*	*< 0.500*	*< 0.500*
As	5	FUS-MS	12.0	23.0	5.00	*< 5.00*	133	*< 5.00*
Ba	2	FUS-ICP	1454	900	2151	227	913	68.0
Be	1	FUS-ICP	3.00	2.00	1.00	7.00	2.00	3.00
Bi	0.1	FUS-MS	2.10	1.70	*< 0.100*	0.300	*< 0.100*	*< 0.100*
Ce	0.05	FUS-MS	139	32.2	28.2	26.1	89.3	15.6
Co	1	FUS-MS	7.00	3.00	2.00	2.00	*< 1.00*	3.00
Cr	20	FUS-MS	30.0	20.0	50.0	20.0	*< 20.0*	*< 20.0*
Cs	0.1	FUS-MS	1.60	3.50	0.900	3.80	1.30	0.300
Cu	10	FUS-MS	30.0	40.0	*< 10.0*	*< 10.0*	*< 10.0*	20.0
Dy	0.01	FUS-MS	1.57	1.83	0.380	1.68	1.71	2.12
Er	0.01	FUS-MS	0.970	1.05	0.270	0.920	0.990	1.34
Eu	0.005	FUS-MS	1.34	0.618	0.317	0.443	0.710	0.193
Ga	1	FUS-MS	16.0	14.0	10.0	11.0	15.0	15.0
Gd	0.01	FUS-MS	2.55	2.06	0.640	1.98	2.27	1.98
Ge	0.5	FUS-MS	0.900	1.30	0.800	1.90	0.900	1.10
Hf	0.1	FUS-MS	4.10	3.10	2.00	3.30	3.50	2.50
Ho	0.01	FUS-MS	0.310	0.360	0.0800	0.320	0.320	0.440
In	0.1	FUS-MS	*< 0.100*	*< 0.100*	*< 0.100*	*< 0.100*	*< 0.100*	*< 0.100*

Table A1.2: *Continued*.

			SS18-055	SS18-062A	SS18-067	SS18-071	UNB-1	UNB-2
	Detection Limit	Analysis method	APL 1	APL 1	APL 1	APL 1	APL 1	APL 1
La (ppm)	0.05	FUS-MS	80.2	17.4	16.7	12.9	49.7	7.16
Lu	0.002	FUS-MS	0.120	0.144	0.0680	0.178	0.146	0.228
Mo	2	FUS-MS	2.00	*< 2.00*	2.00	2.00	2.00	3.00
Nb	0.2	FUS-MS	5.60	3.60	0.600	4.30	5.60	8.90
Nd	0.05	FUS-MS	41.0	11.8	8.90	10.3	26.8	7.61
Ni	20	FUS-MS	30.0	*< 20.0*	*< 20.0*	*< 20.0*	*< 20.0*	*< 20.0*
Pb	5	FUS-MS	13.0	*< 5.00*	29.0	24.0	33.0	19.0
Pr	0.01	FUS-MS	13.3	3.44	2.72	2.86	8.49	1.96
Rb	1	FUS-MS	47.0	91.0	28.0	26.0	63.0	10.0
Sb	0.2	FUS-MS	1.90	0.700	0.400	0.300	3.50	0.800
Sc	1	FUS-ICP	4.00	3.00	1.00	3.00	2.00	3.00
Sm	0.01	FUS-MS	5.32	2.14	1.07	2.17	3.74	2.15
Sn	1	FUS-MS	*< 1.00*	21.0	*< 1.00*	2.00	4.00	*< 1.00*
Sr	2	FUS-ICP	494	67.0	356	322	101	53.0
Ta	0.01	FUS-MS	0.630	0.510	0.220	0.850	0.60	1.77
Tb	0.01	FUS-MS	0.300	0.320	0.07	0.320	0.310	0.350
Th	0.05	FUS-MS	30.7	24.5	73.7	47.8	21.8	19.1
Tl	0.05	FUS-MS	0.310	0.480	0.0600	0.110	0.460	0.150
Tm	0.005	FUS-MS	0.133	0.149	0.045	0.142	0.144	0.210
U	0.01	FUS-MS	4.75	4.70	8.61	7.72	3.51	8.93
V	5	FUS-ICP	40.0	22.0	12.0	24.0	6.00	9.00
W	0.5	FUS-MS	0.600	3.00	0.500	2.50	1.00	0.6
Y	0.5	FUS-MS	8.40	12.2	2.50	10.4	10.2	14.1
Yb	0.01	FUS-MS	0.780	0.970	0.370	1.05	0.950	1.49
Zn	30	FUS-MS	40.0	*< 30.0*	*< 30.0*	*< 30.0*	40.0	*< 30.0*
Zr	1	FUS-ICP	191	107	53.0	85.0	108	46.0
Eu/Eu*			1.11	0.900	1.17	0.653	0.745	0.286
Ce/Ce*			1.02	1.15	0.887	1.24	1.08	1.35
T_{ZrSat} (°C)			1078	1038	1126	1154	948	1073

Table A1.2: *Continued*.

			SS18-073	SS18-075	SS18-087	SS18-091A	SS18-093	SS18-094
	Detection Limit	Analysis method	APL 2	APL 2	APL 2	APL 2	APL 2	APL 2
SiO_2 (wt. %)	0.01	FUS-ICP	78.6	66.5	78.7	75.6	79.5	75.4
Al_2O_3	0.01	FUS-ICP	12.2	19.4	13.2	13.8	11.6	13.5
FeO_T	0.01	FUS-ICP	1.16	1.25	0.820	1.19	1.09	0.97
MnO	0.001	FUS-ICP	0.0780	0.0220	0.0170	0.0160	0.0160	0.0160
MgO	0.01	FUS-ICP	0.290	0.260	0.110	0.130	0.0900	0.0800
CaO	0.01	FUS-ICP	0.870	1.82	0.680	0.190	0.250	0.340
Na_2O	0.01	FUS-ICP	5.34	9.39	6.19	4.81	3.83	4.36
K_2O	0.01	FUS-ICP	1.19	0.750	0.540	4.11	4.37	4.55
TiO_2	0.001	FUS-ICP	0.0400	0.0410	0.0870	0.0670	0.0400	0.0500
P_2O_5	0.01	FUS-ICP	*< 0.0100*	*< 0.0100*	*< 0.0100*	*< 0.0100*	*< 0.0100*	0.0200
LOI		GRAV	0.590	0.930	0.470	0.310	0.100	0.330
Total	0.01	FUS-ICP	100	100	101	100	101	99.5
Ag (ppm)	0.5	FUS-MS	*< 0.500*	*< 0.500*	*< 0.500*	*< 0.500*	*< 0.500*	*< 0.500*
As	5	FUS-MS	*< 5.00*	*< 5.00*	*< 5.00*	*< 5.00*	*< 5.00*	*< 5.00*
Ba	2	FUS-ICP	74.0	68.0	63.0	70.0	39.0	23.0
Be	1	FUS-ICP	9.00	43.0	8.00	5.00	5.00	6.00
Bi	0.1	FUS-MS	*< 0.100*	*< 0.100*	*< 0.100*	*< 0.100*	*< 0.100*	*< 0.100*
Ce	0.05	FUS-MS	29.5	32.7	52.0	24.0	3.97	9.40
Co	1	FUS-MS	1.00	2.00	*< 1.00*	1.00	*< 1.00*	*< 1.00*
Cr	20	FUS-MS	30.0	20.0	30.0	30.0	20.0	*< 20.0*
Cs	0.1	FUS-MS	0.700	0.300	0.100	0.900	0.500	1.10
Cu	10	FUS-MS	*< 10.0*	30.0	*< 10.0*	*< 10.0*	*< 10.0*	*< 10.0*
Dy	0.01	FUS-MS	2.58	2.57	0.950	1.10	0.780	0.490
Er	0.01	FUS-MS	2.52	2.27	0.590	1.01	0.730	0.550
Eu	0.005	FUS-MS	0.126	0.249	0.202	0.0990	0.0550	0.0680
Ga	1	FUS-MS	26.0	49.0	14.0	24.0	19.0	22.0
Gd	0.01	FUS-MS	2.14	2.19	1.21	0.860	0.470	0.410
Ge	0.5	FUS-MS	2.20	2.50	0.700	1.40	1.40	1.40
Hf	0.1	FUS-MS	5.80	11.9	3.40	4.60	2.60	2.70
Ho	0.01	FUS-MS	0.650	0.580	0.200	0.260	0.190	0.120
In	0.1	FUS-MS	*< 0.100*	*< 0.100*	*< 0.100*	*< 0.100*	*< 0.100*	*< 0.100*

Table A1.2: *Continued*.

			SS18-073	SS18-075	SS18-087	SS18-091A	SS18-093	SS18-094
	Detection Limit	Analysis method	APL 2	APL 2	APL 2	APL 2	APL 2	APL 2
La (ppm)	0.05	FUS-MS	11.4	13.7	26.8	10.0	1.02	2.29
Lu	0.002	FUS-MS	0.940	0.853	0.149	0.308	0.225	0.195
Mo	2	FUS-MS	2.00	43.0	2.00	2.00	*< 2.00*	*< 2.00*
Nb	0.2	FUS-MS	74.6	76.6	12.6	27.2	22.0	20.3
Nd	0.05	FUS-MS	11.4	10.4	12.9	6.48	1.35	1.95
Ni	20	FUS-MS	*< 20.0*	30.0	*< 20.0*	*< 20.0*	*< 20.0*	*< 20.0*
Pb	5	FUS-MS	60.0	22.0	25.0	61.0	18.0	26.0
Pr	0.01	FUS-MS	3.61	3.44	4.86	2.25	0.360	0.670
Rb	1	FUS-MS	45.0	14.0	20.0	133	159	236
Sb	0.2	FUS-MS	0.200	0.300	0.700	0.400	*< 0.200*	*< 0.200*
Sc	1	FUS-ICP	7.00	5.00	*< 1.00*	2.00	1.00	1.00
Sm	0.01	FUS-MS	2.55	2.39	1.80	1.23	0.410	0.530
Sn	1	FUS-MS	2.00	1.00	1.00	2.00	*< 1.00*	1.00
Sr	2	FUS-ICP	62.0	106	56.0	17.0	10.0	8.00
Ta	0.01	FUS-MS	10.8	16.1	1.99	2.67	2.16	2.42
Tb	0.01	FUS-MS	0.390	0.410	0.180	0.160	0.100	0.0800
Th	0.05	FUS-MS	19.3	14.9	42.7	26.6	10.5	15.5
Tl	0.05	FUS-MS	0.130	*< 0.0500*	0.140	0.580	0.740	1.74
Tm	0.005	FUS-MS	0.537	0.469	0.107	0.186	0.139	0.112
U	0.01	FUS-MS	24.2	24.2	8.57	14.5	5.83	5.86
V	5	FUS-ICP	5.00	11.0	*< 5.00*	*< 5.00*	*< 5.00*	*< 5.00*
W	0.5	FUS-MS	3.70	2.50	*< 0.500*	1.00	*< 0.500*	1.30
Y	0.5	FUS-MS	30.1	30.7	6.70	10.6	6.10	5.60
Yb	0.01	FUS-MS	5.05	4.33	0.830	1.57	1.21	0.970
Zn	30	FUS-MS	*< 30.0*	*< 30.0*	*< 30.0*	*< 30.0*	*< 30.0*	*< 30.0*
Zr	1	FUS-ICP	61.0	99.0	77.0	75.0	36.0	49.0
Eu/Eu*			0.165	0.333	0.418	0.294	0.383	0.446
Ce/Ce*			1.35	1.68	1.31	1.64	2.08	3.05
T_{ZrSat} (°C)			1123	1129	948	1036	1024	1022

Table A1.2: *Continued*.

			SS18-104	SS18-105	SS18-053A	SS18-066	SS18-069	SS18-070
	Detection Limit	Analysis method	APL 2	APL 2	TON	TON	TON	TON
SiO_2 (wt. %)	0.01	FUS-ICP	75.9	72.6	59.6	55.4	58.0	56.3
Al_2O_3	0.01	FUS-ICP	12.8	15.9	14.8	13.5	11.7	11.7
FeO_T	0.01	FUS-ICP	1.24	1.64	7.12	8.56	9.95	8.92
MnO	0.001	FUS-ICP	0.0230	0.0270	0.111	0.140	0.145	0.152
MgO	0.01	FUS-ICP	0.130	0.370	4.55	7.73	7.51	8.26
CaO	0.01	FUS-ICP	0.440	1.90	5.17	8.38	6.91	7.75
Na_2O	0.01	FUS-ICP	3.20	5.72	2.89	1.80	1.78	2.14
K_2O	0.01	FUS-ICP	5.45	1.27	2.25	1.48	1.81	1.29
TiO_2	0.001	FUS-ICP	0.0910	0.112	0.581	0.528	0.668	0.539
P_2O_5	0.01	FUS-ICP	0.0200	0.0400	0.300	0.170	0.200	0.170
LOI		GRAV	0.120	0.800	2.16	1.96	2.07	1.67
Total	0.01	FUS-ICP	99.4	100	99.5	99.6	101	98.8
Ag (ppm)	0.5	FUS-MS	*< 0.500*	*< 0.500*	0.500	*< 0.500*	*< 0.500*	*< 0.500*
As	5	FUS-MS	*< 5.00*	*< 5.00*	11.0	11.0	11.0	21.0
Ba	2	FUS-ICP	52.0	295	666	511	485	430
Be	1	FUS-ICP	7.00	1.00	2.00	1.00	2.00	1.00
Bi	0.1	FUS-MS	*< 0.100*	*< 0.100*	0.700	0.200	0.400	0.200
Ce	0.05	FUS-MS	49.6	5.94	135	75.4	75.3	87.3
Co	1	FUS-MS	1.00	2.00	17.0	34.0	42.0	38.0
Cr	20	FUS-MS	*< 20.0*	20.0	190	460	560	640
Cs	0.1	FUS-MS	1.20	0.400	8.50	3.50	13.2	4.30
Cu	10	FUS-MS	*< 10.0*	30.0	20.0	50.0	70.0	50.0
Dy	0.01	FUS-MS	0.940	0.350	3.53	2.73	3.19	3.00
Er	0.01	FUS-MS	0.740	0.200	1.79	1.32	1.52	1.56
Eu	0.005	FUS-MS	0.154	0.214	1.99	1.40	1.39	1.53
Ga	1	FUS-MS	20.0	19.0	18.0	16.0	16.0	15.0
Gd	0.01	FUS-MS	1.11	0.530	5.28	3.98	4.51	4.51
Ge	0.5	FUS-MS	1.20	0.600	1.70	1.40	1.60	1.30
Hf	0.1	FUS-MS	2.70	2.00	3.70	3.00	2.90	2.80
Ho	0.01	FUS-MS	0.220	0.0700	0.630	0.480	0.580	0.540
In	0.1	FUS-MS	*< 0.100*	*< 0.100*	*< 0.100*	*< 0.100*	*< 0.100*	*< 0.100*

Table A1.2: *Continued*.

			SS18-104	SS18-105	SS18-053A	SS18-066	SS18-069	SS18-070
	Detection Limit	Analysis method	APL 2	APL 2	TON	TON	TON	TON
La (ppm)	0.05	FUS-MS	23.4	2.91	69.6	37.7	31.9	43.0
Lu	0.002	FUS-MS	0.198	0.0270	0.225	0.190	0.215	0.204
Mo	2	FUS-MS	16.0	2.00	2.00	*< 2.00*	*< 2.00*	*< 2.00*
Nb	0.2	FUS-MS	20.8	0.600	5.40	3.80	5.50	4.00
Nd	0.05	FUS-MS	11.1	2.74	51.9	32.2	34.3	34.5
Ni	20	FUS-MS	*< 20.0*	*< 20.0*	60.0	180	120	190
Pb	5	FUS-MS	54.0	8.00	9.00	10.0	14.0	11.0
Pr	0.01	FUS-MS	4.19	0.700	15.1	8.80	9.33	9.91
Rb	1	FUS-MS	240	26.0	95.0	59.0	97.0	53.0
Sb	0.2	FUS-MS	*< 0.200*	*< 0.200*	1.20	1.00	0.900	1.10
Sc	1	FUS-ICP	2.00	1.00	14.0	25.0	26.0	25.0
Sm	0.01	FUS-MS	1.61	0.580	8.17	5.20	5.85	5.92
Sn	1	FUS-MS	1.00	*< 1.00*	1.00	1.00	1.00	1.00
Sr	2	FUS-ICP	20.0	403	473	409	325	343
Ta	0.01	FUS-MS	2.24	0.0600	0.300	0.280	0.460	0.350
Tb	0.01	FUS-MS	0.160	0.0700	0.730	0.520	0.620	0.590
Th	0.05	FUS-MS	29.0	1.45	16.5	8.63	7.55	10.2
Tl	0.05	FUS-MS	1.49	0.390	0.580	0.320	0.640	0.370
Tm	0.005	FUS-MS	0.142	0.0300	0.250	0.193	0.224	0.206
U	0.01	FUS-MS	9.62	0.940	2.16	1.42	2.12	1.37
V	5	FUS-ICP	5.00	10.0	99.0	118	193	117
W	0.5	FUS-MS	*< 0.500*	*< 0.500*	1.10	*< 0.500*	1.40	0.700
Y	0.5	FUS-MS	8.50	2.30	17.6	13.8	15.1	14.6
Yb	0.01	FUS-MS	1.11	0.190	1.55	1.24	1.50	1.30
Zn	30	FUS-MS	*< 30.0*	*< 30.0*	90.0	90.0	100	90.0
Zr	1	FUS-ICP	52.0	68.0	157	120	106	107
Eu/Eu*			0.352	1.18	0.926	0.941	0.827	0.905
Ce/Ce*			1.51	1.07	0.954	0.881	0.872	1.01
T_{ZrSat} (°C)			990	1040	954	1083	1095	1112

Table A1.2: *Continued*.

			SS18-129	SS18-020	SS18-021	SS18-054	SS18-057	SS18-058
	Detection Limit	Analysis method	TON	GND	GND	GND	GND	GND
SiO_2 (wt. %)	0.01	FUS-ICP	63.8	67.9	69.0	63.5	67.0	69.1
Al_2O_3	0.01	FUS-ICP	14.8	14.3	14.6	15.9	14.8	15.2
FeO_T	0.01	FUS-ICP	5.25	3.52	3.56	6.05	4.48	3.88
MnO	0.001	FUS-ICP	0.0980	0.0520	0.0480	0.0580	0.0520	0.0340
MgO	0.01	FUS-ICP	1.98	1.07	1.09	2.33	1.88	1.10
CaO	0.01	FUS-ICP	3.91	2.32	1.90	4.28	3.10	2.09
Na_2O	0.01	FUS-ICP	3.98	3.77	3.77	3.38	3.53	3.52
K_2O	0.01	FUS-ICP	1.61	2.96	3.01	2.56	2.84	2.90
TiO_2	0.001	FUS-ICP	0.503	0.340	0.347	0.573	0.409	0.365
P_2O_5	0.01	FUS-ICP	0.190	0.130	0.130	0.260	0.150	0.140
LOI		GRAV	4.22	2.09	1.96	1.25	1.12	1.48
Total	0.01	FUS-ICP	100	98.5	99.4	100	99.4	99.8
Ag (ppm)	0.5	FUS-MS	0.500	0.600	0.600	0.900	0.500	0.700
As	5	FUS-MS	11.0	16.0	17.0	8.00	9.00	8.00
Ba	2	FUS-ICP	680	1041	1062	924	1105	1604
Be	1	FUS-ICP	2.00	2.00	2.00	2.00	2.00	2.00
Bi	0.1	FUS-MS	*< 0.100*	0.100	0.200	0.500	0.100	*< 0.100*
Ce	0.05	FUS-MS	104	137	143	64.1	115	131
Co	1	FUS-MS	12.0	5.00	6.00	10.0	9.00	18.0
Cr	20	FUS-MS	40.0	30.0	30.0	50.0	40.0	40.0
Cs	0.1	FUS-MS	2.80	4.80	5.70	7.80	3.80	2.40
Cu	10	FUS-MS	40.0	40.0	30.0	50.0	20.0	100
Dy	0.01	FUS-MS	2.52	2.42	2.58	2.45	2.34	2.27
Er	0.01	FUS-MS	1.26	1.18	1.33	1.26	1.14	1.19
Eu	0.005	FUS-MS	1.41	1.41	1.48	1.39	1.47	1.35
Ga	1	FUS-MS	17.0	18.0	18.0	20.0	18.0	18.0
Gd	0.01	FUS-MS	3.97	3.79	4.14	3.60	3.69	3.91
Ge	0.5	FUS-MS	1.00	1.20	1.20	1.20	1.10	0.800
Hf	0.1	FUS-MS	3.90	3.70	4.30	6.10	3.70	4.30
Ho	0.01	FUS-MS	0.440	0.390	0.440	0.450	0.400	0.420
In	0.1	FUS-MS	*< 0.100*	*< 0.100*	*< 0.100*	*< 0.100*	*< 0.100*	*< 0.100*

Table A1.2: *Continued*.

			SS18-129	SS18-020	SS18-021	SS18-054	SS18-057	SS18-058
	Detection Limit	Analysis method	TON	GND	GND	GND	GND	GND
La (ppm)	0.05	FUS-MS	53.8	73.4	77.3	28.1	62.5	70.5
Lu	0.002	FUS-MS	0.178	0.167	0.190	0.198	0.161	0.155
Mo	2	FUS-MS	2.00	2.00	*< 2.00*	2.00	25.0	2.00
Nb	0.2	FUS-MS	5.70	4.90	5.90	6.20	5.00	5.40
Nd	0.05	FUS-MS	38.9	46.0	48.6	26.5	39.3	44.0
Ni	20	FUS-MS	20.0	*< 20.0*	*< 20.0*	30.0	20.0	20.0
Pb	5	FUS-MS	11.0	15.0	14.0	17.0	11.0	10.0
Pr	0.01	FUS-MS	11.0	14.0	15.1	7.26	12.2	13.5
Rb	1	FUS-MS	54.0	97.0	107	99.0	68.0	77.0
Sb	0.2	FUS-MS	1.10	1.40	1.40	0.500	1.10	0.600
Sc	1	FUS-ICP	9.00	5.00	5.00	11.0	7.00	5.00
Sm	0.01	FUS-MS	5.74	6.23	6.72	4.95	5.81	5.99
Sn	1	FUS-MS	1.00	1.00	1.00	1.00	1.00	1.00
Sr	2	FUS-ICP	296	452	363	656	448	377
Ta	0.01	FUS-MS	0.460	0.590	0.700	0.430	0.570	0.610
Tb	0.01	FUS-MS	0.490	0.470	0.520	0.490	0.470	0.460
Th	0.05	FUS-MS	15.6	25.9	28.7	19.3	19.3	26.5
Tl	0.05	FUS-MS	0.580	0.470	0.620	0.590	0.190	0.230
Tm	0.005	FUS-MS	0.175	0.174	0.193	0.183	0.154	0.169
U	0.01	FUS-MS	3.17	4.00	4.86	2.77	3.47	3.53
V	5	FUS-ICP	82.0	37.0	39.0	87.0	64.0	56.0
W	0.5	FUS-MS	1.80	2.50	2.50	0.600	0.500	2.90
Y	0.5	FUS-MS	13.0	11.9	13.0	12.3	11.4	11.8
Yb	0.01	FUS-MS	1.11	1.15	1.14	1.26	0.99	1.01
Zn	30	FUS-MS	60.0	50.0	70.0	50.0	40.0	< 30
Zr	1	FUS-ICP	150	155	165	254	141	174
Eu/Eu*			0.903	0.887	0.858	1.01	0.971	0.853
Ce/Ce*			0.919	0.939	0.948	1.05	1.01	0.944
T_{ZrSat} (°C)			966	965	1025	995	1133	1096

Table A1.2: *Continued*.

			SS18-061	SS18-063	SS18-065	SS18-072	JS18-374
	Detection Limit	Analysis method	GND	GND	GND	GND	GRN 1
SiO_2 (wt. %)	0.01	FUS-ICP	69.5	61.8	59.6	54.2	76.6
Al_2O_3	0.01	FUS-ICP	14.0	15.8	15.3	16.2	13.0
FeO_T	0.01	FUS-ICP	3.63	6.86	7.80	9.14	2.22
MnO	0.001	FUS-ICP	0.0520	0.0850	0.0700	0.118	0.0230
MgO	0.01	FUS-ICP	1.21	2.79	2.28	5.26	0.360
CaO	0.01	FUS-ICP	1.62	4.97	3.97	7.75	0.280
Na_2O	0.01	FUS-ICP	3.05	3.46	3.42	2.19	3.45
K_2O	0.01	FUS-ICP	3.26	1.88	1.80	1.97	4.17
TiO_2	0.001	FUS-ICP	0.345	0.667	0.840	0.690	0.013
P_2O_5	0.01	FUS-ICP	0.130	0.190	0.410	0.230	0.0500
LOI		GRAV	1.65	1.61	2.90	2.62	0.590
Total	0.01	FUS-ICP	98.4	100	98.3	100	101
Ag (ppm)	0.5	FUS-MS	0.600	0.800	0.500	*< 0.500*	*< 0.500*
As	5	FUS-MS	28.0	10.0	7.00	9.00	*< 5.00*
Ba	2	FUS-ICP	1153	497	605	626	1218
Be	1	FUS-ICP	2.00	2.00	2.00	2.00	1.00
Bi	0.1	FUS-MS	0.100	0.600	1.70	1.00	*< 0.100*
Ce	0.05	FUS-MS	135	107	87.2	73.4	75.2
Co	1	FUS-MS	6.00	20.0	17.0	33.0	1.00
Cr	20	FUS-MS	30.0	50.0	*< 20.0*	70.0	20.0
Cs	0.1	FUS-MS	4.00	6.10	2.80	24.3	1.40
Cu	10	FUS-MS	20.0	30.0	70.0	50.0	10.0
Dy	0.01	FUS-MS	2.23	2.64	4.30	2.40	5.83
Er	0.01	FUS-MS	1.08	1.38	1.96	1.20	2.31
Eu	0.005	FUS-MS	1.44	1.62	2.05	1.37	0.890
Ga	1	FUS-MS	18.0	21.0	20.0	18.0	18.0
Gd	0.01	FUS-MS	3.76	4.27	6.05	3.58	9.11
Ge	0.5	FUS-MS	1.20	1.40	1.50	1.80	1.10
Hf	0.1	FUS-MS	4.30	5.70	1.90	2.50	2.50
Ho	0.01	FUS-MS	0.390	0.470	0.750	0.410	0.930
In	0.1	FUS-MS	*< 0.100*	*< 0.100*	*< 0.100*	*< 0.100*	*< 0.100*

Table A1.2: *Continued*.

			SS18-061	SS18-063	SS18-065	SS18-072	JS18-374
	Detection Limit	Analysis method	GND	GND	GND	GND	GRN 1
La (ppm)	0.05	FUS-MS	72.6	56.7	42.0	36.3	36.7
Lu	0.002	FUS-MS	0.165	0.190	0.230	0.171	0.250
Mo	2	FUS-MS	2.00	*< 2.00*	2.00	3.00	2.00
Nb	0.2	FUS-MS	6.00	6.60	5.80	3.60	0.700
Nd	0.05	FUS-MS	43.5	42.0	43.2	31.9	39.4
Ni	20	FUS-MS	*< 20.0*	50.0	30.0	70.0	*< 20.0*
Pb	5	FUS-MS	9.00	15.0	6.00	8.00	16.0
Pr	0.01	FUS-MS	13.9	11.9	10.8	8.54	9.30
Rb	1	FUS-MS	117	79.0	78.0	123	75.0
Sb	0.2	FUS-MS	0.900	1.00	1.50	0.800	0.700
Sc	1	FUS-ICP	5.00	13.0	13.0	20.0	9.00
Sm	0.01	FUS-MS	5.83	6.37	7.89	5.01	10.6
Sn	1	FUS-MS	1.00	1.00	1.00	1.00	1.00
Sr	2	FUS-ICP	324	416	397	570	84.0
Ta	0.01	FUS-MS	0.670	0.590	0.350	0.270	0.120
Tb	0.01	FUS-MS	0.460	0.550	0.840	0.480	1.22
Th	0.05	FUS-MS	24.1	13.0	7.17	8.04	14.9
Tl	0.05	FUS-MS	0.540	0.460	0.300	0.740	0.320
Tm	0.005	FUS-MS	0.159	0.190	0.260	0.165	0.296
U	0.01	FUS-MS	4.93	2.86	1.45	1.53	1.09
V	5	FUS-ICP	40.0	110	112	187	7.00
W	0.5	FUS-MS	5.00	0.900	3.30	1.20	4.20
Y	0.5	FUS-MS	11.5	13.6	20.0	12.6	27.1
Yb	0.01	FUS-MS	1.06	1.17	1.54	1.03	1.80
Zn	30	FUS-MS	50.0	70.0	60.0	90.0	*< 30.0*
Zr	1	FUS-ICP	168	231	63.0	108	46.0
Eu/Eu*			0.940	0.950	0.907	0.989	0.277
Ce/Ce*			0.969	0.900	0.859	0.842	1.20
T_{ZrSat} (°C)			1071	1085	1102	1076	935

Table A1.2: *Continued*.

			JS18-377	SS18-084	SS18-085	SS18-118	SS18-109
	Detection Limit	Analysis method	GRN 1	GRN 2	GRN 2	IVC	IDK
SiO_2 (wt. %)	0.01	FUS-ICP	76.5	76.5	75.7	63.1	74.1
Al_2O_3	0.01	FUS-ICP	13.0	12.6	12.7	14.7	15.7
FeO_T	0.01	FUS-ICP	2.18	1.65	1.48	5.91	1.35
MnO	0.001	FUS-ICP	0.0230	0.0420	0.0250	0.0970	0.0210
MgO	0.01	FUS-ICP	0.210	0.190	0.330	1.88	0.310
CaO	0.01	FUS-ICP	0.420	0.550	0.340	3.36	2.20
Na_2O	0.01	FUS-ICP	3.78	3.69	4.01	0.360	5.11
K_2O	0.01	FUS-ICP	4.10	4.36	4.18	3.23	1.23
TiO_2	0.001	FUS-ICP	0.0310	0.114	0.125	0.805	0.126
P_2O_5	0.01	FUS-ICP	0.0200	0.0100	0.0100	0.230	0.0400
LOI		GRAV	0.320	0.270	0.460	6.32	0.650
Total	0.01	FUS-ICP	101	99.9	99.4	100	101
Ag (ppm)	0.5	FUS-MS	*< 0.500*	*< 0.500*	*< 0.500*	0.9	*< 0.500*
As	5	FUS-MS	*< 5.00*	*< 5.00*	*< 5.00*	*< 5.00*	*< 5.00*
Ba	2	FUS-ICP	1422	167	137	336	575
Be	1	FUS-ICP	*< 1.00*	7.00	5.00	1.00	1.00
Bi	0.1	FUS-MS	*< 0.100*	*< 0.100*	*< 0.100*	*< 0.100*	*< 0.100*
Ce	0.05	FUS-MS	31.5	59.8	45.2	90.6	14.3
Co	1	FUS-MS	*< 1.00*	1.00	1.00	10.0	1.00
Cr	20	FUS-MS	*< 20.0*	20.0	20.0	*< 20.0*	20.0
Cs	0.1	FUS-MS	0.700	4.10	3.00	2.10	0.800
Cu	10	FUS-MS	*< 10.0*	*< 10.0*	*< 10.0*	*< 10.0*	20.0
Dy	0.01	FUS-MS	2.39	1.80	1.22	5.74	0.560
Er	0.01	FUS-MS	1.18	1.19	0.92	3.17	0.300
Eu	0.005	FUS-MS	0.651	0.299	0.196	1.62	0.349
Ga	1	FUS-MS	18.0	20.0	20.0	20.0	19.0
Gd	0.01	FUS-MS	3.09	1.70	1.37	6.39	0.830
Ge	0.5	FUS-MS	0.800	1.30	1.20	1.10	0.600
Hf	0.1	FUS-MS	1.90	4.00	3.20	6.60	2.40
Ho	0.01	FUS-MS	0.440	0.360	0.270	1.11	0.110
In	0.1	FUS-MS	*< 0.100*	*< 0.100*	*< 0.100*	*< 0.100*	*< 0.100*

Table A1.2: *Continued*.

			JS18-377	SS18-084	SS18-085	SS18-118	SS18-109
	Detection Limit	Analysis method	GRN 1	GRN 2	GRN 2	IVC	IDK
La (ppm)	0.05	FUS-MS	15.3	31.3	23.3	45.3	7.23
Lu	0.002	FUS-MS	0.141	0.316	0.231	0.485	0.0470
Mo	2	FUS-MS	*< 2.00*	2.00	*< 2.00*	*< 2.00*	*< 2.00*
Nb	0.2	FUS-MS	5.80	20.5	15.00	12.5	1.00
Nd	0.05	FUS-MS	14.1	16.3	12.1	36.7	5.59
Ni	20	FUS-MS	*< 20.0*	*< 20.0*	*< 20.0*	*< 20.0*	*< 20.0*
Pb	5	FUS-MS	12.0	40.0	17.0	14.0	10.0
Pr	0.01	FUS-MS	3.67	5.80	4.30	9.81	1.58
Rb	1	FUS-MS	69.0	281	216	78.0	30.0
Sb	0.2	FUS-MS	0.300	*< 0.200*	*< 0.200*	3.80	*< 0.200*
Sc	1	FUS-ICP	3.00	2.00	2.00	11.0	1.00
Sm	0.01	FUS-MS	3.40	2.55	1.90	7.12	1.09
Sn	1	FUS-MS	1.00	2.00	2.00	3.00	*< 1.00*
Sr	2	FUS-ICP	62.0	49.0	34.0	34.0	392
Ta	0.01	FUS-MS	0.360	2.55	1.70	0.980	0.0800
Tb	0.01	FUS-MS	0.450	0.290	0.220	0.970	0.100
Th	0.05	FUS-MS	4.80	40.3	38.6	14.8	2.15
Tl	0.05	FUS-MS	0.33	1.74	1.54	0.510	0.370
Tm	0.005	FUS-MS	0.165	0.207	0.152	0.453	0.0490
U	0.01	FUS-MS	0.950	17.4	9.65	4.31	0.940
V	5	FUS-ICP	*< 5.00*	5.00	6.00	77.0	10.0
W	0.5	FUS-MS	*< 0.500*	*< 0.500*	0.800	2.30	0.700
Y	0.5	FUS-MS	11.9	13.2	9.80	32.0	3.50
Yb	0.01	FUS-MS	0.970	1.72	1.28	3.06	0.320
Zn	30	FUS-MS	*< 30.0*	*< 30.0*	*< 30.0*	40.0	*< 30.0*
Zr	1	FUS-ICP	44.0	93.0	85.0	268	82.0
Eu/Eu*			0.614	0.439	0.371	0.734	1.12
Ce/Ce*			1.25	1.34	1.37	1.12	1.16
T_{ZrSat} (°C)			1067	988	958	1087	1053

Note: FUS-ICP = fusion-inductively coupled plasma; FUS-MS = fusion mass-spectrometry; GRAV = gravimetric. Italicized values are below detection. $Eu/Eu^* = Eu_N/[Sm_N \times Gd_N]^{½}$. $Ce/Ce^* = Ce_N/[Nd_N^2/Sm_N]$. T_{ZrSat} = Zircon saturation temperature (Watson et al. 2006).

Appendix 2: U-Pb geochronology and zircon mineral chemistry of syn-volcanic and plutonic intrusions in the Yellowknife greenstone belt, NWT, Canada: understanding an Archean magmatic plumbing system

Appendix 2.1: CA-TIMS U-Pb geochronology methodology

U-Pb dates were obtained by the CA-TIMS method from analyses composed of single zircon grains, modified after Mattinson (2005), at Boise State University. Zircon was removed from polished mounts and placed in a muffle furnace at 900°C for 60 hours in quartz beakers. Zircon was removed from the epoxy mounts for dating based on clarity.

Zircon was put into 3 ml Teflon PFA beakers and loaded into 300 µl Teflon PFA microcapsules. Fifteen microcapsules were placed in a large-capacity Parr vessel and the zircon partially dissolved in 120 µl of 29 M HF for 12 hours at 190°C. Zircon was returned to 3 ml Teflon PFA beakers, HF was removed, and zircon was immersed in 3.5 M HNO_3, ultrasonically cleaned for an hour, and fluxed on a hotplate at 80°C for an hour. The HNO_3 was removed and zircon was rinsed twice in ultrapure H_2O before being reloaded into the 300 µl Teflon PFA microcapsules (rinsed and fluxed in 6 M HCl during sonication and washing of the zircon) and spiked with the Boise State University mixed ^{233}U-^{235}U-^{205}Pb tracer solution (BSU-1B). Zircon was dissolved in Parr vessels in 120 µl of 29 M HF with a trace of 3.5 M HNO_3 at 220°C for 48 hours, dried to fluorides, and re-dissolved in 6 M HCl at 180°C overnight. U and Pb were separated from the zircon matrix using an HCl-based anion-exchange chromatographic procedure, eluted together and dried with 2 µl of 0.05 N H_3PO_4 (Krogh 1973).

Pb and U were loaded on a single outgassed Re filament in 5 µl of a silica-gel/phosphoric acid mixture, and U and Pb isotopic measurements were made on a GV Isoprobe-T multicollector thermal ionization mass spectrometer equipped with an ion-counting Daly detector (Gerstenberger and Haase 1997). Pb isotopes were measured by

peak-jumping all isotopes on the Daly detector for 160 cycles and corrected for 0.16 ± 0.03%/a.m.u. (1σ) mass fractionation. Transitory isobaric interferences due to high-molecular weight organics, particularly on ^{204}Pb and ^{207}Pb, disappeared within approximately 60 cycles, while ionization efficiency averaged 10^4 cps/pg of each Pb isotope. Linearity (to ≥1.4 x 10^6 cps) and the associated deadtime correction of the Daly detector were determined by analysis of NBS982. Uranium was analyzed as UO_2^+ ions in static Faraday mode on 10^{12} ohm resistors for 300 cycles and corrected for isobaric interference of $^{233}U^{18}O^{16}O$ on $^{235}U^{16}O^{16}O$ with an $^{18}O/^{16}O$ of 0.00206. Ionization efficiency averaged 20 mV/ng of each U isotope. U mass fractionation was corrected using the known $^{233}U/^{235}U$ ratio of the Boise State University tracer solution.

U-Pb dates and uncertainties were calculated using the algorithms of Schmitz and Schoene (2007), calibration of BSU-1B tracer solution of $^{235}U/^{205}Pb$ of 77.93 and $^{233}U/^{235}U$ of 1.007066 for, U decay constants recommended by Jaffey et al. (1971), and $^{238}U/^{235}U$ of 137.818 (Hiess et al. 2012). $^{206}Pb/^{238}U$ ratios and dates were corrected for initial ^{230}Th disequilibrium using $D_{Th/U}$ = 0.20 ± 0.05 (1σ) and the algorithms of Crowley et al. (2007), increasing the $^{206}Pb/^{238}U$ dates of ~0.09 Ma. All common Pb in analyses was attributed to laboratory blank and subtracted based on the measured laboratory Pb isotopic composition and associated uncertainty. U blanks are estimated at 0.013 pg.

The $^{207}Pb/^{206}Pb$ dates are used in age interpretations because they are not affected by recent Pb loss, unlike the $^{206}Pb/^{238}U$ dates. The effects of recent Pb loss are considered to be minimal because most dates are concordant within the decay constant uncertainties

on Concordia; the discordance is 0.0-0.4% for 30 of the 31 analyses. The effects of ancient Pb loss are considered to be minimal because all dates are equivalent within each sample (probability of fit >0.05).

Weighted mean $^{207}Pb/^{206}Pb$ dates are calculated from equivalent dates (probability of fit >0.05) using Isoplot 3.0 (Ludwig 2003). Errors are at the 95% confidence interval. It is computed as the internal standard deviation multiplied by the Student's t-distribution multiplier for a two-tailed 95% critical interval and n-1 degrees of freedom when the reduced chi-squared statistic, mean squared weighted deviation (MSWD), takes a value less than its expectation value plus its standard deviation at the same confidence interval, which is when MSWD is <1+2*sqrt[2/(n-1)] (Wendt and Carl 1991). This error is expanded via multiplication by the sqrt(MSWD) when the MSWD is ≥1+2*sqrt[2/(n-1)] to accommodate unknown sources of over dispersion. Errors on weighted mean $^{207}Pb/^{206}Pb$ dates are given as ± x / z, where x is the internal error based on analytical uncertainties only, including counting statistics, subtraction of tracer solution, and blank and initial common Pb subtraction, and z includes the ^{238}U and ^{235}U decay constant uncertainties propagated in quadrature. Internal errors should be considered when comparing our dates with $^{206}Pb/^{238}U$ dates from other laboratories that used the same tracer solution or a tracer solution that was cross-calibrated using EARTHTIME gravimetric standards. Errors including the ^{238}U decay constant should be considered when comparing our dates with those derived from other decay schemes (e.g., $^{40}Ar/^{39}Ar$, ^{187}Re-^{187}Os) (Jaffey et al. 1971). Errors on individual dates are at 2σ.

Table A2.1: U-Pb geochronology data used to calculate Concordia ages, upper intercept ages, and interpret inheritance and crystallization ages of YGB intrusions. The colour and analytical location are given for each sample. Whenever a zircon was large enough for two ablations, a core and rim analysis were done, even if a xenocrystic core was not observed, otherwise ablations were focused on the tip or exterior (ext) of the grain.

Sample	Lith.	Zircon Colour	Area	U (ppm)	Th (ppm)	U/Th	^{204}Pb (Cps)	2σ	%Pb*	^{207}Pb/ ^{235}U	2σ	^{206}Pb/ ^{238}U	2σ	Error corr.	% Conc.	^{207}Pb/ ^{206}Pb	2σ
SS18-008-c - 39†	FQP	C	ext	1200	2296	0.52	17	17	95.8	10.42	0.180	0.420	0.009	0.85	84.4	2631	18
SS18-008-c - 40†	FQP	C	ext	391	524	0.75	23	22	100.0	13.68	0.240	0.532	0.009	0.75	103.9	2692	24
SS18-008-c - 44†	FQP	C	ext	296	301	0.98	12	15	99.0	12.61	0.150	0.495	0.008	0.62	95.4	2695	19
SS18-008-c - 74†	FQP	C	ext	595	943	0.63	65	20	100.0	13.33	0.490	0.522	0.010	0.76	104.7	2660	54
SS18-008-v - 10*†	FQP	V	ext	167	129	1.30	-3	13	99.8	13.24	0.210	0.523	0.008	0.42	100.8	2689	25
SS18-008-v - 16*†	FQP	V	ext	190	162	1.17	14	14	99.5	13.15	0.200	0.516	0.008	0.59	99.6	2694	23
SS18-008-v - 8*†	FQP	V	core	324	352	0.92	0	15	99.4	12.98	0.150	0.512	0.007	0.41	98.9	2689	22
SS18-051-c - 12*	FQP	C	ext	467	482	0.97	37	35	99.9	13.00	0.520	0.518	0.017	0.90	101.8	2663	25
SS18-051-c - 28*	FQP	C	ext	230	254	0.91	47	40	99.9	12.60	0.440	0.508	0.015	0.63	95.6	2610	30
SS18-051-c - 30*	FQP	C	core	482	540	0.89	26	27	100.0	12.95	0.430	0.517	0.013	0.67	103.5	2644	21
SS18-051-c - 30*	FQP	C	rim	434	492	0.88	18	26	99.8	12.77	0.420	0.512	0.015	0.80	98.6	2650	15
SS18-051-c - 39*	FQP	C	ext	402	454	0.89	-18	34	99.7	12.78	0.550	0.504	0.020	0.88	104.1	2626	29
SS18-051-c - 49*	FQP	C	ext	419	645	0.65	9	32	98.7	12.80	0.510	0.503	0.020	0.91	97.0	2694	19
SS18-051-c - 50*	FQP	C	core	569	868	0.66	42	35	98.8	12.85	0.600	0.509	0.021	0.91	97.6	2692	20
SS18-051-v - 15*	FQP	V	ext	411	446	0.92	21	34	100.0	12.96	0.420	0.516	0.013	0.64	101.7	2693	18

*: Data used to calculate a concordant age.

†: Data used to calculate an upper intercept age or for the interpretation of a crystallization age.

%Pb*: Percentage of radiogenic Pb.

C = colourless; V = violet; Y = yellow; TY = turbid yellow; G = grey; CG = cloudy grey; O = orange; Lith. = lithology.

Table A2.1: *Continued*.

Sample	Lith.	Zircon Colour	Area	U (ppm)	Th (ppm)	U/Th	^{204}Pb Cps	2σ	%Pb*	^{207}Pb/ ^{235}U	2σ	^{206}Pb/ ^{238}U	2σ	Error corr.	% Conc.	^{207}Pb/ ^{206}Pb	2σ
SS18-051-v - 34*	FQP	V	ext	379	305	1.24	10	32	99.9	13.09	0.450	0.515	0.014	0.39	97.0	2658	32
SS18-051-v - 4*	FQP	V	core	724	555	1.30	-9	24	99.4	12.86	0.510	0.513	0.019	0.94	98.7	2657	14
SS18-051-v - 4_1*	FQP	V	ext	330	274	1.20	-3	28	99.0	12.71	0.440	0.510	0.016	0.70	98.4	2674	28
SS18-051-v - 5*	FQP	V	ext	251	202	1.24	12	35	99.4	13.09	0.500	0.517	0.018	0.84	100.0	2686	26
SS18-051-v - 6*	FQP	V	ext	354	322	1.10	47	25	99.3	13.22	0.560	0.518	0.020	0.81	99.6	2699	33
SS18-051-v - 7*	FQP	V	ext	334	489	0.68	19	32	99.0	12.84	0.440	0.504	0.014	0.58	95.6	2710	22
SS18-051-v - 8*	FQP	V	ext	206	200	1.03	-13	25	99.7	12.71	0.460	0.511	0.016	0.77	104.4	2701	28
SS18-051-v - 9*	FQP	V	ext	406	351	1.16	16	53	99.4	12.95	0.480	0.516	0.018	0.79	101.9	2694	22
SS18-100-c - 1*	FQP	C	ext	440	231	1.91	15	18	97.5	12.32	0.390	0.472	0.008	0.81	88.8	2741	24
SS18-100-c - 2*	FQP	C	core	524	267	1.96	-7	15	96.5	11.72	0.500	0.451	0.014	0.93	84.6	2740	28
SS18-100-c - 2*	FQP	C	rim	464	276	1.68	4	15	96.9	12.29	0.430	0.465	0.010	0.83	84.7	2784	27
SS18-100-c - 3*	FQP	C	core	267	60	4.44	3	19	96.6	12.24	0.450	0.468	0.010	0.83	86.5	2760	31
SS18-100-c - 3_1*	FQP	C	ext	539	298	1.81	9	17	97.6	12.89	0.380	0.486	0.007	0.77	88.2	2790	24
SS18-125-c - 2*	FQP	C	core	319	266	1.20	6	24	99.5	12.41	0.440	0.494	0.018	0.67	98.8	2625	46
SS18-125-c - 2*	FQP	C	rim	614	786	0.78	13	31	99.9	12.58	0.420	0.508	0.019	0.89	95.6	2608	42
SS18-125-c - 32*	FQP	C	ext	162	128	1.27	14	22	99.7	12.39	0.480	0.505	0.020	0.69	101.3	2647	51
SS18-125-c - 33*	FQP	C	ext	113	85	1.33	-1	21	99.4	11.98	0.430	0.498	0.020	0.77	94.9	2652	47
SS18-125-gy - 6_1*	FQP	G	ext	262	281	0.93	-4	27	99.9	12.45	0.440	0.506	0.020	0.69	98.1	2657	45
SS18-125-y - 24*	FQP	Y	ext	359	364	0.99	2	26	99.9	12.37	0.410	0.495	0.018	0.38	99.7	2636	45
SS18-125-y - 35*	FQP	Y	ext	134	90	1.48	4	24	99.5	12.47	0.500	0.506	0.019	0.57	98.6	2654	52
SS18-125-y - 5*	FQP	Y	core	66	35	1.90	-27	29	98.8	12.07	0.610	0.505	0.029	0.73	100.5	2615	61
SS18-125-y - 5*	FQP	Y	rim	125	86	1.44	27	24	99.5	11.96	0.460	0.508	0.021	0.77	102.7	2627	51
SS18-125-y - 7*	FQP	Y	ext	380	517	0.74	-4	27	99.6	12.30	0.450	0.500	0.021	0.87	97.7	2649	44

Table A2.1: *Continued*.

Sample	Lith.	Zircon Colour	Area	U (ppm)	Th (ppm)	U/Th	^{204}Pb Cps	2σ	%Pb*	^{207}Pb/ ^{235}U	2σ	^{206}Pb/ ^{238}U	2σ	Error corr.	% Conc.	^{207}Pb/ ^{206}Pb	2σ
SS18-128-c - 11*	FQP	C	ext	115	94	1.23	3	17	99.6	13.14	0.210	0.524	0.013	0.41	102.8	2664	39
SS18-128-c - 19*	FQP	C	ext	311	223	1.39	3	15	99.4	13.06	0.250	0.515	0.014	0.71	100.6	2690	37
SS18-128-c - 3*	FQP	C	ext	554	557	0.99	13	26	99.4	12.77	0.370	0.512	0.018	0.88	103.6	2697	37
SS18-128-gr y - 4*	FQP	TY	ext	280	231	1.21	5	16	99.6	12.81	0.180	0.513	0.012	0.47	100.6	2660	38
SS18-128-gr y-1_1*	FQP	TY	ext	430	374	1.15	13	24	99.6	12.79	0.250	0.509	0.014	0.73	98.6	2651	37
SS18-128-y - 10*	FQP	Y	core	308	421	0.73	7	20	99.6	12.76	0.220	0.513	0.014	0.72	101.7	2646	36
SS18-128-y - 14*	FQP	Y	ext	282	210	1.34	9	18	99.3	13.11	0.240	0.516	0.014	0.70	98.1	2670	36
SS18-128-y - 18*	FQP	Y	ext	185	176	1.05	31	16	99.4	13.13	0.210	0.521	0.014	0.57	100.9	2681	37
SS18-128-y - 33*	FQP	Y	ext	120	79	1.52	-5	19	98.9	13.02	0.300	0.511	0.013	0.53	98.2	2698	45
SS18-128-y - 36*	FQP	Y	ext	219	179	1.22	6	24	99.6	12.75	0.220	0.512	0.013	0.72	101.6	2646	38
SS18-128-y - 42*	FQP	Y	ext	115	79	1.46	3	15	99.6	13.12	0.240	0.525	0.014	0.63	104.5	2647	39
SS18-128-y - 6*	FQP	Y	ext	185	145	1.28	16	18	99.1	12.72	0.210	0.510	0.013	0.63	99.9	2660	37
SS18-082-c - 11_1†	QZP	C	ext	1900	362	5.25	11	21	88.9	7.45	0.200	0.283	0.007	0.80	52.0	2772	19
SS18-082-c - 27*	QZP	C	ext	2350	305	7.70	12	20	99.9	16.47	0.320	0.569	0.010	0.85	99.8	2903	11
SS18-082-c - 33†	QZP	C	rim	2790	332	8.40	39	28	96.6	12.34	0.340	0.465	0.012	0.95	87.8	2753	15
SS18-082-c - 35†	QZP	C	ext	1624	240	6.77	40	21	94.9	11.35	0.350	0.428	0.013	0.91	80.3	2759	15
SS18-082-c - 40†	QZP	C	ext	1351	195	6.93	-8	16	99.3	14.46	0.410	0.539	0.014	0.94	100.5	2785	12
SS18-082-c - 6_1*	QZP	C	ext	878	686	1.28	17	17	99.4	16.77	0.340	0.575	0.011	0.87	100.1	2923	13
SS18-082-c - 9*	QZP	C	rim	1211	878	1.38	17	18	98.9	16.60	0.390	0.574	0.014	0.94	100.6	2918	8
SS18-082-cg - 1†	QZP	CG	ext	1156	63	18.47	4	28	95.3	11.91	0.280	0.448	0.011	0.90	83.3	2770	14
SS18-082-cg - 10†	QZP	CG	rim	952	363	2.62	4	18	99.5	14.10	0.300	0.532	0.011	0.87	99.6	2760	12
SS18-082-cg - 5_1†	QZP	CG	ext	3630	473	7.67	-3	18	91.3	9.48	0.280	0.355	0.009	0.90	66.6	2766	17
SS18-082-v - 11_1†	QZP	V	ext	2160	183	11.80	-8	15	96.5	12.24	0.240	0.463	0.010	0.86	86.5	2760	12

Table A2.1: *Continued*.

Sample	Lith.	Zircon Colour	Area	U (ppm)	Th (ppm)	U/Th	^{204}Pb Cps	2σ	%Pb*	^{207}Pb/ ^{235}U	2σ	^{206}Pb/ ^{238}U	2σ	Error corr.	% Conc.	^{207}Pb/ ^{206}Pb	2σ
SS18-082-v - 18†	QZP	V	core	1630	582	2.80	33	14	98.9	13.75	0.250	0.513	0.010	0.79	96.8	2763	11
SS18-082-v - 4*	QZP	V	rim	282	152	1.85	-9	14	99.9	16.49	0.300	0.571	0.010	0.49	100.1	2907	15
SS18-082-v - 4_1†	QZP	V	ext	1323	63.8	20.74	-19	36	92.8	10.14	0.300	0.385	0.011	0.88	72.3	2751	19
SS18-082-v - 7_1*	QZP	V	ext	1465	70	21.02	8	25	100.0	16.61	0.340	0.586	0.013	0.93	100.4	2909	9
SS18-082-v - 8 *	QZP	V	rim	904	190	4.75	-33	21	100.0	16.33	0.280	0.574	0.010	0.51	100.4	2900	13
SS18-082-v - 9_1*	QZP	V	ext	338	210	1.61	10	15	99.5	16.27	0.300	0.567	0.011	0.52	100.9	2901	16
UNB-1-c - 11*	APL 1(a)	C	ext	510	569	0.90	4	46	99.5	12.39	0.410	0.500	0.010	0.53	96.3	2670	49
UNB-1-c - 12*	APL 1(a)	C	ext	540	416	1.30	85	54	98.7	12.60	0.870	0.512	0.020	0.71	101.5	2664	96
UNB-1-c - 21*	APL 1(a)	C	ext	830	1067	0.78	27	37	99.6	13.00	0.510	0.508	0.014	0.81	97.0	2708	50
UNB-1-c - 24*	APL 1(a)	C	ext	419	344	1.22	36	35	99.6	13.21	0.450	0.519	0.010	0.58	99.3	2701	49
UNB-1-c - 29*	APL 1(a)	C	ext	313	231	1.35	59	36	98.9	12.67	0.690	0.515	0.017	0.66	101.6	2671	84
UNB-1-c - 3*	APL 1(a)	C	ext	642	587	1.09	174	53	99.2	12.63	0.430	0.506	0.011	0.48	97.9	2672	76
UNB-1-c - 34*	APL 1(a)	C	ext	390	234	1.67	16	26	100.0	13.31	0.450	0.527	0.010	0.59	102.2	2681	48
UNB-1-c - 38*	APL 1(a)	C	ext	435	336	1.29	-15	28	99.9	12.94	0.460	0.520	0.011	0.77	102.1	2656	49
UNB-1-g - 1*	APL 1(a)	G	ext	273	224	1.22	-9	26	99.7	12.80	0.470	0.511	0.011	0.65	99.6	2669	51
UNB-1-g - 16*	APL 1(a)	G	ext	474	359	1.32	20	23	99.9	13.37	0.430	0.522	0.010	0.27	99.6	2702	51
UNB-1-g - 20*	APL 1(a)	G	ext	430	306	1.41	50	36	99.3	12.79	0.880	0.514	0.013	0.65	103.5	2632	84
UNB-1-g - 3*	APL 1(a)	G	ext	289	230	1.26	6	21	99.5	12.58	0.580	0.510	0.017	0.94	101.0	2639	46
UNB-1-g - 7*	APL 1(a)	G	ext	440	402	1.09	23	31	99.8	13.16	0.460	0.520	0.012	0.60	100.4	2687	49
SS18-029-c - 11†	APL 1(b)	C	ext	519	990	0.52	47	36	91.8	7.86	0.610	0.319	0.020	0.97	61.8	2659	54

Table A2.1: *Continued*.

Sample	Lith.	Zircon Colour	Area	U (ppm)	Th (ppm)	U/Th	^{204}Pb Cps	2σ	%Pb*	^{207}Pb/ ^{235}U	2σ	^{206}Pb/ ^{238}U	2σ	Error corr.	% Conc.	^{207}Pb/ ^{206}Pb	2σ
SS18-029-c - 16†	APL 1(b)	C	ext	391	359	1.09	-14	28	90.6	6.90	0.420	0.278	0.013	0.95	55.4	2639	54
SS18-029-c - 17†	APL 1(b)	C	core	790	527	1.50	-41	32	90.1	6.42	0.400	0.265	0.015	0.92	52.8	2617	56
SS18-029-c - 17†	APL 1(b)	C	rim	607	540	1.12	5	32	93.3	9.49	0.360	0.376	0.010	0.90	74.2	2664	50
SS18-029-c - 17_1†	APL 1(b)	C	ext	476	499	0.95	5	26	93.7	9.70	0.500	0.382	0.021	0.96	74.1	2686	52
SS18-029-c - 21†	APL 1(b)	C	ext	421	349	1.21	26	43	91.7	8.28	0.350	0.332	0.010	0.85	63.7	2679	52
SS18-029-c - 22†	APL 1(b)	C	ext	203	910	0.22	32	39	95.2	9.84	0.550	0.405	0.017	0.86	78.6	2644	51
SS18-029-c - 23_1†	APL 1(b)	C	ext	457	313	1.46	16	31	93.9	9.29	0.530	0.376	0.020	0.95	74.9	2636	51
SS18-029-c - 24_1†	APL 1(b)	C	ext	1136	609	1.87	36	42	95.6	10.04	0.490	0.410	0.014	0.96	81.5	2629	50
SS18-029-c - 25†	APL 1(b)	C	core	484	290	1.67	43	25	91.6	8.42	0.410	0.330	0.013	0.94	65.0	2676	49
SS18-029-c - 25†	APL 1(b)	C	rim	815	359	2.27	29	47	91.0	7.79	0.480	0.310	0.016	0.90	60.5	2671	61
SS18-029-c - 25_1†	APL 1(b)	C	ext	530	280	1.89	-1	43	91.2	7.48	0.310	0.302	0.010	0.82	60.0	2640	54
SS18-029-c - 27†	APL 1(b)	C	ext	247	224	1.10	-40	32	97.9	11.53	0.440	0.462	0.012	0.75	91.2	2653	50
SS18-029-c - 28†	APL 1(b)	C	ext	701	351	2.00	-6	42	90.5	7.47	0.290	0.297	0.010	0.73	57.4	2680	51
SS18-029-c - 29†	APL 1(b)	C	ext	220	150	1.47	6	30	92.0	7.56	0.350	0.312	0.012	0.76	63.5	2597	59
SS18-029-c - 30†	APL 1(b)	C	ext	828	771	1.07	41	27	93.3	8.84	0.400	0.358	0.014	0.92	71.3	2635	48
SS18-029-c - 32†	APL 1(b)	C	ext	446	130	3.43	3	33	99.0	0.48	0.029	0.057	0.002	0.22	87.9	650	130
SS18-029-c - 33†	APL 1(b)	C	ext	723	315	2.30	-12	35	94.3	9.51	0.440	0.385	0.015	0.92	76.5	2637	50
SS18-029-v - 1†	APL 1(b)	V	core	283	201	1.41	31	40	94.8	10.59	0.460	0.414	0.013	0.81	80.3	2693	53

Table A2.1: *Continued*.

Sample	Lith.	Zircon Colour	Area	U (ppm)	Th (ppm)	U/Th	^{204}Pb Cps	2σ	%Pb*	^{207}Pb/ ^{235}U	2σ	^{206}Pb/ ^{238}U	2σ	Error corr.	% Conc.	^{207}Pb/ ^{206}Pb	2σ
SS18-029-v - 20†	APL 1(b)	V	ext	711	3400	0.21	7	37	86.3	3.76	0.250	0.153	0.009	0.93	58.0	2654	60
SS18-029-v - 22†	APL 1(b)	V	ext	190	153	1.24	-22	34	94.5	9.44	0.390	0.387	0.015	0.70	75.0	2649	65
SS18-029-v - 23†	APL 1(b)	V	rim	381	248	1.53	14	41	90.0	6.66	0.280	0.266	0.008	0.64	53.5	2638	56
SS18-029-v-23_1*†	APL 1(b)	V	ext	76	63	1.21	-1	29	99.5	12.86	0.500	0.512	0.014	0.64	96.6	2638	59
SS18-029-v - 24	APL 1(b)	V	ext	394	316	1.25	-16	32	97.9	11.67	0.480	0.464	0.012	0.76	92.6	2650	54
SS18-029-v - 25	APL 1(b)	V	ext	775	634	1.22	35	34	85.3	3.56	0.160	0.140	0.006	0.88	54.7	2714	53
SS18-029-v - 28	APL 1(b)	V	ext	97	60	1.61	-23	30	99.2	12.33	0.500	0.495	0.012	0.58	98.5	2644	57
SS18-029-v - 30	APL 1(b)	V	ext	358	155	2.31	6	32	93.8	8.79	0.630	0.362	0.025	0.94	71.5	2627	61
SS18-029-v - 31	APL 1(b)	V	ext	729	443	1.65	-15	33	86.6	3.95	0.300	0.159	0.011	0.97	58.9	2647	54
SS18-029-v - 32	APL 1(b)	V	core	465	520	0.89	6	47	95.4	10.48	0.490	0.415	0.017	0.91	83.0	2652	59
SS18-029-v - 32	APL 1(b)	V	rim	348	200	1.74	35	42	90.0	7.24	0.330	0.286	0.012	0.90	54.7	2696	50
SS18-029-v - 33	APL 1(b)	V	core	367	299	1.23	7	24	98.9	11.92	0.440	0.483	0.012	0.82	95.2	2644	50
SS18-029-v - 33*†	APL 1(b)	V	rim	309	232	1.33	15	30	99.8	12.79	0.430	0.518	0.011	0.35	100.9	2673	52
SS18-029-v - 5*†	APL 1(b)	V	ext	170	105	1.61	26	34	98.8	12.66	0.470	0.503	0.013	0.40	98.6	2668	58
SS18-029-v - 8†	APL 1(b)	V	ext	218	172	1.27	10	35	97.7	11.94	0.540	0.478	0.016	0.57	94.3	2655	68
SS18-066-c - 18*	TON	C	ext	236	279	0.85	15	22	99.2	12.45	0.470	0.507	0.017	0.91	97.7	2661	34
SS18-066-c - 21*	TON	C	ext	615	1207	0.51	14	16	99.7	12.42	0.280	0.501	0.009	0.75	96.7	2668	28
SS18-066-c - 28*	TON	C	ext	639	1391	0.46	-13	15	100.0	12.78	0.300	0.512	0.009	0.86	100.6	2658	27
SS18-066-c - 34*	TON	C	ext	349	636	0.55	5	17	99.8	12.75	0.290	0.505	0.009	0.49	99.7	2659	29

Table A2.1: *Continued*.

Sample	Lith.	Zircon Colour	Area	U (ppm)	Th (ppm)	U/Th	^{204}Pb Cps	2σ	%Pb*	^{207}Pb/^{235}U	2σ	^{206}Pb/^{238}U	2σ	Error corr.	% Conc.	^{207}Pb/^{206}Pb	2σ
SS18-066-v - 16*	TON	V	ext	271	324	0.84	35	20	99.9	12.84	0.330	0.511	0.010	0.80	97.5	2645	30
SS18-066-v - 2*	TON	V	ext	388	657	0.59	-4	17	99.7	12.47	0.310	0.508	0.009	0.80	103.9	2678	29
SS18-066-v - 20*	TON	V	ext	360	478	0.75	12	24	99.9	12.49	0.330	0.503	0.009	0.59	98.6	2629	35
SS18-066-v - 28*	TON	V	ext	437	667	0.65	-20	17	99.7	12.78	0.310	0.511	0.010	0.68	99.7	2666	33
SS18-066-v - 35*	TON	V	ext	273	398	0.69	-20	20	99.4	12.64	0.320	0.505	0.010	0.69	97.0	2682	33
SS18-066-v - 39*	TON	V	ext	450	711	0.63	-6	14	99.7	12.49	0.330	0.507	0.011	0.86	101.6	2657	30
SS18-066-v - 44*	TON	V	ext	559	933	0.60	-8	18	99.8	12.66	0.360	0.512	0.012	0.85	101.1	2644	30
SS18-066-v - 52*	TON	V	ext	130	154	0.84	12	21	98.9	12.81	0.320	0.503	0.010	0.24	97.3	2692	35
SS18-058-c - 55*	GND	C	ext	406	444	0.91	38	22	99.6	12.72	0.290	0.511	0.011	0.85	100.3	2662	12
SS18-058-c - 56*	GND	C	ext	1163	2350	0.49	18	21	99.9	12.32	0.270	0.503	0.011	0.77	100.5	2624	12
SS18-058-c - 80*	GND	C	ext	357	452	0.79	16	16	100.0	12.79	0.280	0.519	0.011	0.71	101.6	2649	12
SS18-058-c - 89*	GND	C	ext	541	536	1.01	-2	20	99.5	12.27	0.340	0.502	0.013	0.92	100.0	2625	12
SS18-058-c - 93*	GND	C	ext	245	210	1.17	11	23	99.6	12.45	0.310	0.505	0.012	0.85	98.7	2651	14
SS18-058-v - 1*	GND	V	ext	289	209	1.38	-13	22	99.5	12.68	0.380	0.512	0.014	0.90	100.2	2654	17
SS18-058-v - 9*	GND	V	ext	428	422	1.01	4	22	99.5	12.56	0.400	0.507	0.015	0.93	99.1	2639	15
SS18-058-y - 26*	GND	Y	ext	358	432	0.83	2	21	100.0	12.68	0.300	0.511	0.011	0.65	100.1	2655	16
SS18-058-y - 44*	GND	Y	ext	790	1298	0.61	23	22	100.0	12.67	0.260	0.509	0.010	0.75	99.4	2661	9
SS18-058-y - 49*	GND	Y	ext	391	390	1.00	18	28	99.9	12.57	0.290	0.509	0.011	0.76	101.2	2659	15
SS18-058-y - 64*	GND	Y	ext	406	364	1.11	14	22	99.4	12.59	0.350	0.508	0.014	0.93	99.1	2658	13
SS18-058-y - 66*	GND	Y	ext	462	477	0.97	-3	24	99.4	12.38	0.370	0.504	0.014	0.92	97.9	2654	16

Table A2.1: *Continued*.

Sample	Lith.	Zircon Colour	Area	U (ppm)	Th (ppm)	U/Th	^{204}Pb Cps	2σ	%Pb*	^{207}Pb/ ^{235}U	2σ	^{206}Pb/ ^{238}U	2σ	Error corr.	% Conc.	^{207}Pb/ ^{206}Pb	2σ
JS18-377-c - 11*†	GRN 1	C	ext	1610	890	1.81	111	45	98.6	11.48	1.100	0.493	0.039	0.98	100.4	2559	16
JS18-377-c - 16*†	GRN 1	C	ext	396	242	1.64	1	45	98.9	11.77	0.890	0.493	0.028	0.91	99.8	2588	22
JS18-377-c - 48*†	GRN 1	C	core	4630	1290	3.59	18	45	100.0	12.00	0.900	0.497	0.027	0.90	97.1	2578	18
JS18-377-y - 24*†	GRN 1	C	core	58	21	2.76	-2	31	99.6	13.18	1.100	0.518	0.030	0.69	95.8	2654	41
JS18-377-c - 35_1†	GRN 1	C	ext	83	31	2.69	37	41	99.6	13.42	1.200	0.517	0.029	0.50	99.1	2718	70
JS18-377-c - 53†	GRN 1	C	core	190	131	1.45	-5	41	97.1	11.49	0.860	0.451	0.025	0.64	94.8	2614	38
JS18-377-c - 53†	GRN 1	C	rim	138	77	1.79	30	47	94.7	10.34	0.780	0.411	0.024	0.74	83.5	2634	49
SS18-084-c - 1*	GRN 2	C	ext	956	802	1.19	4	23	99.4	11.60	0.250	0.490	0.011	0.93	101.0	2582	12
SS18-084-c - 2*	GRN 2	C	ext	716	586	1.22	24	29	99.9	11.58	0.220	0.491	0.009	0.83	101.0	2562	18
SS18-084-c - 58*	GRN 2	C	ext	976	861	1.13	-22	26	99.5	11.77	0.240	0.493	0.012	0.92	96.8	2617	12
SS18-084-g - 15*	GRN 2	G	core	628	604	1.04	-1	30	98.9	11.89	0.460	0.497	0.019	0.96	98.2	2613	17
SS18-084-o - 17_1*	GRN 2	O	ext	1786	777	2.30	27	27	99.1	11.39	0.210	0.481	0.010	0.95	95.9	2595	9
SS18-051-v - 17*	FQP	V	ext	339	288	1.18	5	30	99.8	13.18	0.430	0.519	0.013	0.68	100.1	2692	21
SS18-051-v - 18*	FQP	V	ext	537	744	0.72	-18	37	99.9	12.88	0.430	0.512	0.013	0.77	97.8	2692	18
SS18-051-v - 20*	FQP	V	ext	214	139	1.54	4	23	100.0	13.17	0.450	0.518	0.014	0.68	98.7	2704	25
SS18-051-v - 23*	FQP	V	core	508	729	0.70	14	68	99.5	12.71	0.490	0.511	0.015	0.66	104.5	2617	44
SS18-051-v - 29*	FQP	V	ext	419	345	1.21	-13	32	99.5	12.98	0.530	0.513	0.019	0.87	100.1	2677	21

Table A2.1: *Continued*.

Sample	Lith.	Zircon Colour	Area	U (ppm)	Th (ppm)	U/Th	^{204}Pb Cps	2σ	%Pb*	^{207}Pb/ ^{235}U	2σ	^{206}Pb/ ^{238}U	2σ	Error corr.	% Conc.	^{207}Pb/ ^{206}Pb	2σ
SS18-029-c - 12†	APL 1(b)	C	ext	268	338	0.79	24	33	91.4	7.86	0.330	0.313	0.011	0.93	61.2	2668	53
SS18-029-c - 13†	APL 1(b)	C	ext	397	297	1.34	34	26	95.6	10.23	0.390	0.416	0.010	0.80	82.4	2636	51
SS18-029-c - 15†	APL 1(b)	C	ext	1215	1694	0.72	18	28	86.5	2.75	0.250	0.119	0.008	0.98	53.9	2569	64
SS18-029-v - 11†	APL 1(b)	V	ext	226	149	1.52	33	40	97.8	12.73	0.500	0.489	0.014	0.63	92.9	2729	56
SS18-029-v - 14†	APL 1(b)	V	ext	158	100	1.57	5	29	92.7	9.28	0.380	0.366	0.010	0.59	69.6	2704	59
SS18-029-v - 15†	APL 1(b)	V	rim	392	372	1.05	-1	28	90.5	6.82	0.320	0.282	0.010	0.81	54.9	2637	54
SS18-029-v- 15_1†	APL 1(b)	V	ext	241	174	1.38	-13	29	98.8	10.59	0.480	0.497	0.014	0.69	96.5	2682	53
SS18-029-v - 18†	APL 1(b)	V	ext	1232	689	1.79	-5	29	92.9	6.96	0.250	0.307	0.008	0.82	64.0	2512	48
SS18-066-c - 38*	TON	C	ext	621	1497	0.42	12	32	99.3	12.47	0.390	0.504	0.014	0.89	99.4	2635	32
SS18-066-c - 43*	TON	C	ext	494	977	0.51	13	24	100.0	12.59	0.320	0.509	0.010	0.87	102.4	2672	30
SS18-066-v - 13*	TON	V	ext	340	594	0.57	0	27	99.8	12.89	0.360	0.514	0.012	0.85	97.5	2648	31
SS18-066-v - 14*	TON	V	ext	478	741	0.65	-14	22	99.6	12.57	0.370	0.508	0.012	0.93	102.6	2624	29

Table A2.2: CA-TIMS of single grain zircon for U-Pb geochronology of select YGB lithologies, including two FQP dike, one QZP dike, one aplite-1(a) dike, one aplite 1(b) dike, and tonalite. Individual zircon grains are labelled for each analysis, and grains that share a number are fragments from the same grain. A detailed description of the methodology is given within the text.

								Radiogenic Isotope Ratios							
Sample	$\frac{Th}{U}$	$^{206}Pb^*$ x10^{-13} mol	mol % $^{206}Pb^*$	Pb* (pg)	Pb_c (pg)	$\frac{Pb^*}{Pb_c}$	$\frac{^{206}Pb}{^{204}Pb}$	$\frac{^{208}Pb}{^{206}Pb}$	$\frac{^{207}Pb}{^{206}Pb}$	% error	$\frac{^{207}Pb}{^{235}U}$	% error	$\frac{^{206}Pb}{^{238}U}$	% error	corr. coef.
SS18-008, FQP															
z5	1.01	0.28	99.3	8.3	0.16	52	2599	0.279	0.181	0.09	12.737	0.26	0.510	0.22	0.936
z4b	0.76	1.92	99.8	55.1	0.25	223	11653	0.210	0.181	0.06	12.749	0.13	0.511	0.08	0.959
z2	0.92	0.25	99.4	7.5	0.13	59	2980	0.256	0.181	0.12	12.733	0.26	0.510	0.20	0.879
z4a	0.67	0.72	99.7	20.2	0.20	101	5362	0.185	0.181	0.07	12.747	0.18	0.511	0.14	0.936
z1	0.68	0.61	99.7	17.3	0.17	100	5286	0.190	0.181	0.07	12.734	0.16	0.510	0.11	0.934
SS18-029, aplite-1(b)															
z5	0.75	0.48	99.3	49.8	0.28	50	2616	0.209	0.181	0.08	12.736	0.19	0.510	0.14	0.914
z1	0.86	1.42	99.8	148.1	0.28	148	7586	0.238	0.181	0.07	12.745	0.14	0.511	0.09	0.933
z6	0.66	1.23	99.6	90.4	0.38	90	4825	0.183	0.181	0.07	12.742	0.15	0.511	0.10	0.939
z4b	0.86	1.92	99.8	154.1	0.37	154	7889	0.239	0.181	0.06	12.747	0.14	0.511	0.08	0.947
z4a	0.88	1.66	99.8	206.2	0.24	206	10508	0.245	0.181	0.07	12.735	0.14	0.511	0.08	0.944
SS18-066, tonalite															
z2a	1.41	2.13	99.9	69.2	0.17	396	18282	0.392	0.181	0.06	12.749	0.13	0.511	0.08	0.959
z5	1.16	0.71	99.7	22.1	0.20	111	5348	0.323	0.181	0.07	12.747	0.16	0.511	0.11	0.937
z4	1.53	1.85	99.9	61.4	0.19	326	14722	0.425	0.181	0.06	12.740	0.13	0.510	0.08	0.955
z2b	1.39	1.60	99.9	51.7	0.17	298	13791	0.385	0.181	0.06	12.758	0.14	0.511	0.08	0.947
z3	1.63	1.06	99.8	35.8	0.21	172	7673	0.451	0.181	0.06	12.724	0.14	0.510	0.09	0.951

corr. coef. = correlation coefficient; % disc. = percent discordance

Table A2.2: *Continued*.

	Isotopic Dates						
Sample	$^{207}Pb/^{206}Pb$	error ±	$^{207}Pb/^{235}U$	error ±	$^{206}Pb/^{238}U$	error ±	% disc.
SS18-008, FQP							
z5	2662.63	1.54	2660.39	2.41	2657.45	4.69	0.19
z4b	2661.85	1.04	2661.28	1.24	2660.54	1.65	0.05
z2	2662.17	2.05	2660.13	2.40	2657.45	4.43	0.18
z4a	2662.40	1.18	2661.15	1.71	2659.51	3.04	0.11
z1	2661.69	1.14	2660.20	1.50	2658.24	2.42	0.13
SS18-029, aplite-1(b)							
z5	2662.82	1.40	2660.30	1.77	2656.99	2.95	0.22
z1	2662.35	1.12	2660.96	1.34	2659.14	1.95	0.12
z6	2661.65	1.10	2660.79	1.40	2659.65	2.12	0.08
z4b	2661.32	1.06	2661.12	1.30	2660.84	1.84	0.02
z4a	2661.16	1.08	2660.24	1.28	2659.03	1.77	0.08
SS18-066, tonalite							
z2a	2662.63	1.02	2661.30	1.22	2659.54	1.63	0.12
z5	2662.51	1.11	2661.13	1.49	2659.31	2.41	0.12
z4	2662.26	1.03	2660.63	1.24	2658.48	1.69	0.14
z2b	2662.09	1.05	2661.95	1.27	2661.77	1.77	0.01
z3	2661.83	1.04	2659.44	1.31	2656.30	1.88	0.21

Table A2.2: *Continued*.

Sample	Th/U	$^{206}Pb^*$ x10^{-13} mol	mol % $^{206}Pb^*$	Pb* (pg)	Pb_c (pg)	Pb*/Pb_c	$^{206}Pb/^{204}Pb$	Radiogenic Isotope Ratios: $^{208}Pb/^{206}Pb$	$^{207}Pb/^{206}Pb$	% error	$^{207}Pb/^{235}U$	% error	$^{206}Pb/^{238}U$	% error	corr. coef.
SS18-082, QZP															
z1a	0.81	7.16	100.0	728.2	0.29	728	36980	0.220	0.209	0.06	16.330	0.13	0.568	0.07	0.968
z1b	0.84	6.18	100.0	1041.2	0.18	1041	52558	0.229	0.209	0.06	16.304	0.13	0.567	0.07	0.960
z6	0.45	5.70	99.9	442.8	0.35	443	24156	0.124	0.208	0.06	16.179	0.13	0.565	0.07	0.964
z5	0.35	4.31	99.9	424.5	0.27	424	23780	0.095	0.202	0.07	15.460	0.15	0.555	0.11	0.923
z2	0.54	3.27	99.9	485.2	0.19	485	26144	0.148	0.200	0.06	15.120	0.13	0.550	0.07	0.968
z4	0.21	0.53	99.0	31.1	0.44	31	1823	0.057	0.192	0.09	14.101	0.26	0.532	0.22	0.941
SS18-125, FQP															
z5	0.64	2.66	99.9	74.6	0.19	390	20853	0.177	0.181	0.06	12.738	0.13	0.510	0.08	0.961
z3	0.61	0.52	99.6	14.5	0.19	76	4097	0.170	0.181	0.07	12.728	0.21	0.510	0.17	0.944
z4	0.73	1.73	99.9	49.4	0.20	253	13290	0.202	0.181	0.06	12.753	0.13	0.511	0.08	0.954
z2	0.75	2.13	99.9	61.0	0.23	262	13692	0.209	0.181	0.06	12.740	0.13	0.510	0.07	0.960
z6	0.72	0.62	99.7	17.7	0.17	105	5545	0.198	0.181	0.07	12.732	0.16	0.510	0.11	0.933
UNB-1, aplite-1(a)															
z6	0.67	0.31	99.2	8.9	0.21	43	2273	0.187	0.181	0.09	12.761	0.23	0.511	0.19	0.933
z2	0.83	0.15	98.5	4.5	0.19	24	1244	0.230	0.181	0.13	12.621	0.35	0.505	0.29	0.931
z1	0.83	0.68	99.7	19.9	0.17	117	6031	0.231	0.181	0.07	12.775	0.15	0.512	0.10	0.932
z4	0.76	0.17	98.6	5.0	0.21	24	1275	0.211	0.181	0.13	12.760	0.40	0.511	0.36	0.946
z3	0.80	0.14	98.2	4.0	0.21	19	1013	0.222	0.181	0.17	12.734	0.42	0.510	0.36	0.920

Table A2.2: *Continued*.

	Isotopic Dates						
Sample	$\frac{^{207}Pb}{^{206}Pb}$	error ±	$\frac{^{207}Pb}{^{235}U}$	error ±	$\frac{^{206}Pb}{^{238}U}$	error ±	% disc.
SS18-082, QZP							
z1a	2895.38	0.98	2896.32	1.20	2897.66	1.64	-0.08
z1b	2894.05	0.99	2894.80	1.22	2895.89	1.70	-0.06
z6	2886.85	0.98	2887.40	1.22	2888.19	1.71	-0.05
z5	2842.07	1.10	2844.01	1.47	2846.73	2.53	-0.16
z2	2822.07	1.00	2822.82	1.20	2823.87	1.60	-0.06
z4	2760.55	1.52	2756.49	2.46	2750.95	4.80	0.35
SS18-125, FQP							
z5	2663.13	1.01	2660.49	1.22	2657.02	1.62	0.23
z3	2662.96	1.20	2659.72	1.93	2655.47	3.64	0.28
z4	2662.64	1.03	2661.61	1.26	2660.26	1.74	0.09
z2	2662.44	1.04	2660.65	1.22	2658.31	1.59	0.15
z6	2662.24	1.14	2660.02	1.50	2657.10	2.40	0.19
UNB-1, aplite-1(a)							
z6	2663.20	1.48	2662.18	2.20	2660.85	4.10	0.09
z2	2663.15	2.15	2651.76	3.24	2636.86	6.26	0.99
z1	2662.77	1.14	2663.17	1.44	2663.71	2.24	-0.04
z4	2662.08	2.20	2662.07	3.80	2662.07	7.79	0.00
z3	2661.44	2.80	2660.16	3.98	2658.49	7.78	0.11

Table A2.3**:** Zircon mineral chemistry from representative felsic intrusions in the YGB. Data were filtered by the calculated $^{207}Pb/^{206}Pb$ ages given in Chapter 3. Data has been filtered for P, Ti, and Si to avoid analyses that ablated inclusions and a value of 47 wt. % Zr was used as an internal standard. The Pb_T shown is a calculated total Pb based on isotopic abundances. - = not analyzed.

Sample	SS18-008	SS18-008	SS18-008	SS18-008	SS18-008	SS18-008	SS18-008	SS18-008	SS18-051	SS18-051
Lithology	FQP	FQP	FQP	FQP	FQP	FQP	FQP	FQP	FQP	FQP
Ce (ppm)	53.0	96.8	96.4	61.9	146	93.8	226	86.0	66.9	217
Dy	105	154	125	148	151	138.8	170	140	106	302
Er	-	-	-	-	-	-	-	-	-	-
Eu	6.40	7.80	17.2	12.6	32.5	19.8	25.1	11.5	15.4	49.1
Gd	54.9	67.0	92.0	72.5	116	92.9	123	68.4	44.0	252
Hf	10150	8330	10900	8930	10380	10410	10090	9080	10200	9600
Ho	31.2	56.9	31.2	49.9	45.1	39.1	47.4	48.1	35.5	78.2
La	6.90	4.60	10.1	2.07	19.5	9.46	56.0	4.26	6.60	18.5
Lu	59.9	107.8	52.0	91.3	76.0	70.2	72.2	86.0	70.5	101
Nd	38.4	32.9	95.8	36.9	122	95.6	158	59.1	32.2	245
P	70.0	1280	450	350	1830	250	130	0.00	203	203
Pb_T	372	629	433	539	478	577	674	448	359	379
^{204}Pb	93.0	24.7	136	31.5	47.0	145	164	49.0	1.10	1.30
^{206}Pb	828	1559	954	1366	1240	1322	1466	1089	1006	967
^{207}Pb	236	330	292	296	286	373	420	253	200	196
^{208}Pb	229	345	263	277	221	333	433	248	139	197
Pr	5.60	4.71	13.2	4.62	19.7	12.7	26.3	8.80	4.67	34.4
Si	166500	169700	161800	177500	171700	172100	165700	160600	193400	176100
Sm	27.2	25.1	66.4	28.5	80.4	68.5	88.1	36.2	17.1	166

Table A2.3: *Continued*.

Sample	SS18-008	SS18-008	SS18-008	SS18-008	SS18-008	SS18-008	SS18-008	SS18-008	SS18-051	SS18-051
Lithology	FQP	FQP	FQP	FQP	FQP	FQP	FQP	FQP	FQP	FQP
Tb (ppm)	11.5	16.8	16.8	16.1	20.7	18.9	22.8	16.4	11.2	42.2
Th	344	1007	257	751	493	356	597	646	481	813
Ti	7.10	10.0	31.1	10.6	15.0	26.3	20.4	21.0	26.3	64.4
Tm	30.5	52.0	25.3	46.4	37.3	31.82	38.2	42.3	31.6	53.7
U	291	636	351	543	474	457	528	472	429	533
Y	987	1779	941	1574	1381	1187	1369	1489	1148	2450
Yb	274	467	239	434	342	316	357	405	314	487

Table A2.3: *Continued*.

Sample	SS18-051	SS18-051	SS18-051	SS18-051	SS18-051	SS18-051	SS18-051	SS18-051	SS18-100	SS18-100
Lithology	FQP	FQP	FQP	FQP	FQP	FQP	FQP	FQP	FQP	FQP
Ce (ppm)	49.4	74.5	92	85.5	147	50.4	102	81.1	23.2	32.3
Dy	85.5	191	167	139	226	112	149	170	177	133
Er	-	-	-	-	-	-	-	-	-	-
Eu	8.50	16.2	15.7	20.0	30.0	10.5	20.5	12.7	5.26	9.60
Gd	41.2	133	103	72.0	135	58.4	117	93.0	56.2	52.5
Hf	10970	10390	10880	9930	9700	8180	10070	10460	9218	11480
Ho	28.2	47.2	44.9	47.2	69.2	32.4	40.4	52.1	64.4	42.1
La	2.53	8.90	8.90	10.8	10.8	3.43	8.60	7.80	1.71	3.20
Lu	57.3	55.5	64.3	93.6	114	49.4	68.1	78.4	115	70.7
Nd	35.4	83.0	88.0	53.5	164	42.7	98.0	65.0	12.1	29.4
P	146	241	280	810	277	248	204	260	567	237
Pb_T	263	180	275	520	537	143	343	397	313	159
^{204}Pb	1.30	5.30	5.20	2.40	3.50	0.800	2.30	6.80	3.40	0.500
^{206}Pb	772	520	780	1390	1413	393	896	1080	976	533
^{207}Pb	154	107	161	290	285	80.0	184	219	201	111
^{208}Pb	82.2	59.1	99.3	232	256	58.1	165	169	63.5	11.6
Pr	3.87	11.7	10.9	6.39	19.5	5.99	11.0	8.80	1.33	4.22
Si	176200	170600	176100	181100	165200	158300	175900	162500	166700	155700
Sm	20.9	70.0	57.7	30.9	93.0	34.5	58.0	39.4	13.3	22.4

Table A2.3: *Continued*.

Sample	SS18-051	SS18-051	SS18-051	SS18-051	SS18-051	SS18-051	SS18-051	SS18-051	SS18-100	SS18-100
Lithology	FQP	FQP	FQP	FQP	FQP	FQP	FQP	FQP	FQP	FQP
Tb (ppm)	9.29	27.4	20.8	14.5	27.0	13.72	19.3	19.7	16.4	13.8
Th	292	199	339	683	1130	213	579	804	246	64.2
Ti	9.90	25.1	21.7	15.3	38.3	20.9	18.7	32.8	15.7	24.2
Tm	26.1	27.2	32.5	42.4	56.5	24.6	32.5	39.3	58.1	35.9
U	352	243	368	586	864	197	404	604	470	285
Y	883	1400	1350	1480	2170	946	1330	1523	1989	1280
Yb	254	250	295	421	574	230	310	380	537	340

Table A2.3: *Continued*.

Sample	SS18-125	SS18-125	SS18-128	SS18-128	SS18-128	SS18-128	SS18-128	SS18-128	SS18-082	SS18-082
Lithology	FQP	FQP	FQP	FQP	FQP	FQP	FQP	FQP	QZP	QZP
Ce (ppm)	2310	134	38.3	922	31.2	132	19.2	110	174	189
Dy	273	200	68.3	381	72.4	194	36.2	186	250	291
Er	-	-	-	-	-	-	-	-	-	-
Eu	70.7	58.0	1.62	55.2	8.50	25.7	7.30	24.2	27.0	67.8
Gd	237	172	22.7	262	33.0	99.7	23.1	101	178	119
Hf	10720	10140	8848	10674	10238	10400	11569	9998	11080	13320
Ho	62.9	47.9	26.5	84.6	21.6	55.5	8.96	51.0	73.1	106
La	1153	16.3	0.0980	517	1.06	7.31	1.40	4.34	20.4	34.9
Lu	77.4	57.6	71.1	78.5	51.4	102.8	17.3	81.2	101	223
Nd	878	175	3.18	391	14.8	50.5	15.4	48.5	183	216
P	1464	229	390	2350	340	370	40.0	570	450	240
Pb_T	372	128	336	296	228	524	66.5	561	816	1199
^{204}Pb	24.2	2.20	1.10	18.8	1.80	17.2	3.90	3.60	23.5	9.20
^{206}Pb	982	379	922	809	680	1432	203	1482	2551	3871
^{207}Pb	216	77.3	189	171	139	284	41.9	304	565	814
^{208}Pb	168	37.7	138	121	64.3	223	15.9	262	145	166
Pr	238	28.2	0.282	93.5	1.84	7.82	2.11	6.82	26.4	31.9
Si	175100	157000	158300	174700	174000	173500	152600	181000	169000	173900
Sm	216	123	5.83	122	13.7	41.1	12.2	44.0	123	77.7

Table A2.3: *Continued*.

Sample	SS18-125	SS18-125	SS18-128	SS18-128	SS18-128	SS18-128	SS18-128	SS18-128	SS18-082	SS18-082
Lithology	FQP	FQP	FQP	FQP	FQP	FQP	FQP	FQP	QZP	QZP
Tb (ppm)	40.7	30.8	6.28	54.9	8.44	23.9	4.95	24.3	32.8	26.0
Th	576	201	413	344	224	924	58.1	874	510	621
Ti	16.9	20.3	6.30	10.9	5.80	15.5	10.9	11.1	39.0	26.5
Tm	39.5	32.2	28.8	45.0	21.8	46.5	7.56	39.6	61.1	105
U	491	271	373	420	301	839	131	681	1304	1741
Y	1959	1540	840	2430	694	1695	283	1494	2214	2920
Yb	387	283	294	387	219	470	77	379	525	1054

Table A2.3: *Continued*.

Sample	SS18-082	SS18-082	SS18-082	SS18-082	SS18-082	SS18-082	UNB-1	UNB-1	UNB-1	UNB-1	UNB-1
Lithology	QZP	QZP	QZP	QZP	QZP	QZP	APL 1a	APL 1a	APL 1a	APL 1a	APL 1a
Ce (ppm)	178	33.6	24.3	232	16.1	36.5	54.3	77.2	98.0	92.8	77.6
Dy	50.9	74.8	237	154	129	212	126	163	261	246	185
Er	-	-	-	-	-	-	-	-	-	-	-
Eu	67.5	3.91	1.06	29.4	0.700	5.20	5.41	7.00	15.9	12.5	8.23
Gd	54.2	45.3	50.5	231	22.8	57.2	39.6	58.4	104	79.5	59.9
Hf	15010	15240	11800	15210	13690	11250	10440	10070	9790	10370	9820
Ho	21.1	27.1	96.1	31.3	55.7	83.9	44.2	60.5	79.9	76.8	66.1
La	33.9	5.23	5.62	32.0	3.70	4.15	3.82	3.38	7.90	14.3	3.54
Lu	84.4	84.2	158	40.4	112	165	88.8	115	120	110	115
Nd	203	36.2	10.2	359	5.60	40.0	25.0	31.4	65.0	52.3	27.5
P	320	355	690	60.0	680	2230	298	512	519	582	477
Pb_T	768	619	667	962	1748	2118	240	469	402	448	433
^{204}Pb	39.0	0.300	4.10	153	23.2	30.0	5.40	20.0	35.0	132	14.2
^{206}Pb	2549	2121	2180	2925	5760	6930	699	1347	1119	1041	1234
^{207}Pb	573	449	453	736	1218	1474	144	283	252	317	258
^{208}Pb	50.5	15.9	79.1	177	174	233	76.6	156	146	241	150
Pr	29.7	4.96	1.70	51.6	1.19	6.32	3.75	4.90	10.4	9.60	4.48
Si	172200	147300	154400	187600	171500	179200	147800	172100	163400	160600	162300
Sm	66.6	33.8	10.7	230	4.77	22.4	15.9	21.8	48.0	34.8	24.6

Table A2.3: *Continued*.

Sample	SS18-082	SS18-082	SS18-082	SS18-082	SS18-082	SS18-082	UNB-1	UNB-1	UNB-1	UNB-1	UNB-1
Lithology	QZP	QZP	QZP	QZP	QZP	QZP	APL 1a	APL 1a	APL 1a	APL 1a	APL 1a
Tb (ppm)	6.20	8.30	18.8	32.2	9.39	17.8	11.0	16.2	28.5	24.1	17.4
Th	49.8	66.9	387	134	449	682	338	444	391	359	607
Ti	18.3	13.3	19.7	74.0	4.00	17.6	18.6	12.8	13.0	11.6	11.2
Tm	30.8	35.5	93.1	21.9	60.6	88.2	43.5	57.9	65.0	64.9	60.5
U	1044	1235	2030	1244	3020	3187	391	577	544	496	604
Y	712	849	2740	975	1690	2540	1349	1867	2450	2310	1991
Yb	357	386	848	193	581	849	415	544	589	592	543

Table A2.3: *Continued*.

Sample	UNB-1	SS18-029	SS18-066	SS18-066	SS18-066	SS18-066	SS18-066	SS18-066	SS18-066	SS18-066	SS18-058
Lithology	APL 1a	APL 1b	TON	TON	TON	TON	TON	TON	TON	TON	GND
Ce (ppm)	300	330	-	-	-	-	-	-	-	-	-
Dy	368	1440	-	-	-	-	-	-	-	-	-
Er	-	-	39.8	82.8	34.8	111	48.6	136	117	110	227
Eu	37.2	103	1.58	12.5	6.42	14.1	11.0	6.34	6.65	13.2	30.5
Gd	204	930	8.47	60.4	22.9	68.3	30.7	43.1	36.5	47.4	102
Hf	10600	10090	8190	7594	8142	7367	7578	7131	7424	7400	10744
Ho	92.0	324	8.64	22.5	8.79	28.6	12.4	31.1	27.4	25.1	54.4
La	44.0	37.7	-	-	-	-	-	-	-	-	-
Lu	91.0	219	25.0	37.4	19.9	49.4	25.3	65.1	59.2	58.7	95.3
Nd	239	404	4.07	51.9	19.1	50.3	24.4	17.0	21.4	64	178
P	539	760	73.0	148	96.9	141	174	167	160	131	536
Pb_T	462	285	185	238	104	206	97.4	253	356	453	547
^{204}Pb	245	4.00	0.100	2.20	0.500	0.900	1.50	0.50	1.20	1.10	1.20
^{206}Pb	920	771	511	632	296	516	274	632	875	1130	1538
^{207}Pb	341	153	101	122	59.8	102	54.2	124	173	223	301
^{208}Pb	309	126	76.9	113	38.1	113	37.0	141	206	253	212
Pr	44.0	57.4	-	-	-	-	-	-	-	-	-
Si	162800	176200	-	-	-	-	-	-	-	-	-
Sm	141	431	3.29	32.7	12.7	31.3	14.5	14.9	14.2	28.0	72.6

Table A2.3: *Continued*.

Sample	UNB-1	SS18-029	SS18-066	SS18-066	SS18-066	SS18-066	SS18-066	SS18-066	SS18-066	SS18-066	SS18-058
Lithology	APL 1a	APL 1b	TON	TON	TON	TON	TON	TON	TON	TON	GND
Tb (ppm)	46.0	190	2.28	11.7	4.17	12.2	5.59	9.74	8.31	9.40	21.2
Th	1160	1060	268	298	128	424	133	511	684	902	868
Ti	24.9	38.4	4.19	15.5	9.60	79.0	8.30	10.7	7.60	9.00	30.4
Tm	58.3	174	9.56	17.0	7.25	22.5	10.5	28.7	26.0	23.7	46.8
U	472	555	232	252	147	263	128	300	380	535	807
Y	2800	10100	280	691	271	868	398	973	864	782	1739
Yb	525	1370	-	-	-	-	-	-	-	-	-

Table A2.3: *Continued*.

Sample	SS18-058	SS18-058	SS18-058	SS18-058	SS18-058	SS18-058	SS18-058	SS18-058	SS18-058	SS18-058
Lithology	GND	GND	GND	GND	GND	GND	GND	GND	GND	GND
Ce (ppm)	-	-	-	-	-	-	-	-	-	-
Dy	-	-	-	-	-	-	-	-	-	-
Er	213	114	339	132	144	195	148	321	148	199
Eu	10.4	12.5	30.6	2.01	27.4	28.3	35.7	36.5	28.4	21.8
Gd	54.9	61.6	166	27.1	50.4	111	89.7	158	76.8	98.5
Hf	10309	9926	7852	9414	10395	10720	10839	9700	10480	9725
Ho	48.8	25.1	85.3	30.1	32.8	46.0	35.8	77.5	32.8	48.6
La	-	-	-	-	-	-	-	-	-	-
Lu	93.1	59.8	130	52.1	73.0	78.3	73.3	136	72.4	77.9
Nd	65.4	130	117	13.0	59.2	277	209	219	237	142
P	760	212	448	770	221	580	742	334	331	386
Pb_T	522	276	628	149	387	383	403	819	503	305
^{204}Pb	2.90	1.40	0.200	0.900	1.70	4.00	2.10	2.10	1.30	1.70
^{206}Pb	1421	797	1424	428	1073	1060	1169	2084	1385	828
^{207}Pb	281	158	281	84.3	214	210	230	411	274	165
^{208}Pb	224	93.9	427	51.3	155	156	136	434	208	133
Pr	-	-	-	-	-	-	-	-	-	-
Si	-	-	-	-	-	-	-	-	-	-
Sm	25.6	55.4	81.6	8.62	22.8	99.1	74.7	106	73.7	62.8

Table A2.3: *Continued*.

Sample	SS18-058	SS18-058	SS18-058	SS18-058	SS18-058	SS18-058	SS18-058	SS18-058	SS18-058	SS18-058
Lithology	GND	GND	GND	GND	GND	GND	GND	GND	GND	GND
Tb (ppm)	13.5	8.92	34.7	7.36	9.75	18.0	13.9	28.7	11.4	18.1
Th	845	347	1610	169	593	682	435	1664	759	483
Ti	12.1	25.0	18.5	11.9	22.7	28.8	34.6	12.1	37.6	25.9
Tm	45.2	25.0	66.4	27.1	31.3	39.6	32.4	66.3	31.9	39.6
U	718	362	687	183	515	572	632	1040	681	381
Y	1524	822	2680	885	1142	1465	1184	2456	1073	1496
Yb	-	-	-	-	-	-	-	-	-	-

Table A2.3: *Continued*.

Sample	SS18-058	SS18-058	SS18-058	SS18-058	SS18-058	SS18-058	SS18-058	JS18-377	JS18-377
Lithology	GND	GND	GND	GND	GND	GND	GND	GRN 1	GRN 1
Ce (ppm)	-	-	-	-	-	-	-	30.5	65.0
Dy	-	-	-	-	-	-	-	509	207
Er	143	149	156	154	200	251	142	-	-
Eu	5.36	11.5	37.3	3.98	18.0	71.6	9.60	3.57	2.47
Gd	30.4	35.6	136	34.6	51.4	181	34.9	149	67.6
Hf	8453	10282	11064	7690	9300	9715	10361	12620	11240
Ho	31.9	33.7	44.1	35.9	46.9	68.3	31.9	168	67.7
La	-	-	-	-	-	-	-	4.85	15.1
Lu	58.7	71.3	62.0	63.0	78.5	93.0	69.8	189	92.7
Nd	20.9	49.1	256	13.7	53.4	346	30.7	16.3	33.8
P	1080	810	184	374	283	1230	422	1410	595
Pb_T	95.3	380	397	160	187	542	427	1181	283
^{204}Pb	2.40	4.00	2.60	2.20	1.90	1.60	2.00	18.4	18.8
^{206}Pb	265	1086	1117	450	550	1455	1217	3800	848
^{207}Pb	52.7	215	219	89.6	109	288	243	736	184
^{208}Pb	38.0	135	152	61.4	58.9	246	154	197	72.1
Pr	-	-	-	-	-	-	-	2.14	6.30
Si	-	-	-	-	-	-	-	182900	177500
Sm	11.6	15.7	103	10.8	27.0	128	14.8	25.3	20.4

Table A2.3: *Continued*.

Sample	SS18-058	SS18-058	SS18-058	SS18-058	SS18-058	SS18-058	SS18-058	JS18-377	JS18-377
Lithology	GND	GND	GND	GND	GND	GND	GND	GRN 1	GRN 1
Tb (ppm)	7.88	8.85	23.0	9.26	12.3	30.5	8.00	46.7	20.7
Th	130	541	573	209	225	1020	508	950	194
Ti	17.9	9.30	33.1	12.9	17.7	51.3	7.20	13.0	15.8
Tm	29.6	33.0	30.1	31.4	40.5	47.8	31.5	128	56.4
U	114	535	643	199	262	768	531	1720	413
Y	960	1065	1385	1074	1380	2304	1015	4690	1970
Yb	-	-	-	-	-	-	-	1074	469

Table A2.3: *Continued*.

Sample	JS18-377	JS18-377	JS18-377	SS18-084	SS18-084	SS18-084	SS18-084	SS18-084	SS18-084	SS18-084
Lithology	GRN 1	GRN 1	GRN 1	GRN 2	GRN 2	GRN 2	GRN 2	GRN 2	GRN 2	GRN 2
Ce (ppm)	99.8	84.0	58.1	-	-	-	-	-	-	-
Dy	369	494	222	-	-	-	-	-	-	-
Er	-	-	-	169	190	216	278	233	183	260
Eu	11.3	17.3	8.50	3.57	5.06	7.21	9.27	6.27	3.42	7.19
Gd	178	238	102	42.3	52.4	67.4	93.8	64.1	42.5	70.3
Hf	10520	10660	10740	9974	11030	11040	9282	8725	10730	10810
Ho	100	133	52.0	39.8	42.6	47.2	67.0	54.8	43.3	59.5
La	25.7	11.7	5.40	-	-	-	-	-	-	-
Lu	85.3	99.0	45.6	63.8	85.4	109	97.8	98.8	73.6	108
Nd	77.6	90.0	35.6	15.2	32.4	81.8	56.9	36.8	15.9	46.6
P	594	780	509	249	176	302	739	762	219	367
Pb_T	464	123	125	352	590	1004	422	707	777	906
^{204}Pb	25.7	10.7	28.0	0.300	0.200	0.100	3.90	5.50	1.70	4.40
^{206}Pb	1370	353	331	996	1814	3166	1100	1956	2275	2801
^{207}Pb	285	74.7	81.7	191	350	594	211	367	432	526
^{208}Pb	136	40.6	51.2	135	144	211	212	297	256	220
Pr	13.5	12.8	5.7	-	-	-	-	-	-	-
Si	151900	152300	178500	-	-	-	-	-	-	-
Sm	61.6	87.0	39.0	14.7	26.0	46.3	45.5	27.2	13.5	35.4

Table A2.3: *Continued*.

Sample	JS18-377	JS18-377	JS18-377	SS18-084	SS18-084	SS18-084	SS18-084	SS18-084	SS18-084	SS18-084
Lithology	GRN 1	GRN 1	GRN 1	GRN 2	GRN 2	GRN 2	GRN 2	GRN 2	GRN 2	GRN 2
Tb (ppm)	46.1	58.0	27.9	12.0	14.1	15.6	24.2	16.3	11.7	19.3
Th	427	212	259	506	970	1070	902	927	856	1454
Ti	12.1	48.0	35.5	8.10	8.60	19.7	22.2	14.9	14.3	12.8
Tm	57.4	77.0	29.7	35.5	41.9	49.9	57.2	50.5	39.6	59.6
U	700	312	167	501	948	1732	592	985	1021	1278
Y	2641	3630	1430	1285	1470	1826	2241	1864	1388	2108
Yb	462	587	245	-	-	-	-	-	-	-

Curriculum Vitae

Sarah Catherine Speight, Ph. D.

EDUCATION

2023 **Doctor of Philosophy in Earth Sciences – University of New Brunswick**

Dissertation: Assembling an Archean magmatic plumbing system: geochemical evolution, emplacement, and metallogenic implications of subvolcanic intrusions in the Yellowknife greenstone belt, N.W.T., Canada

Supervisors: Dr. Chris McFarlane, Dr. Jacob Hanley

2013 **Master of Science – Laurentian University**

Thesis: A study of the composition, distribution, and genesis of pyrrhotite in the copper cliff offset, Sudbury, Ontario, Canada

Supervisor: Dr. Andy McDonald

2011 **Bachelor of Science, with Honours – University of New Brunswick**

Thesis: The petrogenesis of calc-alkaline lamprophyres from Mali, West Africa

Supervisor: Dr. Chris McFarlane

SCHOLARSHIPS AND AWARDS

2022 $600 – Travel Grant (Precambrian Division)

2022 $300 – Travel Grant (Canadian Tectonics Group)

2018 $0 – Yellowknife Geoscience Forum Poster Award (Northwest Territories Association of Professional Engineers and Geoscientists)

2018 $500 – Travel Award (UNB School of Graduate Studies)

2018 $100 – RFG Jérôme H. Remick III Student Poster Award (GAC-MAC)

2018 $500 – Travel Scholarship (Mineralogical Association of Canada)

2017 $4500 –Board of Governors Merit Awards (UNB)

2016 $7000 – New Brunswick Innovation Fund (UNB)

2016 $63000 – Postgraduate Scholarship – D (Natural Sciences and Engineering Research Council of Canada)

2016 $0 – Hawley Medal (Canadian Mineralogist)

2010 $600 – Frank S. Shea Memorial Award (Atlantic Universities Geoscience Conference)

2010 $1250 – A. L. McAllister Scholarship (UNB)

2010 $400 – Lowell Trembath Memorial Award (UNB)

2009 $5000 – Teck Scholarship (UNB)

2006 $1500 – William and Lois Paine Founder's Scholarship (UNB)

2006 $550 – Laura B. McCain Memorial Scholarship (UNB)

PUBLICATIONS

*Recipient of the Hawley Medal for the best paper to appear in the Canadian Mineralogist in 2015.

Gordon, S.C.*, and McDonald, A.M. (2015) A study of the composition, distribution and genesis of pyrrhotite in the Copper Cliff Offset, Sudbury, Ontario. The Canadian Mineralogist. 53: 859-878.

CONFERENCE PRESENTATIONS

*Recipient of the Yellowknife Geoscience Forum Poster Award (Northwest Territories Association of Professional Engineers and Geoscientists)
**Recipient of the RFG Poster Award (GAC-MAC)
***Recipient of Frank S. Shae Memorial Award (Atlantic Universities Geoscience Conference)

Speight, S.C., Hanley, J.J., McFarlane, C.R.M. (2022) A preliminary investigation of zircon-hosted melt and mineral inclusions from intermediate and felsic intrusions within the Yellowknife greenstone belt, NWT, Canada. GAC-MAC-IAH-CNC-CSPG Joint Meeting.

Speight, S.C., Hanley, J.J., McFarlane, C.R.M. (2021) Geodynamic evolution of felsic magmatism in the Yellowknife greenstone belt: evidence for Archean magmatism in a volatile-saturated environment. (Ph. D.)

Speight, S.C., Hanley, J.J., McFarlane, C.R.M. (2021) The geochemical evolution of felsic magmatic intrusions in the Yellowknife greenstone belt, NWT: identifying adakites in the Archean. PDAC Student Colloquium. (Ph. D.)

Speight, S.C., McFarlane, C.R.M., Hanley, J.J. (2019) Evidence for sulfur saturation from zircon-hosted melt inclusions in felsic plutons and dikes of the Yellowknife greenstone belt, NWT. GAC-MAC Conference. (Ph. D.)

Speight, S.C., McFarlane, C.R.M., Hanley, J.J. (2019) New U-Pb ages and compositional data from zircons to establish the timing and evolution of porphyritic intrusions and plutonic bodies in the Yellowknife greenstone belt, NWT. GAC-MAC-IAH Conference. (Ph. D.)

Speight, S.C.*, Lentz, D.R., McFarlane, C.R.M. (2018) Petrographic analysis of syn- to post-tectonic granitic dykes in the Yellowknife greenstone belt, NWT: evidence for late-stage H_2O-rich fluids. Yellowknife Geosciences Forum. (Ph. D.)

Speight, S.C., Lentz, D.R., McFarlane, C.R.M. (2018) New insights into barren and Au-mineralized intrusions using whole-rock and trace element geochemistry from the Yellowknife greenstone belt, NWT. Yellowknife Geosciences Forum. (Ph. D.)

Speight, S.C., Lentz, D.R., McFarlane, C.R.M. (2018) In-situ trace element analysis of quartz phenocrysts from porphyritic intrusions in the Yellowknife greenstone belt, NWT. Resources for Future Generations Conference. (Ph. D.)

Speight, S.C.**, Lentz, D.R., McFarlane, C.R.M. (2018) SEM-Cathodoluminescence imaging and analysis of quartz phenocrysts and phenoclasts from porphyritic intrusions in the Yellowknife greenstone belt, NWT. (Ph. D.)

Speight, S.C., Lentz, D.R., McFarlane, C.R.M. (2017) Petrographic and μ-XRF study of the Kam Group lithologies in the Au-bearing Yellowknife greenstone belt, Northwest Territories, Canada. Society for Geology Applied to Mineral Deposits (SGA) Biennial Conference. (Ph. D.)

Speight, S.C., Lentz, D.R., McFarlane, C.R.M. (2016) Porphyry or pyroclastic? A petrographic comparison of lithologies from the Hebert-Brent showing in the Yellowknife greenstone belt, NWT. Yellowknife Geosciences Forum (Ph. D.)

Banerjee, N.R., Van Loon, L.L., **Speight, S.C.**, Lu, L., Bajwa, C., Flynn, T., Sexton, A., Setterfield, T., Campbell, J., Kerswill, J., Carpenter, R. (2016) Insights into gold mineralization at the Yellowknife City Gold Project using synchrotron X-ray spectroscopy. Yellowknife Geosciences Forum (Ph. D.)

Speight, S.C. (2016) Gold mineralization at the Hebert-Brent showing in the Yellowknife greenstone belt, NWT: Preliminary petro-geochemical results. Geological Association of Canada-Mineralogical Association of Canada (Ph. D.)

Gordon, S.C., and McDonald, A.M. (2013) A mineralogical study of the origin, evolution and spatial distribution of NC pyrrhotite along the Copper Cliff Offset Dike, Sudbury, ON. PDAC-Society of Economic Geologists Minerals Colloquium (M. Sc.)

Gordon, S.C., and McDonald, A.M. (2012) A mineralogical study of hexagonal pyrrhotite along the Copper Cliff Offset, Sudbury. Geological Association of Canada-Mineralogical Association of Canada (M. Sc.)

Gordon, S.C.* ** (2010) The petrogenesis of calc-alkaline lamprophyres from Mali, West Africa. Atlantic Universities Geoscience Conference (B. Sc.)

TEACHING EXPERIENCE

2016 Teaching Assistant – Department of Earth Sciences – University of New Brunswick
ESCI 1036 – Geology Lab for Foresters
ESCI 2321 – Structural Geology I

2011-2013 Teaching Assistant – Department of Earth Sciences – Laurentian University
GEOL 1007 – Introductory Geology II
GEOL 2006 – Field Geology I
GEOL 2127 – Optical Mineralogy (x3)
GEOL 3206 – Igneous Petrography

INDUSTRY EXPERIENCE

2016-2018 **Consulting geologist** – Gold Terra Resources Corp., Yellowknife, Northwest Territories

2015 **Drill geologist** – Northquest Ltd, Whale Cove, Nunavut

2015 **Lab assistant** – UNB, Fredericton, New Brunswick

2014 **Drill geologist** – Northquest Ltd, Whale Cove, Nunavut

2013 **Drill geologist** – Probe Mines Ltd, Chapleau, Ontario

2012 **Geologist-Researcher** – Northern Gold Mining Inc., Kirkland Lake, Ontario

2011 **Senior field and drill geologist** – Rainy River Resources, Fort Frances, Ontario

2010 **Senior field geologist** – Ontario Geologic Survey, Hungry Lake, Ontario

2009 **Assistant field geologist** – NB Dept. of Natural Resources, Sussex, New Brunswick

2008 **Assistant field geologist** – Rukwa Uranium, Northern Quebec